

Forschungsbericht 2025-11

Analysis and Modelling of Side Edge Noise from Wing Tips and Flaps

Karl-Stéphane Rossignol

Deutsches Zentrum für Luft- und Raumfahrt
Institut für Aerodynamik und Strömungstechnik
Braunschweig



DLR

Deutsches Zentrum
für Luft- und Raumfahrt

Forschungsbericht 2025-11

Analysis and Modelling of Side Edge Noise from Wing Tips and Flaps

Karl-Stéphane Rossignol

Deutsches Zentrum für Luft- und Raumfahrt
Institut für Aerodynamik und
Strömungstechnik
Braunschweig

208 Seiten
118 Bilder
6 Tabellen
137 Literaturstellen



Deutsches Zentrum
für Luft- und Raumfahrt



Herausgeber:

Deutsches Zentrum
für Luft- und Raumfahrt e. V.
Wissenschaftliche Information
Linder Höhe
D-51147 Köln

ISSN 1434-8454
ISRN DLR-FB-2025-11
Erscheinungsjahr 2025
DOI: [10.57676/fqme-t746](https://doi.org/10.57676/fqme-t746)

Erklärung des Herausgebers

Dieses Werk – ausgenommen anderweitig gekennzeichnete Teile – ist lizenziert unter den Bedingungen der Creative Commons Lizenz vom Typ Namensnennung 4.0 International (CC BY 4.0), abrufbar über <https://creativecommons.org/licenses/by/4.0/legalcode>

Lizenz



Creative Commons Attribution 4.0 International

Seitenkantenschall, Flügelspitzenlärm, Klappenlärm, Modellierung, Semi-empirisch, Wirbelschall, Flügelspitzenwirbel

Karl-Stéphane ROSSIGNOL

DLR, Institut für Aerodynamik und Strömungstechnik, Braunschweig

Analyse und Modellierung von Seitenkantenschall an Flügelspitzen und Klappen

Technische Universität Braunschweig

Diese Arbeit befasst sich mit der Ausarbeitung eines semi-empirischen Vorhersagemodells für akustische Emissionen von Klappenseitenkanten und Flügelspitzen. Eine Klappenseitenkante versteht sich hier als eine Extremität einer ausgefahrenen Hinterkantenklappe herkömmlicher Hochauftriebsflügel. Flügelspitzen beziehen sich auf das freie Ende eines Tragflächenprofils, ohne dass es Teil eines Hochauftriebsflügels ist.

In der vorliegenden Arbeit wird ein strömungsbasierter akustischer Modellierungsansatz gewählt, der sich von den in der Literatur verfügbaren geometriebasierten Standardvorhersageverfahren unterscheidet. Die geometriebasierte Methode liefert Vorhersagen über den abgestrahlten Schalldruck, dessen parametrische Abhängigkeiten durch eine Proportionalitätsbeziehung zu den charakteristischen geometrischen Abmessungen der Klappenseitenkante oder der Flügelspitze bestimmt werden. Beim strömungsbasierten Ansatz hingegen werden diese Beziehungen auf der Grundlage einer Analyse des spezifischen Strömungsfeldes der Klappenseitenkante oder der Flügelspitze ermittelt. Der Vorteil des letztgenannten Ansatzes ist eine größere Flexibilität bei der Vorhersage, insbesondere wenn er mit der Strömungsberechnung gekoppelt wird, um die erforderlichen Eingangsgrößen zu ermitteln. Dadurch wird der Anwendungsbereich des Vorhersageschemas erweitert, so dass unkonventionelle Flugzeugkonfigurationen besser berücksichtigt werden können.

Eine besondere Herausforderung bei der Etablierung eines solchen strömungsbasierten Vorhersageansatzes liegt in der Definition von Metriken, die in engem Zusammenhang mit den Schallquellenmechanismen stehen. Zu diesem Zweck wurden umfangreiche experimentelle aeroakustische Untersuchungen an zwei freitragenden Klappenmodellen (Maßstab 1:1 und 1:1,6) sowie an einem Hochauftriebsflügel (Maßstab 1:6,33) durchgeführt, um die erforderliche Strömungsfeld- und Akustikdatenbasis für die Entwicklung des Vorhersageverfahrens zu schaffen.

Strömungsdaten im Nahfeld wurden mit Hilfe der Sieben-Loch-Sonden-Messtechnik am Klappenmodell im Maßstab 1:1,6 erfasst. Diese Daten ermöglichten eine Quantifizierung des mittleren Strömungsfeldes an der Spitze als Funktion der Klappenbelastung, d. h. im Vergleich zum Klappenwinkel, und die Identifizierung von Bereichen, die von starken Strömungsgradienten entlang der Klappenränder dominiert werden. Es wird angenommen, dass es sich bei diesen Bereichen um Zentren hoher Turbulenzaktivität und Schallerzeugung handelt, die durch lokale charakteristische Wirbellängen und -geschwindigkeiten gekennzeichnet sind. Diese Skalen stehen in einem linearen Zusammenhang mit der Klappenbelastung, d. h. mit dem Auftriebskoeffizienten, oder mit der Wirbelzirkulation an der Spitze. Beide Parameter lassen sich leicht aus RANS-Berechnungen gewinnen.

Die akustischen Untersuchungen wurden sowohl mit Standard-Freifeldmikrofonmessungen des Fernfeldschalls als auch mit der Phased-Microphone-Array-Technik durchgeführt. Insbesondere wurde ein speziell angefertigtes traversierbares Phased Array mit kleiner Apertur verwendet, um Messungen der akustischen Richtwirkung des 1:1,6 Kragflügelmodells durchzuführen. Die gemessenen Geräuschintensitäten sind proportional zur 5,5-ten Potenz der charakteristischen Geschwindigkeit für den niederfrequenten Teil des Spektrums und proportional zur 6,5-ten Potenz der charakteristischen Geschwindigkeit für den hochfrequenten Teil. Die Ergebnisse der Richtwirkungsmessung zeigen, dass das gemessene ausgeprägte rückwärtige Strahlungsmaximum der niederfrequenten Spektraldaten nicht mit dem klassischen Mechanismus der Kantenstreuung von Strömungsturbulenzen übereinstimmt. Die Schallabstrahlung kann auf eine Mischung aus klassischer Kantenstreuung in Kombination mit instationären Kraftschwankungen am Profil als Folge von Wirbelinstabilität und Schallwellenbeugung zurückgeführt werden. Bei hohen Frequenzen skalieren die Spektraldaten nach einem Proportionalitätsgesetz mit einem 6,5-ten Potenzexponenten der charakteristischen

Geschwindigkeit, was der typischen dipolartigen Quellenstrahlung nahekommt. Es wurde gezeigt, dass der maximale Schalldruckpegel mit der Verschmelzung von primärem und sekundärem Wirbel zusammenhängt, wodurch das Strömungsfeld starken, plötzlichen, lokalen Fluktuationen ausgesetzt wird. Dies deutet auf eine Kombination aus klassischer Kantenstreuung und quadropolartiger Schallerzeugung durch intensive und stark instationäre Kraftschwankungen auf dem Profil als Folge der Wirbelinstabilität während des Verschmelzungsprozesses hin. Die Richtcharakteristiken deuten auch auf eine mögliche Abschirmung der Schallquelle durch den Flügel hin, was zu einem rückwärtigen Maximum der Abstrahlung führt.

Auf der Grundlage der obigen Erkenntnisse wird ein empirisches Vorhersageschema vorgeschlagen, das anhand der gemessenen Schallabstrahlung einer großen Anzahl von Windkanalmodellen unterschiedlicher Komplexität, Geometrie und Größe validiert wird. Die hier vorgelegten Ergebnisse zeigen, dass die Kenntnis der globalen Eigenschaften des Strömungsfeldes um eine Klappenseitenkante oder Flügelspitze für die Vorhersage der Schallemissionen in einer Vielzahl von Fällen ausreicht.

Side edge noise, wing tip noise, flap noise, modelling, semi-empirical, vortex sound, wing tip vortex

(Published in English)

Karl-Stéphane ROSSIGNOL

German Aerospace Center (DLR), Institute of Aerodynamics and Flow Technology,
Braunschweig

Analysis and Modelling of Side Edge Noise from Wing Tips and Flaps

Technische Universität Braunschweig

This thesis deals with the elaboration of a semi-empirical prediction scheme for the acoustic emissions from flap side-edges and wing tips. More specifically, a flap side-edge is recognized as one of the free ends of a deployed trailing-edge flap as part of conventional high-lift devices. In comparison, wing tips refer to the free end of an airfoil of some type without it being included as part of a high-lift device.

In the present effort, a flow-based acoustic modelling approach is adopted which differs from standard geometry-based prediction schemes available in the literature. The geometry-based method provides predictions of the radiated acoustic pressure whose parametric dependencies are determined by some proportionality relationship to characteristic geometric dimensions of the flap side-edge or wing tip. On the other end, the flow-based approach established those relationship based on an analysis of the specific flap side-edge or wing tip flow field. The advantage of the last approach is an increased prediction flexibility, especially when coupled with computational fluid dynamics to gather the necessary input flow quantities. It thus extends the applicability range of the prediction scheme to better deal with unconventional aircraft configurations.

A particular challenge in the establishment of such a flow-based prediction approach lies in the definition of metrics closely related to the sound source mechanisms. To this end, extensive experimental aeroacoustics investigations were performed at two cantilever flap models (1:1 and 1:1.6 scales) as well as at a high-lift wing (1:6.33 scale) to provide the necessary flow field and acoustic database for the development of the prediction scheme. Because of its central importance to the noise radiation problem, much attention is also given to the characterization of the tip vortex and its formation process.

Near field flow data was gathered using the seven-hole probe measurement technique at the 1:1.6 scale flap model. This data enabled a quantification of the tip mean flow field as a function of flap loading, i.e. vs. flap deployment angle, and the identification of regions dominated by large mean flow gradients along the flap edges. These regions are hypothesized to be centers of high turbulence activity and sound production, characterized by local vortex characteristic length and velocity scales. Those scales are found to relate linearly with variations in flap loading, i.e. its lift coefficient, or tip vortex circulation. Through linear regression analysis, parametric relationships were devised which should simplify greatly the task of comparing results from similar experiments done in different wind tunnel environment and using different wing models. Furthermore, a wing's lift coefficient or its tip vortex circulation are parameters which can be easily obtained from RANS computations.

The acoustic investigations were performed using both standard free-field microphone measurements of the far-field sound as well as the phased microphone array technique. In particular, a custom-made traversable small aperture phased array was utilized to performed measurements of the acoustic directivity of the 1:1.6 scale cantilever flap model. The acoustic data for this configuration are found to be broadband in nature with a maximum noise level at a frequency of approximately 0.8 kHz. Measured noise intensities are proportional to the 5.5th power of the characteristic velocity for the low-frequency part of the spectrum and proportional to the 6.5th power of the characteristic velocity for its high-frequency part. The directivity measurement results indicate that the measured distinct rear-arc radiation maximum of the low frequencies spectral data is not consistent with the classical mechanism of edge scattering of flow turbulence which would imply a cardioid directivity with a maximum in upstream direction. The sound radiation can be attributed to a mixture of classical edge scattering in combination with unsteady force fluctuations on the airfoil as a consequence of vortex unsteadiness and sound

wave diffraction. At high frequencies, spectral data scale according to a proportionality law with a 6.5th power exponent of the characteristic velocity, which is close to the typical dipole-like source radiation. It was shown that the maximum sound pressure level, found at 3.15 kHz, is related to the merging of the primary tip vortex (forming on the tip face) with the secondary vortex (forming on the airfoil's suction side), subjecting the flow field to strong sudden local fluctuations. This suggests as source mechanism, a combination of classical edge scattering and quadrupole-like sound generation due to intense and highly unsteady force fluctuations on the airfoil as a result of vortex unsteadiness during the merging process. The directivity patterns indicate also a possible shielding of the acoustic source by the wing leading to rear-arc maximum in radiation.

Based on the above findings an empirical prediction scheme is proposed which is validated against the measured noise radiation from a large set of wind tunnel models of various complexity, geometries and scale. The results provided herein demonstrate that a knowledge of the bulk characteristics of the flow field about a flap side-edge or wing tip is sufficient for the prediction of the sound emission in a wide range of cases.

TU Braunschweig – Niedersächsisches
Forschungszentrum für Luftfahrt

Berichte aus der Luft- und Raumfahrttechnik

Forschungsbericht 2025-06

Analysis and Modelling of Side Edge Noise from Wing Tips and Flaps

Karl-Stéphane Rossignol

Deutsches Zentrum für Luft- und Raumfahrt
Institut für Aerodynamik und Strömungstechnik
DLR Braunschweig

Diese Veröffentlichung wird gleichzeitig in der Berichtsreihe „NFL
- Forschungsberichte“ geführt.

Diese Arbeit erscheint gleichzeitig als von der Fakultät für Maschinenbau der Technischen Universität Carolo-Wilhelmina zu Braunschweig zur Erlangung des akademischen Grades eines Doktor-Ingenieurs genehmigte Dissertation.

Analysis and Modelling of Side Edge Noise from Wing Tips and Flaps

Von der Fakultät für Maschinenbau
der Technischen Universität Braunschweig

zur Erlangung der Würde

eines Doktor-Ingenieurs (Dr.-Ing.)
genehmigte Dissertation

von: Karl-Stéphane Rossignol M.Sc.

geboren in: Gaspé, Kanada

eingereicht am: 29.10.2024

mündliche Prüfung am: 7.3.2025

Vorsitz: Prof. Dr.-Ing. Jens Friedrichs

Gutachter: Prof. Dr.-Ing. Jan Werner Delfs

Gutachter: Prof. Dr.-Ing. Sabine C. Langer

2025

Abstract

This thesis deals with the elaboration of a semi-empirical prediction scheme for the acoustic emissions from flap side-edges and wing tips. More specifically, a flap side-edge is recognized as one of the free end of a deployed trailing-edge flap as part of conventional high-lift devices. In comparison, wing tips refer to the free end of an airfoil of some type without it being included as part of a high-lift device.

In the present effort, a flow-based acoustic modelling approach is adopted which differs from standard geometry-based prediction schemes available in the literature. The geometry-based method provides predictions of the radiated acoustic pressure whose parametric dependencies are determined by some proportionality relationship to characteristic geometric dimensions of the flap side-edge or wing tip. On the other end, the flow-based approach established those relationship based on an analysis of the specific flap side-edge or wing tip flow field. The advantage of the last approach is an increased prediction flexibility, especially when coupled with computational fluid dynamics to gather the necessary input flow quantities. It thus extends the applicability range of the prediction scheme to better deal with unconventional aircraft configurations.

A particular challenge in the establishment of such a flow-based prediction approach lies in the definition of metrics closely related to the sound source mechanisms. To this end, extensive experimental aeroacoustics investigations were performed at two cantilever flap models (1:1 and 1:1.6 scales) as well as at a high-lift wing (1:6.33 scale) to provide the necessary flow field and acoustic database for the development of the prediction scheme. Because of its central importance to the noise radiation problem, much attention is also given to the characterization of the tip vortex and its formation process.

Near field flow data was gathered using the seven-hole probe measurement technique at the 1:1.6 scale flap model. This data enabled a quantification of the tip mean flow field as a function of flap loading, i.e. vs. flap deployment angle, and the identification of regions dominated by large mean flow gradients along the flap edges. These regions are hypothesized to be centers of high turbulence activity and sound production, characterized by local vortex characteristic length and velocity scales. Those scales are found to relate linearly with variations in flap loading, i.e. its lift coefficient, or tip vortex circulation. Through linear regression analysis, parametric relationships were devised which should simplify greatly the task of comparing results from similar experiments done in different wind tunnel environment and using different wing models. Furthermore a wing's lift coefficient or its tip vortex circulation are parameters which can be easily obtained from RANS computations.

The acoustic investigations were performed using both standard free-field microphone measurements of the far-field sound as well as the phased microphone array technique. In particular, a custom-made traversable small aperture phased array was utilized to performed measurements of the acoustic directivity of the 1:1.6 scale cantilever flap model. The acoustic data for this configuration are found to be broadband in nature with a maximum noise level at a frequency of approximately 0.8 kHz. Measured noise intensities are proportional to the 5.5th power of the characteristic velocity for the low-frequency part of the spectrum and proportional to the 6.5th power of the characteristic velocity for its high-frequency part. The directivity measurement results indicate that the measured distinct rear-arc radiation maximum of the low frequencies spectral data is not consistent

with the classical mechanism of edge scattering of flow turbulence which would imply a cardioid directivity with a maximum in upstream direction. The sound radiation can be attributed to a mixture of classical edge scattering in combination with unsteady force fluctuations on the airfoil as a consequence of vortex unsteadiness and sound wave diffraction. At high frequencies, spectral data scale according to a proportionality law with a 6.5th power exponent of the characteristic velocity, which is close to the typical dipole-like source radiation. It was shown that the maximum sound pressure level, found at 3.15 kHz, is related to the merging of the primary tip vortex (forming on the tip face) with the secondary vortex (forming on the airfoil's suction side), subjecting the flow field to strong sudden local fluctuations. This suggests as source mechanism, a combination of classical edge scattering and quadrupole-like sound generation due to intense and highly unsteady force fluctuations on the airfoil as a result of vortex unsteadiness during the merging process. The directivity patterns indicate also a possible shielding of the acoustic source by the wing leading to rear-arc maximum in radiation.

Based on the above findings an empirical prediction scheme is proposed which is validated against the measured noise radiation from a large set of wind tunnel models of various complexity, geometries and scale. The results provided herein demonstrate that a knowledge of the bulk characteristics of the flow field about a flap side-edge or wing tip is sufficient for the prediction of the sound emission in a wide range of cases.

Zusammenfassung

Diese Arbeit befasst sich mit der Ausarbeitung eines semi-empirischen Vorhersagemodells für akustische Emissionen von Klappenseitenkanten und Flügelspitzen. Eine Klappenseitenkante versteht sich hier als eine Extremität einer ausgefahrenen Hinterkantenklappe herkömmlicher Hochauftriebsflügel. Flügelspitzen beziehen sich auf das freie Ende eines Tragflächenprofils, ohne dass es Teil eines Hochauftriebsflügels ist.

In der vorliegenden Arbeit wird ein strömungsbasierter akustischer Modellierungsansatz gewählt, der sich von den in der Literatur verfügbaren geometriebasierten Standardvorhersageverfahren unterscheidet. Die geometriebasierte Methode liefert Vorhersagen über den abgestrahlten Schalldruck, dessen parametrische Abhängigkeiten durch eine Proportionalitätsbeziehung zu den charakteristischen geometrischen Abmessungen der Klappenseitenkante oder der Flügelspitze bestimmt werden. Beim strömungsbasierten Ansatz hingegen werden diese Beziehungen auf der Grundlage einer Analyse des spezifischen Strömungsfeldes der Klappenseitenkante oder der Flügelspitze ermittelt. Der Vorteil des letztgenannten Ansatzes ist eine größere Flexibilität bei der Vorhersage, insbesondere wenn er mit der Strömungsberechnung gekoppelt wird, um die erforderlichen Eingangsgrößen zu ermitteln. Dadurch wird der Anwendungsbereich des Vorhersageschemas erweitert, so dass unkonventionelle Flugzeugkonfigurationen besser berücksichtigt werden können.

Eine besondere Herausforderung bei der Etablierung eines solchen strömungsbasierten Vorhersageansatzes liegt in der Definition von Metriken, die in engem Zusammenhang mit den Schallquellenmechanismen stehen. Zu diesem Zweck wurden umfangreiche experimentelle aeroakustische Untersuchungen an zwei freitragenden Klappenmodellen (Maßstab 1:1 und 1:1,6) sowie an einem Hochauftriebsflügel (Maßstab 1:6,33) durchgeführt, um die erforderliche Strömungsfeld- und Akustikdatenbasis für die Entwicklung des Vorhersageverfahrens zu schaffen.

Strömungsdaten im Nahfeld wurden mit Hilfe der Sieben-Loch-Sonden-Messtechnik am Klappenmodell im Maßstab 1:1,6 erfasst. Diese Daten ermöglichten eine Quantifizierung des mittleren Strömungsfeldes an der Spitze als Funktion der Klappenbelastung, d. h. im Vergleich zum Klappenwinkel, und die Identifizierung von Bereichen, die von starken Strömungsgradienten entlang der Klappenränder dominiert werden. Es wird angenommen, dass es sich bei diesen Bereichen um Zentren hoher Turbulenzaktivität und Schallerzeugung handelt, die durch lokale charakteristische Wirbellängen und -geschwindigkeiten gekennzeichnet sind. Diese Skalen stehen in einem linearen Zusammenhang mit der Klappenbelastung, d. h. mit dem Auftriebskoeffizienten, oder mit der Wirbelzirkulation an der Spitze. Beide Parameter lassen sich leicht aus RANS-Berechnungen gewinnen.

Die akustischen Untersuchungen wurden sowohl mit Standard-Freifeldmikrofonmessungen des Fernfeldschalls als auch mit der Phased-Microphone-Array-Technik durchgeführt. Insbesondere wurde ein speziell angefertigtes traversierbares Phased Array mit kleiner Apertur verwendet, um Messungen der akustischen Richtwirkung des 1:1,6 Kragflügelmodells durchzuführen. Die gemessenen Geräuschintensitäten sind proportional zur 5,5-ten Potenz der charakteristischen Geschwindigkeit für den niederfrequenten Teil des Spektrums und proportional zur 6,5-ten Potenz der charakteristischen Geschwindigkeit für den hochfrequenten Teil. Die Ergebnisse der Richtwirkungsmessung zeigen, dass das gemessene ausgeprägte rückwärtige Strahlungsmaximum der niederfrequenten Spektraldaten nicht mit dem klassischen Mechanismus der Kantenstreuung von Strömungsturbulenzen über-

einstimmt. Die Schallabstrahlung kann auf eine Mischung aus klassischer Kantenstreuung in Kombination mit instationären Kraftschwankungen am Profil als Folge von Wirbelinstabilität und Schallwellenbeugung zurückgeführt werden. Bei hohen Frequenzen skalieren die Spektraldaten nach einem Proportionalitätsgesetz mit einem 6,5-ten Potenzexponenten der charakteristischen Geschwindigkeit, was der typischen dipolartigen Quellenstrahlung nahekommt. Es wurde gezeigt, dass der maximale Schalldruckpegel mit der Verschmelzung von primärem und sekundärem Wirbel zusammenhängt, wodurch das Strömungsfeld starken, plötzlichen, lokalen Fluktuationen ausgesetzt wird. Dies deutet auf eine Kombination aus klassischer Kantenstreuung und quadrupolartiger Schallerzeugung durch intensive und stark instationäre Kraftschwankungen auf dem Profil als Folge der Wirbelinstabilität während des Verschmelzungsprozesses hin. Die Richtcharakteristiken deuten auch auf eine mögliche Abschirmung der Schallquelle durch den Flügel hin, was zu einem rückwärtigen Maximum der Abstrahlung führt.

Auf der Grundlage der obigen Erkenntnisse wird ein empirisches Vorhersageschema vorgeschlagen, das anhand der gemessenen Schallabstrahlung einer großen Anzahl von Windkanalmodellen unterschiedlicher Komplexität, Geometrie und Größe validiert wird. Die hier vorgelegten Ergebnisse zeigen, dass die Kenntnis der globalen Eigenschaften des Strömungsfeldes um eine Klappenseitenkante oder Flügelspitze für die Vorhersage der Schallemissionen in einer Vielzahl von Fällen ausreicht.

Acknowledgements

The thesis was completed in the course of my duties as a research scientist at DLR's Institute of Aerodynamics and Flow Technology in Braunschweig and certainly would not have been completed without the support of numerous individuals. Firstly, I would like to thank my supervisor, Prof. Jan Delfs, for giving me the chance to attempt this project and for his invaluable technical support. I am also more than grateful to my colleagues at DLR's Technical Acoustic Branch for their technical and personal support throughout those years. Special thanks go to Michaela Herr, Michael Pott-Pollenske, Heino Buchholz, Daniela Almonet, Jan Täger and Detlef Martin. Also, not to be forgotten, the exceptional mental support from my former colleague and "Ph.D. teammate" Dirk Franke as well as my office mate Nan Hu.

Last but not least, I am greatly indebted to my wonderful wife Katja, for her patience and support in the course of this long endeavor, and to my fantastic kids; in order of appearance: Julika, Mathilde and Janosch.

Contents

Nomenclature	12
1. Introduction	22
1.1. Background and Motivation	22
1.2. State-of-the-Art Semi-Empirical Modelling of FSE Noise	24
1.3. Scope and Research Objectives	27
2. Current Knowledge on Flap Side-Edge Noise	29
2.1. Tip Vortices and their Relation to the FSE Noise Problem	29
2.1.1. Near Field Characteristics	29
2.1.2. Far-Field Characteristics	34
2.2. Theoretical Approaches	34
2.2.1. Source Mechanisms Based on Lighthill’s Analogy	35
2.2.2. Source Mechanisms Based on Vortex Sound Theory	37
2.3. Experimental Investigations on FSE Noise	39
2.3.1. Practical Relevance of Flap Side-Edge Noise	40
2.3.2. FSE noise at Free Wing Tips	41
2.3.3. FSE Noise in High-Lift Wing Configurations	44
2.3.4. On the Role of the Flap Tip Geometry	47
2.3.5. Noise Reduction Concepts and their Relation to the Source Mechanisms	49
3. Investigations	51
3.1. Experimental Strategy	51
3.2. Wind Tunnels	51
3.3. Reference Test Cases	53
3.3.1. Setup 1: Cantilever Wing	53
3.3.2. Setup 2: High-Lift Wing Configuration	55
3.4. Complementary Test Cases	56
3.4.1. Tip Geometry Modifications and Leading-Edge Add-On	58
3.4.2. Wing Profile and Aspect ratio Variations	58
3.4.3. Reynolds Number and Tip Raking Variations	59
4. Data Acquisition and Post-Processing	63
4.1. Far-Field Noise Measurements	63
4.2. Microphone Array Measurements	64
4.2.1. Microphone Layouts and Systems Characteristics	65
4.2.2. Conventional Beamforming	68
4.2.3. CLEAN-SC	73

4.2.4.	Data Quality	75
4.3.	Aerodynamic Measurements	76
4.3.1.	7-hole Probe Flow Measurements	76
4.3.2.	Static Pressure Measurements	77
5.	Results of the Flow Investigations	79
5.1.	Reference Cantilever Wing: Flow Visualization	79
5.2.	Global Characteristics of the Tip Flow Field	84
5.3.	Static Pressure Distributions	87
5.4.	Aeroacoustic Source Regions	87
5.4.1.	Flat-Tip, Sharp-Edge FSE	88
5.4.2.	Complementary Test Cases	95
5.5.	Summary of findings	99
6.	Results of the Acoustic Investigations	100
6.1.	Cantilever Wing Configurations	100
6.1.1.	Source Maps, Noise Spectra and Scaling Parameters	100
6.1.2.	Effect of Model Scale	109
6.1.3.	Effect of Tip Raking	109
6.1.4.	Effect of Tip Geometry Variations and LE Vane Add-On	113
6.1.5.	Effect of Profile Shape	115
6.1.6.	Source Directivity	118
6.2.	High-Lift Wing Configurations	128
6.2.1.	Source Maps and Interated Noise Spectra	128
6.2.2.	Source Directivity	130
6.2.3.	Effect of Airfoil Profile	136
6.3.	Summary of Findings	138
7.	Semi-Empirical Prediction Scheme for Flap Side Edge Noise	141
7.1.	Theoretical Background	141
7.2.	Application and Validation	147
7.2.1.	Reference Configurations	148
7.2.2.	Complementary Test Cases, Profile Variations	151
7.2.3.	Complementary Test Cases, Tip Shape Variations	152
7.2.4.	Complementary Test Cases, Leading Edge Vane	152
7.2.5.	Concluding Remarks and Unresolved Issues	152
8.	Conclusion and Perspectives	154
8.1.	Motivation and Goal of the Work	154
8.2.	Experimental Strategy	154
8.3.	Novel Results Derived from the Present Investigations	155
8.4.	Open Questions and Perspectives	157
A.	Experimental Setups	159
B.	Static Pressure Distributions	165

C. Spectral Results for Various Tip Modifications	171
D. Beamforming Source Maps for Various Tip Modifications	180
E. Effect of Tip Add-ons and Geometry on FSE Noise Directivity	187
F. Phased Array Source Maps From DNW-NWB Experiment	194

Nomenclature

C_L	Lift coefficient, $C_L = L/(0.5\rho U_0^2 A)$	-
C_p	Pressure coefficient, $C_p = (p - p_0)/(0.5\rho U_0^2)$	-
$D(\varphi_x, \varphi_y)$	Directivity function	-
$L_{p,1/3,n}$	Normalized 1/3-octave band sound pressure level	dB
$L_{p,1/3}$	1/3-octave band sound pressure level	dB
M_0	Mach number, $= U_0/a_0$	-
M_m	Mach number, $= U_m/a_0$	-
Re	Reynolds number, $= U_0 c/\nu$	-
St	Strouhal number, $= fl/u$	-
St_0	Strouhal number, $= fc/U_0$	-
St_c	Strouhal number, $= fc/U_c$	-
St_d	Strouhal number, $= fd/U_d$	-
U	Mean flow velocity scale	-
U_0	Free-stream velocity	m/s
U_c	Cross-flow velocity	m/s
U_0	Free stream velocity	m/s
U_{cv}	Convection velocity of turbulent eddies	m/s
U_m	Maximum velocity along lower tip edge [19]	m/s
U_{ref}	Reference velocity scale	m/s
\mathbf{x}	3D spatial coordinates ($\mathbf{x} = x_i = x_1\hat{e}_1 + x_2\hat{e}_2 + x_3\hat{e}_3$)	m
ω	Radial frequency ($\omega = 2\pi f$)	Radian
a_0	Speed of sound	m/s
c	Flap chord length	m

d	Flap maximum thickness	m
f	Third-octave band central frequency	Hz
f_c	Third-octave band central frequency	Hz
l	Length scale	m
l_i	Noise source correlation length scale	m
p	Pressure	Pa
r, R	Reference distance	m
α	Main element angle of attack	°
β_{cv}	Angle between U_0 and U_{cv}	°
δ^*	Boundary displacement thickness	m
δ_S	Slat deflection angle	°
δ_F	Flap deflection angle	°
ν	Kinematic viscosity	m ² /s
ϕ	Azimuthal angle	°
ρ	Density of air	kg/m ³
θ	Polar angle	°
φ_x	Azimuthal angle rel. to the free-stream direction	°
φ_y	Polar angle	°

List of Figures

1.1.	Major sources of airframe noise during approach and landing. Courtesy of Michael Pott-Pollenske, DLR.	23
2.1.	Vortex filament, with circulation Γ , moving about a semi-infinite half-plane along the dashed path. The plane occupies the domain $y_2 = 0, y_1 < 0$. Sketch from Howe [70]. Lines of constant Ψ represent streamlines of a hypothetical potential flow around the half-plane.	36
2.2.	Vortex ring, with circulation Γ , passing near a semi-infinite half-plane along a linear path. The plane occupies the domain $y_2 = 0, y_1 < 0$. Sketch from Kambe et al. [76]. Lines of constant Ψ represent streamlines of an hypothetical potential flow around the half-plane.	39
2.3.	Sketch of the tip vortex flow field and corresponding surface pressure distributions	42
2.4.	Sketch of postulated aeroacoustic noise source mechanisms. At each section cut, a typical instantaneous distribution of vorticity is shown in the inserts. Red spots correspond to positive vorticity while the blue spots are for negative vorticity.	42
3.1.	Acoustic Wind Tunnel Braunschweig (AWB).	52
3.2.	Low-Speed Wind Tunnel Braunschweig (NWB).	53
3.3.	General AWB coordinate system definition. Origin is the nozzle center point.	54
3.4.	Experimental models	55
3.5.	Static pressure taps positions.	56
3.6.	Microphone arrays. a),c) Cantilever flap model installed. b) high-lift wing installed ($\delta_f = 0^\circ$).	57
3.7.	Wind-tunnel model and add-ons.	58
3.8.	Geometry of the tested wing models.	59
3.9.	Cantilever DU96 airfoil and Clark-Y wing with part-span square tip flap, experimental setups in AWB. In (b), the part-span flap also has a Clark-Y profile. Its tip, shown in white, is exchangeable. It was tested, however, only with a square tip.	60
3.10.	Large scale wing in the open test section of the DNW-NWB low-speed wind tunnel. Reference configuration, rectangular planform.	61
3.11.	Large scale model. Details of the models geometries. Baseline wing represented by the dashed lines. The raked-tip wing is represented by the solid lines. For each geometry, dimensions are given in meters.	62
4.1.	Fly-over coordinate system definition	63

4.2. Microphone array layouts. AWB small aperture array: 48 microphones (0.47 m). AWB large aperture array: 96 microphones (0.97 m).	66
4.3. Small directional phased array positions (empty dots) used for directivity measurements in AWB	67
4.4. Microphone array's PSF. Theoretical calculations based on the actual experimental microphone distributions and for a single point source located at $\mathbf{x} = [0, 0, 0]$. Levels are normalized by the maximum value at $\mathbf{x} = [0, 0, 0]$. $w_{1/2}$ is the half-width of the PSF main lobe, 3dB down from its maximum. Twice this value ($2w_{1/2}$) gives the theoretical minimum separation between two incoherent noise source which can be resolved.	68
4.5. Evaluation of the AWB large aperture phased array resolution using two loudspeakers (L1, L2). L1 is located at $\mathbf{x} = [0.0, 0.2, 0.0]$ and is held fixed. L2 is free to move in y , away from L1. Post-processing using the CLEAN-SC algorithm, with a constant integration domain around L1. Left, comparison of the absolute spectra for L1 alone vs. the phased array central microphone. Right, difference in integrated power levels for L1 vs. loudspeaker separation relative to L1 when both L1 and L2 are turned on.	69
4.6. Principle of operation of the delay-and-sum algorithm.	70
4.7. Reference high-lift wing configuration. 2D source maps, $f_c = 6.3$ kHz. Conventional beamforming without DR (left) and with DR (right). The integration region is shown by the dashed line.	71
4.8. Reference cantilever flap. 2D source maps, $f_c = 6.3$ kHz. Conventional beamforming without DR (left) and with DR (right). The integration region is shown by the dashed line.	72
4.9. 2D source maps at $f_c = 6.3$ kHz, with diagonal removal. Conventional beamforming (left) versus CLEAN-SC deconvolution (right). $\alpha_g = 0^\circ$, $\delta_F = 34^\circ$, $U_0 = 60$ m/s. The integration region is shown by the dashed line.	74
4.10. 7-hole pressure probe measurement technique.	77
5.1. Surface streaklines visualization on the tip face. Approximative streaklines are sketched. (a) $\delta_F = 20^\circ$. (b) $\delta_F = 25^\circ$. (c) $\delta_F = 30^\circ$	81
5.2. Surface streaklines visualization. Approximative streaklines are sketched. $\delta_F = 20^\circ$. (a) Pressure side. (b) Suction side.	82
5.3. Surface streaklines visualization. Approximative streaklines are sketched. $\delta_F = 25^\circ$. (a) Pressure side. (b) Suction side.	82
5.4. Surface streaklines visualization. Approximative streaklines are sketched. $\delta_F = 30^\circ$. (a) Pressure side. (b) Suction side.	83
5.5. Measured vortex core path vs. δ_F . (a) Top view. (b) Side view. The blue symbols refer to vortices originating from the lower edge and the red symbols to those originating from the upper edge.	85
5.6. Mean flow field at the wing tip, $\delta_F = 20^\circ$, $M_0 = 0.18$. The measurement planes are chord-normal. Wing geometry shown in grey. White patches in the contours plots are due to data rejection in the experiment, where flow angularity exceeds the range of the 7-hole probe technique. Velocity vector components displayed in the wind tunnel coordinate system, see figure 4.10b	86

5.7.	Static pressure distributions at mid span and at the model tip face. $U_0 = 60$ m/s In the top figure, empty symbols are used for the pressure side measurements while solid symbols correspond to measurements at the suction side.	88
5.8.	Streamwise evolution of the mean flow velocity components at the pressure side edge. The x/c positions where characteristic velocity scale, $u = \sqrt{U_2'^2 + U_3'^2}$, is picked is shown by the solid symbols.	90
5.9.	Streamwise evolution of the mean flow velocity components at the pressure side edge. reference wing vs. metal foam tip for varying porous extents. . .	91
5.10.	Streamwise evolution of the mean flow vector components at the suction side edge. Between $x/c = 0.4$ and $x/c = 0.6$, missing experimental data are obtained through extrapolation using best-fits.	92
5.11.	Characteristic velocity scales. Reference wing.	94
5.12.	Measured vortex circulation at $x/c = 1.1$ vs. δ_F and the characteristic velocity scales, $u = \sqrt{U_2'^2 + U_3'^2}$ at the pressure side and suction side. . . .	94
5.13.	Characteristic velocities vs. C_L . Left; lift polar according to CFD results in [13]. A δ_F correction between the AWB and free-field conditions is given as $\Delta\delta_F = -3.9C_L - 0.56$	95
5.14.	Left, measured lift polars for all configurations. Right, distribution of surface static pressure coefficient (C_p) vs. normalized streamwise position (x/c) for selected δ_F . In each inset three C_p distributions are plotted, respectively for the configurations without (A) and with (B) vane.	96
5.15.	Comparison of the normalized cross-flow velocity magnitude near the tip lower edge for two values of δ_F . The velocity vector components are projected onto a wing-fixed coordinate system.	97
5.16.	Maximum value of the spanwise velocity magnitude vs. δ_F . Dashed line: linear regression.	98
6.1.	Microphone array noise maps, side view, 1/3-octave band frequencies. $M_0 = 0.18$. The model is represented by the solid black line.	101
6.2.	Microphone array noise maps, bottom view, 1/3-octave band frequencies. $M_0 = 0.18$. The model is represented by the solid black line.	102
6.3.	Solid vs. porous FSE noise, comparison of small and large array results. 1/3-octave band integrated SPL spectra. Bottom view power integration performed over the range $0.2 \text{ m} \leq x \leq 1.0 \text{ m}$ and $-0.2 \text{ m} \leq y \leq 0.2 \text{ m}$. Side view power integration performed over the range $0.2 \text{ m} \leq x \leq 1.0 \text{ m}$ and $-0.6 \text{ m} \leq z \leq 0.6 \text{ m}$. The shaded regions indicate the frequency limits of the measurements.	105
6.4.	Integrated noise spectra, comparison of small aperture and large aperture arrays. Bottom view, 1/3-octave band frequencies. Symbols : Small aperture array. Lines : large aperture array.	106
6.5.	Integrated noise spectra, comparison of small aperture and large aperture arrays. Side view, 1/3-octave band frequencies. Symbols : Small aperture array. Lines : large aperture array.	106
6.6.	Scaled integrated noise spectra. Bottom view, 1/3-octave band frequencies.	107
6.7.	Scaled integrated noise spectra. Side view, 1/3-octave band frequencies. . .	108

6.8.	Large scale cantilever flap model. Scaled integrated noise spectra. Bottom view, 1/3-octave band frequencies. δ_F increased by $+2^\circ$ when scaling the full-scale model data compared to the reference cantilever wing data. Geometrical δ_F given in the figures. Solid line indicates scaled results for the reference cantilever wing at $\delta_F = 25^\circ$ and $M_0 = 0.18$	111
6.9.	Schematic representation of the tip vortex path on a rectangular and a raked-tip planform according to [87]	111
6.10.	Large scale cantilever flap model. Effect of δ_F , baseline vs. raked tip. Integrated noise spectra. Bottom view, 1/3-octave band frequencies.	112
6.11.	Relative noise impact of the different tip add-ons. Noise spectra measured with the phased array for various flap deflections. $M_0 = 0.18$. Reference spectrum: baseline configuration. Fly-over measurement position, i.e. $\varphi_x = 90^\circ$, $\varphi_y = 0^\circ$, e.g. figure 4.1.	115
6.12.	Relative noise impact of the different add-ons ($\Delta L_{p,1/3}$ dB). Noise spectra measured with the phased array for various flap deflections. $M_0 = 0.18$. Reference spectrum: baseline configuration. Side-line measurement position, i.e. $\varphi_x = 90^\circ$, $\varphi_y = 90^\circ$, e.g. figure 4.1.	116
6.13.	Clark-Y airfoil. Scaled integrated noise spectra. Bottom view, 1/3-octave band frequencies.	117
6.14.	DU96 wing model. Scaled integrated noise spectra. Bottom view, 1/3-octave band frequencies.	118
6.15.	Noise directivity maps vs. St_0 . $M_0 = 0.15$. Maximum angle range given in upper left plot $\rightarrow A : \phi = 0^\circ, \theta = 90^\circ$; $B : \phi = 40^\circ, \theta = 0^\circ$; $C : \phi = 0^\circ, \theta = -90^\circ$; $D : \phi = -20^\circ, \theta = 0^\circ$	122
6.16.	Noise directivity maps vs. St_0 . $M_0 = 0.18$. Maximum angle range given in upper left plot $\rightarrow A : \phi = 0^\circ, \theta = 90^\circ$; $B : \phi = 40^\circ, \theta = 0^\circ$; $C : \phi = 0^\circ, \theta = -90^\circ$; $D : \phi = -20^\circ, \theta = 0^\circ$	123
6.17.	Large scale cantilever wing reference configuration. Contours of constant relative sound pressure levels as a function of emission angles and δ_F and $M_0 = 0.21$. Levels are normalized by the level measured at the position marked by the black "cross" mark at $\varphi_x = 90^\circ$, $\varphi_y = 0^\circ$	124
6.18.	Large scale cantilever wing sweep configuration. Contours of constant relative sound pressure levels as a function of emission angles and δ_F and $M_0 = 0.21$. Levels are normalized by the level measured at the position marked by the black "cross" mark at $\varphi_x = 90^\circ$, $\varphi_y = 0^\circ$	125
6.19.	Large scale cantilever wing reference configuration. Contours of constant relative sound pressure levels as a function of emission angles and M_0 , $\delta_F = 25^\circ$. Levels are normalized by the level measured at the position marked by the black "cross" mark at $\varphi_x = 90^\circ$, $\varphi_y = 0^\circ$	126
6.20.	Large scale cantilever wing sweep configuration. Contours of constant relative sound pressure levels as a function of emission angles and M_0 , $\delta_F = 25^\circ$. Levels are normalized by the level measured at the position marked by the black "cross" mark at $\varphi_x = 90^\circ$, $\varphi_y = 0^\circ$	127

6.21. High-lift wing with half-span flap with retracted slat. SPL contour plots, phased array located below the model. Top view, i.e. looking towards the model from above. 1/3-octave band frequencies. $\alpha_g = 0^\circ$, $\delta_F = 34^\circ$, $M_0 = 0.18$	128
6.22. Integrated 1/3-octave band noise spectra. Bottom view. Power integration performed over the range $0.6 \text{ m} \leq x \leq 0.95 \text{ m}$ and $-0.15 \text{ m} \leq y \leq 0.15 \text{ m}$ (see figure 6.21). (a) solid symbols: $\alpha_g = 0^\circ$, empty symbols: $\alpha_g = 7^\circ$. (b) solid symbols only: $\alpha_g = 0^\circ$	129
6.23. Reference high-lift configuration. Scaled integrated noise spectra. Bottom view, 1/3-octave band frequencies.	131
6.24. High-lift wing configuration. Contours of phased array integrated SPL as a function of radiation angles and flap deployment angle. The angular emission directions are according to the coordinate system definition of figure 3.3. Levels are first propagated to a reference distance of 1 m from the airfoil center point and normalized by the SPL value at $(\phi = 0^\circ, \theta = -90^\circ)$. $M_0 = 0.18$, $f_c = 3.15 \text{ kHz}$, $St_0 = 6$	132
6.25. High-lift wing configuration. Fly-over directivity, $\varphi_y = 0^\circ$. $M_0 = 0.18$	132
6.26. Fly-over directivity, $\varphi_y = 0^\circ$. Comparison between the reference high-lift configuration in AWB (AWB-HL), $\alpha = 7^\circ$, $\delta_F = [20^\circ, 34^\circ]$, $M_0 = 0.18$, the reference cantilever configuration in AWB (AWB-CL), $\delta_F = [20^\circ, 30^\circ]$, $M_0 = 0.18$ and the large scale cantilever configuration in NWB (NWB-CL), $\delta_F = [20^\circ, 30^\circ]$, $M_0 = 0.2$. Solid black line: dipole directivity approximation, i.e. $D(\varphi_x, \varphi_y = 0^\circ) = \cos^2(\varphi_x + 115^\circ)$	134
6.27. Azimuthal directivity, $\varphi_x = 90^\circ$. Comparison between the reference high-lift configuration in AWB (AWB-HL), $\alpha = 7^\circ$, $\delta_F = [20^\circ, 34^\circ]$, $M_0 = 0.18$, the reference cantilever configuration in AWB (AWB-CL and AWB-CL2), $\delta_F = [20^\circ, 30^\circ]$, $M_0 = 0.18$ and the large scale cantilever configuration in NWB (NWB-CL), $\delta_F = [20^\circ, 30^\circ]$, $M_0 = 0.2$. Solid black line: directivity approximation. Emission angles definition according to figure 4.1.	135
6.28. High-lift configuration with 3/4-span flap with Clark-Y profile. Integrated noise spectra. Bottom view, 1/3-octave band frequencies.	137
7.1. Fly-over coordinate system definition	143
7.2. Two-component representation of the FSE noise spectrum	147
7.3. A320-type cantilever wing FSE noise prediction. Solid symbols: measurements. Lines: prediction.	148
7.4. High-lift wing model FSE noise prediction. Solid symbols: measurements. Lines: prediction.	149
7.5. Large scale reference cantilever wing FSE noise prediction for the baseline tip case. Solid symbols: measurements. Lines: prediction.	149
7.6. Large scale reference cantilever wing FSE noise prediction, swept tip case. Here slightly modified calibration constants and length scales necessary: $C_1 = 134 \text{ dB}$, $C_2 = 161 \text{ dB}$, $l_{low} = 0.145c$, $l_{high} = 0.03c$. Solid symbols: measurements. Lines: prediction.	150
7.7. Half-model FSE noise. Solid symbols: measurements. Lines: prediction.	150

7.8.	DU-96 cantilever wing FSE noise prediction. Solid symbols: measurements. Lines: prediction.	151
7.9.	Clark-Y cantilever wing FSE noise prediction. Solid symbols: measurements. Lines: prediction. Here modified length scales necessary: $l_{low} = 0.18c$, $l_{high} = 0.02c$. $C_1 = 125$ dB, $C_2 = 160$ dB	152
7.10.	Reference+Tip#2 cantilever wing FSE noise prediction. Solid symbols: measurements. Lines: prediction. Here slightly modified calibration constants necessary: $C_1 = 139$ dB, $C_2 = 140$ dB.	153
A.1.	Reference cantilever wing setup in the AWB. Coordinate system definition and microphone locations (towards upstream perspective). Microphone array located on the left hand side, far-field microphones mounted on a linear support lying on the ground. The flow direction is in positive x direction.	159
A.2.	Reference cantilever wing setup in the AWB. Coordinate system definition and microphone locations (side perspective). Note that free-field microphone #1 is actually located upstream of the nozzle exit plane (negative x-coordinate). Both the microphone array and the free-field microphone are below the wing. The flow direction is in positive x direction.	160
A.3.	Reference high-lift wing setup in the AWB. Coordinate system definition (top perspective). The flow direction is in positive x direction.	161
A.4.	Reference high-lift wing setup in the AWB. Coordinate system definition and microphone locations (side perspective). Note that far-field microphone #1 is actually located upstream of the nozzle exit plane (negative x-coordinate). Both the microphone array and the far-field microphone are below the wing. The flow direction is in positive x direction.	162
A.5.	Large scale cantilever wing setup in the NWB. Coordinate system definition and microphone array location (top perspective on the model). The flow direction is in positive x direction.	163
A.6.	Large scale cantilever wing setup in the NWB. Coordinate system definition and microphone array location (side perspective on the model). The flow direction is in positive x direction.	163
A.7.	Large scale cantilever wing setup in the NWB. Coordinate system definition and free-field microphone locations (downstream perspective on the model). The flow direction is in positive x direction.	164
B.1.	Distribution of surface static pressure coefficient (C_p) vs. normalized stream-wise position (x/c) for different incidence angles. Configuration: Reference, $U_0 = 60$ m/s. Solid symbols: suction side. Empty symbols: pressure side. .	165
B.2.	Distribution of surface static pressure coefficient (C_p) vs. normalized stream-wise position (x/c) for different incidence angles. Configuration: Tip #1, $U_0 = 60$ m/s. Solid symbols: suction side. Empty symbols: pressure side. .	166
B.3.	Distribution of surface static pressure coefficient (C_p) vs. normalized stream-wise position (x/c) for different incidence angles. Configuration: Tip #1+Vane, $U_0 = 60$ m/s. Solid symbols: suction side. Empty symbols: pressure side. .	167

B.4.	Distribution of surface static pressure coefficient (C_p) vs. normalized stream-wise position (x/c) for different incidence angles. Configuration: Tip #2, $U_0 = 60$ m/s. Solid symbols: suction side. Empty symbols: pressure side. .	168
B.5.	Distribution of surface static pressure coefficient (C_p) vs. normalized stream-wise position (x/c) for different incidence angles. Configuration: Tip #2+Vane, $U_0 = 60$ m/s. Solid symbols: suction side. Empty symbols: pressure side. .	169
B.6.	Distribution of surface static pressure coefficient (C_p) vs. normalized stream-wise position (x/c) for different incidence angles. Configuration: Vane, $U_0 = 60$ m/s. Solid symbols: suction side. Empty symbols: pressure side. .	170
C.1.	Effect of M_0 , bottom view, 1/3-octave band spectra. Power integration of the microphone array noise maps. $\delta_F = 25^\circ$	172
C.2.	Effect of δ_F , bottom view, 1/3-octave band spectra. Power integration of the microphone array noise maps. $M_0 = 0.18$	173
C.3.	Effect of M_0 , side view, 1/3-octave band spectra. Power integration of the microphone array noise maps. $\delta_F = 25^\circ$	174
C.4.	Effect of δ_F , side view, 1/3-octave band spectra. Power integration of the microphone array noise maps. $M_0 = 0.18$	175
C.5.	Scaled noise spectra. Bottom view. Effect of M_0 , $\delta_F = 25^\circ$	176
C.6.	Scaled noise spectra. Bottom view. Effect of δ_F , $M_0 = 0.18$	177
C.7.	Scaled noise spectra. Side view. Effect of M_0 , $\delta_F = 25^\circ$	178
C.8.	Scaled noise spectra. Side view. Effect of δ_F , $M_0 = 0.18$	179
D.1.	Identification of a quasi-tonal source for configuration Tip #1+Vane. Source map at $f_c = 2.5$ kHz, $\delta_F = 32^\circ$, $M_0 = 0.18$. The given percentages refer to the taped extent (ex.: 20% \rightarrow up to $x/c = 0.2$).	181
D.2.	Identification of a high-frequency tonal source for configuration Tip #1+Vane. Source map at $f_c = 12.5$ kHz, $\delta_F = 25^\circ$, $M_0 = 0.18$	182
D.3.	Comparison of the source distributions for configurations Tip #1 and Tip #2. Source map at $f_c = 2.5$ kHz, $M_0 = 0.18$, side view.	183
D.4.	Comparison of the source distributions for configurations Tip #1 and Tip #2. Source map at $f_c = 2.5$ kHz, $M_0 = 0.18$, bottom view.	184
D.5.	Comparison of the source distributions for configurations Reference, Vane, Tip #1+Vane and Tip #2+Vane. Source map at $f_c = 2.5$ kHz, $M_0 = 0.18$, side view.	185
D.6.	Comparison of the source distributions for configurations Reference, Vane, Tip #1+Vane and Tip #2+Vane. Source map at $f_c = 2.5$ kHz, $M_0 = 0.18$, bottom view.	186
E.1.	Fly-over directivity. Effect of tip geometry modifications. $\varphi_y = 0^\circ$, $\delta_F = 20^\circ$, $M_0 = 0.18$	188
E.2.	Sideline directivity. Effect of tip geometry modifications. $\varphi_x = 90^\circ$, $\delta_F = 20^\circ$, $M_0 = 0.18$	189
E.3.	Fly-over directivity. Effect of tip geometry modifications. $\varphi_y = 0^\circ$, $\delta_F = 25^\circ$, $M_0 = 0.18$	190
E.4.	Sideline directivity. Effect of tip geometry modifications. $\varphi_x = 90^\circ$, $\delta_F = 25^\circ$, $M_0 = 0.18$	191

E.5. Fly-over directivity. Effect of tip geometry modifications. $\varphi_y = 0^\circ$, $\delta_F = 25^\circ$, $M_0 = 0.18$	192
E.6. Sideline directivity. Effect of tip geometry modifications. $\varphi_x = 90^\circ$, $\delta_F = 30^\circ$, $M_0 = 0.18$	193
F.1. Reference configuration. SPL contour plots. $M_0 = 0.21$	195
F.2. Reference configuration. SPL contour plots. $M_0 = 0.21$	196
F.3. Raked tip configuration. SPL contour plots. $M_0 = 0.21$	197
F.4. Raked tip configuration. SPL contour plots. $M_0 = 0.21$	198

1. Introduction

1.1. Background and Motivation

OVER the past 40 years, air traffic has experienced a continuous growth. According to the International Air Transport Association IATA [2], the volume of air travel, measured in RPK (revenue passenger kilometer), has expanded tenfold over this period. A factor of three more than the world's economic growth over the same period. The absolute increase in air travel movements has increased by a factor of 3.5 while flight frequencies show a 2.5 times rise between 1980 and 2006. At the same time, the price of air travel for consumers has fallen by about 60%. This price decline is strongly coupled with efforts made by the industry in becoming operationally more efficient and the development of modern, more environment friendly, aircraft.

In spite of this technological progress, the global growth in air traffic is such that its absolute impact on the environment still increases. Overall CO₂ emission as well as perceived noise levels rise each year, fleet renewal merely slowing down the increase rate. The problem has gained much public interests in the past years, stimulating the political awareness regarding this issue and forcing European law makers to act. The European Union's *Vision 2020* [1] from January 2001, provides guidelines regarding the future evolution of the aeronautical industry in Europe and defines precise goals regarding airplane noise as well as CO₂ emissions reduction. The following is an excerpt of the *Vision 2020* report, regarding aircraft noise.

- *“A reduction in perceived noise to one half of current average levels.”*
- *“Eliminate noise nuisance outside the airport boundary by day and night by quieter aircraft, better land planning and use around airports and systematic use of noise reduction procedures.”*

A reduction of one half in perceived noise corresponds to a 10 dB noise reduction (or -90% in sound power). A similar but more ambitious approach was also taken in the United States. The US strives to achieve a 10 dB reduction within 10 years relative to 1997 technology and 20 dB within 25 years [109]. This calls for new ideas and innovative technologies for the US and European aircraft noise reduction targets to be met.

There are two contributors to aircraft noise namely, engine noise and airframe noise. The engines dominate noise emission at take off while airframe noise plays an important role in the approach and landing phases. This ranking of the importance of both contributors is the result of extensive efforts made in the last four decades to reduce engine noise emission. A technological milestone was the introduction of high-bypass ratio engines in the seventies. Initially developed to reduce aircraft fuel consumption, the new engines also had the interesting side-effect of being much quieter [33, 86]. The further evolution

of the high-bypass ratio concept coupled with the successful development of engine liner technology has put airframe and engine noise on a comparable level, during approach and landing. Airframe noise no longer plays a secondary role, but potentially sets a lower bound to aircraft noise. A further reduction of current noise emission levels will therefore only be possible through a combined acoustic optimization of both the propulsion system and the airframe.

The present work is concerned with one major component of noise generation through interaction of the flow of air about the airframe. Power plant noise, due to e.g. propellers, turbo-props or others is not considered. A successful reduction of flow-generated noise means developing new low-noise airframe components and/or new aircraft designs [33, 86]. Flow induced noise occurs at many locations on the aircraft fuselage and lifting surfaces and depends on both the geometrical characteristics and the local aerodynamic conditions. Because an overall noise reduction can only be achieved through an equal reduction of all sources, each of them has to be considered independently. The dominant noise source contribution will always set the lowest achievable impact level of a given aircraft. The main sources of airframe noise are depicted in figure 1.1.

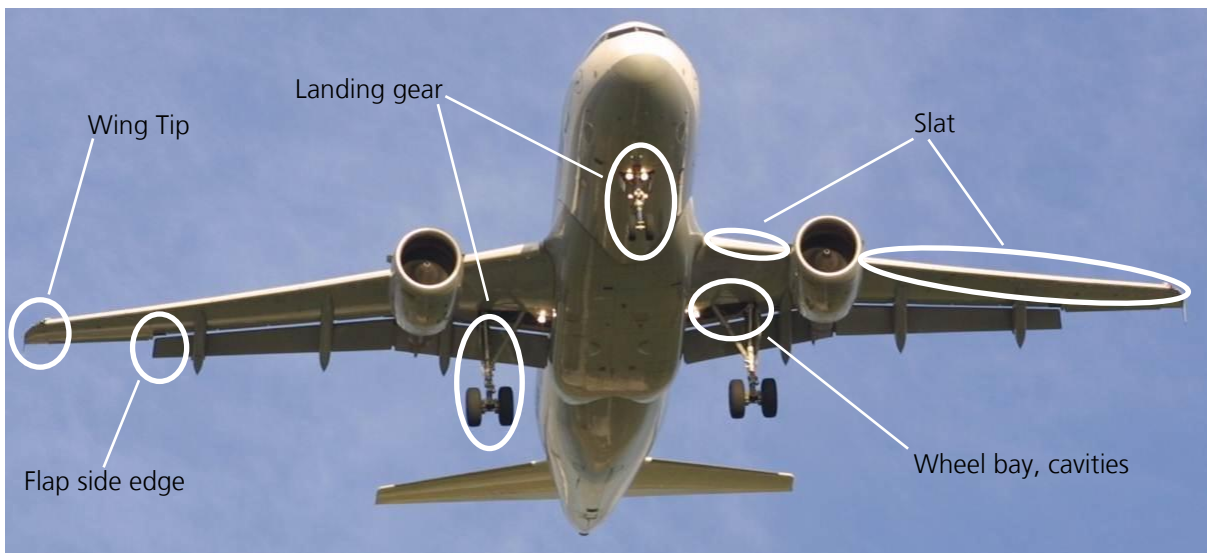


Figure 1.1.: Major sources of airframe noise during approach and landing. Courtesy of Michael Pott-Pollenske, DLR.

The source ranking (in order of importance) for today's conventional airplanes in landing configuration is, according to [33], as follows,

- landing gears,
- slotted slats,
- edges of lifting surfaces (flap and slat side edges, wing tips, trailing edges)
- flap and slat tracks,
- spoilers,
- component interaction noise sources (e.g. gear-wake/flap, jet/flap).

This typical ranking depends, of course, on the type of aircraft considered and could change according to specific design variations. While, for regional and single-aisle aircraft, high-lift system noise is comparable to the landing gear noise contribution, landing gear noise largely dominates for current wide-body airplanes [33]. Moreover, and particularly for short take-off and landing (STOL) aircraft, higher lift coefficients of the wing system may be achieved through a redirection of the engine exhaust flow over the wing's components. These techniques are known as *external blowing* and *upper surface blowing*. For such configurations, a different source ranking is most probably to be awaited, with an increased role of flap side-edge and flap track noise.

The central subject of the present work is set on the experimental analysis of the flap side-edge (FSE) noise source with emphasis on the formulation of a semi-empirical prediction scheme. The present effort will try to contribute to a better understanding of the FSE noise source as well as to provide novel engineering tools for design-to-noise applications. A good understanding of the FSE noise source working mechanism is also important for the development of retrofit treatments or novel low-noise technologies. A review of the state-of-the-art knowledge about FSE noise prediction is presented hereafter. The review will try to answer the following four central questions. **(1)** What prediction models/methodologies are available? **(2)** What is/are the postulated source mechanisms for FSE noise? **(3)** What are their limitations? **(4)** How can we improve existing models? This will finally pave the way for a definition of research goals for the present work.

1.2. State-of-the-Art Semi-Empirical Modelling of FSE Noise

In this section a discussion on the state-of-the-art modelling approaches for flap side-edge noise is presented. The goal of this exercise is to provide background information on the variety of existing approaches as well as a critical review of their capabilities and limitations.

In the context of noise prediction within conceptual design, low computational cost methodologies are most appropriate. Semi-empirical prediction models offer this kind of efficiency, however, suffer from an obvious lack of generality in its representation of the physics of the FSE noise problem. The earliest attempt to predict airframe noise using a semi-empirical paradigm is reported by Fink [42, 43]. In this attempt, however, the flap-side edge is not accounted for as an independent noise source.

In a comprehensive effort towards componential modelling and prediction of airframe noise by Brooks and Marcolini [19] and Brooks et al. [22], a first attempt was made to model FSE noise. In this work, a semi-empirical approach to FSE noise prediction is presented which is based on a comparison of experimental data from two- and three-dimensional wings. The experimental quantification of FSE noise relies on the assumption that it corresponds to the far-field noise difference between the 3D and 2D spectra. The acoustic modeling starts with the assumption of a trailing-edge (TE) noise generation mechanism where noise is due to the passage of turbulent eddies over the TE in the tip region. The characteristic length and velocity scales are chosen as the separation extent, i.e. vortex size, on the suction side near the tip TE and the maximum vortex core outer velocity (U_m), i.e. the separation line velocity. Both are approximately linear function of

the wing's local tip angle of attack and depend on the tip shape [47]. The spectral shape of the radiated noise is estimated using surface pressure measurements on delta wings as in George and Chou [47]. Sound pressure levels are assumed proportional to $M_0^2 M_m^3$, with M_0 the free-stream Mach number and M_m the Mach number based on U_m , which renders the best collapse of the data. A parabolic fit provides a representation of the universal, i.e. scaled spectrum as a function of the Strouhal number. No specific account is made of the FSE noise directivity. As a first approximation, the authors propose the application of the TE noise directivity pattern. Using potential theory arguments, an angle of attack correction is proposed which relates the effective wing tip angle to the spanwise lift slope near the tip. Although this discussion emphasizes the role of the tip vortex on the sectional lift coefficient (and angle of attack), the assumption of an elliptical loading distribution limits its applicability. The tip vortex was found by McAlister and Takahashi [87] to induce a strong and sharp suction peak close to the wing tip, which is not caught by a potential theory representation.

The most recent work dedicated to FSE noise prediction using semi-empirical approach is reported by Guo and Joshi [56] and Sen et al. [119]. The overall sound pressure level is modelled by a functional relationship between a set of the most relevant aerodynamic parameters, with coefficients determined from a large experimental database (Boeing 737, 757, 777, DC-10, MD-10 scaled model airplanes). The noise spectral shape is represented by a high-order polynomial obtained through regression analysis on the average measured spectra. Central parameters for the prediction of FSE noise are the tip cross-flow velocity and the tip vortex strength. Both being inferred through potential flow theory. The large variability in the database measurements and also the limited number of aircraft used in deriving the FSE spectral shape combined with the need for assumptions to define some parameters, limits its application to conventional airplane configurations without important geometric variations. The model also reveals a surprisingly weak and counter-intuitive role of both the vortex strength and cross-flow velocity. Finally, no FSE-specific directivity function is provided by the authors. However, a directivity factor is derived from total airframe noise measurements at a DC-10 over a wide range of radiation angles.

Brooks and Humphreys Jr. [21] propose two different approaches to a practical FSE noise prediction based on a knowledge of the tip unsteady surface pressure fluctuations. A first method, named *causality spectra prediction*, builds upon the Ffowcs Williams and Hawkings equation [41] for low Mach number flows and for surfaces with steady or no motion relative to an observer (as in Guo [55]). Only dipole source contributions are assumed to be important. The method requires a knowledge of the unsteady surface pressures and their correlation with the radiated noise in the far field. In practical applications, surface pressure measurements near the tip are correlated to standard far-field noise measurements and summed up to obtain the total tip noise. Hereby the dimension of the radiating surface is assumed to be proportional to, say Ll_2 , with L being the length over which surface pressure sensors are applied and l_2 , the spanwise correlation length scale. An estimate of l_2 is provided by turbulent boundary layer pressure scaling assumptions, i.e. $l_2 = U_c/(\eta\omega)$ with $\eta = 0.3$ and U_c the eddies convection velocity. The predicted spectra are found to agree well with the measurements as long as the source region and spatial sampling (number of microphones) are representative and sufficient, respectively.

The second method presented in Brooks and Humphreys Jr. [21] is named *scatter edge noise prediction* and is based on an adaptation of Howe's theory of TE noise [66]. The

shedding of unsteady vorticity about the tip edges is assumed to generate noise in a manner similar to the TE noise mechanism described in Howe’s theory. The convection velocity of the vorticity perturbations and their skew angle relative to the tip face normal are defining parameters. The theory assumes that the local edge thickness is much smaller than the related acoustic wavelength. Similar to the *causality spectra method*, the predicted far-field noise levels are due to the summed contributions from measurements at each surface pressure sensor. An estimate of the streamwise correlation scale (l_1) is necessary. From turbulent boundary layer theory, $l_1 = U_c \cos \beta (\xi \omega)^{-1}$ with $\xi = 2.0$ and β the flow’s skew angle relative to the tip’s face normal direction. As mentioned above, the experimental results do not allow the authors to determine the value of ξ . Nevertheless, a good agreement between measurements and predictions is also found. Regarding the directivity, the theoretical cardioid pattern does not generally hold. The authors believe this to be a consequence of the finite dimensions of the flap tip compared to Howe’s theoretical infinite thin plate assumption. Although both prediction methods give good results, they are both dependent on a knowledge of the tip unsteady surface pressure spectra. This kind of information is not easily acquired nor can it be readily generalized to different tip shapes or wing sectional geometries. Also, turbulent boundary layer assumptions are necessary to define spanwise and chordwise correlation length scales. Although these assumptions appear, at least in this context, reasonable, there is no certainty on their generality. The perturbation velocity magnitude U_c as well as its skew angle β are not known and would require a detailed analysis of the tip flow field.

In a recent work, Guo [54] adopts a different modelling approach taking advantage of the experimental evidence that FSE noise mostly results from the summed contribution of two different noise generation mechanisms. These two sources are treated independently and are defined in terms of local parameters, characteristic for the regions along the flap where they dominate. Shear-layer instabilities caused by flow separation in the forward part of the flap are responsible for high-frequency noise generation while interaction of the tip vortical structures with the flap corner and edges is mostly responsible for low-frequency noise generation. Guo argues that the noise generation scales on characteristic lengths of the flow features in each region of interest. He therefore assumes high-frequency noise to be proportional to the flap thickness while low-frequency noise is assumed to be related to the flap chord length. Although these hypothesis appear reasonable, they are not further discussed by the author. Because of their different flow characteristics and locations on the flap, each source component is postulated to obey different Mach number dependencies and possess different directivities. The low-frequency source intensity varies according to M_0^5 while the high-frequency source intensity is assumed proportional to M_0^6 . A general solution of the Ffowcs Williams and Hawkings equation [41] is derived for an aircraft flying at constant Mach number in a medium at rest with constant properties. The functional dependency of the radiated noise and its spectral shape are found by dimensional analysis of the solution. Guo emphasizes the fact that the Mach number dependency of the radiated noise is not exclusively represented by the spectral shape function but rather is partly included in other model parameters e.g. flow quantities. Next, a semi-analytical model for the directivity is derived again based on the general Ffowcs Williams and Hawkings equation [41]. It is a function of the Mach number only and possesses a dipole character, with maxima normal to the flap chord. The directivity pattern does predict increased noise levels in the forward arc with maximum noise radiation at about 60° to

the sideline below the flight path. The role of the flap geometry is not explicitly treated in the model and assumptions about the characteristics of the unknown Green's function have to be made. Furthermore diffraction effects due to the non-compactness of the source are not included in the derivation. The influence of geometrical variations on the radiated noise is considered briefly through the addition of a geometry-related coefficient to the model. This coefficient is adapted for a good representation of experimental data. Guo's approach provides the most general framework to date for FSE noise prediction.

Limitations of Current Prediction Methodologies.

From the preceding discussion of currently available prediction schemes for FSE noise, one notices that it is **(1)** often necessary to revert to estimates of the input parameters because of the difficulty of their experimental quantification. The validity of these estimates is questionable as they are mostly based on knowledge from turbulent boundary layer theory and also from potential theory. These are certainly important simplifications of the very complex FSE flow field. **(2)** Each prediction method can only be applied to a limited range of aircraft types, being calibrated on specific databases. This is a necessary difficulty associated with empirical modeling which needs, however, to be overcome to achieve realistic design-to-noise studies. **(3)** Also, most methods are built on relating geometrical characteristics to the noise production mechanisms. An approach which is justified by a desire to base the schemes on readily available input parameters. A drawback of this type of modelling is, however, that it is a priori very difficult to account for variations of the wing profile shape nor it is possible to account for tip modification or add-ons e.g. cavities and winglets without available specific experimental knowledge.

Current semi-empirical airframe noise prediction schemes fail to accurately evaluate noise emission from unconventional aircraft. Still, the demand for precise airframe noise level estimation at low computational cost remains important and this requires prediction schemes to become more fine-grained. The work of Guo [54] is the only one which provides a basic framework general enough to tackle the above limitations; although the model remains, to some extent, more descriptive than predictive because some of the parameters remains unknowns. To achieve a more fine-grained prediction, one will have to move away from a geometry-based modelling towards flow-based approaches, i.e. which utilize flow information from experiment or CFD in defining functional dependencies related to the acoustic radiation.

1.3. Scope and Research Objectives

In the present effort, a flow-based modelling approach is adopted, moving away from standard geometry-based prediction schemes. Although this approach appears very promising, due to its flexibility, some hurdles still remain for such an empirical model to be a useful design-phase quick-turnaround prediction tool. The goal of the present effort is to develop a noise prediction scheme which is lightweight, in terms of computational cost, precise (within the experimental error margins) and flexible. Ultimately, a general framework is sought which will allow a coupling with computational fluid dynamics (CFD), therefore opening new possibilities regarding empirical noise prediction for unconventional aircraft.

In contrast to prediction schemes found in the literature and discussed in the preceding section, input parameters needed for the prediction will have to be reduced to a minimum and be as straightforward to obtain as possible from CFD computations. Attention will therefore only be given to the mean flow field and its derived aerodynamic quantities. Distinctive and important features of the flow field will be identified and related to noise source mechanisms responsible for FSE noise production. Hereby assumptions have to be made on the nature of the sound generation mechanisms. The above assumptions inherently impose strong constraints on the resulting prediction scheme. It is, however, postulated that a knowledge of the bulk characteristics of the flow field is sufficient for the representation of a wide range of practically relevant cases.

Extensive experimental investigations of FSE noise radiation were performed at two cantilever flap models (1:1 and 1:1.6 scales) as well as at an high-lift wing (1:6.33) to provide the necessary database for the development of the prediction scheme. Because of its central importance to the noise radiation problem, much attention is also given to the characterization of the tip vortex and its formation process. Although much is already known about the characteristics of trailing tip vortices, the near field (or formation phase) of the tip vortex is documented only to a limited extent. The current approach is in contrast to most studies found in the literature and enables a very detailed investigation of the FSE acoustic and aerodynamic characteristics on a single flap model and for a common set of Reynolds and Mach numbers. The results of the acoustic and aerodynamic investigations will be directly used to construct an improved prediction scheme, relative to previously published work.

The proposed empirical prediction scheme is validated against the measured noise radiation from a large set of wind tunnel models of increasing complexity and a discussion of its range of validity is presented. Issues related to the extrapolation of the prediction scheme capabilities to full scale configurations and its integration to full aircraft design-phase noise prediction tools are discussed and methodologies to resolve these difficulties are proposed.

Following this introduction, in chapter 2, a more elaborate presentation of the fundamentals of FSE noise, as well as tip vortices, and their relation to the noise problem is given. Chapter 3 and 4 provide details about the experimental methodology and post-processing procedures. Results from the flow field investigations are presented in chapter 5 and those from the acoustic investigations in chapter 6. The knowledge gained in those previous two chapters will serve as basis for the formulation of a new semi-empirical prediction scheme in chapter 7. In this last chapter, the semi-empirical prediction scheme is presented and discussed to emphasize its advantages as well as its limitations. Finally future research needs regarding FSE noise modelling are identified.

2. Current Knowledge on Flap Side-Edge Noise

In this chapter a broad overview of the current fundamental knowledge about flap side-edge noise is given. In section 2.1, the current knowledge on tip vortices is presented and put in relation to the FSE noise problem and its modelling. Generally speaking δ_F will refer to the flap deflection angle when considering a high-lift wing and to an airfoil angle of attack when considering two-dimensional or cantilever airfoils. In section 2.2 a discussion of available theoretical approaches is given and their ability to represent the experimental observations is discussed. In section 2.3, the most important experimental efforts are presented and discussed, providing an insight into the spectral characteristics of FSE noise.

2.1. Tip Vortices and their Relation to the FSE Noise Problem

Noise generation at the flap side-edge is closely related to the characteristics of the flap side-edge vortex (or equivalently, tip vortex). Most interesting for FSE noise production are 1) the vortex strength and size, which determine the peak radiation level and frequency and 2) the proximity of the vortex to the solid edges and its topology, which also impact its peak level while defining its spectral content. One desires to know how these factors depend on flap deployment and geometry, but also on flight and local flow velocities.

It is therefore of great interest to investigate the details of this type of flow in its different phases of development. The phase of vortex formation takes place in the close proximity of the wing and is limited to the range $0 \leq x/c \leq 1$. As soon as the FSE vortex leaves the trailing edge ($x/c = 1$), it enters the free field, a domain where the wing does not influence the vortex anymore. In the context of the current work, those two spatial regions are defined as the FSE vortex near field. This definition is not in line with the terminology of other authors working on tip vortices [4, 32], but is appropriate for our intent. While trailing vortices emanating from three-dimensional lifting surfaces may exist over very large distances, the aeroacoustic problem is mostly tied to the first two phases of evolution. As there is not a large body of work available on flap tip vortices, the following review will also consider studies done at simple cantilever wings. The term “tip vortex” will be used in a general fashion for both cantilever wings and flaps.

2.1.1. Near Field Characteristics

Experimental Studies. Although a lot of research efforts were made to better understand the development of trailing vortices (to be discussed in more detail in the upcoming

sections), the number of publications concerned with the formation of tip vortices in its early stages is much more limited. This is certainly related to the inherent complexity of the flow field which makes experimental quantification of tip vortex characteristics difficult. See for example flow visualizations made by Freymuth et al. [46] and Francis and Kennedy [44].

Francis and Katz [45] studied the topology of the wing tip vortex formation in more detail through dye visualization in a water-filled towing tank. Empirical relations are formulated which describe the chordwise evolution of the vortex characteristics as a function of incidence angle and free-stream velocity, i.e. Reynolds number, Re . There is a strong dependency of the vortex size and position on both δ_F and Re , however, with opposing effects. Increasing the Re reduces the vortex size while increasing wing incidence works to increase its size. The tip vortex moves inboard and downward with an increase in Re , moving outboard and upward with an increase in δ_F . The tendencies observed by Francis and Katz [45] are also supported by flow visualizations as well as LDV measurements made by Higuchi et al. [62] at an elliptical cantilever wing with a NACA 66₂-415 section. More recent measurements at a NACA 0012 wing with a flat tip and a curved cross-section tip from Giuni and Green [51] and Giuni [50] also partly support these observations. Their flow visualizations reveal a smooth and progressive vortex formation with only few vortical structures for the round tip, resulting in a more axisymmetric vortex. It is also noted that an increase in Re leads to a stronger reduction of the vortex core diameter for the rounded tip. In contrast, the flat tip wing forces the build-up of a more complicated tip vortex system with multiple structures. The interaction of these vortices is found to increase turbulent mixing and diffusion; the vortex system is time-dependent. First signs of time-dependency are noticed when the tip and top surface vortices merge. During and after merging, the tip vortices are also found to oscillate from the tip face to the suction side surface, reflecting the important unsteadiness of the merged vortex. The authors also note an independent initial development of the top and side vortices.

Using the visualization technique of Francis and Katz [45], Katz and Galdo [77] investigated the role of surface roughness on the development of wing tip vortices. Although they found that surface roughness had limited impact on vortex size and location, it does affect the position at which the tip vortex moves to the wing's upper side, moving upstream with an increase in surface roughness. They conclude that an increase in surface roughness substantially reduces the tip vortex strength. Similar observations are made by McAlister and Takahashi [87] for leading-edge tripping devices. Their observations provide some insight in the working mechanisms of porous treatments used as noise reduction technologies. A rectangular wing with a flat tip geometry forces the flow to separate at its edges and can be viewed as an effective tripping or increased surface roughness which reduces the local flow velocity magnitude compared to, e.g. a rounded wing tip. Larger tangential velocities and a smaller vortex core should be expected for smooth tip geometries where the flow is allowed to follow the tip contour without separating. A conclusion supported by measurements from McAlister and Takahashi [87] and Chow et al. [26].

McAlister and Takahashi [87] studied the near- and far-field development of a tip vortex at a semispan NACA0015 wing with flat and round tips. They found that a wing with a round tip shape eliminated the secondary vortex on the wing upper surface. The existence of a double-vortex system appears to be characteristic for a wing with a flat tip. They also found that the maximum vertical component of velocity near the vortex core, is directly

(almost linearly) dependent on δ_F and independent of the Reynolds number. For both tip geometries the spanwise static pressure distribution displays a strong and sudden peak in the outermost 4% of the wing, due to the presence of the tip vortex over the wing's upper surface. The flat tip wing vortex is found to be almost insensitive to changes in Re , which differs from observations made for the round tip case. The authors postulate that this difference results from the transition-fixing nature of the flat tip wing. Increasing the wing angle of attack leads, in both cases, to a large increase in overall lift. This change in lift is, however, larger in the round tip case. Looking at the trailing vortex from a square tip wing, the authors observed a strong dependency of its circulation on δ_F (keeping chord and Re constant). The authors therefore postulate that δ_F might be the more important determinant of the core maximum vertical velocity, compared to Re . Plotting the magnitude of the maximum vertical velocity in the trailing vortex against δ_F indeed shows a linear dependency which pertains both near the TE ($x/c = 0.1$) and downstream of the TE ($x/c = 4$). The wing's aspect ratio ($6.6 \leq AR \leq 9.6$) was not found to play an important role in defining the trailing vortex characteristics.

Chow et al. [25, 26] studied the roll-up of a turbulent tip vortex on a semi-span straight NACA 0012 wing with a round tip. Over the wing, peak levels of turbulence were identified where the tip shear layer departed from the tip surface, near a position where maximum tangential velocity occurs. Turbulence intensities are found to rapidly decay with the progressive winding of fluid into the tip vortex (due to rotation effects Devenport et al. [31]), the same being also true in the wake. The axial vorticity, ω_1 , along the vortex center line is the most important component of vorticity generated during vortex roll-up. The authors found that the strongest increase in ω_1 occur over the wing's surface while, in the wake, much lower rate of increase are measured. The center-line velocity is a function of Re , δ_F , x/c and the aspect ratio, AR , through the following empirical formula due to Chow et al. [26],

$$U/U_0 = a_1 Re^{a_2} (\delta_F / deg)^{a_3} (x/c + 1)^{a_4} AR^{a_5}, \quad (2.1)$$

with $a_1 = 0.56$, $a_2 = 0.041$, $a_3 = 0.25$, $a_4 = -0.13$, $a_5 = -0.14$. An increase in Re or δ_F therefore leads to higher velocities while an increase in x/c or AR has the opposite effect. The angle of attack is the most important parameter in determining the center line axial velocity.

The first measurements of the flap tip flow field in a high-lift configuration were performed by Radeztsky et al. [110]. Using a 5-hole pressure probe the authors studied the chordwise evolution of the tip flow field over a set of chord-normal planes. The experiments were performed in NASA's Quiet Flow Facility (QFF) using an unswept NACA 63₂-215 Mod B airfoil. As for the cantilever wings, a double-vortex structure is revealed by the 5-hole probe measurements. The tip flow field is found to be very similar for both flap angles studied ($\delta_F = 29^\circ, 39^\circ$). Increasing δ_F leads to a spatial shift of the flow structures towards the flap leading edge. After vortex merging, the core axial velocity reaches levels of over twice the free-stream velocity; in accordance with observation made by Chow et al. [26]. At $\delta_F = 39^\circ$, the 5-hole probe data indicate the existence of a zone of vortex breakdown, responsible for an important far-field noise increase.

A similar study was also performed by Berkman et al. [14] at a three-element high-lift wing with a profile geometry typical of an energy efficient transport wing (EET).

The experiments were performed in NASA Langley’s Low Turbulence Pressure Tunnel (LTPT) over Reynolds number ranging from 3.6 to 19.2 million and Mach numbers of 0.125, 0.2 and 0.3. Measurements include steady and unsteady surface pressures. RANS computations complement the experiments. Their results revealed that the dominant flow structures in the flap side-edge region are relatively independent of the Reynolds number for $Re > 7 \times 10^6$. Contrary to the observation of Radeztsky et al. [110], the authors found the top edge vortex to be stronger than the vortex released at the bottom edge. It is conjectured that this is related to the different geometry compared to Radeztsky et al. [110]. Although the merged vortex eventually lifts-up the surface, this occurs later than in the experiments of Radeztsky et al. [110]. Vortex bursting occurs in the RANS computations for both flap deflection angles, in discordance with the results of Radeztsky et al. [110], who identified vortex bursting only for the largest flap angle ($\delta_F = 39^\circ$). Also, vortex merging occurs after bursting, and not before as in Radeztsky et al. [110].

Birch et al. [15, 16] studied the development of the tip flow at three different wing models. In a first study flow measurements were performed at a Bombardier R&D cambered wing of 0.508 m chord length. A miniature 7-hole pressure probe as well as PIV was used to reveal the details of the tip flow field along the wings and in the near wake. In a following study, they used a NACA 0015 and a Bombardier R&D cambered wing with a chord of 0.254 m. They found that the vortex core at a fixed x/c is not a strong function of the Reynolds number but is strongly influenced by changes in wing deflection. The vortex strength and diameter are found respectively to increase with δ_F , through a constant feeding of vorticity into the tip vortex from the pressure side shear layer, and decrease with Re (in agreement with the results of Francis and Katz [45]). Vortex strength was also found to increase with an increase in sweep angle. Comparisons with the NACA 0015 wing show that the core radius size remains very similar for both wings. The cambered wing produces higher tangential velocities and a stronger vortex with a smaller core size. For both wings the maximal vortex strength, tangential velocity and streamwise core velocity increase linearly with an increase in δ_F .

The effect of sweep and taper on the near field tip vortex development was investigated by Gerontakos and Lee [48] using two NACA 0015 wings. The taper ratio was $\lambda = 0.375$ and the sweep angle at the quarter chord $\Lambda = 24^\circ$. Measurements of the flow field in plane normal to the flow direction were realized with a miniature seven hole pressure probe as in Birch et al. [15, 16]. The vortex size, axial velocity, tangential velocity and vorticity are quantified for angles of attack $4^\circ < \alpha < 14^\circ$. A lower peak vorticity and an increased peak tangential velocity were measured for the swept wing compared to the straight wing. The core radius of the straight wing tip vortex was also found to be larger. At $x/c = 3.75$, downstream of the TE, the vortex core size is found to be independent of x/c and δ_F , regardless of the wing considered. The core diameter being about $0.16c$. In the tip region of the straight rectangular wing larger lift forces, compared to the swept wing, are measured implying a stronger vortex and higher induced drag. In fact, the lift-curve slope of the swept wing is not significantly affected by the tip effects whereas the straight wing is.

Bailey et al. [9] studied the role of upstream turbulence on vortex formation and in the near field. They used a NACA0012 wing with a flat tip geometry and exposed it to varying levels of grid turbulence. The tip flow field was characterized through single- and four-wire hot-wire probes. They identified three vortices, the primary vortex forming at

the wing tip, a secondary vortex on the suction side as well as a third smaller vortex near the tip TE. This third vortex is formed as low velocity fluid rolls over to the suction side. They found that increased upstream turbulence act to increase the vortices turbulence levels but does not impact noticeably the formation process.

The main conclusions which can be taken from the above discussion are summarized hereafter.

- The most important parameter determining the tip vortex characteristics are Re and δ_F .
- Increasing Re results in a smaller tip vortex while increase δ_F has the opposite effect.
- The tip vortex moves inboard and downward with an increase in Re , moving outboard and upward with an increase in δ_F .
- For the round tip wing, a smooth and progressive vortex formation is observed with only few vortical structures. The flat tip wing forces the build-up of a more complicated tip vortex system with multiple structures.
- A wing with a flat tip acts as a tripping device, forcing the flow at its edges to separate, therefore leading to the formation of a weaker vortex. The opposite is true for smooth tips.
- Primary and secondary vortices first evolve independently along x/c , until merging takes place.
- The merged vortex has a time-dependent character, oscillating between the tip face and the top surface.
- Surface roughness and leading edge tripping devices lead to an earlier vortex merging and a weaker vortex.
- The above characteristics hold through a wide range of wing section geometry typical for current transport aircraft.
- Wing section geometry can, however, play a crucial role in setting the properties of a tip vortex e.g. sharp vs. smooth edges. Berkman et al. [14] has also shown that a completely different vortex system can be obtained for wing's of atypical sectional shape.
- A swept wing will induce weaker tip vortices compared to a straight one.
- The tip vortex characteristics are not strongly dependent on upstream turbulence (or flow perturbations).

Computational Studies of the Vortex Formation Process. Computational studies are not further discussed in the context of the present report as they provide no quantitative information about the tip vortex formation, but mostly a qualitative view of the flow topology. The interested reader is referred to the work of Dacles-Mariani et al. [30] on the same geometry than that of Chow et al. [26], the work of Khorrami et al. [79], which is complementary to the experiments of Radeztsky et al. [110], the computations of Imamura et al. [73] on a NACA 0012 and those of Murayama et al. [100] on a high-lift configuration. Also, Ghias et al. [49], Revell et al. [112] and Jiang et al. [74] present results obtained through LES simulations.

2.1.2. Far-Field Characteristics

Due to the inherent complexity of the flow field, only a few authors have attempted to derive a theoretical description of trailing vortices. All theoretical developments rest on a light-loading hypothesis. Kaden [75] first modelled the formation of trailing vortices as the spiral roll-up of the wake semi-infinite vortex sheet. Batchelor [11] studied the existence of a strong axial flow in the core region of a vortex originating from one end of a wing. His analysis is based on the assumption of axisymmetric laminar line vortices. The balance between the centrifugal force and the radial gradient of pressure across the vortex cross-section is shown to result in an axial gradient of velocity. An increase in azimuthal velocity at the edge of the vortex core leads to a decrease in core pressure and an increased core flow velocity. Moore and Saffman [97], using ideas put forward by Kaden [75], extended Batchelor's work by considering the effect of viscosity on the roll-up of laminar trailing vortices.

Phillips [103], Govindaraju and Saffman [52] and Saffman [115] studied the inviscid roll-up of a turbulent trailing vortex assuming an isotropic turbulent eddy viscosity. The structure of the vortex core appears to be divided in three regions with distinct characteristics. Hoffmann and Joubert [63] and Phillips [103], based on similarity arguments, derive an analytical representation of the vortex core circulation in all three regions. Application to experimental data reveals that the core axial velocity gradient, imposed by the initial conditions at the wing, appears not to affect the self-similar form reached by the vortex. It does, however, delay its occurrence. Self-similar inner circulation profiles are already found 1.44 chord lengths downstream of the wing's trailing edge [82].

The common assumptions of light loading, small axial velocity perturbation relative to the free-stream i.e. large development distances, axisymmetry of the trailing vortex and isotropy of its turbulence, are all violated in practical applications. A direct application of the above observations in the framework of the current work is therefore limited. It remains, however, to be verified if the self-similar properties of trailing vortices can be put at use when modelling FSE noise.

2.2. Theoretical Approaches

Because of the complexity of the flow dynamics driving FSE noise generation, an analytical solution to Lighthill's analogy is not available. Analytic work is therefore limited to simplified cases still pertinent enough to reveal dominant factors responsible for the noise production.

In this section the different theoretical approaches describing noise generation at flap side-edges are presented and discussed. The main goal of this presentation is to provide information necessary for the later formulation of a prediction model. Respective theories are not provided in details but rather the most important aspects with respect to the present work are given. The interested reader is referred to the corresponding bibliographic references for a deeper look in the different theories.

2.2.1. Source Mechanisms Based on Lighthill's Analogy

A general theoretical treatment of the aeroacoustic noise problem is given by Ffowcs Williams and Hawkings [41] who provided an analytical description of noise generation by surfaces in arbitrary motion in a turbulent stream. The turbulence itself leads to a quadrupole-type source while surface and body interactions with the surrounding medium (flow) give rise to dipole and monopole-type radiation respectively. The solid body's surface is effectively replaced by a distribution of surface monopole and dipole type sources. The Ffowcs Williams and Hawkings equation [41] builds upon the original work of Lighthill [84, 85] which describes noise generation by an arbitrary source region surrounded by a quiescent fluid and that of Curle [29] who extended Lighthill's ideas to include the effect of the presence of a fixed solid boundary on noise generation in low Mach number flows.

For the current application, the typical flow Mach number is less than $M_0 < 0.3$. In that case, noise production is dominated by the dipole contribution, which relates to the fluctuating forces acting on the body. Curle [29] used dimensional analysis for a compact body and large Helmholtz (He) number ($He \gg 1$), to find that sound intensity (I) is proportional to,

$$I \propto \frac{1}{|\mathbf{x}^2|} \frac{\rho_0}{a_0^3} L^2 U^6, \quad (2.2)$$

where \mathbf{x} is the observer's position vector relative to the source center (with source-centered coordinate system's origin), L a characteristic scale of the body and U , the convection velocity of noise generating turbulent eddies. U being usually taken to be the mean free-stream velocity.

For compact non-moving bodies embedded in a stream, sound intensity therefore scales with the sixth power of the stream mean velocity. Ffowcs Williams and Hall [40] considered the flow of turbulent eddies about a non-compact semi-infinite half-plane (i.e. trailing edge (TE) noise). Their analysis shows that sound intensity scales according to an exponent of five and therefore that the presence of the edge greatly increases the efficiency of the noise production mechanism compared to noise generated by free turbulence.

A treatment similar to that of Ffowcs Williams and Hall [40] is made by Crighton [28] for a vortex filament moving about a non-compact semi-infinite half-plane (see figure 2.1). Using matched asymptotic expansions, Crighton was able to perform the first analytical treatment of a simplified version of the tip vortex noise problem. Noise intensity is also found to be proportional to the fifth power of the free-stream velocity. Sound is radiated with a cardioid-like directional factor, $D(\theta) = \sin(\theta/2)$.

Hardin [59] also considered the infinite thin half-plane of Crighton [28]. Using conformal mapping, the movement of the vortex about the edge is deduced and, with the aid of a two-dimensional low-frequency Green's function derived by Howe [70], an estimate of the far-field noise could be obtained. Hardin's theory also predicts a noise directivity as $D = \sin(\theta/2)$. The radiated noise intensity depends strongly on the proximity of the vortex to the edge and on its circulation, $I \propto \Gamma^2 \propto R_0^{-1/2}$, with R_0 the vortex distance from the plane. Meecham [92] followed the same modelling methodology for the flow swept around a sharp corner. However, he raised concerns about the validity of Hardin's result when adapting his 2D computations to 3D. Therefore, instead of using the simplified Green's function of Howe, he carried out computation of the far-field radiation based on

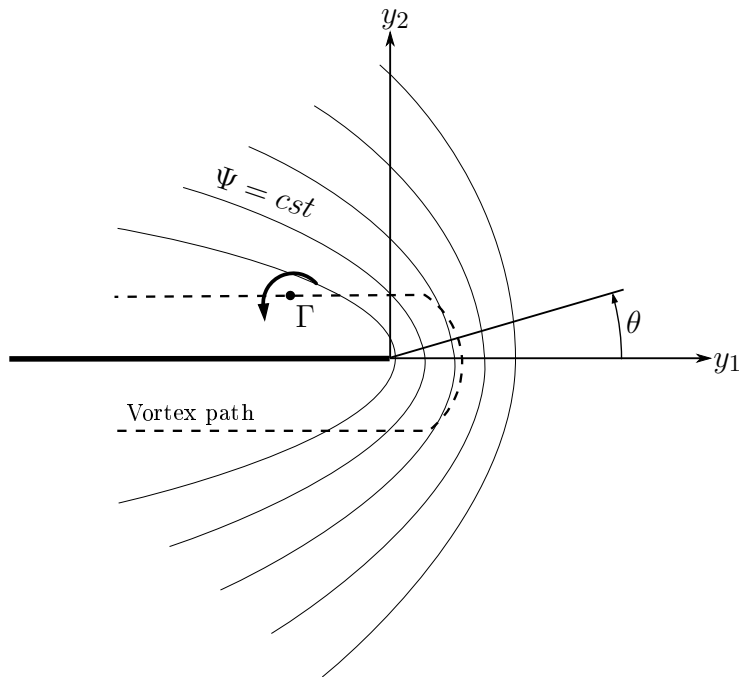


Figure 2.1.: Vortex filament, with circulation Γ , moving about a semi-infinite half-plane along the dashed path. The plane occupies the domain $y_2 = 0, y_1 < 0$. Sketch from Howe [70]. Lines of constant Ψ represent streamlines of a hypothetical potential flow around the half-plane.

Lighthill's analogy. Also, only noise generation at the lower tip corner is considered. A noise directivity according to $D = \sin^2 \theta$ is found with sound intensity proportional to the sixth power of the spanwise flow velocity. Interestingly, as the vortex moves closer to the edge an important slowdown is predicted due to the influence of its image vortex, effectively increasing the time span over which noise is generated.

The premises of Hardin were later reconsidered by Sen [117] who proposed to model the side edge flow field by a steady base vortex in a potential flow around a two-dimensional thick edge. The base vortex represents the time-averaged tip vorticity distribution and provides a picture consistent with experimental observations [26, 110]. It does not follow the flow field but rather remains at a constant equilibrium position near the side edge. This view is in contrast to that of Hardin [59] and Meecham [92], where single pockets of vorticity are convected by the potential flow. Next, the base vortex stability to small disturbance is analyzed. It is found that the base vortex remains stable as long as it stays at a distance from the edge less than 0.56 times the edge thickness, a value consistent with experimental evidences. This result poses an upper limit on the base vortex size. With the equilibrium position of the vortex set, Sen shows that the radiated noise frequency (due to the unstable oscillation of the vortex itself) is proportional to its circulation and inverse proportional to the edge thickness squared, $f \propto \Gamma/h^2$. Noise production is found to occur mainly for vortex movement across streamlines i.e. oscillations normal to the side-edge face, inline with Howe's result [70]. Motion parallel to the side-edge face i.e. less noisy modes occur for a vortex position close to the wall or near the stability boundary ($\epsilon \approx 0.56h$). The introduction of a small perturbing vortex on top of the base vortex promotes complex oscillations of the base vortex which translates into a broadening of the

far-field spectra. Sen's analysis also reveals the usual $D = \sin^2(\theta/2)$ directivity pattern. Noise intensity is found to be related to the lift coefficient, C_L like $I \propto C_L^2$ [60].

The most recent effort to model side-edge noise analytically, building upon the work of Hardin [59] and Meecham [92], is due to Guo [55]. A thick flap with a flat tip is considered, with vorticity production occurring only at the tip top and bottom edges. The model allows the computation of the dynamics of multiple point vortices ejected from the upper and lower corner as well as the pressure fluctuations on the flap surface. Next, the unsteady surface pressures are propagated to the far field using a formulation based on the Ffowcs Williams and Hawkins equation [41]. The far-field noise intensity is estimated as, $I \propto M_c^5$, with M_c , the cross-flow Mach number, in spanwise direction towards the flap tip. An extension of this model with application to flaps with side-edge fences is presented by Guo in [53].

Flap side-edge noise generation for an installed and deployed flap, i.e. a flap installed in a high-lift wing, is analyzed by Howe [67]. Howe does not adopt the idealized potential flow theory described above but rather considers a generic representation of the deployed flap embedded in a uniform flow. The gap existing between a deployed flap tip and its neighboring wing is represented by a simple slot of varying width. No concern is given to the complex tip flow field. A solution to the problem is found by using the evanescent wave theory of Chandiramani [23]. The theory reveals a half-baffled dipole directivity pattern at low frequency while at high frequency, noise is radiated according to a monopole-like pattern. Flap edge noise is found to be radiated more effectively at low values of the slot Strouhal number, $\omega s/U_3$, with $2s$ the slot width and U_3 the spanwise mean flow velocity.

2.2.2. Source Mechanisms Based on Vortex Sound Theory

The source of sound in vortical flow was shown by Powell [107, 108] to be related to the concept of *vortex force* [116]. Consider a small vortex ring of circulation Γ and ring area A . The flow induced by that vortex ring is the same as that from a potential point dipole, and its vortex strength (i.e circulation Γ times area A) was shown by Powell [107] to be equivalent to the strength of the point dipole. Now consider a solid and fixed body embedded in a fluid flow and subjected to a fluctuating aerodynamic force. This body could be effectively replaced by an equivalent and opposite body force (\mathbf{F}) acting on the fluid volume occupied by the body. This fluctuating force being equivalent to an appropriate distribution of potential point dipole. The fluid momentum at location ξ_i is given by $\rho_i \mathbf{D} = \rho_i \Gamma A$ and therefore the equivalent body force is

$$\mathbf{F} = \rho_i \frac{d\mathbf{D}}{dt} = \rho_i \frac{d\Gamma A}{dt}. \quad (2.3)$$

This force is proportional to the rate of change of the vortex ring strength (ΓA). For a general distribution of vorticity, the vortex force is given by [115],

$$\mathbf{F} = \rho_i \int (\boldsymbol{\omega} \times \mathbf{u}) dV. \quad (2.4)$$

Powell relates the far-field sound pressure to the vortex force,

$$p(\mathbf{x}) = \frac{1}{4\pi \mathbf{x}c} \frac{d\mathbf{F}}{dt} = \frac{\rho_i}{4\pi \mathbf{x}c} \frac{d^2(\Gamma A)}{dt^2} = \frac{\rho_i}{4\pi \mathbf{x}c} \frac{d}{dt} \int (\boldsymbol{\omega} \times \mathbf{u}) dV. \quad (2.5)$$

The far-field pressure results from the rate of change of the vortex force or the accelerating change in vortex strength. The same conclusion is drawn by Powell [107] for a lifting wing with its bound vortex. Any change in velocity and/or circulation is related to a change in vortex force and therefore leads to noise production. Also in the case of a vortex ring passing near a fixed cylinder in an otherwise still medium, vortex sound does also occur due to the induced force, by the passing vortex ring, on the cylinder.

This vorticity-based treatment of the aerodynamic sound problem is described by the vortex sound theory [70, 93, 107, 108]. The above ideas of Powell [107] were later revisited by Howe [70] who further generalized the theory. It is based on a different form of Lighthill's acoustic analogy with the total enthalpy, B (equation 2.6) as the independent acoustic variable instead of the fluid density.

$$B = \int \frac{dp}{\rho} + \frac{v^2}{2}. \quad (2.6)$$

The low Mach number vortex sound equation (Howe [69], generalization by Möhring [93]),

$$\left(\frac{1}{c_0^2} \frac{\partial^2}{\partial t^2} - \nabla^2 \right) B = \nabla \cdot (\boldsymbol{\omega} \times \mathbf{u}), \quad (2.7)$$

with $\boldsymbol{\omega} \times \mathbf{u}$, also called the *Lamb vector*, clearly emphasize the role of vorticity in the noise production. There can be no generation of sound waves in the absence of vorticity or when no moving boundaries exist. Equation 2.7 holds for a compact distribution of vorticity and for $M \ll 1$, with $c = c_0$ and $\rho = \rho_0$ and also neglecting any non-linear propagation effects and scattering of sound waves by due to vorticity.

At high Re , vorticity is concentrated in a very limited area of the whole fluid domain surrounding an airfoil i.e. vorticity is said to be “bound” to the lifting/aerodynamic surfaces. Outside that region, the flow field can be considered as an irrotational flow where viscosity does not play an important role and noise generation cannot occur.

Howe [70] reconsidered the problem of noise generation by a vortex filament near a semi-infinite half-plane discussed above using the theory of vortex sound. His result agrees with the prediction of Crighton [28] in terms of source exponent and directivity. Howe's result is, however, more explicit and reveals that noise production occurs as the vortex filament “cuts” across streamlines of an hypothetical flow bounding the half-plane, i.e. $p \propto D\Psi/Dt$, with Ψ the stream function and D/Dt the material derivative.

The generic case of a vortex ring moving linearly about a solid semi-infinite sharp half-plane (see figure 2.2), was studied theoretically and experimentally by Kambe et al. [76]. He applied the vortex sound theory to establish the temporal and angular dependency of the radiated far-field noise as,

$$I \propto \frac{U^5}{L^4} \sin^2(\theta/2) \sqrt{\sin \phi}, \quad (2.8)$$

with the azimuthal angle ϕ defined in the $y_2 = 0$ plane. A result consistent with that of Ffwoes Williams and Hall [40]. Sound intensity is found to scale according to $I \propto U^5 L^{-4}$, with U the vortex ring convection velocity, and has a cardioid-like directivity. The azimuthal directivity is found to obey ($I \propto \sin \phi$). Their result also shows that the far-field pressure is a function of the rate of change of the total volume flux through the vortex ring as it moves through the potential flow.

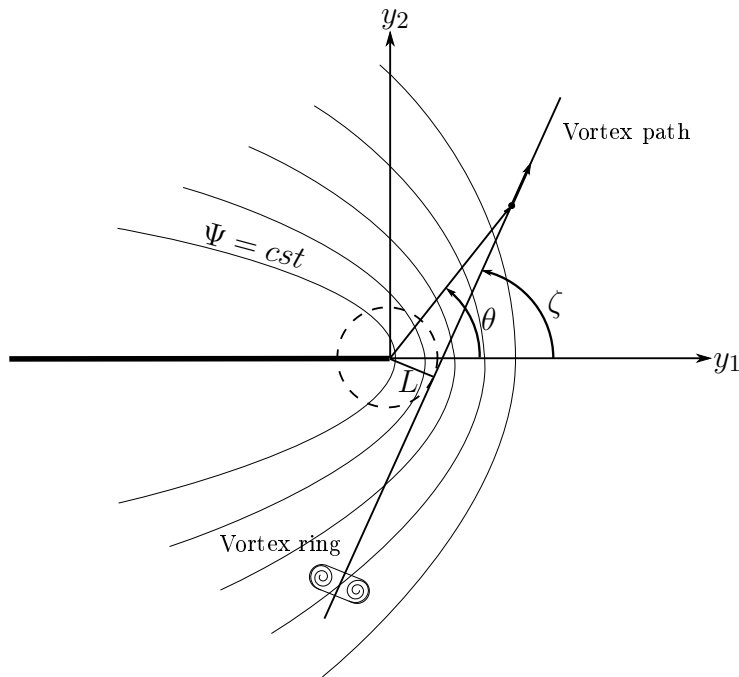


Figure 2.2.: Vortex ring, with circulation Γ , passing near a semi-infinite half-plane along a linear path. The plane occupies the domain $y_2 = 0, y_1 < 0$. Sketch from Kambe et al. [76]. Lines of constant Ψ represent streamlines of an hypothetical potential flow around the half-plane.

Tang and Ko [128, 129] studied theoretically sound generation in inviscid vortex interactions at low Mach numbers. Although their results do not directly transfer to the case of a wing tip vortex system, they provide some insight into relevant vortex related noise production. They consider three generic types of interactions, *leapfrogging*, *coalescence and collision*. The authors suggest that vortex sound occurs because of two independent mechanisms. The unsteady dynamics of the vortex centroid is responsible for low frequency noise radiation. This frequency being close to the rotational speed of the vortex centroid. Important low-frequency noise radiation occurs when vortices are subjected to high transverse accelerations therefore setting an imbalance in transverse vortex force on their cores. High-frequency noise is produced through shape deformation of the vortex core and increase with an increase in the rate of change of the vortex core asymmetry. As the vortices gets stronger i.e. larger circulation, so does the magnitude and frequency of the radiated waves. Therefore the intensity of the radiated sound is closely related to the vortex's own circulation. These findings agree with Powell [108] who states that noise radiation results from the “[...] accelerating change of total vortex strength through changing circulation or vorticity”.

2.3. Experimental Investigations on FSE Noise

In this section, a review of the most important experimental investigations on FSE noise is presented. Special attention is given to source mechanisms postulated and described in the literature. Spectral characteristics and derived scaling laws are discussed as well as sound source directivity. Finally, the effect of tip geometry variations on flap side-edge

noise is depicted and noise reduction concepts are shortly discussed. The goal of this section is to provide a physical basis onto which the subsequent modelling will rest.

2.3.1. Practical Relevance of Flap Side-Edge Noise

Early experimental work done by Ahtye et al. [3] and Miller et al. [94], in wind tunnel tests first revealed the occurrence of a dominant noise source at the wing tip using microphone correlation techniques. Miller et al. [94] found that the outboard FSE is a dominant source of aerodynamic noise in the landing configuration exceeding 2D flap noise (i.e. flap trailing edge noise) by more than 10 dB. The measurements were performed at a large scale i.e. 6.7 m half-model with a triple-slotted flap, and no leading edge device, in NASA Ames 40 ft. X 80 ft. low-speed wind tunnel. Making this configuration almost equivalent to full-scale tests. Although the results of Ahtye et al. [3] and Miller et al. [94] do provide evidences that the FSE is a significant source of aerodynamic noise, it does not answer the question on a component basis, i.e. its ranking compared to other sources.

An answer to this question is provided by Dobrzynski et al. [37] who found that the FSE noise radiation per unit source area surpasses that of the slat over the whole frequency range while clearly dominating at high frequencies. When the equivalent source spatial extent is taken into account in the calculations, the slat becomes the dominant component at low frequencies while otherwise both components appear to be equally strong. Their conclusions are based on wind-tunnel tests of a 1:10 scaled Airbus-type high-lift wing and including 4 flap side edges (i.e. contribution from the whole wing) in the calculation. Similar observations were made by Hayes et al. [61] who studied airframe noise from a McDonnell-Douglas 4.7% scale DC-10 in NASA Ames 40- by 80-foot wind tunnel. With the slat deployed, the FSE is identified as a dominant noise source at the outboard edge of the outboard flap (7 dB higher peak level rel. to slat level). Up to 8 kHz, both slat and flap are dominant sound sources, beyond 8 kHz, the FSE alone dominates. Direct comparison of the upscaled wind tunnel data with flyover noise measurements reveals a good agreement at low frequencies, while at high frequencies discrepancies are observed, the small-scale noise levels being up to 7 dB lower. The authors relate this discrepancy to Reynolds number effects and a lack in geometrical fine-scale fidelity. FSE noise is ranked as third most important airframe noise source (total component noise) for a 7% scale Bombardier CRJ-700 model tested in NASA 7- by 10-foot wind tunnel.

The relative importance of the FSE noise source varies among aircraft, depending on the number of flap side-edges as well as their size. Also important is the arrangement of the high-lift system relative to the power plants e.g. powered lift concepts. For future low-noise aircraft (e.g. upper wing engine, powered lift and blended-wing-body configurations), the FSE noise source may play a much more important role than for conventional aircraft [111].

Further experimental evidences from Storms et al. [124] also revealed the importance of slat tip noise, responsible for a broadband noise increase of 7 dB relative to the full span 2D slat. The importance of slat tip noise was also noted by Soderman et al. [121] for a 7% scale Bombardier CRJ-700 model. Although slat tip noise could be considered a different source in itself, it does share a common source mechanism with FSE noise and therefore also falls under the same category. It would also contribute to an increased overall ranking of the FSE noise source.

The influence of the Reynolds number on the above observation cannot be readily verified as only sparse experimental data are available. Dobrzynski et al. [38] did measurements in the DNW large-scale wind tunnel at a full-scale Airbus A320 wing and showed that there is an influence of the Reynolds number on unsteady surface pressure fluctuations in the aft part of the FSE while this was not the case in the forward part.

2.3.2. FSE noise at Free Wing Tips

Consider, as in figure 2.3, a finite wing of square planform and aspect ratio $AR > 3$ so that there is no important interaction between both tip vortices. The tip face geometry is flat or square i.e. normal to the spanwise direction (see figure 2.3). If not otherwise mentioned, both terms will be used interchangeably throughout this thesis. Also, if not otherwise mentioned, the wing tip geometry is flat and smooth.

Brooks and Marcolini [19] studied vortex formation noise at the tip of an extended set of isolated wings of various chord and span, with rounded tips. The authors assumed the noise production to be the results of turbulent boundary layer flow over the tip trailing edge region. Therefore, FSE noise is taken as a kind of TE noise occurring in a spatially very limited region in the vicinity of the wing tip. Their analysis is built upon the theoretical result for trailing edge noise from 2D wings [66].

The work of Brooks and Marcolini [19] was done at a time where only very limited knowledge about the tip vortices was available and provided a first effort in modelling FSE noise. The edge scattering effect describe by Brooks and Marcolini [19] is now known to be due to the formation of a double-vortex structure at the flap tip, and its interaction with the flap surface (see figure 2.3). The vortices are formed by the rapid roll-up of the suction side and pressure side shear layers shed off the tip edges. One vortex develops on the suction side and a second one on the tip face, in an independent manner [88, 89] until they merge to a single larger vortical structure around mid-chord, where the tip vortex moves to the suction side. At low deflection angles this vortex system remains near the flap surface, eventually reaching the tip's trailing-edge (TE). Large flap deflections lead to an earlier lift-off of the merged vortex from the suction side. Once this formation process his completed, a trailing vortex is released from the wing.

Two different mechanisms responsible for FSE noise are described in the literature [124], **(1)** flow unsteadiness in the shear-layer and **(2)** flow unsteadiness in the vortex-core. These two mechanisms are most effective when direct interaction with the FSE surfaces and edges is possible. The first mechanism refers explicitly to the unsteady shear layers shed at the suction side and pressure side sharp edges in the forward half of the model (see locations 1 and 2 in figure 2.4). The initial underlying characteristic wavelength of the unsteady shear layer is on the order of the pressure side boundary layer thickness [12] ($l \ll d$). A stability analysis made by Streett [125] as well as wind tunnel measurements made by Choudhari et al. [24] suggest that the shear layer instability mechanism should contribute to the mid-to-high frequency part of the FSE noise spectrum.

Although the flow at the tip edges is subjected to rapid distortions, the magnitude of the unsteadiness in their immediate vicinity is small because the shear layer development is at an early stage [82]. It is therefore unlikely that this mechanism alone is an important contributor to the total emitted noise. This is supported by unsteady pressure measurements near the flap edges which show levels an order of magnitude lower over the whole

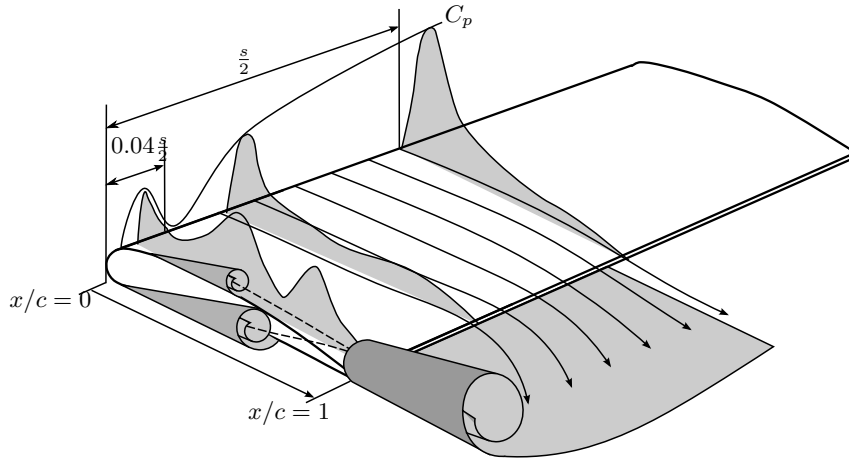


Figure 2.3.: Sketch of the tip vortex flow field and corresponding surface pressure distributions

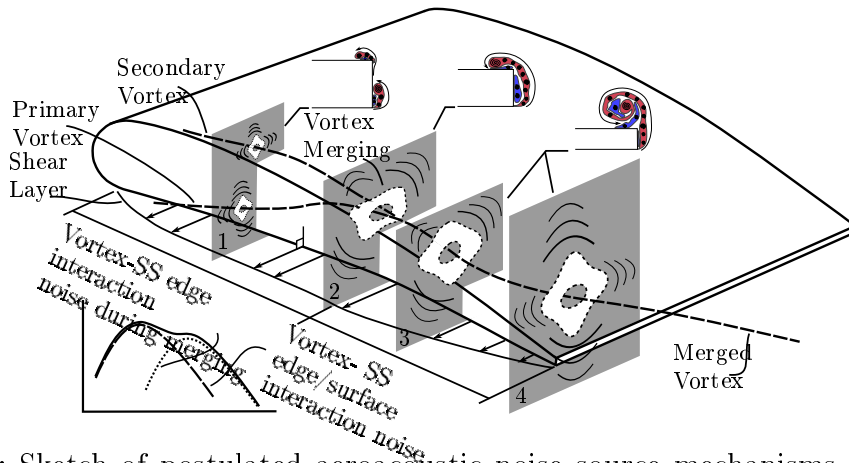


Figure 2.4.: Sketch of postulated aeroacoustic noise source mechanisms. At each section cut, a typical instantaneous distribution of vorticity is shown in the inserts. Red spots correspond to positive vorticity while the blue spots are for negative vorticity.

frequency range on the pressure side relative to suction side levels [18, 57, 124]. Guo et al. [57] used correlation analysis between surface sensors on a 4.7% DC-10 aircraft in NASA Ames 40×80 foot wind tunnel to identify a dominant source of noise near the suction side edge, underneath the path of the vortex. The double-vortex system which forms at the flap tip is found to leave its trace in the unsteady surface pressure fluctuations in the form of spectral level humps. These humps are measured only under the helical path of the vortex and are therefore directly related to unsteady motion due to the vortex.

A probable source mechanism is therefore a combined contribution from a pure shear layer instability mechanism at the pressure side and suction side edge and the interaction of the resulting unsteady velocity/vorticity fluctuations with the tip suction side edge during vortex merging [82, 83, 90]. The second mechanism is related to vortex-structure interactions in the aft half of the model chord in the vicinity of the flap tip upper edge (see locations 3 and 4 in figure 2.4). It is an efficient radiator in the mid- to long-wavelength range [24, 57, 90, 125]. Storms et al. [124] refers to this mechanism as “vortex scrubbing”. This is supported by unsteady surface pressure measurements at a full-scale flap of an

Airbus A320 wing made by Dobrzynski et al. [38], that reveal a spectral peak around $x/c = 0.4$ for the high-frequency range and near $x/c = 0.7$ for the low-frequency range.

A stability analysis of the flap-side edge flow field performed by Streett [125] and Streett et al. [126] supports the above experimental evidences. The authors used RANS with artificial forcing and observed the amplification of perturbations as a function of frequency. Two types of instability were identified, shear-layer and vortex instabilities. The shear layer instability grows mainly in the cylindrical shear layer itself and its characteristics are frequency dependent. At low frequencies, amplification occurs over an extended spatial range reaching into the vortex. At high frequencies, most of the amplification is concentrated near the lower tip edge. The tip vortex is also assumed to be unstable in the streamwise direction due, in-part, to the strong jet-like flow in the core region. This is indeed the case and vortex instabilities are found to occur for wavelengths on the order of a quarter to half of the vortex diameter. The shear layer instabilities cover the range 5 to 30 kHz while vortex instabilities are mostly important in the range 1 to 10 kHz. The vortex instability mechanism is expected to provide enhanced levels of TE noise. The authors suggests that rapid distortion of the flow structures is essential for the scattering of energy into modes which propagates at sonic phase speeds. Interestingly, the spectral features postulated and identified by the authors are found to be very similar across multiple configurations. The low-frequency spike observed by Choudhari et al. [24], and due to the vortex interacting with the flap TE corner, is dependent on the proximity of the vortex to the flap upper surface.

Scaling Laws Even with the knowledge accumulated over the last decade, there is no consent on appropriate scaling laws for FSE noise. A common assumption is to use geometric wing dimensions e.g. chord length and/or flap thickness as characteristic length scales. Numerous experimental studies have revealed that FSE noise intensity is proportional to $I \propto U_0^n$, with $4.5 \leq n \leq 6.5$ and U_0 being the free-stream velocity. This range covers the scattering half-plane case ($n = 5$), discussed theoretically by Ffwoocs Williams and Hall [40], and that of free turbulence moving about a compact body ($n = 6$), treated by Curle [29].

Based on airframe noise study of a 4.7% DC-10 aircraft in the 40X80 feet wind tunnel at NASA Ames, Guo et al. [57] found that an increase in flap angle results in a slight peak frequency decrease in the surface pressure spectra. Flow dependent scaling parameters are needed to represent this effect. Guo et al. [57] also suggests that the characteristic length scale of the dominant flow features should be the local coherence length of the vortical structures, a quantity dependent on the flow conditions and flap geometry.

In the early work of Brooks and Marcolini [19], a mixed scaling based on the free-stream and the maximum tip cross-flow velocities is proposed, with

$$I \propto \frac{U_0^2 U_m^3 l^2}{R^2}. \quad (2.9)$$

The length l and the velocity U_m are related to the tip's effective angle of attack like, $l/c \approx 0.008\delta_F$ and $M_m/M_0 \approx (1 + 0.036\delta_F)$. For square tip wing tips, George and Chou [47] propose $l/c \approx 0.023 + 0.0089\delta_F$ and the same velocity relationship as above. Scaling of the experimental data using equation 2.9 provides an acceptable amount of collapse and is better than a scaling with M_0^5 . A relatively important scatter is observed in the processed

data which is inherent to the post-processing procedure selected to extract far-field noise data in that particular experiment. The scaled noise spectra are represented by a fitted parabolic curve around a peak Strouhal number of $St = fl/U_0 = 0.5$. Interestingly the authors expect higher noise levels for a wing with a square tip due to higher turbulence intensities near the tip edges. This affirmation is not supported by recent measurement at a wing tip with round edges (to be discussed herein).

McInerny et al. [88, 89] measured surface pressure cross-correlations between surface sensors on a NACA0012 wing profile. They found that the characteristic length scale of the convected vortices is of order $d/3$, with d the thickness of the airfoil. They suggest a scaling of the data using the vortex diameter and the vortex core velocity or free-stream velocity. They, however, did not test their ideas on measured acoustic data.

Drobietz and Borchers [39] studied FSE noise generation at generic side edge models. Their model consists in a vertical flat plate installed at an angle relative to the flow direction, its extremities reaching outside the tunnel shear layers in the spanwise direction. The authors also found that shear-layer instabilities generate noise in the mid- to high-frequency range while the merged vortex interactions with the side and upper surfaces leads to noise generation in the low- to mid-frequency range. Noise intensity is found to be proportional to $I \propto U_0^{5.5}$ for the low frequency part and $I \propto U_0^{6.5}$ for the high-frequency part. For slim side edges, a low-frequency noise increase was observed combined with a high-frequency noise reduction. This is explained through the reduced side surface available for the shear layer to interact with. The tip vortex moves to the upper side more rapidly and interacts with the surface as usual. This result give some clues about the possibility to represent smooth tip edges by a reduced effective thickness.

Directivity There is no study on the directivity of the radiated noise from a generic cantilever wing with a free FSE available in the literature. A discussion of the directivity of FSE noise is always made for high-lift wing configurations (see below). The case of a free FSE might differ in the shape of its radiation pattern due to the absence of a wing upstream of the flap but also because of different flow conditions near the flap tip.

2.3.3. FSE Noise in High-Lift Wing Configurations

This section covers FSE noise generation in high-lift wing configurations. In the present context, the term *high-lift wing* is used to describe any variation of **model** or **real** wing **with** or **without** leading edge slat.

Although the high-lift wing configuration, greatly differs from the cantilever case, the flow field about the tip of a straight flap (no sweep and no taper) as well as the intensity of its sound radiation are known to be almost entirely dictated by the flap deflection angle [21, 90, 130, 135]. This is, however, no true for swept and/or tapered wings, where the FSE tip static pressure distribution are greatly affected by a change in main wing angle of attack, with noise levels increasing as the angle of attack increases [135].

For a straight flap in a high-lift system one could therefore assume that the generic source mechanisms described in the previous section are also valid. Using source correlation techniques, Meadows et al. [90] indeed found that high-frequency noise originates from the tip vortex merging position while low-frequency noise mostly originates from the tip TE. This was later observed by Storms et al. [124] using the microphone array

technique and Brooks and Humphreys Jr. [21] using the COP method. Storms et al. [124] also suggests that high-frequency noise is produced in the forward section of the FSE through vortex scrubbing as the lower tip boundary layer moves around the tip along the FSE face. Raking the FSE into the flow reduces high-frequency noise radiation while a raking away from the flow promotes high-frequency noise production. Low frequency noise increases when raking into the flow while the inverse holds when raking away from it. Further evidences of the edge-scattering noise generation mechanism are provided by Brooks and Humphreys Jr. [21] who found that, contrary to classical TBL TE noise, noise levels increase when moving closer to the flap edges. It is postulated that this increase in intensity is related to the release of two shear-layers at the flap edges which can be represented by a chordwise distribution of dipoles radiating with opposite phase. In the case of a round flap edge, the authors assume a similar generation mechanism without further proof. More recently, Tiedemann et al. [131] and Tiedemann [130] used microphone array and PIV measurements to come to a similar conclusion about the noise source mechanisms. Furthermore, his results also show that the vorticity convection velocity around the flap tip increases with distance downstream of the tip LE. This implies noise generation through acceleration of vorticity pockets (or turbulent eddies) as they move about the FSE [41, 66, 108].

Angland [6–8] studied flap side-edge noise in wind-tunnel experiments on a part-span flap installed in a high-lift wing model without slat. The author used PIV and oil flow visualization techniques to investigate the tip flow field in more detail while acoustic measurements were done using a microphone array as well as unsteady surface pressure sensors. It was found that the cross-flow through the gap between the main element and the flap led to a flattening of the suction side vortex and also to a later merging of side and top vortices. The top side vortex is also pushed more inboard. The formation of a strong shear layer on the main element is also observed. Its vorticity has an opposite sign compared to the flap suction side vortex. At the largest flap deflection the tip vortices have more room to grow, and build up complex non-uniform distributions of vorticity, known to promote flow unsteadiness and therefore noise [82]. Because the top vortex is impeded in its development and pushed away from the tip edges in the high-lift wing configuration, one should expect reduced mid- to high-frequency noise levels compared to the the free FSE case. Also the main wing vorticity is, in part, pulled toward the FSE, further injecting vorticity into the flap tip vortex. Similar conclusions are drawn by Yokokawa et al. [135] for noise generation at a swept and tapered high-lift generic wing.

A comprehensive set of experiments on airframe high-lift component noise were conducted by Dobrzynski et al. [37, 38], Pott-Pollenske and Delfs [105], Pott-Pollenske et al. [106]. Their experiments encompass acoustic data from a small-scale high-lift airfoil, a 1/7.5 scale full-A320 aircraft model and original full-scale Airbus A320 wing as well fly-over measurement data from an Airbus A319. Flap-side edge noise is found to be at least as important as slat noise, but dominates in a higher frequency range.

Scaling Laws As for the generic free FSE case, sound intensities are found to be proportional to $I \propto U_0^n$ with $n = \mathcal{O}(5)$. For large flap deflection angles n tends to increase slightly over 5 [90, 124]. The high-frequency part of the spectra is found to follow a different scaling relation [90, 124, 130, 131]. This aspect is not further investigated in the literature.

Storms et al. [124] consider FSE noise to be essentially trailing-edge noise generated in the vicinity of the flap tip. They found sound intensity levels to be a linear function of the flap lift which itself also linearly depends on the deployment angle, for δ_F larger than 15° . The authors use the trailing edge noise theory of Ffwoocs Williams and Hall [40] to relate local tip aerodynamics to the FSE noise production:

$$p^2 \propto \rho_0^2 M_v^5 \left(\frac{L\delta}{R^2} \right) \sin \alpha \sin^2(\theta/2) \cos^3 \beta. \quad (2.10)$$

Here the local flow Mach number M_v , is estimated by potential flow calculations using measurements of the static pressure distribution in the airfoil's tip vicinity. δ represents the correlation scale of the noise producing structures covering a length L along the tip edge. β represents the effect of wing sweep (or flow angularity relative to the streamwise direction, as in Brooks and Humphreys Jr. [21]). α is the aerodynamic angle of attack and θ the directionality angle with $\theta = 0^\circ$ in the direction of the half-plane, i.e. along the chord in the upstream direction.

Brooks and Humphreys Jr. [21] postulate that the scattering of unsteady pressure fluctuations, due to the formation of two shear layers at the FSE, is the most important noise generation mechanism for FSEs. They propose the cross-flow velocity

$$U_c = \sqrt{U_0^2 + U_2^2} \quad (2.11)$$

as characteristic velocity scale instead of the mean free-stream velocity or the local mean flow velocity. U_2 is defined here as the mean-flow velocity component in spanwise direction. U_c provides a good collapse of the data with $n = 5.0$.

In all these studies, the lack of knowledge about relevant length scales of the noise producing flow structures justifies the choice of geometrical size parameters or the use of length scale approximations based on zero-pressure gradient boundary layer theory. There still exists no consent on the choice of characteristic velocity and length scales relevant for FSE noise.

Dobrzynski et al. [37] postulate that flap side-edge noise results from the accelerated (rotation-) motion of unsteady vorticity about the flap side-edge, and found a velocity proportionality according to $p^2 \propto U_\infty^6$ for a high-lift configuration of the Airbus A319/A320 type. Khorrami et al. [80] reach a similar conclusion from fly-over noise measurements at a Gulfstream G-III regional jet. They note that this scaling holds, for their data, over the whole spectral range attributed to flap side-edge noise.

Directivity The measurements of Ahtye et al. [3], and Miller et al. [94] were the first to provide details about the directivity of FSE noise for high-lift configurations. Ahtye et al. [3] conducted experiments in NASA-Ames 7- by 10-Foot Wind Tunnel using a single-slotted wing flap arrangement. They observed that the FSE is the dominant source of noise, its directionality having a rear-arc maximum. Follow-up investigations by Miller et al. [94] on wing models with double- and triple-slotted flaps in NASA AMES 7- by 10-Foot and 40- by 80-Foot tunnels reveal, however, a directionality with a forward-arc maximum. Both reports providing insights deviating from the classical assumption of dipole-like radiation and emphasizing the significance of the specific flap type considered, i.e. single-slotted vs. double- or triple-slotted flaps.

A similar directivity pattern was later measured by Meadows et al. [90] in NASA QFF at a two-dimensional airfoil with part-span flap and by Hayes et al. [61] and Guo and Joshi [56] at a 4.7%-scale DC-10 Model in NASA Ames 40- by 80-Foot Tunnel. The results of Guo and Joshi [56] contains, however, contributions from both the flap and the slat. Both author observed that FSE noise directivity has a forward radiation pattern at low frequencies which becomes more uniform with increasing frequencies. At low frequencies the directivity resembles that of a baffled dipole [91]. The radiation directivity for a fenced FSE is found to be identical to the unfenced one, suggesting that noise directivity is not a strong function of the tip geometry.

Brooks and Humphreys Jr. [21] observed similar trends at low- and high-frequencies in measurements at a NACA 63₂–215 airfoil with a 30%-chord half-span flap in NASA QFF tunnel. They also identified regions of high sound pressure levels towards the side line. This observation is corroborated by fly-over noise measurement of an aircraft with porous FSEs [34]. Suction side noise levels are generally lower with a tendency to increase in the downstream direction. This is assumed to be related to diffraction/reflections at the flap edge. Similar low-frequency directivities are observed for a flange and round tip geometry. Again, indicative that FSE noise directivity is not a strong function of geometry. However, as frequency increases, the directivity patterns for these latter geometries become more complicated than for the flat edge. A dominant rear-arc radiation pattern is also found by Yokokawa et al. [135].

Finally, component interaction noise is considered in Radeztsky et al. [110] and Storms et al. [124]. The flap flow field is mainly dictated by the conditions at the main element. A comparison of experimental C_p distributions at a flap in the QFF and NASA Ames 7- by 10-Foot Tunnel with CFD computations revealed a very good agreement, even if the main wing angle of attack differs in each case [110]. Oil flow and PSP visualizations revealed flow patterns which are strongly dependent on the flap deflection but not the main wing's angle of attack. As a consequence, the slat has only little effect on FSE noise because their corresponding flow fields are not strongly coupled. Inversely, the flap induces changes in circulation on the main elements which will be noticed by the slat. The effect on slat noise is, however, not important [124].

In approach configuration, i.e. with both leading edge slat and trailing edge flaps deployed, the results of [37, 38, 105, 106] clearly indicate that high-lift airframe noise has a rear-arc dominant directionality. A clear distinction between the slat and flap side-edge contribution cannot be made. But, as stated by the authors, flap side-edge being dominance at high-frequencies suggest that both components directivity are similar.

2.3.4. On the Role of the Flap Tip Geometry

Because the FSE noise source is intimately linked to flow-structure interactions taking place in the vicinity of the flap tip, its geometry (i.e. profile shape) should play an important role. The number of studies on the subject is sparse and they provide only a correspondingly rough image of the physics at play. Below is a list of the most important investigations.

Choudhari et al. [24] studied FSE noise from a high-lift wing without slat in Langley's low-turbulence pressure tunnel. The wing model is a NASA Energy Efficient Transport wing (EET [98]). For this wing model, the author measured a stronger vortex on the flap

suction side instead of its pressure side. A weaker vortex still forms at the FSE which eventually moves to the upper surface and merges with the top vortex. The side gap appears to delay tip vortex formation by flattening the top vortex. Tests with rounded tips only show a slight noise increase, which is unexpected. This is probably due to the strongest vortex being located on the upper surface and it developing independently of the tip conditions.

Brooks and Humphreys Jr. [21] tested three different FSE configurations: flat, round and flanged. The round edge flap is found to be the loudest at low frequencies and the quieter at high frequencies compared to the flat and flanged FSEs. The flanged tip generates a strong quasi-tonal component. Reynolds effects appear to be stronger for the flat tip.

Drobietz and Borchers [39] found tip shape to play an important role regarding noise generation. In particular, streamlined shapes are assumed to minimize energy losses due to separation at the edges which allow for increased flow velocities on the flap upper side and a larger low-frequency noise production.

Tiedemann [130], Tiedemann et al. [131] found that, for a rounded tip, noise was primarily generated near the tip TE corner through vortex-surface interaction on the tip upper surface. High-frequency noise caused by flow separation at the tip edge is practically eliminated. Furthermore, adding a tip cavity provides a broadband noise increase on the order of 10 dB for a cavity depth of $0.43d$ (Tiedemann [130]).

There is only few studies dealing with the impact of fine-scale geometric details and others sources of excess noise at FSEs. Some information can be gained from Storms et al. [124] who found that noise from flap tracks, i.e. brackets, appears in the noise spectra as a strong quasi-tonal component. Also, Dobrzynski et al. [37, 38] studied high-lift noise at a 1/7.5 scaled complete model aircraft and a full scale A320 wing in the German Dutch Wind Tunnel (DNW). Their results emphasize the importance of construction details present on real aircraft compared to idealized wind tunnel wing models. Specifically, for the FSE, a 7 dB noise increase was measured for the real wing configuration compared to a clean flap. These studies are of course not sufficient to get a precise picture of such sources of excess noise at FSEs. They do, however, emphasize that any prediction methodology based on data from idealized wind-tunnel models should be expected to under predict real aircraft noise emissions.

The use of microtabs to energize/stabilize the pressure side shear-layers and, therefore, reduce noise generation have shown only mitigated effectiveness in reducing FSE noise [24]. FSE noise appears to depend only to a lesser extend on the pressure side boundary layer flow characteristics. Similar results were also obtained by Storms et al. [124] using vortex generators and grit.

For common transport aircraft, the flaps usually deploy with their tips at an angle to the flight direction. This means that the FSE are raked-into or -away from the flow. A positive rake (into the flow) is found to reduce overall FSE noise levels while a negative raking (away from the flow) has the opposite effect. Unsteady surface pressure measurements suggest the latter to be related to flow separation near the flap tip LE [65]. Storms et al. [124] note that for a positive rake, the primary vortex moves inboard above the upper surface well before mid-chord and a strong suction peak is detected in the forward section. For a negative rake the opposite occur and the tip vortex stays along the edge for most of the chord. There is no evidence of the formation of a secondary vortex on the upper

surface. The far-field noise radiation displays increased high-frequency noise levels for a negative raking, most probably due to the vortex staying in close proximity to the tip edges while no large vortex forms on the upper side. Low-frequency noise increases for positive raking due to the early movement of the tip vortex to the upper surface allowing it develop to larger scales up to the TE.

2.3.5. Noise Reduction Concepts and their Relation to the Source Mechanisms

In this section a short (and thus incomplete) review of noise reduction concepts for the FSE is presented. The main focus of the discussion is centered on the working mechanism of each concept and its relation to the noise mechanisms already discussed in previous sections.

A first concept is known as the flap-tip fence. It is typically realized by adding an extension plate to the flap tip, the extension being parallel to the FSE tip face. Different variations exist, extending on only one side or both sides of the flap, and with varying dimensions. Flap-tip fences are most effective when extending only on the pressure side and when aligned with the upstream flow. In wind-tunnel tests, the fences provide 2-4 dB broadband noise reduction without affecting the slat loading and noise [65, 122–124] while they were found to provide a 3-4 dB reduction in the range 4-10 kHz during flyover noise measurements [123]. The fence's effect is to enforce a delayed merging of the primary and secondary vortices, also the merged vortex gains in size while moving further away from the tip. Therefore, FSE fences reduce noise by shifting the peak radiation frequency to lower values [57]. An analytical model of the frequency shift is given by Guo [58]. His hypothesis, however, neglects the potentially important role of the flow direction at the pressure side edge where the shear layer is released and which should considerably differ for a fenced airfoil compared to a unfenced one. Horne et al. [65] measured unsteady pressure fluctuations on a multi-element airfoil with a part-span flap and full- and part-span slats.

A second noise reduction concept is the porous FSE. It consists of any porous material applied to the wing tip region rendering it effectively permeable, to a certain degree, to the flow. The working mechanism is postulated to be related to dissipation, vortex modification and reduced surface impedance [124]. Porous treatments tend to reduce the peak vortex radial velocity as well as forcing the vortex location to move away from the tip. There is a significant increase in turbulence levels, but further away from the surface. Porous treatments are only effective when their spanwise extent remains below 5-10% c [6–8, 124]. Also, different regions along the FSE can be related to noise radiation in distinct frequency ranges. Making only the lower and tip surfaces porous greatly reduces high-frequency noise radiation. A porous lower surface alone does not suffice to achieve large noise reductions. This emphasizes the importance of the interaction between turbulent velocity fluctuations and the different FSE solid surfaces. The tip face is where most of the high-frequency noise is produced while low-frequency noise occurs through interactions with the upper surface.

Koop et al. [83] and Koop [82] investigate side-edge blowing as another possible noise reduction approach. Blowing air into the tip vortex contribute in breaking the large vortical structure into smaller ones and pushing them further away from the FSE surface, thus leading to reduced far-field noise levels. Koop observes a scaling-down of the tip

vortex structures due to the blowing which might be due to the tip vortex formation dynamics being impeded. Also the proximity to the surface and between the top/bottom vortices in the early phase most probably has an influence on the speed with which the system merges and develops. This could explain why a thicker profile produces vortices of smaller dimensions compared to thinner profiles.

Hutcheson et al. [72] investigated FSE noise reduction using continuous mold link technology (CML). Compared to a blunt flap edge, CML noise levels are found to be about 10 dB lower over most of the measured frequency range. The most dominant noise source for the CML configuration is identified at the flap LE cove (between main element and flap LE). Noise is produced through pressure scattering at the main element TE and subsequent channeling through the flap LE gap. An important high-frequency quasi-tonal component is produced which, in some case, surpasses the blunt FSE levels. It is very sensitive to small geometrical details on the main element TE. It is, however, not clear to which extent this feature also exists at high Reynolds numbers. Main element TE cove noise could play an important role as it is an extended source, similar to slat noise. Cove noise is strongly dependent on emission angle, with as much as 10 dB differences and a maximum radiation angle in the upstream direction (dipole character).

The work presented in Murayama et al. [101], Takaishi et al. [127], Yamamoto et al. [132, 133], Yokokawa et al. [136], is one of the most recent published effort into quantifying the potential of airframe noise reduction technologies at a full-scale aircraft. The authors presents acoustic results from fly-over measurements at a Cessna Model 680 mid-size business jet. Their research extends from numerical simulations to wind tunnel investigations and flight tests. In particular, the authors deal in more details with the reduction of FSE noise in [136]. They propose the use of a protruding rounded lower edge device in combination with upper side vortex generator. With the tip vortex path about the flap's tip is moved further away from the solid surface and the tip's discontinuity is smoothed out. Thus leading to a reduction in intensity of the tip vortex turbulence velocity fluctuations. The upper side vortex generator further act to modified the tip vortices dynamic, therefore leading to less noise generation. This approach provides a broadband noise reduction of at least 3 dB.

3. Investigations

This chapter provides a description of each experimental setup used in the course of the work while giving insights into the goals pursued in each case.

3.1. Experimental Strategy

The experimental approach followed in this thesis is aimed at gathering a maximum of acoustic data for wing configurations most relevant for the formulation of a widely applicable semi-empirical prediction model for flap side-edge (and also wing tip) noise. To achieve this goal two reference configurations are selected, a cantilever wing model (considered here as an isolated flap model) and a three-element high-lift wing with a half-span flap. Both flaps share a unique profile section but have different scales. This variation in size and overall configuration allows for the study of different aspects of FSE noise which would not be possible by considering a single test configuration. The cantilever wing provides insight into the tip flow dynamics and allows for detailed investigations of the acoustic source region. The high-lift configuration enables the assessment of installation effects. More details about both wing models are given below.

Additionally, measurements at a DU96 wing and a high-lift wing with a part-span flap of Clark-Y profile, were made to reach beyond these references test cases and study the role of a wing's aspect ratio as well as of its tip section shape. The impact of tip raking was also studied using a full-scale version of the reference cantilever wing. The wide range of model size occurring in the experiments also makes it possible to study the role of the Reynolds number on the radiated noise.

Finally, three different tip add-ons were investigated to gain further insight in the underlying mechanism of FSE noise. A porous wing tip add-on was tested at both reference cases. Also a tip cavity add-on and a smooth-edge tip add-on were tested at the reference cantilever wing.

3.2. Wind Tunnels

Most of the experiments were performed in the Acoustic Wind Tunnel Braunschweig (AWB). The only exception is for the investigation a the full-scale cantilever flap which was done in the DNW-NBD low-speed wind tunnel.

The AWB is an open-jet closed-return wind tunnel (Göttingen type) capable of running at speeds of up to 65 m/s (see figure 3.1) [105]. The test section is optimized for noise measurements at frequencies above 250 Hz. This is accomplished through acoustic treatment of the measurement chamber as well as on the channel walls and guiding vanes. The inlet nozzle has a surface of $0.8 \times 1.2 \text{ m}^2$. The tunnel is also equipped with a vertically

Table 3.1.: Geometrical parameters of the wind tunnel models. With c referring to the flap chord length when considering high-lift configurations. Otherwise, for cantilever configurations, c refers to the airfoil chord.¹⁾ $AR = 4b^2/S$ with b the airfoil span and S the airfoil area.²⁾ Sweep angle, Λ .³⁾ Taper ratio, $\lambda = c_{\text{tip}}/c_{\text{root}}$ with c_{tip} taken parallel to the flow direction.⁴⁾ Tip chord length, measured parallel to the tip face. Root chord length is $c_{\text{root}} = 0.664$ m.⁵⁾ Mid-chord span.

Profile	c [m]	$b/2$ [m]	AR^1	Λ [$^\circ$] ²	λ [-] ³	configuration
FNG	0.473	0.4	1.67	0.0	1.0	cantilever
FNG	0.118	0.4	6.78	0.0	1.0	high-lift
FNG	0.633 ⁴	0.699	2.21	0.0	0.95	cantilever
FNG	0.676 ⁴	0.430 ⁵	1.27	0.0	0.96	cantilever
Clark-Y	0.24	0.7	5.83	0.0	1.0	cantilever
Clark-Y	0.096	0.41	8.54	0.0	1.0	high-lift
DU96	0.300	0.6	4.00	0.0	1.0	cantilever

adjustable collector. A feature which is convenient when testing high-lift wing components, to prevent deflection of the tunnel jet into the floor of the test section, therefore, reducing extraneous noise.

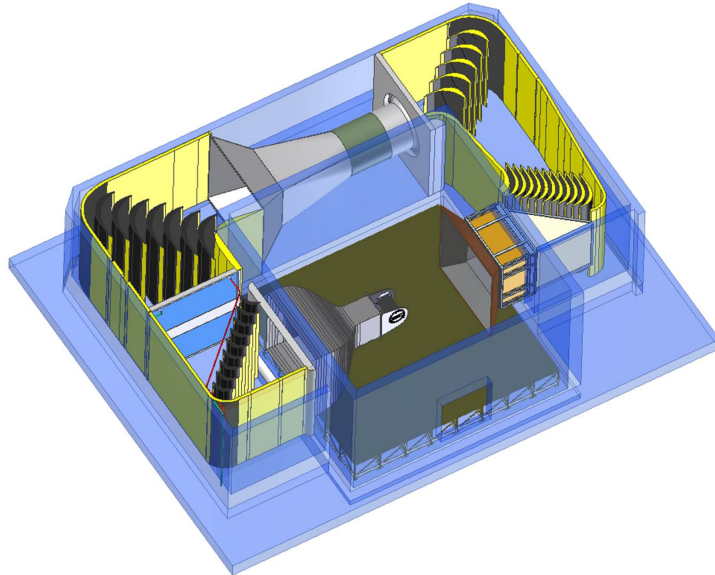


Figure 3.1.: Acoustic Wind Tunnel Braunschweig (AWB).

The AWB coordinate system definition is presented in figure 3.3. It is a right-handed system with its origin at the test section inlet plane center. In this figure, emphasis is put

on the cantilever reference test case. However, the same coordinate system is also used for measurements done with the reference high-lift configuration and all other models.

Tests at the full-scale flap model were performed in the DNW-NWB low-speed wind tunnel in Braunschweig (see figure 3.2). It is an open jet anechoic wind tunnel with an inlet nozzle of dimensions $3.25 \times 2.8 \text{ m}^2$ and a test section length of 6 m. Its can be operated, in the open-jet configuration, at velocities up to 80 m/s. The tunnel has an interchangeable test section which also accommodates a closed-wall test section. The anechoic plenum is certified for $100 \text{ Hz} < f < 40 \text{ kHz}$.

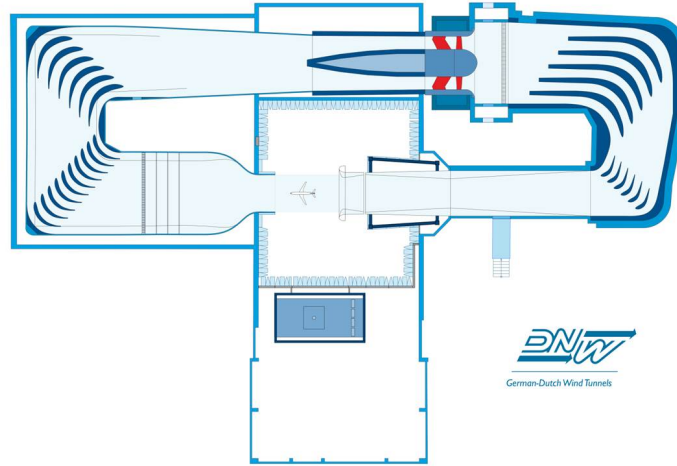


Figure 3.2.: Low-Speed Wind Tunnel Braunschweig (NWB).

Although the NWB has adopted a different coordinate system definition, all results will be presented according to the AWB definition in figure 3.3. If needed, further precision or adaptation of this basis coordinate system will be mentioned throughout the document.

3.3. Reference Test Cases

The reference test cases are depicted in more details hereafter (see figure 3.4). Both were subject to the most extensive acoustic investigations. Flow field investigations are only available for the cantilever wing i.e. setup 1. Detailed sketches of the experimental setups in the AWB and NWB can be found in appendix A.

3.3.1. Setup 1: Cantilever Wing

The wing has a 0.4 m span and a chord of 0.473 m. It is fixed to an acoustically lined turning plate which allows for a variation of the wing's angle of attack relative to the tunnel axis (see figures 3.6a). The cantilever wing model is tested at various angles of attack ranging from $-5.7 \leq \delta_F \leq 32^\circ$. Measurements were done for Mach numbers ranging from $M = 0.087$ to 0.175 , corresponding to Reynolds numbers (based on the flap chord) ranging from $Re = 0.96 \times 10^6$ to 1.92×10^6 . Surface static pressure distributions are

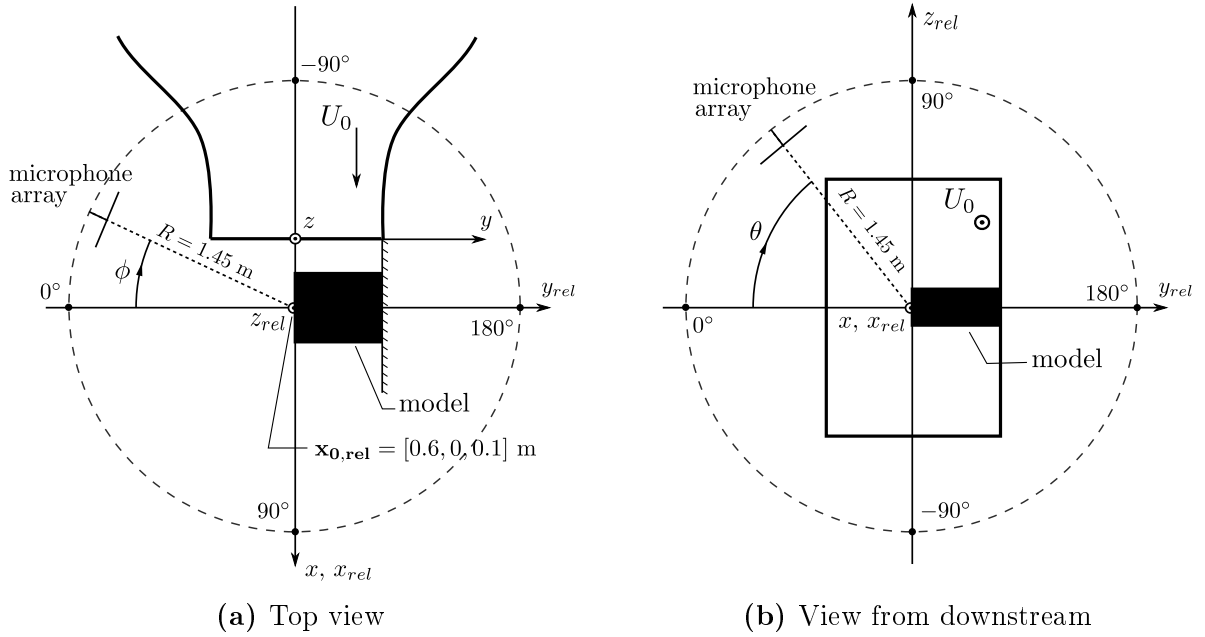


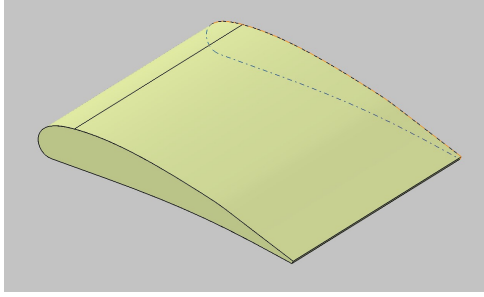
Figure 3.3.: General AWB coordinate system definition. Origin is the nozzle center point.

measured by means of a total of 32 static pressure ports. Static pressure taps are available for 13 positions at the mid-span cross-section (see figure 3.5a) and 19 distributed over the wing's tip face (see figure 3.5b). The suction side and pressure side taps are located at the half-span position.

Sound source localization as well as quantification was performed using both large and small aperture microphone arrays as well as standard far-field microphones, as specified in chapter 4 and depicted in figure 3.6. The large aperture array is used both in vertical and horizontal mounting to assess different radiation directions. The small aperture microphone array is used in combination with a two-axis polar displacement system (see figure 3.6a) to get the most extensive directivity measurements possible. The free-field microphones were installed on the AWB floor aligned in streamwise and traverse fashions (see section 4.1 for more details).

A tripping was used in the first series of measurements on the suction side at $x/c = 0.01$ and on the pressure side at $x/c = 0.34$ in an effort to reduce the appearance of laminar separation related tones as well as to ensure the development of fully turbulent boundary layers and prevent their premature separation. However, it was found that tripping had no impact (positive or negative) on the aerodynamics and acoustics for this model. Laminar-Turbulent boundary layer transition at $\delta_F = 20^\circ$ was found to occur at 8% on the SS and 20% on the PS and on almost the whole model span. Except for the existence of an extended complex recirculation zone near the wall on the SS, no boundary layer separation could be observe up to $\delta_F = 25^\circ$. This behavior being independent of the use (or not) of a tripping device. Therefore, the application of trip strips in subsequent experiments was dropped.

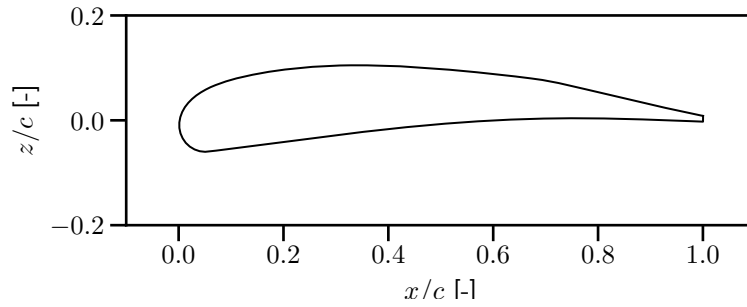
Boundary layer separation was first observed for a flap deflection of $\delta_F = 30^\circ$. Its position and occurrence is not affected by boundary layer tripping. A small zone of detached flow was observed in the mid-span region, on the suction side of the model.



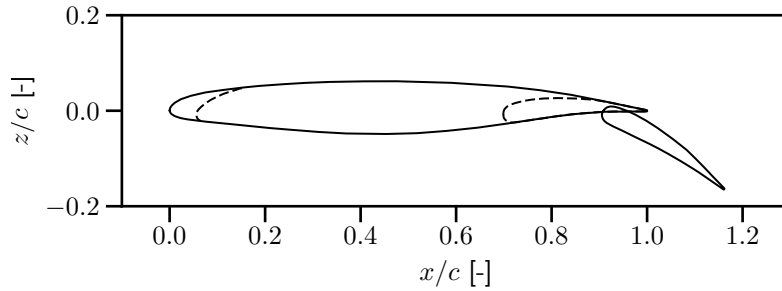
(a) Cantilever flap model ($s_{flap} = 0.4$ m, $c_{flap} = 0.473$ m).



(b) 3-element high-lift model ($s_{flap} = 0.4$ m, $c_{flap} = 0.12$ m).



(c) FNG-type flap. $c_{flap} = 0.473$ m.



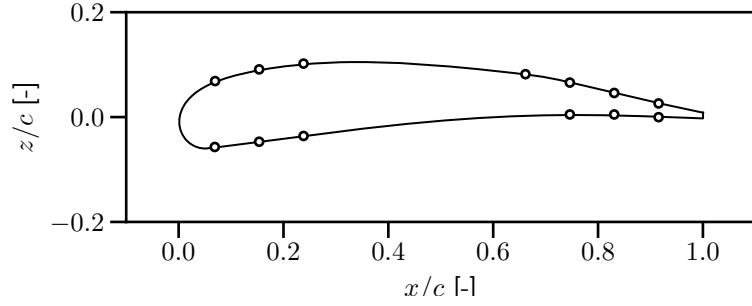
(d) High-lift wing model. $c_{wing} = 0.4$ m, $c_{flap} = 0.12$ m.

Figure 3.4.: Experimental models

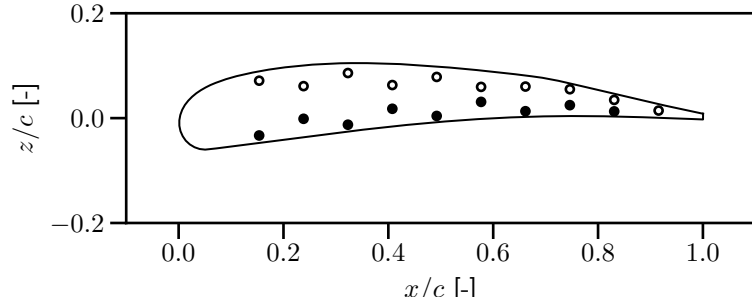
The acoustic measurements were complemented by a study of the tip flow using a 7-hole probe (see Chapter 4).

3.3.2. Setup 2: High-Lift Wing Configuration

The second reference wing model is a generic 3-element high-lift model with a half-span flap (0.12 chord length, 0.4 m span, 1:6, FNG-type geometry). The main wing is mounted between two supporting side plates and spans the entire width of the AWB test section. The flap is attached to the main element by one flap track, 0.1 m from the FSE. The other end of the flap is screwed directly into the wind tunnel side plate. This was done to minimize spurious noise resulting from interactions of three-dimensional corner flow at the flap root with a supporting track.



(a) Distribution of mid-span static pressure taps on both the cantilever wing and high-lift wing flaps



(b) Distribution of tip face static pressure taps.

Figure 3.5.: Static pressure taps positions.

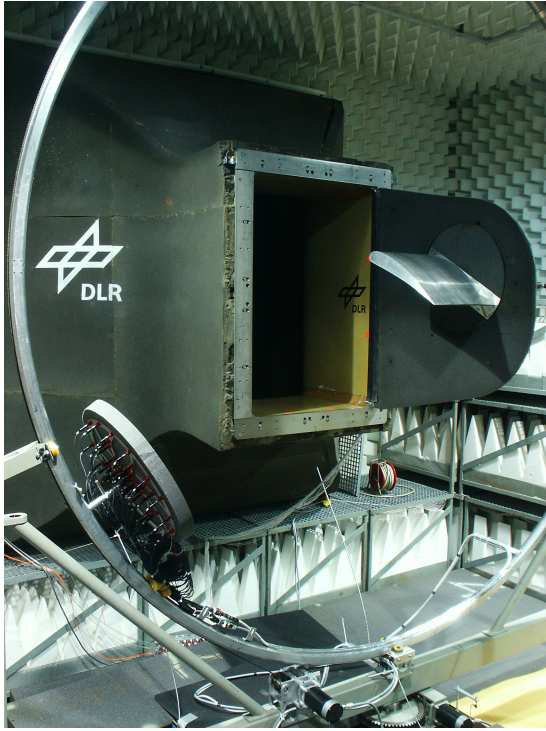
Static pressure taps are available for 12 positions at the mid-span cross-section (see figure 3.5a) Overall the model is equipped with a total of 173 pressure taps distributed over 5 spanwise sections. Four of these sections are located on the main element while one is on the flap. No pressure taps are available on the slat.

This configuration was tested at three flap deployment settings ($\delta_F = 20^\circ, 25^\circ, 34^\circ$) and for three main wing angles of attack (i.e. $\delta_F = 0^\circ, 7^\circ, 10^\circ$). The slat is kept retracted ($\delta_s = 0^\circ$) to ensure a good identification and quantification of the FSE noise source with the microphone array. Tests were done for Reynolds numbers ranging from $Re = 2.4 \times 10^5$ to 4.8×10^5 .

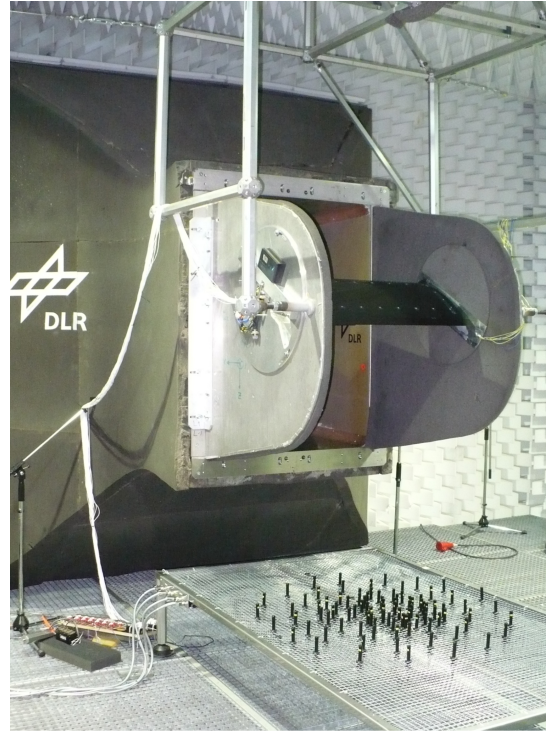
Fixation of the flap to the main wing is done using a streamlined bracket of fixed length. Boundary layer trip strips were applied at 5 percent chord on both the main wing's suction (SS) and pressure side (PS).

3.4. Complementary Test Cases

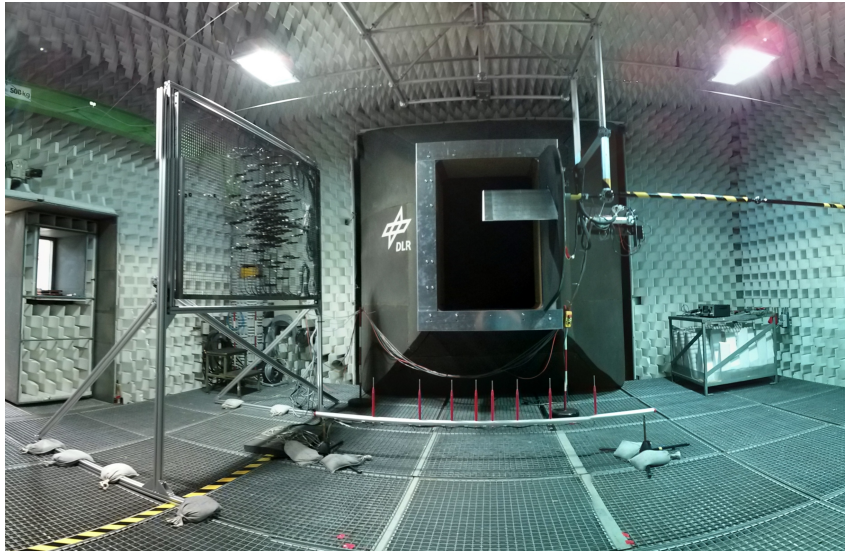
The reference test cases are complemented by measurements at configurations representative real aircraft. Particular interest is put on the effect of tip edge rounding and tip face cavities. The impact of wing section profile and aspect ratio are also investigated for two model profiles. Also the dependency on Reynolds number and tip raking angle is evaluated. Finally, FSE noise radiation in a generic externally blown flap (EBF) configuration is investigated.



(a) Small aperture array on positioning system (48 1/4" Bruel & Kjaer Type 4954 microphones).



(b) Large aperture array (96 1/2" LinearX M51 microphones). Static setup.



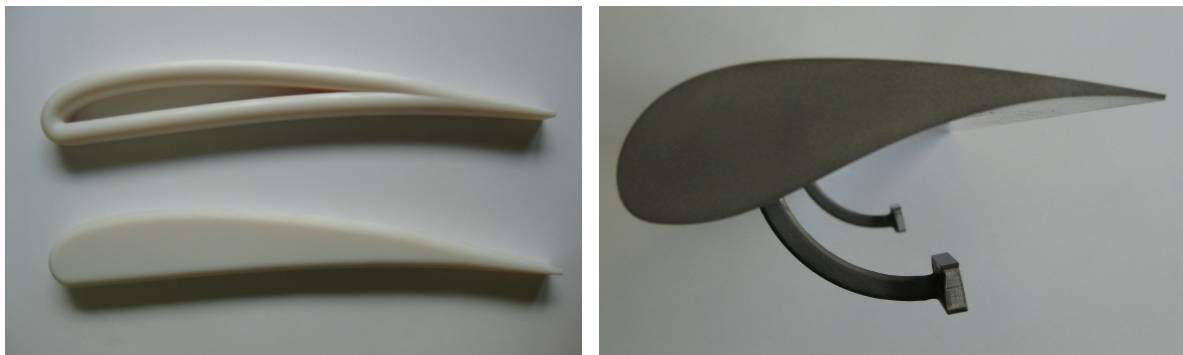
(c) Vertically mounted large aperture array and spanwise distributed free-field microphones. Static setup.

Figure 3.6.: Microphone arrays. a),c) Cantilever flap model installed. b) high-lift wing installed ($\delta_f = 0^\circ$).

Although the complementary experimental setups presented in this section cover a limited range of configurations they provide new results which will allow for refinement in the semi-empirical representation.

3.4.1. Tip Geometry Modifications and Leading-Edge Add-On

Two tip add-ons and a leading edge vane (3.7b) are tested. Tip #1 has a geometry representative of a flap tip sealing. Tip #2 has exactly the same shape as Tip #1 but without central cavity. Its tip face is a flat surface obtained by filling the cavity of Tip #1. Both tip add-ons extend the total flap span by their thickness of 0.035 m. They were built using rapid prototyping. Due to the large size of the wing model, fixing with double-sided tape was easy and sufficient to tightly hold the add-ons in place. An additional strip of aluminum tape is used to ensure a maximum hold of the add-ons and a smooth junction with the wing. The purpose of testing with the leading-edge vane is to evaluate its impact on the FSE noise generation. A leading-edge vane is a lift enhancement device which is readily found in full-scale high-lift wing designs, e.g. Airbus A400M, DC9, DC10.



(a) Tip add-ons. Top: Tip #1, bottom: Tip #2. (b) Vane. Chord length $c=0.124$ m, span $s=0.4$ m.

Figure 3.7.: Wind-tunnel model and add-ons.

To allow the fixation of the vane, two small pockets had to be milled into the wing leading edge (at two spanwise positions). For the remainder of the report the configuration Reference+Vane will be referred to as Vane only.

3.4.2. Wing Profile and Aspect ratio Variations

To assess the effect of different profile shapes, tests were done with a cantilever wing having a DU96 profile section (e.g. figure 3.9a) as well as a high-lift configuration with both main wing and part span flap with a Clark-Y section (e.g. figure 3.9b). For the latter, for a flap deflection set to $\delta_F = 0^\circ$, the wing effectively becomes a cantilever wing with Clark-Y section and aspect ratio $AR = 5.83$.

The DU96 model has a chord length of 0.3 m and a span of 0.6 m while the Clark-Y flap has a chord length of 0.096 m with a fixed span of 0.41 m.

The measurements were carried out in the AWB using the small (DU96) and large aperture arrays (Clark-Y). Both wing model were tripped using zig-zag tape at 5% SS and 10% PS. The high-lift configuration boundary layer had to be further tripped using vortex generator around $x/c = 0.6$ on the SS to get rid of a separation occurring upstream

of the flap leading edge on the main wing SS. This separation bubble was responsible for the generation of loud tones.

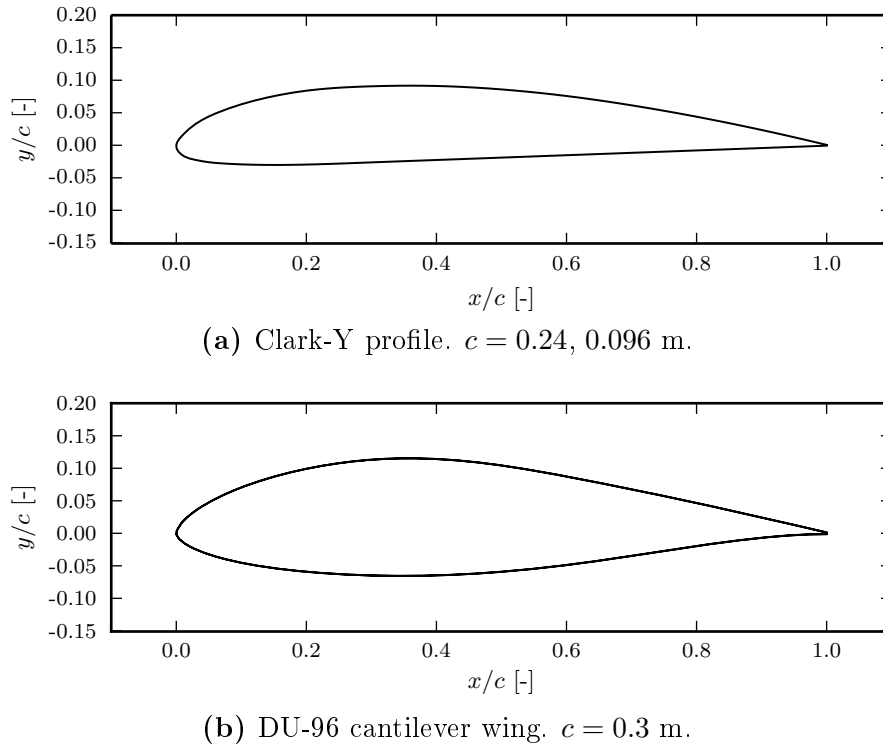
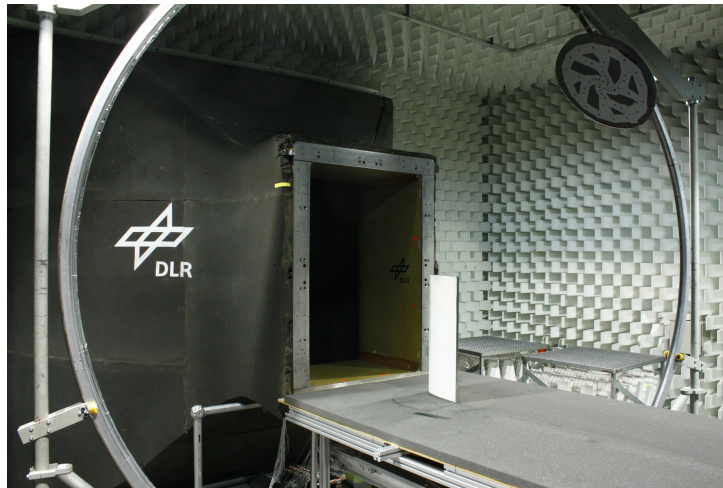


Figure 3.8.: Geometry of the tested wing models.

3.4.3. Reynolds Number and Tip Raking Variations

A study of the Reynolds number effect on the radiated noise is possible through the two reference cases described above. A full-scale wing model with the reference profile is also available which further extends the database. This third model is a slightly tapered version of the reference cantilever flap. Its tip face is flat and two configurations are tested; straight tip and raked tip (see figure 3.11c).

Measurements with the full-scale flap were done in DNW-NWB low-speed wind tunnel in Braunschweig (see section 3.2 and figure 3.10). The wing is mounted on a rotating ground plate positioned in the open jet flow, just above the lower shear layer between the core flow and the wind tunnel plenum. The wing's rotation axis lies at the 50% chord position and is normal to the flow direction. The model, in its reference configuration, is shown in figure 3.11a and the raked tip configuration in figure 3.11b. The wing was tripped using zig-zag tape at 10% on the suction side and 34% on the suction side. No pressure taps are available for this set of measurements. Therefore only geometrical angles are considered. It was checked that the setup did not promote early flow separation on the model using tufts visualizations. Also, the phased microphone array results (see source maps of appendix F) clearly show that the ground plate is not an important source of noise in the frequency range relevant to FSE noise.



(a) Cantilever DU96 airfoil



(b) Cantilever Clark-Y wing with part-span flap

Figure 3.9.: Cantilever DU96 airfoil and Clark-Y wing with part-span square tip flap, experimental setups in AWB. In (b), the part-span flap also has a Clark-Y profile. Its tip, shown in white, is exchangeable. It was tested, however, only with a square tip.

During this test both a large aperture microphone array and a linear distribution of far-field microphones were utilized to measure the free-field noise radiation. Both measurement techniques were used sequentially to minimize interference on the sound field due to their respective supporting structures. Detailed sketches of the NWB experimental setup can be found in appendix A.

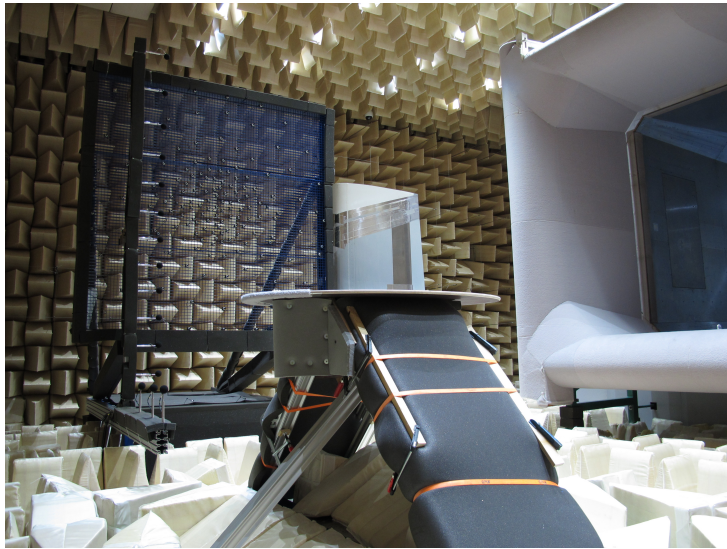
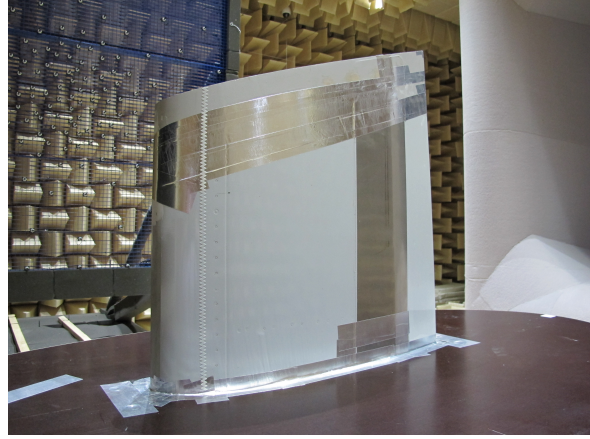


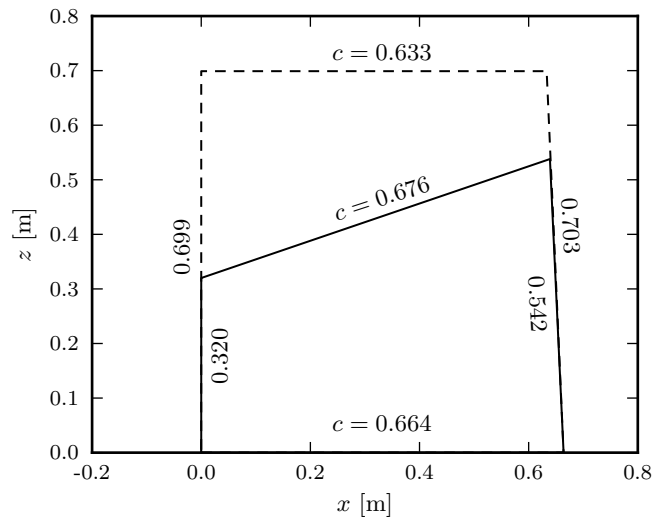
Figure 3.10.: Large scale wing in the open test section of the DNW-NWB low-speed wind tunnel. Reference configuration, rectangular planform.



(a) Reference configuration, rectangular planform.



(b) Raked tip.



(c) Planform of the tested configurations. Dashed line: baseline rectangular planform, Solid line: raked-tip planform.

Figure 3.11.: Large scale model. Details of the models geometries. Baseline wing represented by the dashed lines. The raked-tip wing is represented by the solid lines. For each geometry, dimensions are given in meters.

4. Data Acquisition and Post-Processing

In this chapter, details about the data acquisition hardware and the post-processing chains are presented. The main emphasis is set on describing the different hardware setups used during the measurements as well as providing necessary but concise details about the data processing steps. References to the relevant literature is also given for the interested reader.

4.1. Far-Field Noise Measurements

In the AWB, eight calibrated 1/4" free-field microphones with protective grid (Bruel & Kjaer Type 4136) are installed in a linear fashion underneath the wing model to allow for directivity measurements (see figure 3.6c). Daily calibration of the microphones is made prior to the start of the measurements using a standard pistonphone (RION NC-74, Class 1, 94 dB at 1 kHz). The geometrical layout of the microphones in the AWB is provided in table 4.1. The same procedure is also followed for the NWB far-field noise measurements, except that a total of 15 1/4" free-field microphones distributed on a linear array are used (see figure 3.10). The layout of the far-field microphones in the NWB can be found in table 4.2. Here we introduce the fly-over angles definition in figure 4.1, with the space coordinates x , y and z corresponding to the AWB coordinate system definition of figure 3.3. Furthermore, the 15 microphones are mounted on a linear stage allowing movements parallel to the streamwise direction over a range of angles $63^\circ < \varphi_x < 110^\circ$.

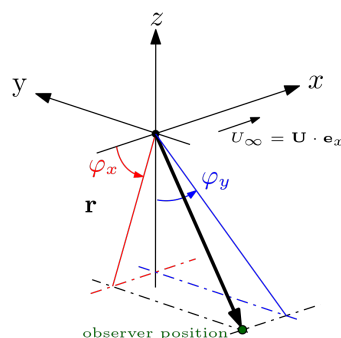


Figure 4.1.: Fly-over coordinate system definition

Measurements are recorded using an acquisition system from GBM Viper with a 16-bit dynamic range. The signals are high-pass filtered at 500 Hz for an optimal usage of the

sensor’s dynamic range. A 25-kHz anti-aliasing filter is also used. The sampling rate for the measurements is set to 50 kHz and a total of 2 002 944 samples is collected for each datapoint (measurement time: 40.05 s). The FFT analysis is performed on 978 blocks of 2048 samples using a Hanning window, yielding a frequency resolution of $\Delta f = 24.4$ Hz. The usable frequency range of the free-field microphones output extends from 1 kHz to 20 kHz. Background noise correction is performed down to 3 dB level differences. The following standard corrections are applied to the output data:

1. Shear layer effects (see Amiet [5]) including sound wave convection
2. Sound wave amplification due to convection effects
3. Distance correction (all levels are back-propagated to a standard distance of 1m)
4. Atmospheric attenuation (see Bass et al. [10])
5. Microphone frequency response
6. Background noise removal

Table 4.1.: Geometrical layout of the free-field microphones in the AWB. φ_x is the fly over angle with $\varphi_x = 0^\circ$ upstream and $\varphi_x = 180^\circ$ downstream. φ_y is the side line angle with $\varphi_y = 0^\circ$ directly below the model. Sign convention for φ_y according to the right-hand rule. See figure 4.1 for reference.

#	streamwise setup					spanwise setup				
	φ_x [°]	φ_y [°]	x [m]	y [m]	z [m]	φ_x [°]	φ_y [°]	x [m]	y [m]	z [m]
1	58.83	0.00	-0.090	0.000	-1.160	90.00	34.38	0.600	-0.750	-1.016
2	68.88	0.00	0.200	0.000	-1.160	90.00	22.32	0.600	-0.450	-1.016
3	76.67	0.00	0.390	0.000	-1.160	90.00	12.85	0.600	-0.250	-1.016
4	83.28	0.00	0.540	0.000	-1.160	90.00	5.21	0.600	-0.100	-1.016
5	87.85	0.00	0.640	0.000	-1.160	90.00	0.00	0.600	0.000	-1.016
6	94.76	0.00	0.790	0.000	-1.160	90.00	-7.79	0.600	0.150	-1.016
7	104.32	0.00	1.000	0.000	-1.160	90.00	-17.71	0.600	0.350	-1.016
8	117.04	0.00	1.306	0.000	-1.160	90.00	-30.67	0.600	0.650	-1.016

4.2. Microphone Array Measurements

In the AWB, two different microphone arrays are used for source localization and sound level quantification. First a large aperture array enables measurements of far-field noise levels towards the ground and to the side-line propagation directions (e.g. 3.6). Second, a small aperture array is used to investigate FSE noise directivity (e.g. 3.6a). Because of its small dimension, this second array integrates far-field noise levels over a smaller area thus providing a better angular resolution. For the NWB investigations, only a large aperture microphone array was used. Except for background noise correction, all microphone

Table 4.2.: Geometrical layout of the free-field microphones in the NWB. φ_y is the side line angle with $\varphi_y = 0^\circ$ directly below the model. Sign convention for φ_y according to the right-hand rule. The free-field microphones were positioned at fixed streamwise positions corresponding to $\varphi_x = [60^\circ, 70^\circ, 80^\circ, 90^\circ, 100^\circ, 110^\circ]$. φ_x is the fly-over angle with $\varphi_x = 0^\circ$ upstream and $\varphi_x = 180^\circ$ downstream. See figure 4.1 for reference.

#	φ_y [°]	x [m]	y [m]	z [m]
1	-45.00	2.399	3.179	1.584
2	-40.00	2.399	3.172	1.145
3	-35.00	2.398	3.171	0.761
4	-30.00	2.399	3.168	0.414
5	-20.00	2.399	3.162	0.104
6	-15.00	2.400	3.161	-0.211
7	-10.00	2.400	3.163	-0.494
8	-5.00	2.400	3.164	-0.768
9	0.00	2.401	3.157	-1.030
10	5.00	2.401	3.157	-1.313
11	10.00	2.402	3.157	-1.591
12	15.00	2.402	3.153	-1.883
13	20.00	2.105	2.483	-1.969
14	25.00	2.096	1.934	-1.963
15	30.00	2.093	1.555	-1.958

corrections applied to the far-field noise measurements were also applied during the phased array measurements.

4.2.1. Microphone Layouts and Systems Characteristics

The AWB large aperture microphone array has a total of 96 (1/2-inch) Linear-X M51 microphones mounted on a wire grid and has an aperture of 0.97 m. The microphones are distributed in a random but optimized manner which is well suited for the frequency range of interest in typical measurements on scaled wing models done in the AWB ($1\text{kHz} < f < 30\text{kHz}$). The AWB small aperture microphone array consists of 48 1/4" Bruel & Kjaer Type 4954A microphones (aperture of 0.47 m) distributed in a logarithmic spiral pattern [99]. The supporting structure holding the microphones is covered with a five centimeter thick foam sheet to minimize sound wave reflections. The transducers are flush mounted through the foam. A computer controlled traversing system enables a precise positioning of the small aperture array around the model (see figure 3.6a). The range of measurement positions for the small microphone array lies between $-90^\circ < \theta < 90^\circ$ and $-30^\circ < \phi < 40^\circ$ when testing the reference cantilever wing. For the reference high-lift configuration, this set of available positions reduces to $-120^\circ < \theta < -60^\circ$ and

$-30^\circ < \phi < 40^\circ$, e.g. figure 4.3. The measurements coordinate system is defined in figure 3.3. The given angular ranges correspond to the maximal displacements attainable considering the physical constraints imposed by the wind tunnel nozzle and jet.

The NWB large aperture microphone array has a total of 140 (1/2-inch) Linear-X M51 microphones mounted on a metal grid and has an aperture of 2.77 m. The array itself is mounted on a linear traversing rail allowing it to be moved to different streamwise locations, covering a radiation angle range of $\Delta\varphi_x = 47^\circ$. The microphone array provides spectral data in $0.5 \text{ kHz} < f < 20.0 \text{ kHz}$. Further detail about the NWB microphone array setup cannot be provided because of confidentiality issues.

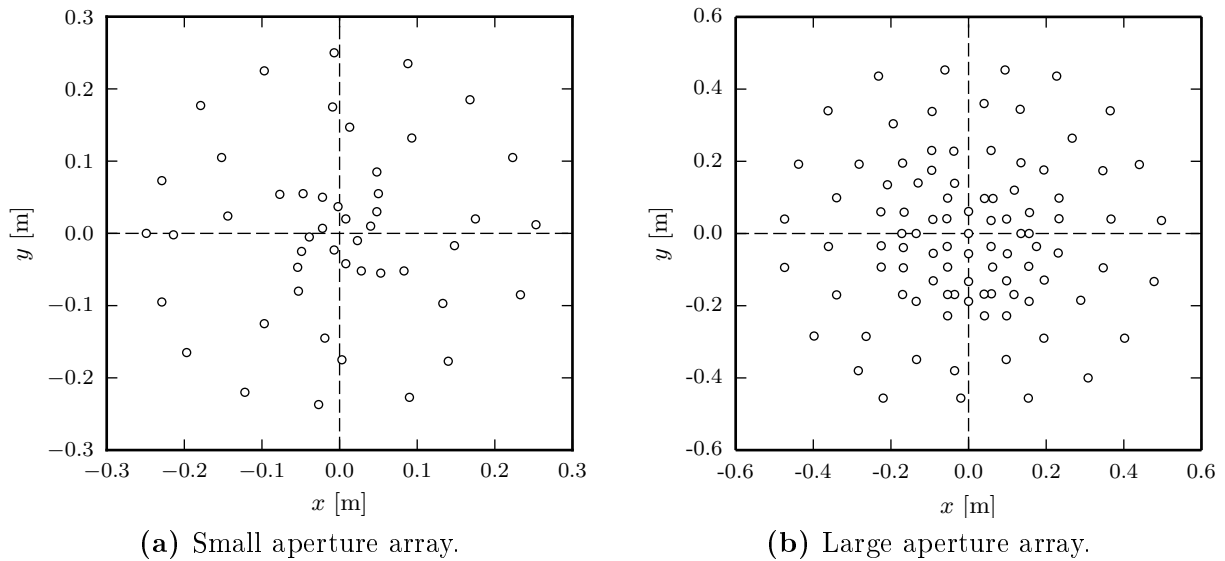


Figure 4.2.: Microphone array layouts. AWB small aperture array: 48 microphones (0.47 m). AWB large aperture array: 96 microphones (0.97 m).

For both microphone arrays, all data channels are simultaneously recorded at a sampling rate of at least 50 kHz and with a 16 bit dynamic range on GBM Viper measuring units. A sampling rate of 50 kHz is sufficient to cover the range of frequencies relevant to FSE noise. According to the literature [82], the FSE is a dominant noise source in the range $1.2 \leq St_d \leq 10$, where St_d is the Strouhal number based of the flap maximum thickness, reaching its maximum around a Strouhal number value of $St_d = 4.0$. This corresponds to a peak frequency $f = 728.0 \text{ Hz}$ for the reference cantilever wing and $f = 2910.0 \text{ Hz}$ for the reference high-lift model. Typically, a total of 1650688 samples per microphone and datapoint was acquired. A 500-Hz high-pass and a 50-kHz anti-aliasing low-pass filter were used. Individual elements of the cross-spectral matrix (\mathbf{R} matrix, see below) for each data record were calculated by partitioning each time signal into non-overlapping segments of 4096 samples. The time history segments were Fourier-transformed applying a rectangular window, yielding a typical frequency resolution of $\Delta f = 13.4 \text{ Hz}$.

In figure 4.4, the point spread function (PSF) of each phased array is plotted vs. frequency. The PSF is the theoretical output of the microphone arrays due to a monopole

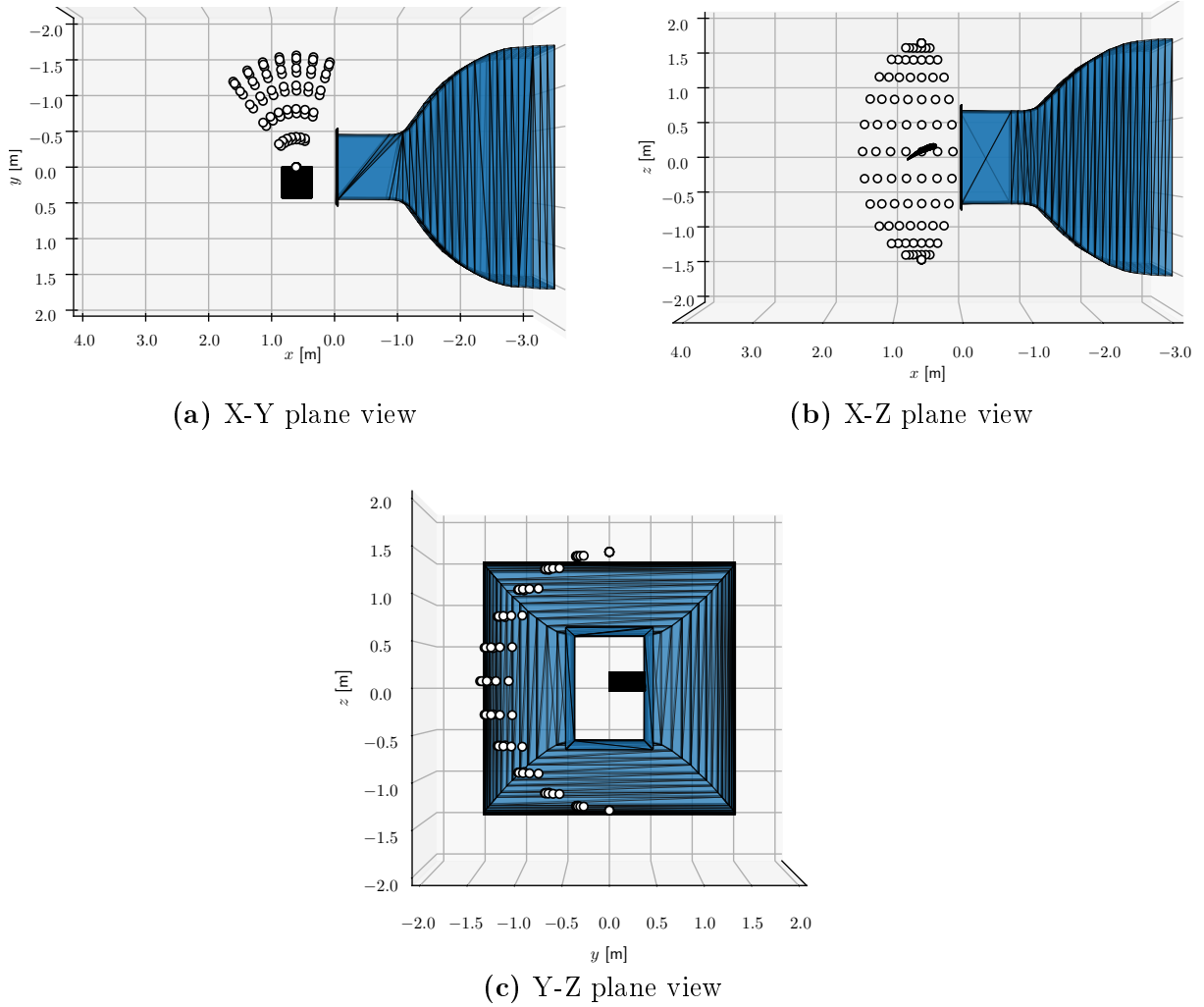


Figure 4.3.: Small directional phased array positions (empty dots) used for directivity measurements in AWB

point source located at $\mathbf{x} = [0, 0, 0]$ i.e. in front of the phased array centers. The ability of the array to resolve a source at a given position depends on the frequency of interest as well as on its aperture and number of microphones [99]. The closest distance between two incoherent sources which can be resolved by the phased arrays is measured by the main lobe width, 3dB down from its maximum. From the results of figure 4.4, an estimate of the lower frequency bound of the phased arrays can be deduced; ≈ 1.6 kHz for the small aperture and ≈ 0.8 kHz for the large aperture array. In practice those estimates only hold in cases where only one dominant source exists. For distributed sources, the lower bound frequencies will increase and one needs to be careful in defining regions for later power integration.

This aspect is further investigated experimentally using two loudspeakers (L1, L2) in an anechoic environment, without flow (see figure 4.5). The loudspeakers do not, however, represent monopole point sources but are closer, in term of directivity and extent, to actual aeroacoustic noise source occurring in the wind tunnel environment. One loudspeaker is held fixed at $\mathbf{x} = [0.0, 0.2, 0.0]$ m, while the second one is allowed to be moved in y . Broadband white noise is used to drive the loudspeaker in the frequency range $0.7 < f <$

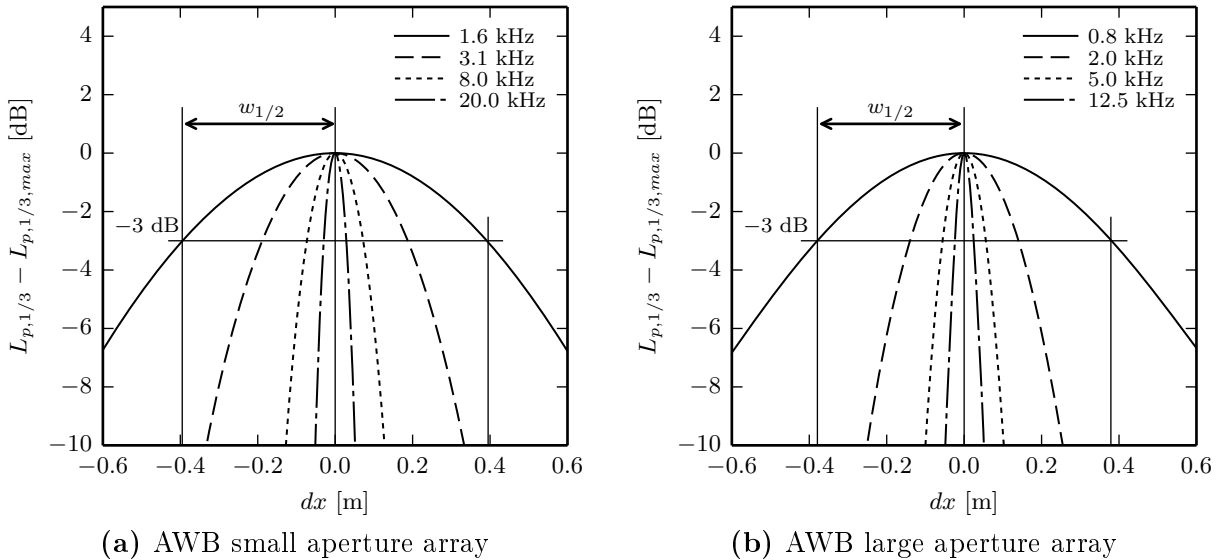


Figure 4.4.: Microphone array's PSF. Theoretical calculations based on the actual experimental microphone distributions and for a single point source located at $\mathbf{x} = [0, 0, 0]$. Levels are normalized by the maximum value at $\mathbf{x} = [0, 0, 0]$. $w_{1/2}$ is the half-width of the PSF main lobe, 3dB down from its maximum. Twice this value ($2w_{1/2}$) gives the theoretical minimum separation between two incoherent noise source which can be resolved.

20 kHz. The measurements are performed using the acquisition chain described previously and post-processing is done using the CLEAN-SC algorithm (see section 4.2.3). The results of these test are given in figure 4.5. In figure 4.5a, the spectrum from the phased array central microphone is compared to the corresponding power integrated spectrum for L1 alone. The spectra are in good agreement, as expected. In figure 4.5b, the difference ($\Delta L_{p,1/3}$) in integrated power for L1 vs. separation to L2, when both loudspeakers are turned on, is plotted. The data are normalized by the results for the case where only L1 was turned on. Therefore, a $\Delta L_{p,1/3} = 0$ value is to be expected if the integrated power level for L1, with L2 turned on, is the same as that for L1 alone. Otherwise, values of $\Delta L_{p,1/3} \neq 0$ indicate errors in the power integration due to a lack of resolution of the phased array. The results of figure 4.5b reveal the ever increasing lower frequency bound of the microphone array with a reduction in sources separation. Furthermore, the results tend to show that the theoretical PSF estimate (i.e. figure 4.4b) of a lower frequency bound at ≈ 0.8 kHz is too conservative. In figure 4.5b sources separated by 0.4 m can still be resolved. These observations are, however, dependent on the source distribution and cannot be deemed to be generally valid. Nonetheless, the theoretical PSF as well as the experimental investigations using loudspeakers provide useful guidelines for the later evaluation of acoustic source maps.

4.2.2. Conventional Beamforming

Before introducing the CLEAN-SC algorithm, the basics of beamforming are given hereafter. For most of the experiments, conventional beamforming (CB) Mueller [99] is used only as a first data processing step. CB provides a global overview of the source distri-

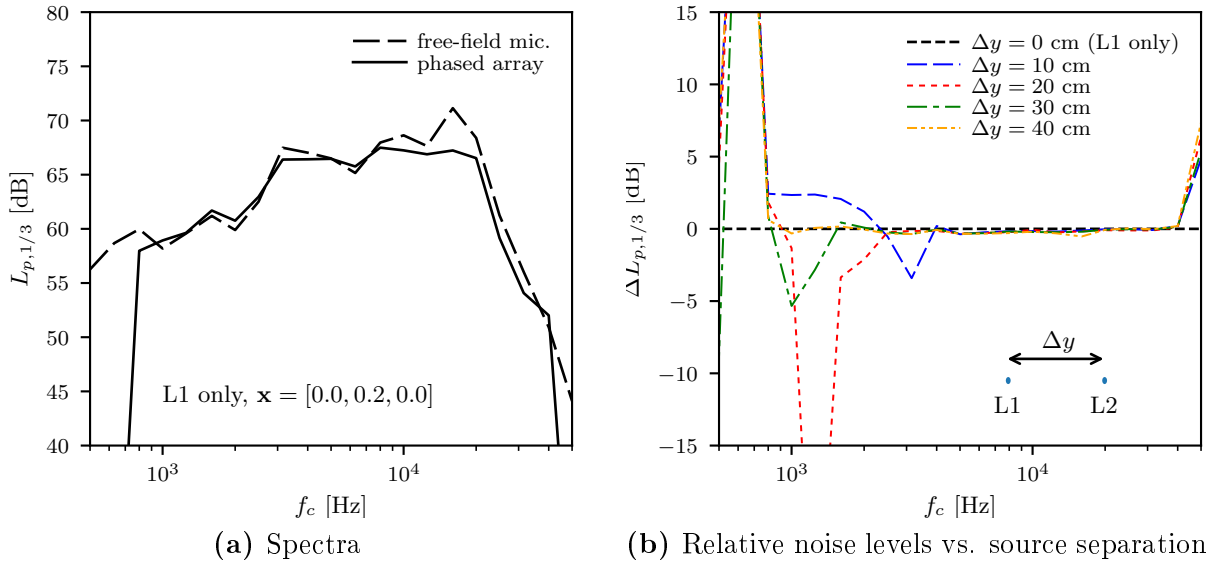


Figure 4.5.: Evaluation of the AWB large aperture phased array resolution using two loudspeakers (L1, L2). L1 is located at $\mathbf{x} = [0.0, 0.2, 0.0]$ and is held fixed. L2 is free to move in y , away from L1. Post-processing using the CLEAN-SC algorithm, with a constant integration domain around L1. Left, comparison of the absolute spectra for L1 alone vs. the phased array central microphone. Right, difference in integrated power levels for L1 vs. loudspeaker separation relative to L1 when both L1 and L2 are turned on.

bution which can subsequently be decomposed into isolated source components using the deconvolution algorithm CLEAN-SC [120]. This second step is necessary when considering small size wing models due to the relatively low emitted noise levels and the existence of numerous noise sources on their surface (spurious/or not). An in depth discussion about the CLEAN-SC algorithm can be found in [120].

CB is a data processing algorithm used for noise source detection. It is closely related to the standard delay-and-sum algorithm used in astronomy and speech recognition. The basic principle of operation of the algorithm is sketched in figure 4.6. In that figure, the microphone array is represented by the set of solid dots. A simple linear array is considered, but the basic principles discussed here also apply to two-dimensional arrays. For the data processing, a set of predefined positions where sources of sound are to be identified (shown in figure 4.6 by the empty dots) is scanned. First, consider only microphones 1 and 2 at position \mathbf{x}_1 and \mathbf{x}_2 . $\mathbf{x}_i = (x_i, y_i, z_i)$ being the i^{th} ($i = 1 \dots N$) microphone position vector. For our purpose, a single monopole source at \mathbf{x}_0 is assumed. For each scan position, the emitted pressure signals (time series) due to the source at \mathbf{x}_0 reach the microphones at different times. The time delay between the signals measured at \mathbf{x}_1 and \mathbf{x}_2 is given by,

$$\Delta t = \frac{|\mathbf{x}_2| - |\mathbf{x}_1|}{c_0} = \frac{d_2 - d_1}{c_0}. \quad (4.1)$$

The beamforming algorithm compensates for this time delay while also accounting for an amplitude reduction with distance from the source. The individually shifted time signals, $p_1(t)$ and $p_2(t)$, are then summed for each scan position. Here, one needs to assume some

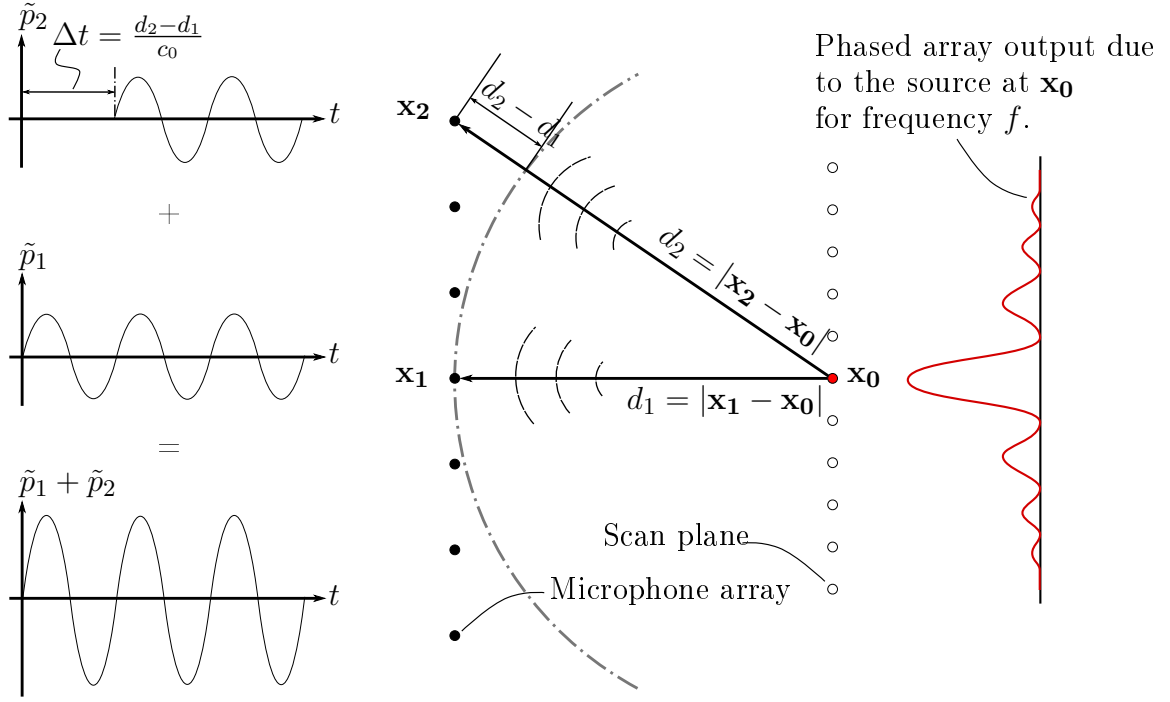


Figure 4.6.: Principle of operation of the delay-and-sum algorithm.

type of sound propagation model between the source and the phased array microphones. In the AWB, conventional beamforming is implemented using the assumption that source distributions are made up of incoherent monopole sources. This is in most cases a sufficient assumption, even for line source distributions. For the source at the scan position \mathbf{x}_0 , an optimal time shift correction of the measured pressure signals at the array microphones will lead to a level amplification. For scan positions adjacent to the actual source position, a noise level reduction occurs in the array output due to the incoherence between the measured time signals. In the process, effects of shear-layer refraction as well as source convection are also accounted for. Shear-layer correction is done according to Amiet's commonly used procedure [5].

Generally speaking, the phased array output at a given scan position (k) can be computed as

$$A_k = \sum_{m=1}^N \sum_{n=1}^N w_{m,k}^* R_{m,n} w_{n,k} \quad (4.2)$$

where $R_{m,n}$ is the cross-power between pairs of microphones ($m, n = 1 \dots N$), N being the total number of microphones. $w_{m,k}$ and $w_{n,k}$ are the components of the steering vector (or weighting factors) which account for the propagation effects and the time delays for microphones m, n to scan position k . The * stands for complex conjugate transposition. In equation 4.2, the steering vectors are determined by the experimental setup and by the choice of an adequate sound source model (i.e. monopole or dipole propagation models). The cross-power matrix can be directly computed from the measured pressure signals. The output of the beamformer, A_k in equation 4.2, directly gives the squared value of the

sound pressure at a given scan position and for a given frequency, as a weighted sum over all microphones.

Diagonal Removal. Diagonal removal (DR) is a special technique used to improve contrast in beamformed maps. The technique simply consists in omitting the main diagonal elements of the \mathbf{R} matrix (see equation 4.2) in the data processing. These are the auto-powers of each microphone and, therefore, contain no phase information. Microphone auto-powers generally have higher levels than the \mathbf{R} matrix off-diagonal elements ($R_{m,n}$ for $m \neq n$). This is usually due to coherence loss between microphones. The diagonal elements enter the data processing at each scan position and can consequently significantly affect the microphone array output. By removing them from the processing, much lower background noise levels in the noise source maps are obtained (see figure 4.7). DR can, however, lead to the occurrence of negative side lobes in the source maps, which can result in inaccurate integrated power levels.

The results presented in the upcoming chapters were obtained using both DR and the full cross-power matrix ($R_{m,n}$) depending on the test configuration. Wing models of smaller scales usually necessitate the use of DR as the number of important sources is larger. Therefore the FSE noise source is not necessarily the most dominant and contamination through spurious or secondary sources is more probable. A much better source localization as well as integrated spectra can be obtained by using DR.

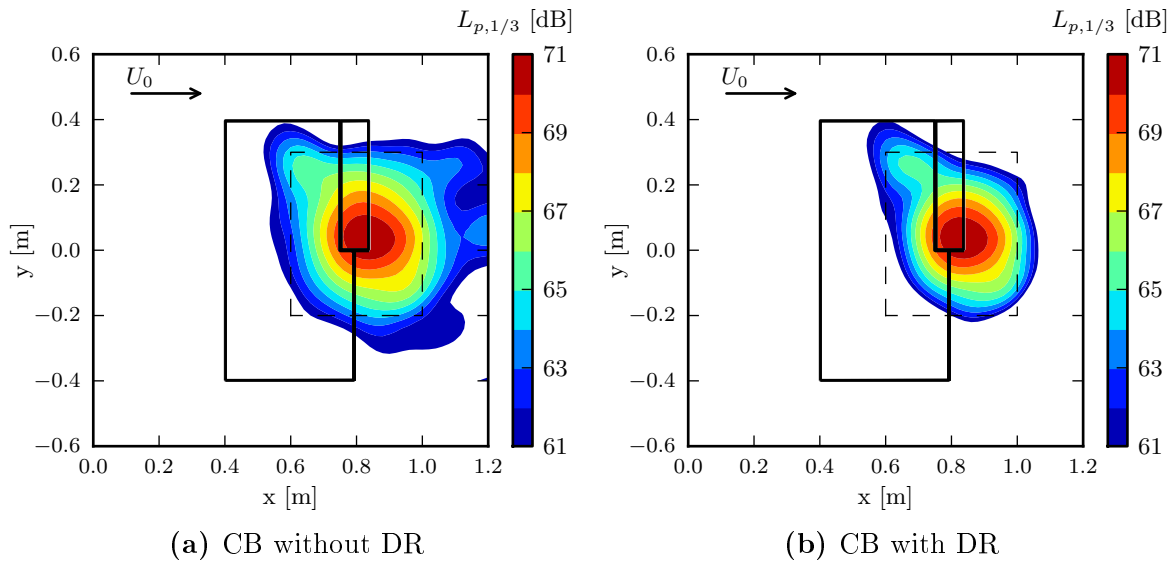


Figure 4.7.: Reference high-lift wing configuration. 2D source maps, $f_c = 6.3$ kHz. Conventional beamforming without DR (left) and with DR (right). The integration region is shown by the dashed line.

Power Integration (Power Spectra Estimation). The microphone array offers the interesting advantage of making the source regions visible. One is, however, not only

interested in locating the noisy domains but also in the quantification of absolute noise levels. Specific scan regions in a spatially relevant domain have to be defined and used to compute the far-field noise spectra (see figure 4.8). For the analysis of measurements made with the microphone array below the model, a large grid extending between $0 \text{ m} \leq x \leq 1.2 \text{ m}$ and $-0.4 \text{ m} \leq y \leq 0.4 \text{ m}$ having a spatial resolution of 0.02 m in both x and y is used for a first processing run. It provides a global overview of the full extent of the test section. Based on the frequency-dependent spatial source distribution, a second smaller scan grid is defined. This second grid covers the range $0.6 \text{ m} \leq x \leq 1.0 \text{ m}$ and $-0.2 \text{ m} \leq y \leq 0.3 \text{ m}$. Both scan grids are rotated according to the wing angle of attack and are aligned with the wing's chord. The smaller second grid is termed *integration grid* and has a spatial resolution of 0.01 m in both x and y directions. Computation of power integrated noise spectra is done according to the method described by Brooks and Humphreys [20] and discussed in Oerlemans and Sijtsma [102]. It basically assumes that a noise source revealed by the beamforming algorithm is due to a single monopole of power equal to the summed power over the integration region divided by the surface of the integration domain.

An optimal (frequency independent) scan grid is defined for each measurement location of the microphone array. Note that in cases when the microphone array will be moved around the model, the integration grids will indeed change depending on the view angle at the model. Shading algorithms (as proposed by Oerlemans and Sijtsma [102]) were not found to be necessary and were not applied in the post-processing. Loss of coherence over the large aperture array is, in fact, not important in the range $1 \text{ kHz} < f < 20 \text{ kHz}$. Both integration grids do not change in shape or size with frequency.

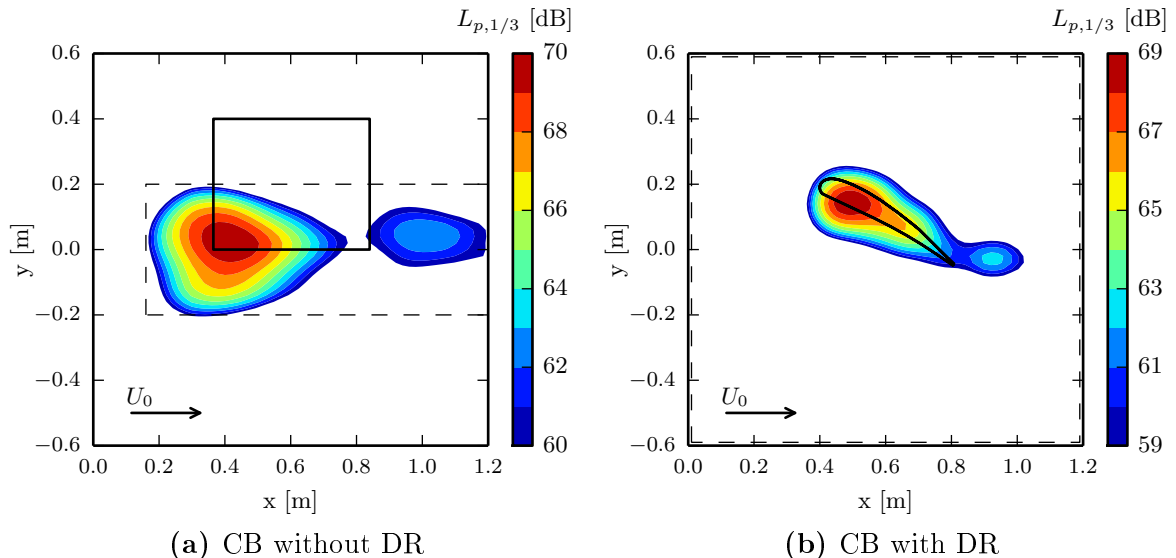


Figure 4.8.: Reference cantilever flap. 2D source maps, $f_c = 6.3 \text{ kHz}$. Conventional beamforming without DR (left) and with DR (right). The integration region is shown by the dashed line.

4.2.3. CLEAN-SC

During the experiment with the high-lift configuration, it was realized that important spurious sources at the junction between the model and the side-plates contaminated the flap side-edge data. Moreover, for the 3-element high-lift model, the flap track was also identified as an additional noise source. An evaluation of their influence on the measurements could not be performed using CB, which motivated the use of CLEAN-SC. Furthermore, CLEAN-SC reduces very efficiently the influence of side-lobes from sources located outside the integration domain. An interesting feature of CLEAN-SC is its ability to mathematically decompose the cross-powers induced by a noise source into its signal and noise parts. When using an integration grid which includes all existing noise sources, this characteristics enables the reconstruction of the far-field spectra over the whole range of frequencies [120]. This is not possible with CB. Further details regarding the CLEAN-SC algorithm can be found in [120].

CLEAN-SC is a coherence based deconvolution algorithm used for beamforming. Its basic working principle rests on the assumption that CB noise maps are made up of the superposition of a number of incoherent source components, each of them producing a maximum (main lobe) and side lobes in the source map. CLEAN-SC uses the fact that the main lobe of a given component is coherent with its side lobes to iteratively decompose the source map. Contrarily to other deconvolution procedures, it is not assumed that a source map is made up of appropriately scaled point spread functions (PSF), the PSF being the phased array impulse response (or output due to a unit point source). The coherence based approach is, therefore, less prone to errors in situations where the beam pattern due to an actual source differs from the theoretical PSF [120].

The iteration loop of the algorithm starts with the computation of a CB source map ($i = 0$, see figure 4.9 left). At iteration i ($i = 1 \dots I$), the position of the maximum value in the phased array output is found ($\xi_{i,max}$) and the coherence with respect to $\xi_{i,max}$ over the complete scan plane is computed. The main lobe (with peak at $\xi_{i,max}$) and its coherent side lobes are then taken out and an equivalent “clean” beam of fixed width is computed. This operation can be written as,

$$A_k^i = A_k^{i-1} - \underbrace{\mathbf{w}_k^* \mathbf{G}^{(i)} \mathbf{w}_k}_{\text{clean beam}}, \quad (4.3)$$

where $\mathbf{G}^{(i)}$ is assumed to be the cross-power matrix due to a single unit source component, \mathbf{h} , located at $\xi_{i,max}$. A_k^i being the degraded source power at iteration i i.e. without the contribution of the component inducing a peak at $\xi_{i,max}$. A constraint is imposed on the choice of $\mathbf{G}^{(i)}$ without, a priori, assuming a unit monopole source at $\xi_{i,max}$. Instead, the coherence between any scan position $\xi_{i,k}$ and $\xi_{i,max}$ is required to be completely determined by $\mathbf{G}^{(i)}$. In other words, the following must hold,

$$\underbrace{\mathbf{w}_k^* \mathbf{R}^{(i-1)} \mathbf{w}_{max}}_{\text{dirty map coherence}} = \underbrace{\mathbf{w}_k^* \mathbf{G}^{(i)} \mathbf{w}_{max}}_{\text{clean beam coherence}} \quad (4.4)$$

where $\mathbf{G}^{(i)}$ is given by,

$$\mathbf{G}^{(i)} = A_{max}^{(i-1)} \mathbf{h}^{(i)} \mathbf{h}^{*(i)}. \quad (4.5)$$

This is the “impulse response” due to \mathbf{h} (not a unit point monopole) scaled by the peak level at $\xi_{i,max}$ ($A_{max}^{(i-1)}$). A solution to equation 4.4 (see [120]) is found when,

$$\mathbf{h}^{(i)} = \frac{1}{\left(1 + \mathbf{w}_{max}^{*(i)} \mathbf{H}^{(i)} \mathbf{w}_{max}^{(i)}\right)^{1/2}} \left[\frac{\mathbf{R}^{(i-1)} \mathbf{w}_{max}^{(i)}}{A_{max}^{(i-1)}} + \mathbf{H}^{(i)} \mathbf{w}_{max}^{(i)} \right], \quad (4.6)$$

where $\mathbf{H}^{(i)}$ contains the diagonal elements of $\mathbf{h}^{(i)} \mathbf{h}^{*(i)}$.

After a number of iterations ($i = 1 \dots I$), one obtains a “cleaned” source map (see figure 4.9 right), theoretically containing only contributions due to a set of acoustic sources, i. e. hydrodynamic pressure fluctuations and electronic noise are rejected. The extracted sources are, per definition, not coherent with each other.

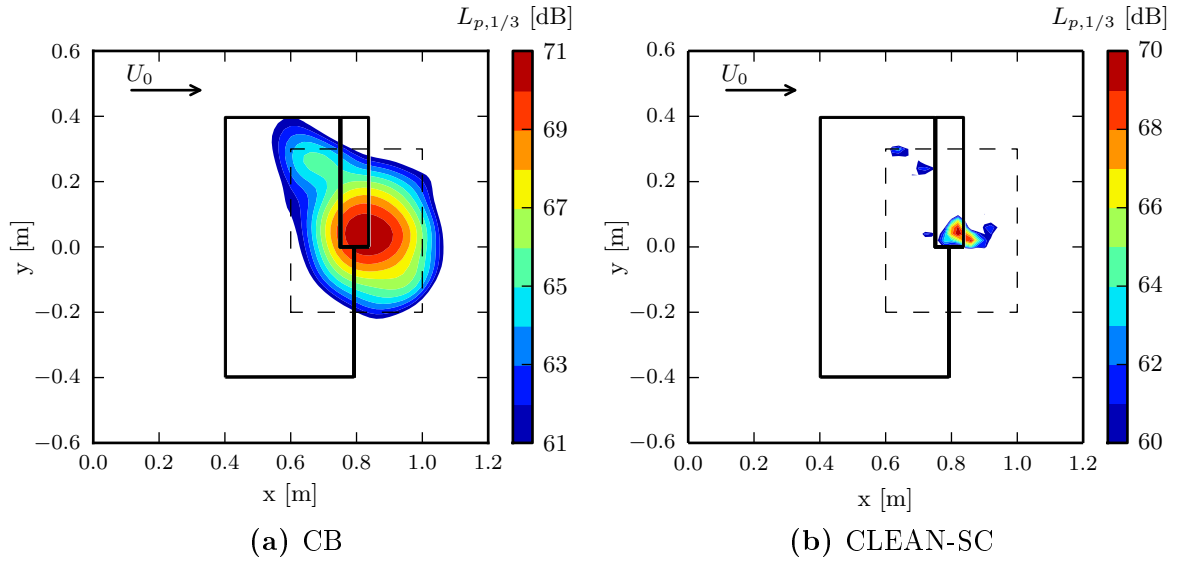


Figure 4.9.: 2D source maps at $f_c = 6.3$ kHz, with diagonal removal. Conventional beamforming (left) versus CLEAN-SC deconvolution (right). $\alpha_g = 0^\circ$, $\delta_F = 34^\circ$, $U_0 = 60$ m/s. The integration region is shown by the dashed line.

The algorithm is very efficient at filtering strong dominant sources which might mask the actual source region of interest (see figure 4.9). This is critical when estimating absolute power spectral levels using integration techniques.

Power Integration (Power Spectra Estimation). Absolute power spectra are now sought, based on the computed source maps shown above. A sub-domain is chosen (length = 0.4 m, width = 0.5 m) as shown by the dashed line in figure 4.9. The integration region is maintained constant in size for all frequencies of interest. It is also rotated according to the model’s angle of attack and rotation axis. Only source components inside of this sub-region are considered in the integration process. There is no need to account for the point-spread function (impulse response) of the phased array as in CB [20]. This is a special feature of CLEAN-SC.

After a number of iterations ($i = 1 \dots I$) the original \mathbf{R} matrix (see equation 4.2) can be expressed as

$$\mathbf{R} = \sum_{i=1}^I \underbrace{A_{max}^{(i-1)} \mathbf{h}^{(i)} \mathbf{h}^{*(i)}}_{\text{signal}} + \underbrace{\mathbf{D}^I}_{\text{noise}}. \quad (4.7)$$

$A_{max}^{(i-1)}$ is the maximum source power (in the scan plane) at iteration $i - 1$, $\mathbf{h}^{(i)}$ is the clean-beam source component responsible for $A_{max}^{(i-1)}$ and \mathbf{D}^I is the remainder of the original \mathbf{R} matrix. Then, the first term on the r.h.s represents the acoustic signal part of the cross-power matrix while the second term is dominated by noise. Equation 4.7 simply states that the cross-power matrix due to the signal part of the measured data is the sum of n independent source components plus some noise.

Power integration is done by computing the average of the trace of the signal part of \mathbf{R} .

$$A_{sc} = \frac{1}{N} \sum_{n=1}^N R_{nn} = \frac{1}{N} \sum_{i=1}^I A_{max}^{(i-1)} \left[\sum_{n=1}^N h_n^{(i)} h_n^{*(i)} \right] \quad (4.8)$$

Where A_{sc} is the effective value of the sound pressure squared due to the I source components (sc). This is true even when the main diagonal of the original cross-power matrix was ignored in the processing due to high noise levels in the microphone auto-spectra. Equation 4.7 contains diagonal elements without spurious noise.

More details regarding CLEAN-SC in general and the power integration method described above can be found in [120].

4.2.4. Data Quality

The microphone array used in the present set of measurements is well suited for the measurement of noise levels for frequencies above a lower limit of 0.8 kHz up to a frequency of 20 kHz. At 0.8 kHz, estimated 1/3-octave band noise levels are considered to be repeatable to a precision of ± 2 dB. Interpretation of the results in that frequency band should be done with care. From 1.0 kHz and up, the accuracy of the estimated source levels is ± 1 dB. These error estimates were obtained using monopole-like test sources in the AWB without wind (no shear layer). Nevertheless, the above uncertainty estimates are considered as representative of the microphone array data precision for the current experiment.

Spectra presented in the following sections are always corrected for convective amplification, source convection and shear-layer refraction. Hereby, use of the well-known shear-layer correction developed by Amiet [5] was made. It is therefore assumed that the interface between the jet and the surrounding environment is an infinite planar shear-layer of negligible thickness. Finally, sound pressure levels were back-propagated to a reference distance of 1 m from the tested models

A better evaluation of the error margins of phased array measurements cannot currently be done. In fact, there is no simple way of evaluating a beamforming algorithm's precision [134].

4.3. Aerodynamic Measurements

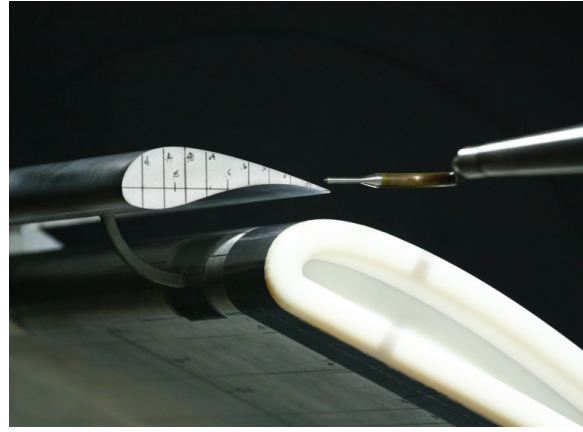
A limited set of aerodynamic measurements were conducted in the course of the investigations. A seven-hole probe was used to assess the tip flow field with enough accuracy to render the dominant flow structures as well as to quantify flow parameters necessary for the subsequent development of a semi-empirical model. Static pressure measurements provide a simple avenue for the evaluation of the wings effective deployment angles.

4.3.1. 7-hole Probe Flow Measurements

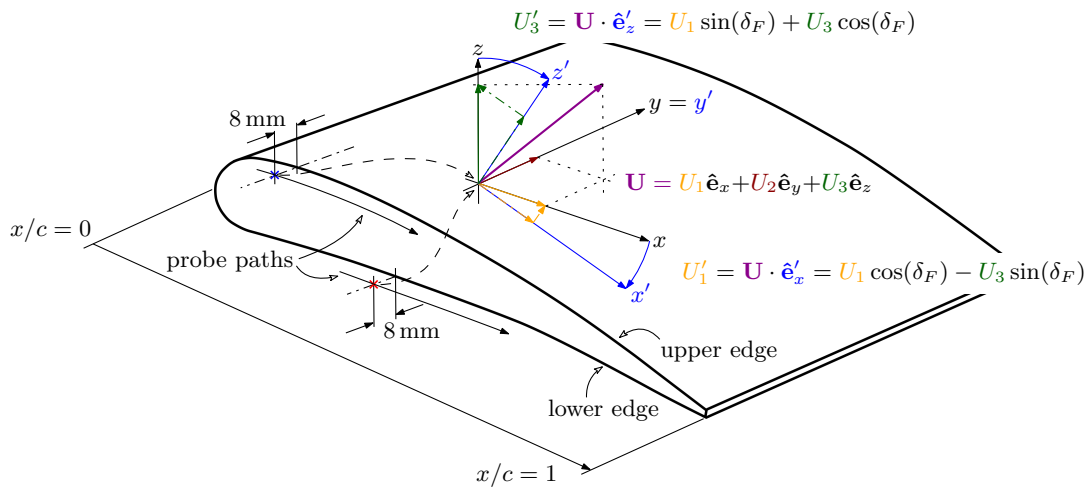
The mean flow velocity in the vicinity of the wing tip is characterized using the 7-hole probe technique. This technique enables the simultaneous measurement of all three components of the mean flow velocity vector. The calibration of the probe follows the principles described by Zilliac [137]. According to [137], errors on the measured velocity magnitude for a seven-hole probe is estimated to be less than 1.0%. Flow angle variations to within 1° can also be measured. This is valid provided that the flow angle, relative to the probe, does not exceed an angle of 70° . For larger angles, extensive flow separation occurs on the probe and makes it impossible to determine the correct velocity from the calibration charts. This aspect proved to be important in the close proximity of the flap side-edge vortex, where very high flow angles occur. Near the lower edge of the flap tip, flow deflection remains, however, always smaller than 70° . This means that the extraction of the cross-flow velocity at that position, and for all test settings, could be readily accomplished with a high degree of confidence. Depending on δ_f , a number of up to 5 different plane locations are chosen where flow field measurements are realized. The measurement planes were selected based on oil-flow visualizations in the wing tip region. The spatial resolution of the 7-hole probe flow measurements is limited to 5 mm in both directions ($\Delta y = 5$ mm, $\Delta z = 5$ mm). The probe has a diameter of 3 mm at its tip and over a length of 30 mm. After this length the diameter of the probe increases to 10 mm (see figure 4.10a). The probe clearance on the wing upper side being greater, the probe can be placed closer to the surface. The nearest measurement position relative to the model side-edge was 8 mm (e.g. figure 4.10b) and relative to the model upper surface was 5 mm. The size of the probe itself prevents from getting closer to the model. Due to the nearly 1:1 size of the isolated flap model, this resolution is sufficient to resolve the dominant features of the mean flow around the tip.

In cases where the flow direction exceeds $\pm 70^\circ$, extensive flow separation occurs on the probe which makes it impossible to determine the velocities from the calibration charts within the above uncertainty margins. This proved to be an issue in the close proximity of the FSE top edge, where large flow angles occur, thus leaving gaps in the velocity profiles where no data is available. The measured velocity profiles along the pressure side and suction side edges are presented in chapter 5.

The measurements were conducted by traversing the 7-hole probe, at a constant distance of $\Delta y = -8$ mm from the tip face, along the top and bottom edge of the tip. In doing so, the body of the probe is constantly held parallel to the upstream flow direction, i.e. parallel to U_0 . The probe, therefore, measures all three components of the velocity vector in the wind tunnel coordinates as specified in figure 4.10b, i.e. $\mathbf{U} = U_1\hat{\mathbf{e}}_x + U_2\hat{\mathbf{e}}_y + U_3\hat{\mathbf{e}}_z$, with $\hat{\mathbf{e}}_x$, $\hat{\mathbf{e}}_y$ and $\hat{\mathbf{e}}_z$ the unit vectors in the x , y and z directions. The position of the probe



(a) Close-up view of the probe in the vicinity of the flap model.



(b) Velocity measurement with the 7-hole probe. Position of the probe along the tip edges schematically given by the \times . Coordinate system definition for the flow measurements, i.e. wind tunnel coordinates (x, y, z) and wing-fixed coordinates (x', y', z') with $(\hat{\mathbf{e}}_x, \hat{\mathbf{e}}_y, \hat{\mathbf{e}}_z)$ and $(\hat{\mathbf{e}}_{x'}, \hat{\mathbf{e}}_{y'}, \hat{\mathbf{e}}_{z'})$ the unit vectors in their respective coordinate systems.

Figure 4.10.: 7-hole pressure probe measurement technique.

will be referenced to the model's leading edge position and will be given in fraction of the chord length. It is, therefore, independent of the model's angle of attack. The traverses have a resolution of $0.025c$, giving 42 measurement points per traverse. In chapter 5, the results of the flow measurements will be presented in the rotated coordinate system, or wing-fixed coordinates, (x', y', z') with $(\hat{\mathbf{e}}_{x'}, \hat{\mathbf{e}}_{y'}, \hat{\mathbf{e}}_{z'})$ the corresponding unit vectors, e.g. figure 4.10b, and x' parallel to the model's chord line. This is done to quantify the velocity magnitudes normal to the tip edges as precisely as possible, particularly when determining relevant velocity scales to which the acoustic sources are related.

4.3.2. Static Pressure Measurements

Measurements were made using a PSI 8400 acquisition system coupled to 32 ports 5-PSI scanner modules ESP-32HD (accuracy: $\pm 0.08\%$ full scale). The sampling rate (SR) is

fixed to 50 Hz, and mean static pressure values for each channel were computed from 10 samples.

5. Results of the Flow Investigations

The results of the flow measurements at the reference cantilever wing with flat tip as well as for the complementary test cases are presented herein. The motivation behind this series of measurements is the identification of characteristics of the mean flow field relevant for a description of the source mechanisms.

First the global flow field characteristics in the tip region are presented to provide an overview of the tip vortex development. Next, results of the investigations of the tip flow field in the vicinity of the tip edges are presented and discussed. Finally, relevant source regions are identified and associated length and velocity scales are defined.

5.1. Reference Cantilever Wing: Flow Visualization

To get a better insight in the complex three-dimensional tip flow field, visualization using soot were performed. A qualitative analysis of the recorded images reveals the global characteristics of the flow field about the wing tip. In figures 5.1 to 5.4 the flow visualizations at three deflection angles are shown ($\delta_F = 20^\circ, 25^\circ$ and 30°). Both, visualizations at the tip face and on the suction side and pressure side surfaces were made. Approximative streamlines have been superposed on the soot streamtraces to improve the images clarity.

First, for the tip flow visualization in figure 5.1, two distinct separation lines can be identified (dashed lines). No movement occurs across these lines near the wing's surface. On both sides of the stagnation lines, the flow is moving in opposite directions, pushing the soot away or toward the line.

At the tip leading edge, the flow is forced to separate thus forming a separation bubble extending to $\approx 0.1c$. At this point the LE flow and the pressure side edge shear layer merge to form the primary vortex. The primary vortex can be identified by the typical S-shaped streamlines it leaves on the surface, between both separation lines (dashed lines).

At about $0.1c$, the primary vortex starts building up, from the pressure side corner shear-layer while being trapped between both separation lines, progressively growing in size until it reaches the suction side. Below the main separation line, a vortex of opposite sense of rotation can be generated as shown by the S-shaped streamlines. This third vortex is sometime referred to as tertiary vortex [6, 26] and it is induced by fluid entrainment from the primary vortex. This vortex can only be identified in the case $\delta_F = 30^\circ$. Its full extent cannot also be precisely determined based on the available visualization.

The aft part of the tip face flow field is no longer dominated by a strong vortical structure. In that part, the flow is mainly aligned along the model tip face, as shown by the observed washing of the applied soot. The soot particles are pushed toward the TE up to another stagnation point located near the TE, at approximately $0.95c$. At that

location, under the influence of the local pressure field, low-velocity fluid coming from upstream positions and low-velocity back-flow coming from the TE meet. The stagnation point approximate location changes from $0.95c$ at $\delta_F = 20^\circ$ to $0.9c$ at $\delta_F = 25^\circ$ and $0.85c$ at $\delta_F = 30^\circ$. The fluid is then deflected toward the suction side where it feeds up the primary vortex. Merging occurs at a position which is dependent on δ_F , moving upstream with increasing deflection angle. As one approaches the TE the vortex grows in size and strength, constantly feeding on the suction side and pressure side corner shear layers. At higher angles of attack, the growth rate of the vortex is much more rapid and its passage to the suction side occurs earlier. Furthermore, due to a larger lift coefficient, the pressure side corner shear layer will follow a path to the suction side which is less close to the tip face as δ_F increases [82].

The evolution of the streamlines on the suction side and pressure side is documented in figures 5.2 to 5.4. The suction side flow is characterized by the formation of the secondary vortex. The vortex is initially located near the tip and slightly moves inwards with increasing chordwise position. This is due to the progressive induction of negative vorticity near the suction side corner by the secondary vortex.

In figures 5.2 to 5.4, on the top surface, a single stagnation line is observed which is linked to the presence of, first, the secondary vortex and, later, of the merged vortex. Because of the tip sharp edges, the flow field cannot follow the model geometry and separates at its edges, thus leaving a recirculation zone on the model suction side near the tip. The width and length of this separated zone grow slightly with a change in δ_F .

As the secondary vortex grows in size and strength, it progressively moves away from the wing's surface, giving rise to a zone of induced negative vorticity (opposite to the vortex rotation direction) production just above the airfoil's surface [82], e.g. figure 2.4. The approximate separation line between both regions is given by the dashed line in figure 5.2 to 5.4. Eventually, the negative vorticity rolls-up into the secondary vortex [82]. During the first phase, the secondary vortex can only feed on the suction side boundary layer vorticity because no connection to the primary vortex exists. In the second phase, the primary vortex moves to the suction side and merges with the secondary vortex. The resulting vortical structure is much larger. In the aft part, once the merging has occurred, the vortex continues to induce a strong bending of the surface streamlines and the flow direction is nearly normal to the wing tip face. This is most noticeable for the $\delta_F = 30^\circ$ case.

The suction side boundary layer near the tip trailing-edge, does not separate for flap angles below $\delta_F = 30^\circ$. At $\delta_F = 30^\circ$ flow separation occurs over approximately half of the whole span over a streamwise length of approximately 1 cm, starting at the trailing edge. In all cases, a separation bubble forms near the side wall. The span of the wall separation bubble is of about 10 cm at $\delta_F = 25^\circ$ and reaches 20 cm at $\delta_F = 30^\circ$ (see figure 5.2 to 5.4).

The pressure side streaklines are bent toward the tip over nearly half of the model span. The curvature being a function of the model deflection angle; higher δ_F meaning a larger curvature. Further away from the tip, the aft part streamlines never get parallel to the flow direction, due to the combined effect of the tip vortex and the side wall boundary layer. The pressure side boundary layer does not separate. The above observations are consistent with the global flow measurements as well as with evidences from the literature [6, 79, 81, 82].

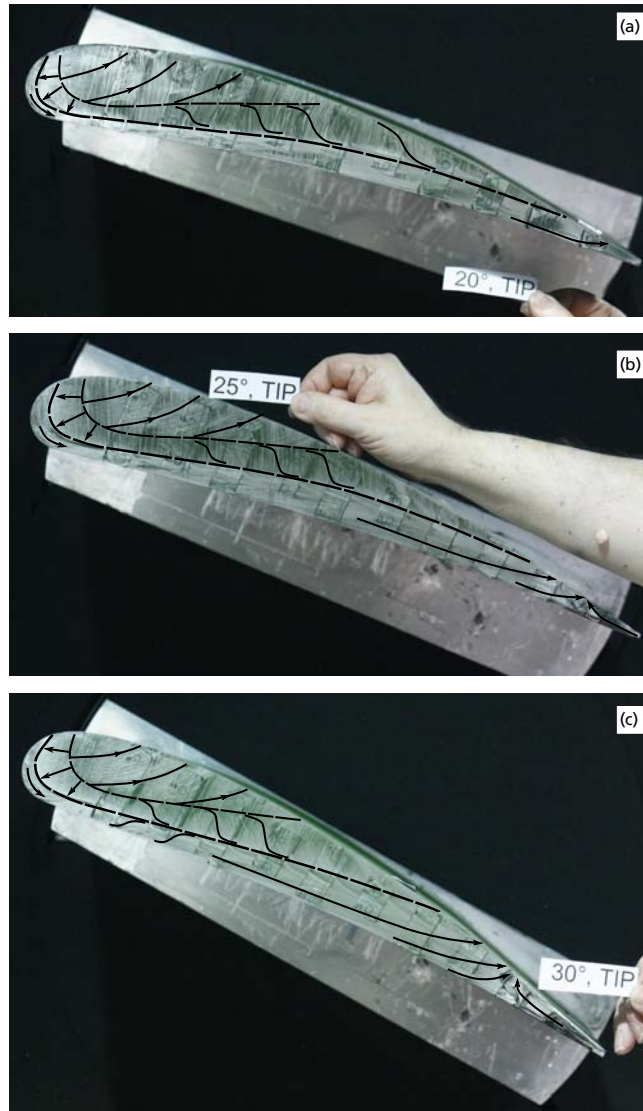


Figure 5.1.: Surface streaklines visualization on the tip face. Approximative streaklines are sketched. (a) $\delta_F = 20^\circ$. (b) $\delta_F = 25^\circ$. (c) $\delta_F = 30^\circ$.

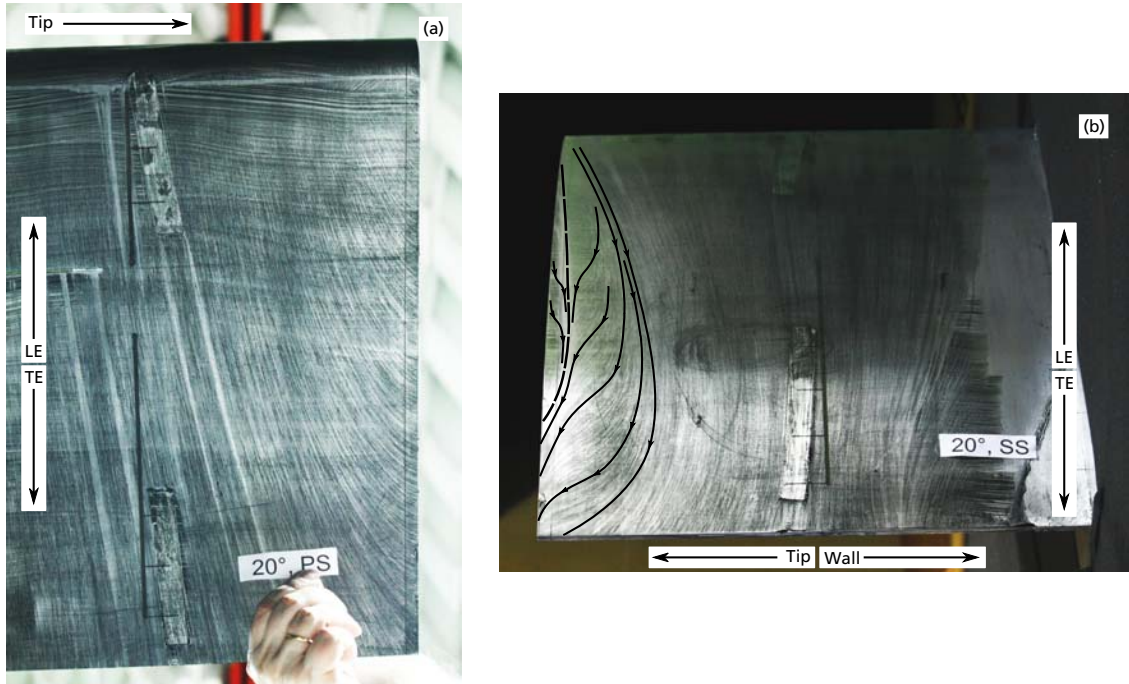


Figure 5.2.: Surface streaklines visualization. Approximative streaklines are sketched. $\delta_F = 20^\circ$. (a) Pressure side. (b) Suction side.

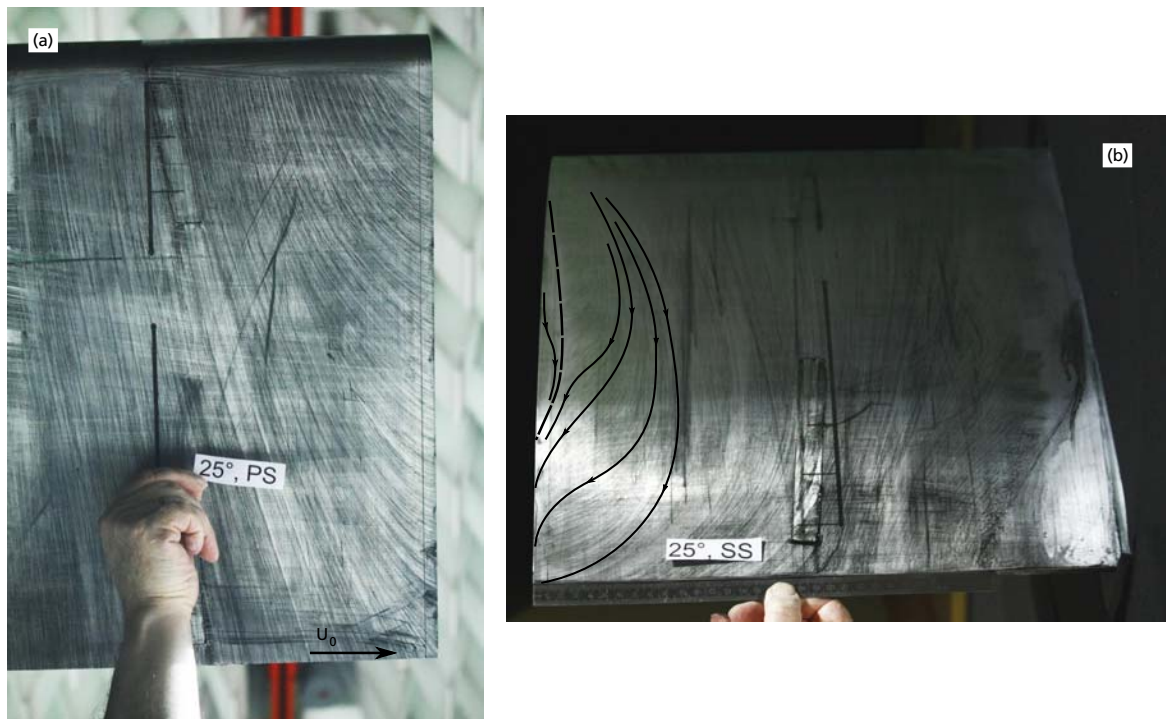


Figure 5.3.: Surface streaklines visualization. Approximative streaklines are sketched. $\delta_F = 25^\circ$. (a) Pressure side. (b) Suction side.



Figure 5.4.: Surface streaklines visualization. Approximative streaklines are sketched. $\delta_F = 30^\circ$. (a) Pressure side. (b) Suction side.

5.2. Global Characteristics of the Tip Flow Field

The vortex formation process can grossly be divided in three main phases. First, at the pressure side edge, a shear layer is ejected which eventually rolls-up to form the primary vortex. Simultaneously, at the suction side edge, the suction side boundary layer near the tip and part of the tip face flow also roll-up to form a second vortex. While the primary vortex quickly moves from the tip face to the suction side, the secondary vortex stays on the suction side and follows a path mostly parallel to the flow direction. The vortices paths are documented in figure 5.5 for three values of δ_F . This position is defined as the location at which the vortex velocity, in the $y - z$ plane, changes sign. The first phase is captured in the flow measurements of figure 5.6a,b. The second phase consists in the merging of both vortex to form a single larger entity (see figure 5.6c). In the third phase, the tip vortex continues to grow while remaining near the model suction side. At some point, the vortex lifts off the model's surface (see figure 5.6d,e). Measured maximal velocities reach $\approx 2.0U_0$ in the streamwise direction and $\approx 1.6U_0$ in the spanwise and normal directions.

Looking in more details at the vortices paths along the model chord (figure 5.5), one can observe slight differences depending on the selected deflection angle (δ_F). At $\delta_F = 10^\circ$, the vortices merge around $x/c = 0.7$. Upstream of this position the suction side vortex slowly moves inboard ($y > 0$). Downstream of the merging position, the vortex moves back towards the edge ($y < 0$). The vortex remains near the wing's top surface, progressively moving away from it in the z direction ($z/c > 0$). For a deflection angle of 20° vortex merging occurs at approximately $x/c = 0.6$. Before this streamwise position, the upper surface vortex moves slightly inboard in a similar fashion as for the case $\delta_F = 10^\circ$. Downstream of $x/c = 0.6$, the merged vortex stays at the tip ($y/c = 0$). Compared to the previous case, the merged vortex moves away from the top surface in a more sudden and rapid manner. At $x/c = 1.0$ the vortex core is at about $z/c = 0.1$ (above the surface compared to $z/c = 0.05$ for the 10° case). For a deflection of $\delta_F = 25^\circ$, the measured vortex path is similar to the case $\delta_F = 20^\circ$. Vortex merging occurs approximately between $0.4 < x/c < 0.6$.

Flow field measurements, as in figure 5.6, are also available for $\delta_F = 25^\circ$ for four x/c positions. From these field measurements an estimate of the primary and secondary vortices diameters can be obtained. The vortex size is estimated from the spatial separation between the maximum and minimum in the normal, U_3 , and spanwise, U_2 , velocity profiles across the vortex center, respectively. The resulting values for the vortex diameter at $x/c = 0.4$ and $x/c = 1.0$ for $\delta_F = 20^\circ$ and $\delta_F = 25^\circ$ are tabulated in table 5.1. The $\delta_F = 10^\circ$ case is not considered to be relevant for the FSE noise as overall lift of the wing does not promote the formation of a strong vortex. At $x/c = 0.4$, only a marginal increase in vortex size is measured while at $x/c = 1.0$ the vortex size increase about 15% from $\delta_F = 20^\circ$ to $\delta_F = 25^\circ$. The order of magnitude obtained in the experimental results is in agreement with CFD computations [13, 81]. In the aft part of the wing tip the vortical flow is subjected to an increasing adverse pressure gradient as δ_F increases. Therefore, the observed vortex size growth is according to expectations [26, 50, 87]. There is, however, a considerable uncertainty in the estimate of the vortex size, l at $\delta_F = 25^\circ$ due to data lacking in regions of large flow angularity, i.e. where the 7-hole probe technique fails.

The vortex size is defined as the distance between the minimum and maximum values of tangential velocity in a section cut crossing the vortex axis at a right angle.

Table 5.1.: Primary vortex size normalized by the chord length (l/c) at $x/c = 0.4$ and $x/c = 1.0$ vs. δ_F . $c = 0.473$ m.

δ_F	$x/c = 0.4$	$x/c = 1.0$
20°	0.0349	0.1655
25°	0.0385	0.1968

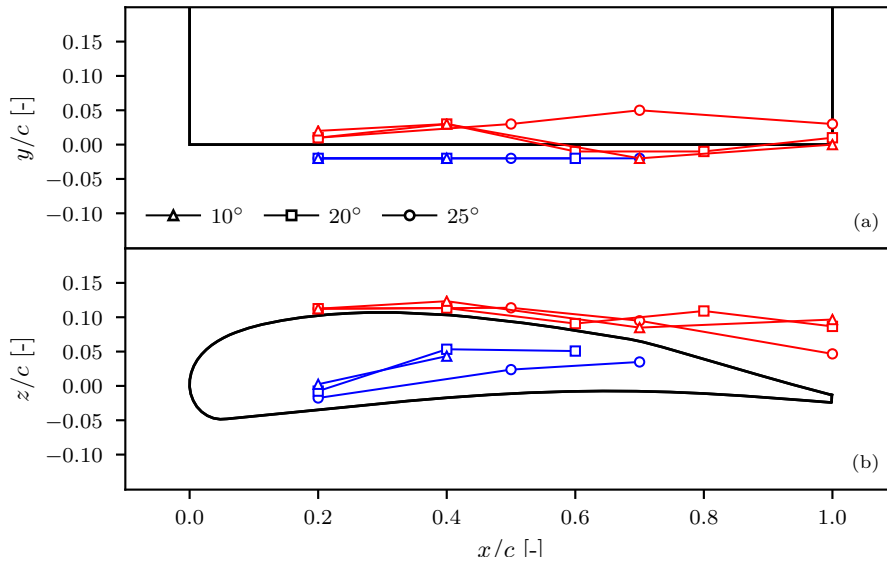


Figure 5.5.: Measured vortex core path vs. δ_F . (a) Top view. (b) Side view. The blue symbols refer to vortices originating from the lower edge and the red symbols to those originating from the upper edge.

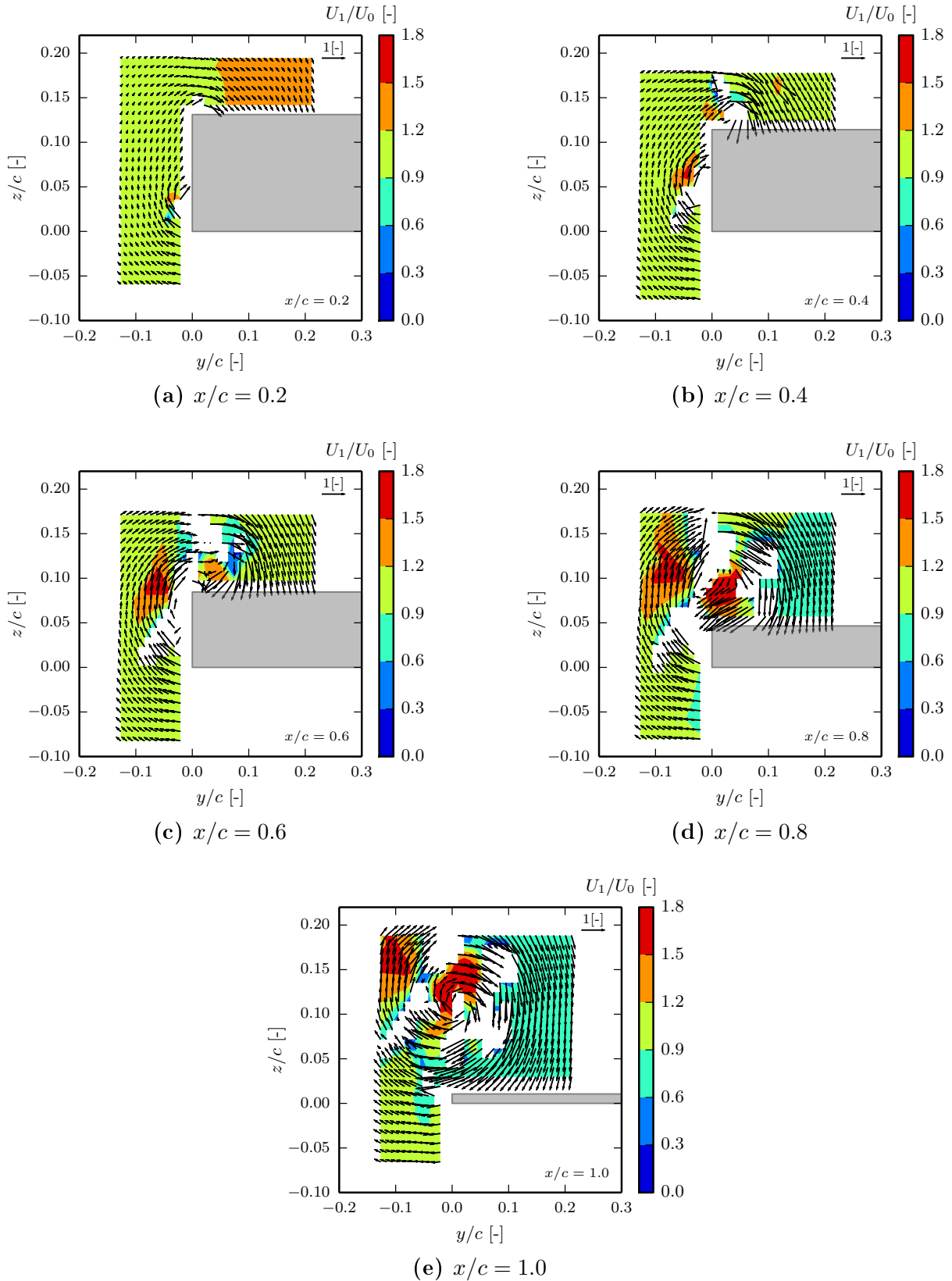


Figure 5.6.: Mean flow field at the wing tip, $\delta_F = 20^\circ$, $M_0 = 0.18$. The measurement planes are chord-normal. Wing geometry shown in grey. White patches in the contours plots are due to data rejection in the experiment, where flow angularity exceeds the range of the 7-hole probe technique. Velocity vector components displayed in the wind tunnel coordinate system, see figure 4.10b

5.3. Static Pressure Distributions

The surface static pressure distributions are presented in figure 5.7. Extensive results for all test cases are provided in appendix B. The topmost plot in figure 5.7 corresponds to measurements at the mid-span section. The other two graphs show the evolution of the static pressure along the wing tip face. For the *tip high* case the pressure taps are located near the suction side edge, while in the *tip low* case static pressures are measured near the pressure side edge. See chapter 3 for more details about the location of the pressure taps.

At mid span the suction peak cannot be completely captured due to a lack of pressure taps directly in the LE region. Part of the suction peak downstream of the LE is, however, still captured. The zero lift angle of attack is approximately reached at $\delta_F = -5.7^\circ$. A qualitative observation of the static pressure distributions reveal that the flow remains attached until $\delta_F = 28^\circ$. The computation of a reliable lift coefficient based on the measured data is, however, not possible. CFD simulations provide avenue around this difficulty [13, 81].

For the tip face pressure distributions (middle and lower part of figure 5.7), two distinct behavior are observed. Near the upper tip corner, an isolated region of strong suction exists. Its extent, as well as its suction peak, are dependent on the model deflection angle. For $\delta_F = 30^\circ$, the region of low static pressure extends from $x/c \approx 0.3$ to $x/c = 0.9$ and a minimum pressure coefficient of $C_p = -3.25$ is reached. At $\delta_F = 10^\circ$, suction occurs between $x/c = 0.55$ and $x/c = 0.9$, with a peak pressure coefficient of $C_p = -1.16$. This characteristic decrease in static pressure is directly linked to the chordwise development of the tip vortex and to its path along the tip surface. The vortex passage from the tip to the suction side marks the starting point of a progressive increase of the pressure coefficient toward the trailing edge. Near the lower edge, an increase in δ_F leads to a uniform static pressure decrease over the whole measurement domain (here from $x/c = 0.15$ to $x/c = 0.83$). Here, the static pressure distribution is mainly influenced by the shear layer ejected at the pressure side corner and its early roll-up. The tip vortex is constantly fed by that shear layer explaining the comparatively uniform suction along the lower edge. When the vortex has moved over to the suction side, a slow pressure recovery is measured between $x/c = 0.58$ and $x/c = 0.83$. The sudden drop in C_p at $x/c = 0.75$ on the tip face is due to the convergence, at that position, of the upstream and downstream flows along the tip, thus forming a stagnation region. This can be clearly observed in the flow visualizations (e.g. figure 5.1).

5.4. Aeroacoustic Source Regions

In this section, the emphasis is put on the identification of distinctive flow features in the vicinity of the airfoil's tip edges which can be related to the noise production mechanism previously discussed in chapter 2. To achieve this goal, mean flow measurements of all three components of the velocity vector are realized using the 7-hole probe technique, e.g chapter 4. The measurement data are acquired near the edges of the model tip, where levels of high flow unsteadiness are known to exist [6, 82]. Regions where large velocity gradients exists are identified, and characteristic parameters are extracted.

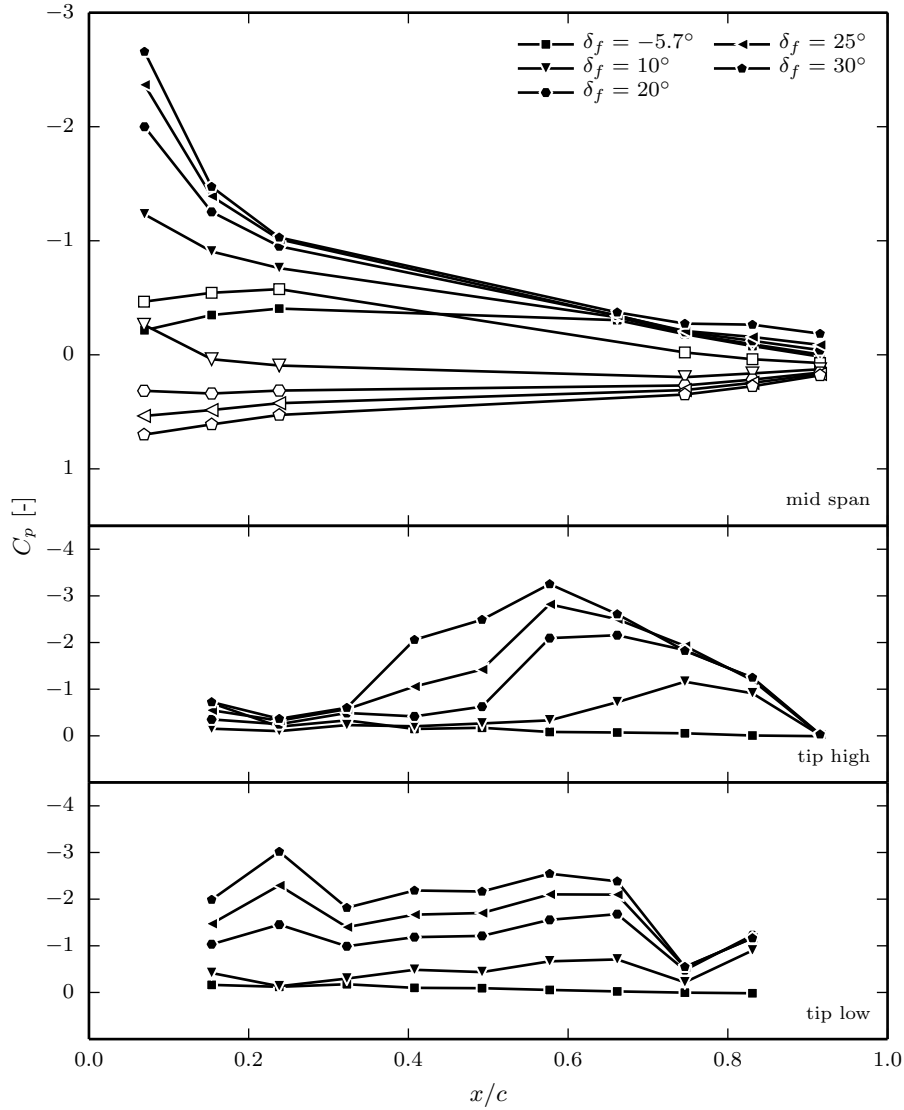


Figure 5.7.: Static pressure distributions at mid span and at the model tip face. $U_0 = 60\text{ m/s}$ In the top figure, empty symbols are used for the pressure side measurements while solid symbols correspond to measurements at the suction side.

5.4.1. Flat-Tip, Sharp-Edge FSE

Velocity in the Vicinity of the Pressure Side Tip Edge

The velocity profiles presented in figures 5.8 to 5.10 are given in wing-fixed coordinates as the components of the flow field normal to the wing's tip edges are assumed to be most relevant for the acoustic problem. The evolution of the mean flow velocity near the lower and upper tip edges is presented in figure 5.8 and 5.10 for three values of δ_F . In these plots, the velocity components are normalized by the free-stream velocity, U_0 . Looking first at figure 5.8, a striking observation is the weak dependency of the U'_1 and U'_3 velocity components on δ_F . Increasing the flap deflection from 20° to 30° has, however, a strong impact on the second velocity component, U'_2 . The chordwise evolution is first characterized by a sudden increase in the U'_1 velocity component and decrease in U'_2

velocity at $x/c = 0.025$. This peak is related to the incoming flow being accelerated in the vicinity of the model LE. This effect does not show up in the U'_3 component, where a progressive increase is observed until $x/c \approx 0.1$. After this first phase, the formation of the primary tip vortex begins under the action of the static pressure difference between the pressure side and suction side. The vortex first remains at the tip face up to a given chordwise position, dependent on flap deployment, before moving to the suction side and merging with the secondary vortex. Marking the start of a progressive drop in the magnitude of both U'_2 and U'_3 towards the trailing edge, e.g. figure 5.8.

In figure 5.9, results of mean flow measurements in the vicinity of the pressure-side edge of the cantilever wing equipped with a partly porous tip are presented. The porous insert is made of metal foam with a porosity of 30 pore-per-inch (ppi) and has been originally designed in the frame of the European project OPENAIR. It has a 83% chordwise and 5% spanwise porous extent (see sketch in figure 5.9) and provides a broadband FSE noise reduction on the order of 10 dB. In figure 5.9, velocity measurements along the upper and lower edge of the porous tip, performed using the same procedure as above for the reference case, are presented. Furthermore, the streamwise porous length was varied, using tape, to investigate the effect on the velocity field. This will be also further discussed in relation with the acoustic radiation in chapter 6. The results of figure 5.9 emphasize that U'_2 is most affected by the application of a porous treatment to the airfoil's tip. The porous insert allows for through-flow, leading to an important reduction of the spanwise velocity magnitude and overall vortex strength leading to an important noise reduction. Reducing the streamwise porous length of the insert has a direct impact on the flow field, with a sudden increase in velocity near the porous/non-porous interface.

Velocity in the Vicinity of the Suction Side Tip Edge

A quite different streamwise evolution of the velocity components is presented in figure 5.10, for the tip upper edge. Strong velocity gradients are measured between $x/c = 0.0$ and $x/c = 0.025$. They are linked to the LE flow separation at the model tip. Downstream of $x/c = 0.025$, the first two components quickly reach a plateau which is sustained up to $x/c \approx 0.4$ ($U'_1/U_0 \approx 1.0$, $U'_2/U_0 \approx 0.2$). The chordwise position of the velocity maximum shift upstream with an increase in δ_F .

The flow around the model LE is bent towards the wing root, e.g. figure 5.2-5.4, feeding the secondary vortex (or suction side vortex). This holds between $x/c = 0.025$ and the position at which the primary vortex moves to the suction side and merges with the secondary vortex. Starting at about $x/c \approx 0.35$ (depending on δ_F), the U'_2 velocity component increases and quickly reaches a peak. This velocity maximum increases with an increase in δ_F , while shifting upstream. The U'_2 velocity component increase coincides with a decrease in U'_3 and U'_1 velocity; the flow is suddenly bent away from the tip. The subsequent gradual variation in U'_2 over the approximate range $0.4 < x/c < 0.8$, is related to the vortex core slightly moving toward the wing root before moving back closer to the tip suction side edge. This is confirmed by the flow visualizations of chapter 5. Afterwards, the spanwise velocity component, U'_2 , changes sign to become negative. The counterclockwise rotation of the primary vortex now induces a negative spanwise velocity in the vicinity of the upper edge. The passage of the primary vortex to the suction side also leads to a delayed sign change of the U'_3 velocity component. A minimum in U'_3 is

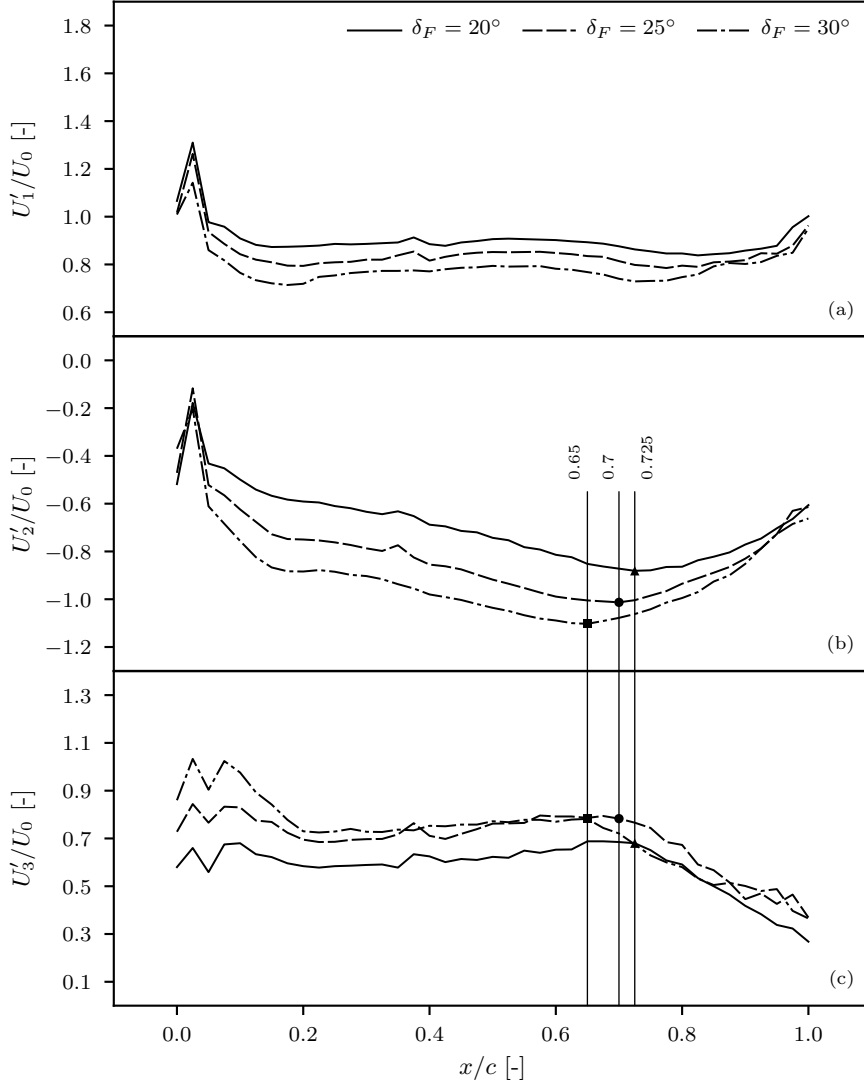


Figure 5.8.: Streamwise evolution of the mean flow velocity components at the pressure side edge. The x/c positions where characteristic velocity scale, $u = \sqrt{U'^2_2 + U'^2_3}$, is picked is shown by the solid symbols.

reached between $0.65 < x/c < 0.75$, its magnitude depends strongly on δ_F . At $\delta_F = 30^\circ$ a peak value of -0.2 is reached, clearly showing that no important downwash occurs in the rear part of the wing tip. Further downstream ($x/c > 0.75$), the magnitude of the streamwise component slowly decreases up to the TE, except for the occurrence of a small hump at about $x/c \approx 0.85$ to $x/c \approx 0.95$, which is related to the stagnation point identified in figures 5.2-5.4. The measurement data obtained near the suction-side edge for positions $x/c > 0.75$ suggest that the probe is in a recirculation zone beneath the vortex as indicated by the flow measurements of figure 5.6 and the visualization results of figures 5.2-5.4. And, as such, not representative of the vortex but mostly of the tip flow separation occurring as the pressure side flow rolls-up into the vortex.

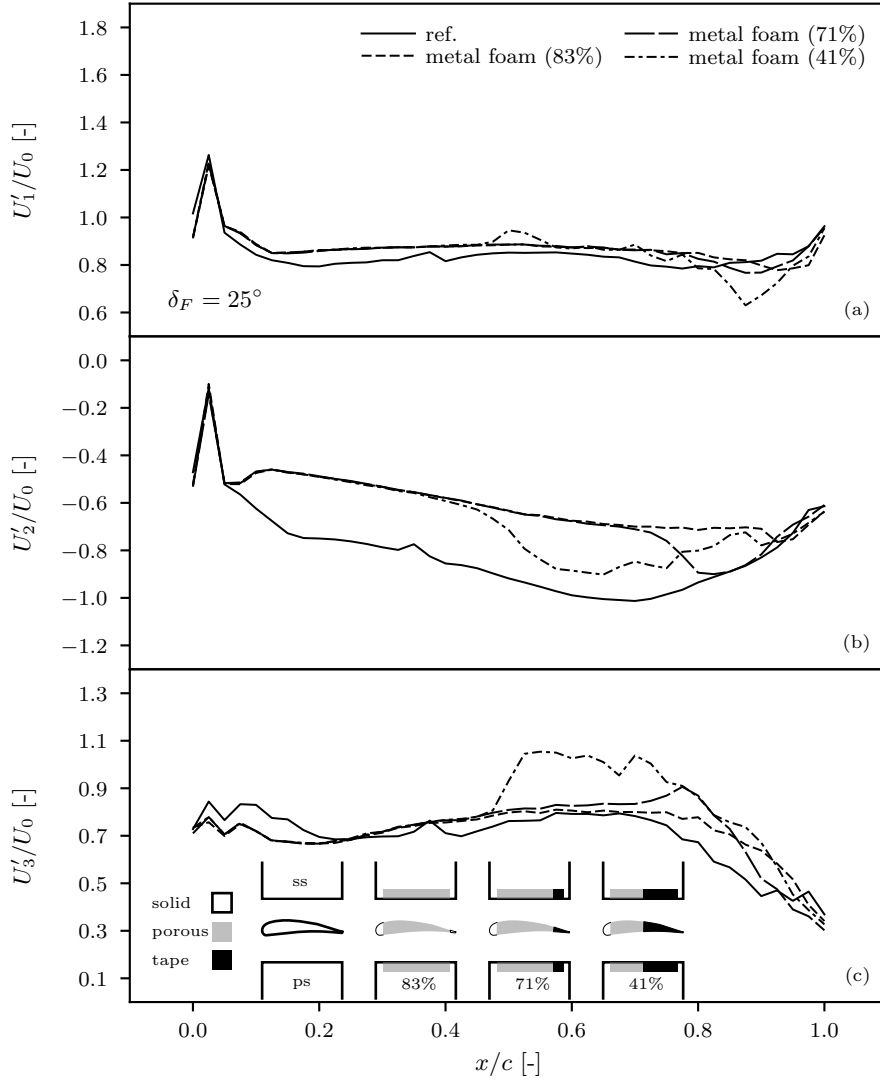


Figure 5.9.: Streamwise evolution of the mean flow velocity components at the pressure side edge. reference wing vs. metal foam tip for varying porous extents.

Characteristic Velocity and Length Scales

As discussed in the introduction, FSE noise results from unsteady fluctuations of the tip vortex position and velocity field [125] in the proximity to the solid edge. From the literature Koop [82], it is known that the FSE acoustic source region has a position along the tip which is dependent on the radiated sound frequency. One thus expects low-frequency noise to be caused by large scale, long wavelength, unsteadiness of the vortex and their interactions with the wing tip mostly near the tip trailing edge corner Koop [82], i.e. where the tip vortex has its largest dimension. Looking at increasingly higher frequencies, the source regions along the wing tip will shift towards decreasing x/c values, i.e. according to the tip vortex dimension. We will later show, in chapter 6, that this observation also holds for the present database.

In chapter 7 we will aim at an empirical description of the wing tip sound radiation using lumped representations of the low and high frequency range using two generic spectral

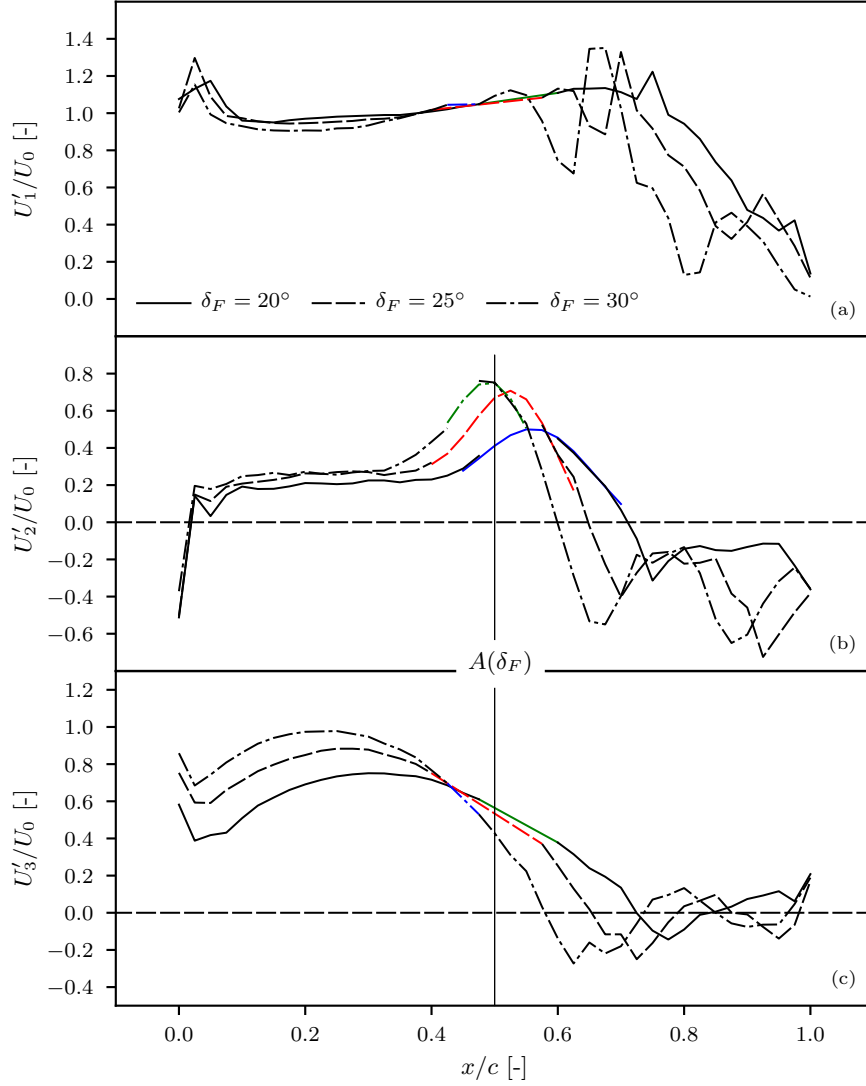


Figure 5.10.: Streamwise evolution of the mean flow vector components at the suction side edge. Between $x/c = 0.4$ and $x/c = 0.6$, missing experimental data are obtained through extrapolation using best-fits.

shape functions. These functions are to be specified on a Strouhal number basis defined by the relevant velocity and length scales of the sound generating mechanisms.

We postulate that, in order of magnitude, sound is generated over a time interval $\sim l/u$, with l a characteristic length scale and u a characteristic velocity scale. The sound frequencies are rendered dimensionless using l and u to define the corresponding Strouhal number, $St = fl/u$. The low-frequency spectral function maximum is specified at $St = fl/u = 1$, with l equalling to the vortex diameter in the vicinity of the trailing-edge and u being equal to a representative vortex rotational velocity, i.e. $u \sim \max(\sqrt{U_2'^2 + U_3'^2})$ near the wing's trailing edge in the range $0.6 < x/c < 0.75$. The results of the vortex core path analysis of figure 5.5 clearly indicate that the vortex slightly lifts off of the wing's suction side before reaching the trailing edge, in the range $0.6 < x/c < 0.8$. Also the oil flow visualizations of figures 5.1, show a zone of stagnant flow near the tip trailing edge, evidences of a possible separation bubble. Because, in the range $x/c > 0.6$ the vortex no longer follows the wing's contour, the value of u vs. δ_F is derived from the velocity

measurements at the tip pressure side, e.g. figure 5.8, prior to vortex lift-off. The values of u derived in this manner are considered to be the most representative of the tip vortex rotational velocity, near the trailing edge, available from the flow measurements. The flow measurements at $x/c = 1$ show that the vortex has grown to a diameter of about $0.16c$, e.g. table 5.1, which will be used for l . Using $u = U_0$ to obtain a first rough order of magnitude estimate of the frequency of the sound generated by the dominant flow structures at $U_0 = 60$ m/s gives $u/l \approx 60/0.16c \approx 0.792$ kHz.

We postulate that high-frequency noise generation occurs, predominantly in the forward half of the FSE, as a consequence of two distinct source mechanisms: 1) edge scattering of the turbulent velocity fluctuations, according to the pressure-side shear-layer instability hypothesis of Brooks and Humphreys Jr. [21], Roger et al. [113], and 2) vortex-edge interaction through the unsteady movement of the primary vortex and its subsequent merging with the secondary vortex. The second mechanism is similar to the postulate made above for low-frequency noise generation. The merging process occurs at high velocities and sound is produced through interaction of unsteady vorticity fluctuations with the upper tip edge [57, 82, 124, 125]. The shear-layer instability mechanism leads to a higher frequency sound radiation compared to the vortex-edge mechanism because of the markedly different flow structures length scales involved, i.e. the boundary layer thickness vs. the vortex dimension. According to Brooks and Humphreys Jr. [21], the boundary layer thickness at the pressure side of the airfoil is estimated to be of order $\delta \sim 0.009c = 0.009 \times 0.473 = 4.3 \times 10^{-3}$ m which is about 4.5 times smaller than the primary vortex size before the vortex merging occurs, i.e. just upstream of position $A(\delta_F)$ in figure 5.10. With this, an order of magnitude estimate of the radiated sound frequency by the shear-layer instability mechanism at $U_0 = 60$ m/s is of order $u/l \approx 14$ kHz. According to Brooks and Humphreys Jr. [21] the contribution of the shear-layer instability mechanism to the overall noise emission is also directly related to the magnitude of the spanwise velocity about the pressure side edge and, therefore, to the flap loading. The characteristic frequency estimate above imply that the shear-layer instability mechanism is mostly relevant at very high frequency. However, the results of chapter 6 will demonstrate that the dominant frequency range of the measured acoustic radiation is well below 14 kHz reaching a maximum at a frequency $f \approx 1$ kHz. In view of the results of chapter 6, the shear-layer instability mechanism is not considered to be a relevant contributor to FSE noise. In comparison, an order of magnitude estimate of the radiated sound frequency due to the high-frequency vortex-edge interaction mechanism at $U_0 = 60$ m/s is of order $u/l \approx 3.17$ kHz, with a characteristic vortex dimension of $l = 0.04c$, see e.g. table 5.1. The relevant characteristic velocity scale for the high-frequency vortex-edge interaction mechanism is defined as $u = \sqrt{U_2'^2 + U_3'^2}$ at the position of vortex merging and near the suction side tip edge, i.e. position $A(\delta_F)$ in figure 5.10.

The extracted characteristic velocity magnitudes at position $A(\delta_F)$, near the suction-side edge, and near the pressure-side edge according to figure 5.8, are given in figure 5.11. Results are given in a wing-fixed coordinate system. The tip vortex streamwise circulation, Γ_1 vs. δ_F is put in relation, in figure 5.12, to the velocity scales discussed above i.e. fig. 5.8 and 5.10. Again, an approximately linear relationship exists between $u = \sqrt{U_2'^2 + U_3'^2}$ and Γ_1 . The knowledge of the tip vortex circulation at $x/c = 1.1$, downstream of the wing's TE, is therefore sufficient to determine all relevant characteristic velocity scales. In figure 5.12a, values of Γ_1 obtained from CFD computations are also plotted [13].

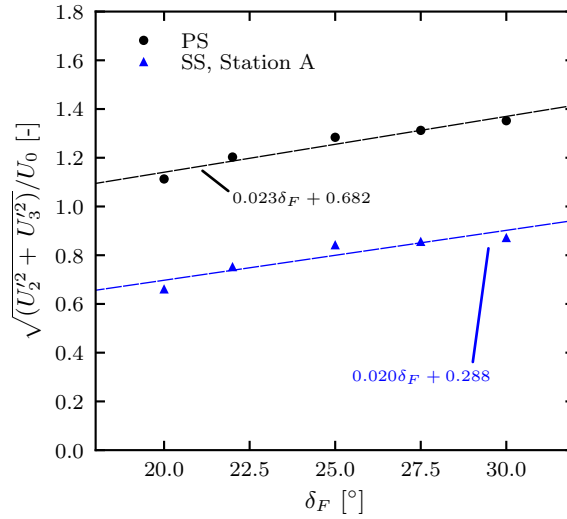
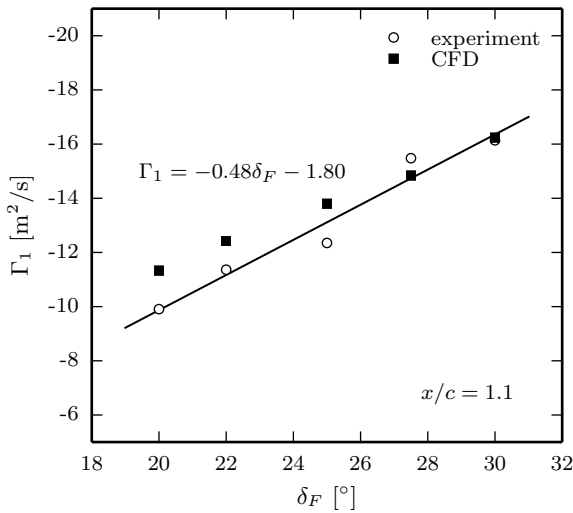


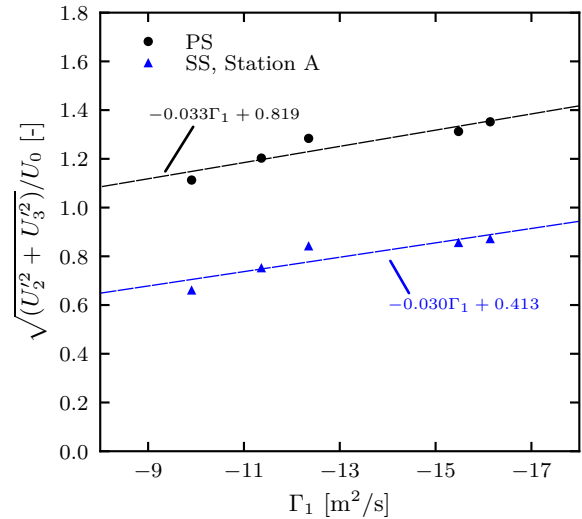
Figure 5.11.: Characteristic velocity scales. Reference wing.

There is a reasonably good agreement between the experimental results and the CFD. The deviation observed at $\delta_F = 20^\circ$ and $\delta_F = 22^\circ$ correspond to an approximate error of 13% on the resulting value for u in figure 5.12b.

Because the static pressure distributions can be computed through CFD with enough accuracy [13], a reliable value of C_L can be recovered and therefore a direct relation with u can be established. The lift polar, in both free field conditions and in the AWB, for the reference cantilever wing, are plotted in figure 5.13a. In figure 5.13b, u is plotted against the free-field condition C_L of figure 5.13a.



(a) Streamwise circulation Γ_1 vs. δ_F



(b) Characteristic velocities vs. streamwise circulation Γ_1

Figure 5.12.: Measured vortex circulation at $x/c = 1.1$ vs. δ_F and the characteristic velocity scales, $u = \sqrt{U_2^2 + U_3^2}$ at the pressure side and suction side.

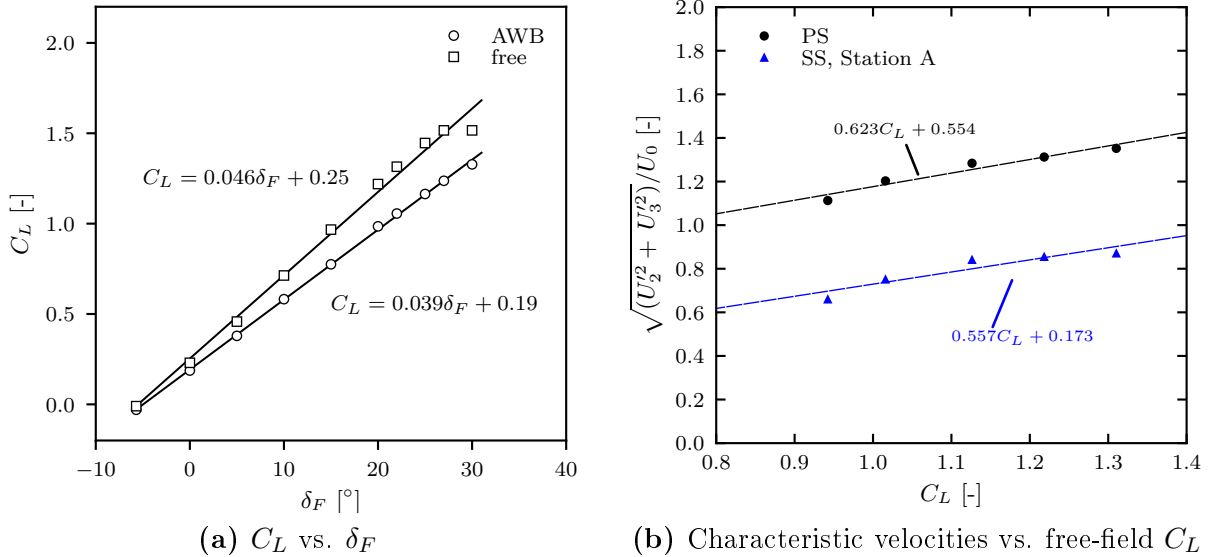


Figure 5.13.: Characteristic velocities vs. C_L . Left; lift polar according to CFD results in [13]. A δ_F correction between the AWB and free-field conditions is given as $\Delta\delta_F = -3.9C_L - 0.56$.

5.4.2. Complementary Test Cases

Next, the flow field and the aerodynamics of the complementary test (e.g. section 3.4) cases with tip modifications are investigated using the same methodology as described in the previous section. Because of the tip modifications, measurements of the velocity with the 7-hole probe technique along the top edge proved difficult, in some cases, due to increased spanwise gradients and higher flow angularity. Because of this, the emphasis is put here on the pressure side edge velocities only. Details about the suction side flow field could be obtained using laser-based measurement techniques, e.g. particle image velocimetry, laser doppler velocimetry, or CFD.

On the left hand side of figure 5.14, a comparison is made of the lift polar, measured at the reference cantilever wing mid-span position, for all test cases (see also appendix B). For all configurations, one observes the consistently higher lift produced by the wing without LE vane. The vane reduces the lift coefficients at the wing by shifting the suction peak towards the vane LE. This is, however, not captured in the experiments due to the lack of pressure taps on the vane. At $\delta_F = 20^\circ$, an approximate 18% loss in C_L is measured when the vane is installed compared to the reference wing. This gap slowly increases with an increase in δ_F . Below $\delta_F = 15^\circ$, a dip is observed in the polar for the configurations with the vane installed. This effect is probably related to the fixed angle of the vane with respect to the wing which is not optimal at lower wing angles.

For an evaluation of the noise impact of the tip modifications relative to the reference cantilever wing, it is necessary to establish a correspondence between all test configurations. Because FSE noise is assumed to be related, to first order, to the total lift force generated by the wing system, comparisons between different configurations should be made at equal lift coefficients. A precise evaluation of the total lift force for each configuration is not possible from the experimental data. We therefore revert to the flow measurements.

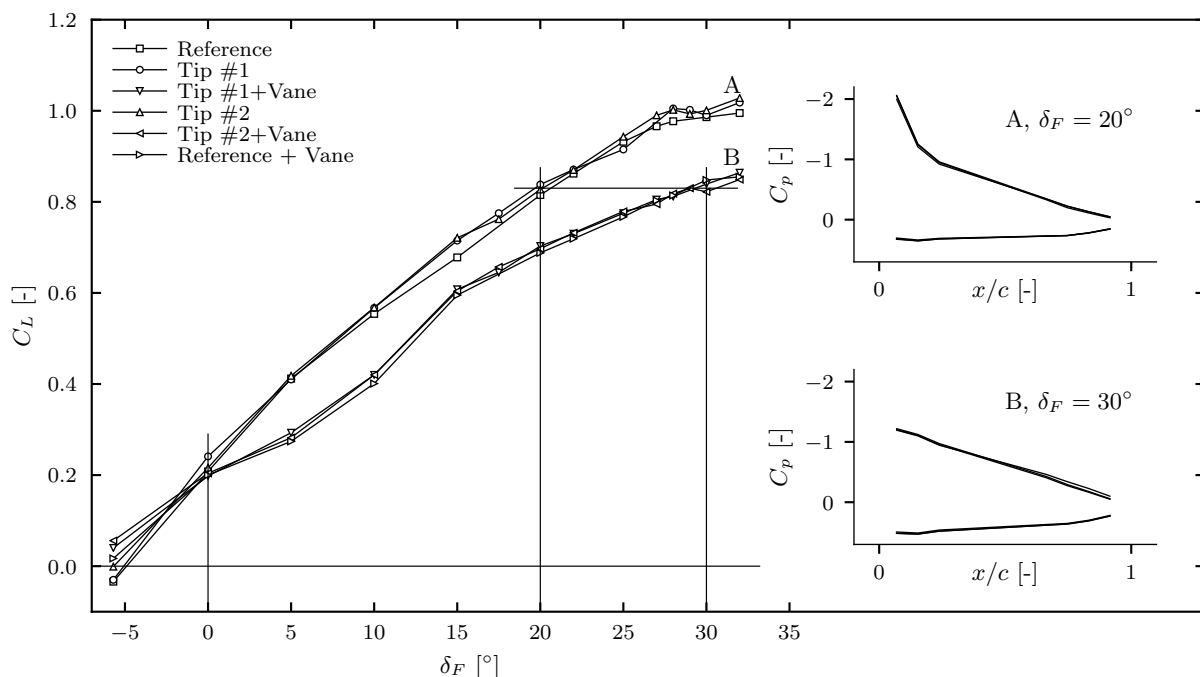


Figure 5.14.: Left, measured lift polars for all configurations. Right, distribution of surface static pressure coefficient (C_p) vs. normalized streamwise position (x/c) for selected δ_F . In each inset three C_p distributions are plotted, respectively for the configurations without (A) and with (B) vane.

At equal wing C_L , the tip cross-flow velocity magnitudes for different airfoils should be equal and a similarly intense FSE noise radiation is expected [114]. In figure 5.15a, the normalized cross-flow velocity ($u = \sqrt{U_2'^2 + U_3'^2}/U_0$) at the tip lower edge is plotted against x/c for the cases “vane” and the reference at two δ_F . The magnitude of the cross-flow velocity is related to the pressure differential between the wing upper and lower surfaces. In other words, an increase in C_L will lead to a corresponding cross-flow velocity increase. Although the vane appears to modify the velocity profiles, the measurements display similar overall trends and magnitudes. The observed differences are vane-related and cannot be accounted for by an angle-of-attack correction.

For test cases “tip #1” and “tip #2”, e.g. figure 3.7, the measured static pressure distributions at mid-span agree very well with those measured on the reference wing. The insets of figure 5.14, also clearly demonstrate that for the given tip add-ons the tip shapes have no significant influence on the wing sectional lift at mid-span. Therefore, any change in spanwise flow (see figure 5.15b) and radiated noise spectral characteristics is a direct consequence of a change in tip geometry only.

The results presented in figure 5.15 reveal interesting trends which need further discussion. In figure 5.15a, the vane is found to have an impact on velocities at both the aft and fore FSE parts. At 20° , the cross-flow profile is almost identical to that of the reference, however, with a 6% slower cross-flow in the aft part. At 30° , the aft part cross-flow now equals the reference values while the fore part flow increases by 16%. At 25° (not shown here), the cross-flow profiles for both configurations lie on top of each other. The vane’s aerodynamic performance appears to increase with increasing δ_F . At low δ_F it mostly

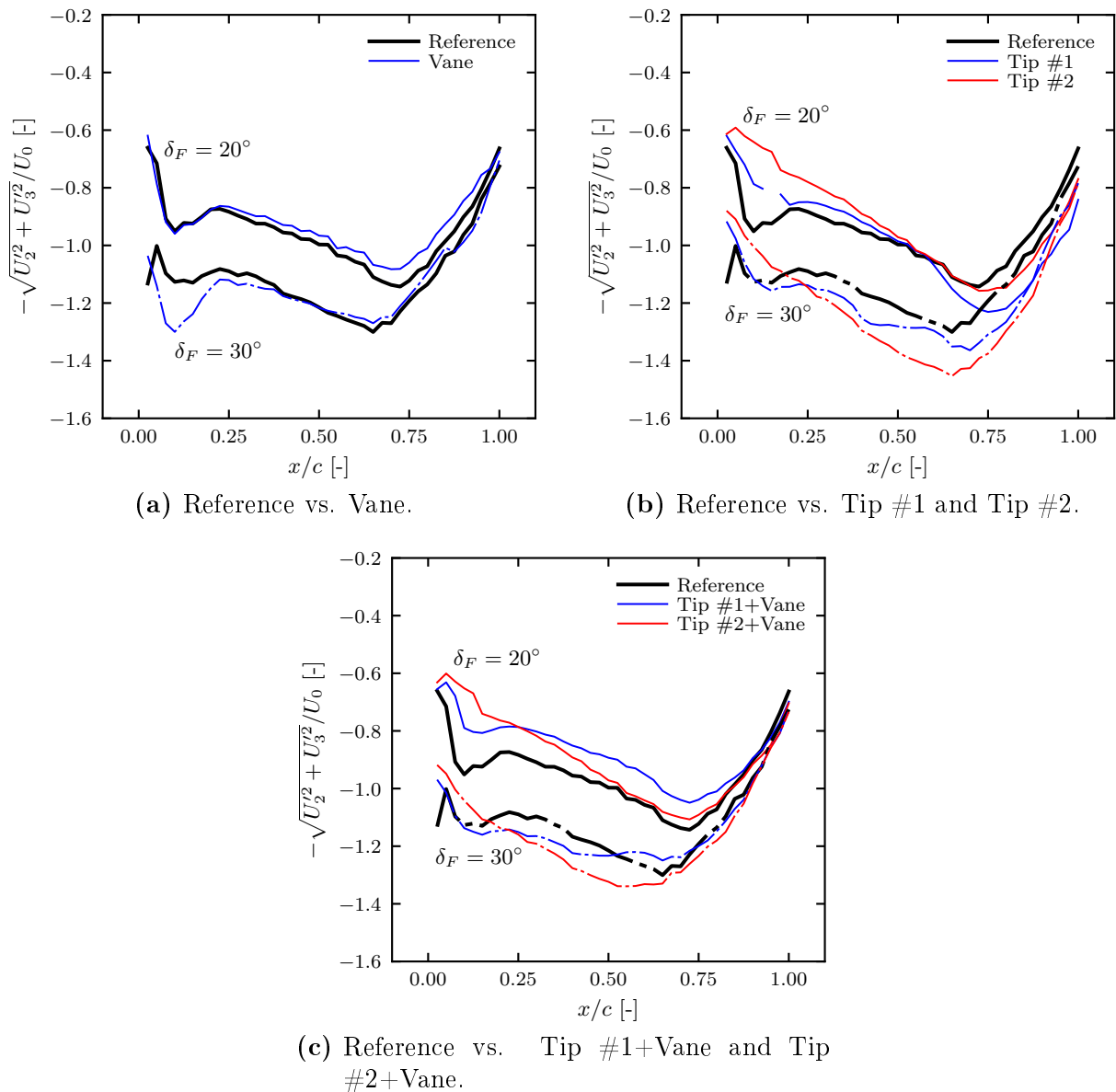


Figure 5.15.: Comparison of the normalized cross-flow velocity magnitude near the tip lower edge for two values of δ_F . The velocity vector components are projected onto a wing-fixed coordinate system.

has a disruptive effect on the main wing tip flow roll-up process which translates into a weaker vortex near the TE.

The cross-flow velocity for case "Reference + tip #2", in figure 5.15b, is characterized by a continuous and moderate increase at both angles up to $x/c \approx 0.7$. In the fore part, the flow is less accelerated, through the rounded edges. The maximum cross-flow magnitude is reached between $x/c = 0.6$ and $x/c = 0.8$, with values as much as 20% higher (at $\delta_F = 30^\circ$) compared to the reference case. Similar trends are reported by McAlister et al. [87]. The effect of "tip #1" on the cross-flow is to impede the smooth tip vortex development forcing the cross-flow characteristics to resemble those of the reference case. There is one exception, at $\delta_F = 20^\circ$ near the TE, a sudden velocity increase is observed. This is due to flow being forced out of "tip #1" cavity, an effect

which is more important the more the flow aligns with the wing's chord. Adding the vane, when the tip add-ons are installed, promotes lower cross-flow velocity in the FSE aft part at $\delta_F = 20^\circ$ (see figure 5.15c) as has been previously observed for the reference configuration without vane. For the case "Vane + tip #1", a different trend is observed and the cross-flow intensity is reduced over the whole chord length. This effect is not understood and requires further study. Interestingly, there is no local cross-flow velocity increase for configurations "tip #1+vane" and "tip #2+vane" near the main wing's LE compared to configurations "tip #1" and "tip #2". In those cases, the wing span (but not the vane's) was increased to 0.43 m, probably inhibiting an efficient interaction of the vane tip vortex with the wing tip flow field.

As was previously done in figure 5.8, the maximum cross-flow velocity at the tip lower edge is extracted from the flow measurements of figure 5.15. The results are given in figure 5.16, as a function of δ_F . Note that the results for the reference wing in figure 5.8 and 5.16 differ slightly as they were obtained in different measurement campaigns, two years apart. Nonetheless, the slope $du/d\delta_F$ can be considered the same. The results suggests two different groupings based on the value of $du/d\delta_F$. The cases Tip #1 and Tip #2 are associated with a larger slope i.e. $du/d\delta_F = 0.029$ and $du/d\delta_F = 0.033$ compared to the remaining test cases. The absolute value of u/U_0 at a fixed value of δ_F should not be overinterpreted as it is dependent on the exact position of the probe relative to the model, which is difficult to replicate for airfoils with different tips. Therefore, a meaningful comparison of the absolute levels is difficult. More important is the slope $du/d\delta_F$. For the reference wing, a smaller slope is expected, compared to Tip #1 and Tip #2, because of the discontinuity at the edges. For the cases with vane, the flatter lift polar, e.g. figure 5.14, could explain the smaller values of $du/d\delta_F$.

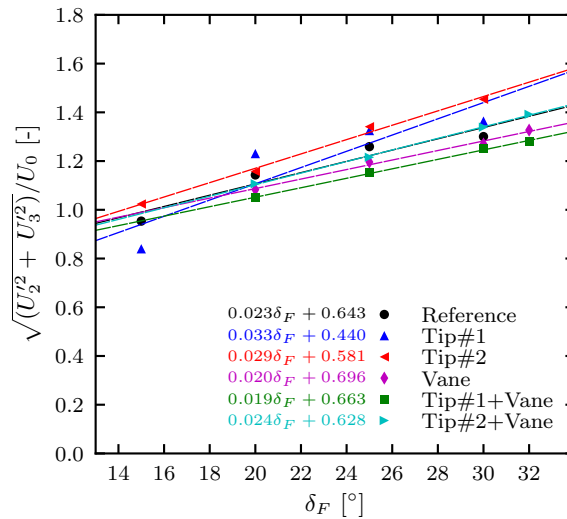


Figure 5.16.: Maximum value of the spanwise velocity magnitude vs. δ_F . Dashed line: linear regression.

5.5. Summary of findings

The results presented above support the hypothesis that low-frequency flap side-edge sound generation is related to unsteadiness of the merged tip vortex in the vicinity of the airfoil's aft part tip edges. This mechanism is characterized by the vortex diameter as a characteristic length scale and the pressure-side maximum cross-flow velocity, $u = U_c = \max(\sqrt{U_2'^2 + U_3'^2})$, as a measure of the vortex rotational velocity. High-frequency sound is mostly generated near the airfoil's mid-chord, in a region characterized by strong velocity gradients, and thus promoting important turbulent mixing, identified along the airfoils upper edge. It is characterized by the velocity $u = U_H = \sqrt{U_2'^2 + U_3'^2}$ measured at the vortex merging position (i.e. position $A(\delta_F)$ in figure 5.10) and the vortex dimension. Thereby we postulate that the increased turbulent mixing occurring due to the existence of the tip vortex and its interaction with the solid geometry is the dominant factor responsible for sound production.

For the reference wing the characteristic velocity scales for the pressure side and suction side flow fields are summarized in table 5.2, where $U_c = \max(\sqrt{U_2'^2 + U_3'^2})$ at the pressure side and $U_H = \sqrt{U_2'^2 + U_3'^2}$ at the merging position. Also included in table 5.2, are linear relationships for the complementary test cases. For these cases, as flow data are only available for the pressure side, only relations for U_c are given. In the following chapter, results from the acoustic investigations are presented and an attempt is made at representing the data using the parameters identified in the current chapter and listed in table 5.2.

Table 5.2.: Summary of all linear relationships derived above.

Case	U	vs. δ_F	vs. C_L	vs. Γ_1
Reference	U_c/U_0	$0.023\delta_F + 0.682$	$0.623C_L + 0.554$	$-0.033\Gamma_1 + 0.819$
Reference	U_H/U_0	$0.020\delta_F + 0.288$	$0.557C_L - 0.173$	$-0.030\Gamma_1 + 0.413$
Tip #1	U_c/U_0	$0.033\delta_F + 0.440$	-	-
Tip #2	U_c/U_0	$0.029\delta_F + 0.581$	-	-
Vane	U_c/U_0	$0.020\delta_F + 0.696$	-	-
Tip #1 + Vane	U_c/U_0	$0.019\delta_F + 0.663$	-	-
Tip #2 + Vane	U_c/U_0	$0.024\delta_F + 0.628$	-	-

6. Results of the Acoustic Investigations

In this section, the results of the acoustic investigations are presented and discussed. Focus is first put on both reference test cases defined in chapter 3 to reveal the baseline acoustic radiation characteristics and scaling behaviors. Classical scaling assumptions are tested and are found to provide only a limited amount of success. New scaling parameters, derived from the aerodynamic investigations presented in chapter 5, allow for a better representation of the acquired acoustic data. Further, exhaustive directivity measurements are presented and discussed. Next, results from the complementary experimental test cases are discussed to put the reference dataset in a broader perspective as well as to lend further support to the new data scaling premises.

When not otherwise mentioned, the notation f_c will be used to refer to one-third octave band center frequencies. For simplicity, the time-averaged value of the pressure fluctuations squared, i.e. $\overline{p'^2}$, will be written as p^2 . As we are performing measurements in the acoustic far-field, we have $a_\infty = \text{cst}$, $\rho_\infty = \text{cst}$ and the far field sound intensity is given by $I = \overline{p'v'} \simeq \overline{p'^2}/\rho_\infty a_\infty$.

6.1. Cantilever Wing Configurations

6.1.1. Source Maps, Noise Spectra and Scaling Parameters

Source maps for $f_c = 1.0$ kHz and $f_c = 3.15$ kHz at $\delta_F = 25^\circ$ and $\delta_F = 30^\circ$ for $U_0 = 60$ m/s ($M_0 = 0.18$), are presented in figures 6.1 and 6.2. The results were obtained using conventional beamforming (CB), with diagonal removal (DR), according to the description of chapter 4, with the large aperture phased microphone array installed below the model and at its side. The CB algorithm identifies, in all cases, a dominant source of noise at the FSE. As frequency increases, so does the resolution of the microphone array and therefore the source maps at $f_c = 3.15$ kHz reveal more details about the source distribution. Low-frequency noise predominantly occurs in a region near the tip trailing-edge corner. The source region moves upstream along the FSE with an increase in frequency. A behavior typical of FSE noise which suggests that the radiated sound's characteristic frequency is closely related to some dimension of the developing tip vortex system [54, 57, 82]. Varying the flap angle only has a marginal impact on the source distribution, while the effect of a change in free-stream velocity is not shown because it does not modify the source distributions and only promotes a broadband increase in radiated noise levels.

One also notes the existence of an almost isolated source region in the source maps, downstream of the tip TE, in figure 6.2 at $f_c = 3.15$ kHz (see also the results of appendix F). This feature does not exist in the contour plots of figure 6.1, where the phased microphone array is positioned to the side of the airfoil. This observation cannot be

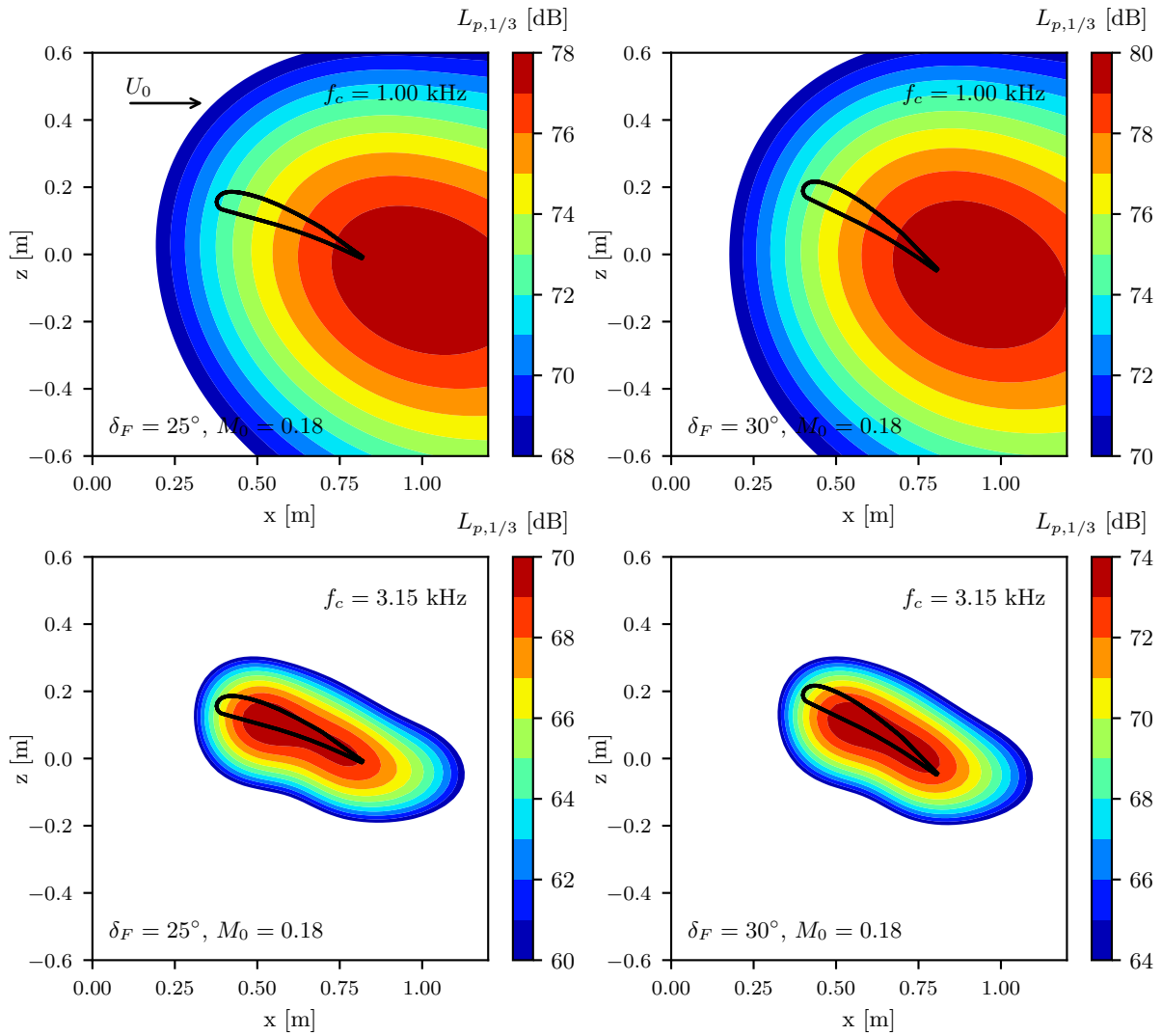


Figure 6.1.: Microphone array noise maps, side view, 1/3-octave band frequencies. $M_0 = 0.18$. The model is represented by the solid black line.

satisfactorily explained based on the available dataset. It could, however, suggest the existence of a source region above the wing, i.e. on the suction side, its sound field being diffracted about the TE before reaching the phased array microphones. Classical trailing-edge noise would be identified directly at the trailing-edge of the airfoil by the phased array and cannot, therefore, explain this observation. One also notices that the position along the tip where the highest SPLs are measured, at $f_c = 3.15$ kHz in figure 6.2 and 6.1 do not exactly match, giving some insights into the source directivity, which will be further discussed in section 6.1.6. Also, the source distribution measured at the side position spreads over a larger part of the tip, compared that measured below the airfoil. Once integrated over the whole of the source region, the radiated sound power towards the side will potentially be higher, e.g. section 6.1.6.

The frequency range in which FSE noise dominates is determined through comparison with measurements at a porous FSE. The porous FSE can achieve a broadband FSE noise reduction up to 15 dB and therefore is considered to almost eliminate the tip noise source. This occurs through a modification of the tip flow field, damping of turbulent velocity fluctuations and a pressure release near the wing tip [6, 8]. The comparison

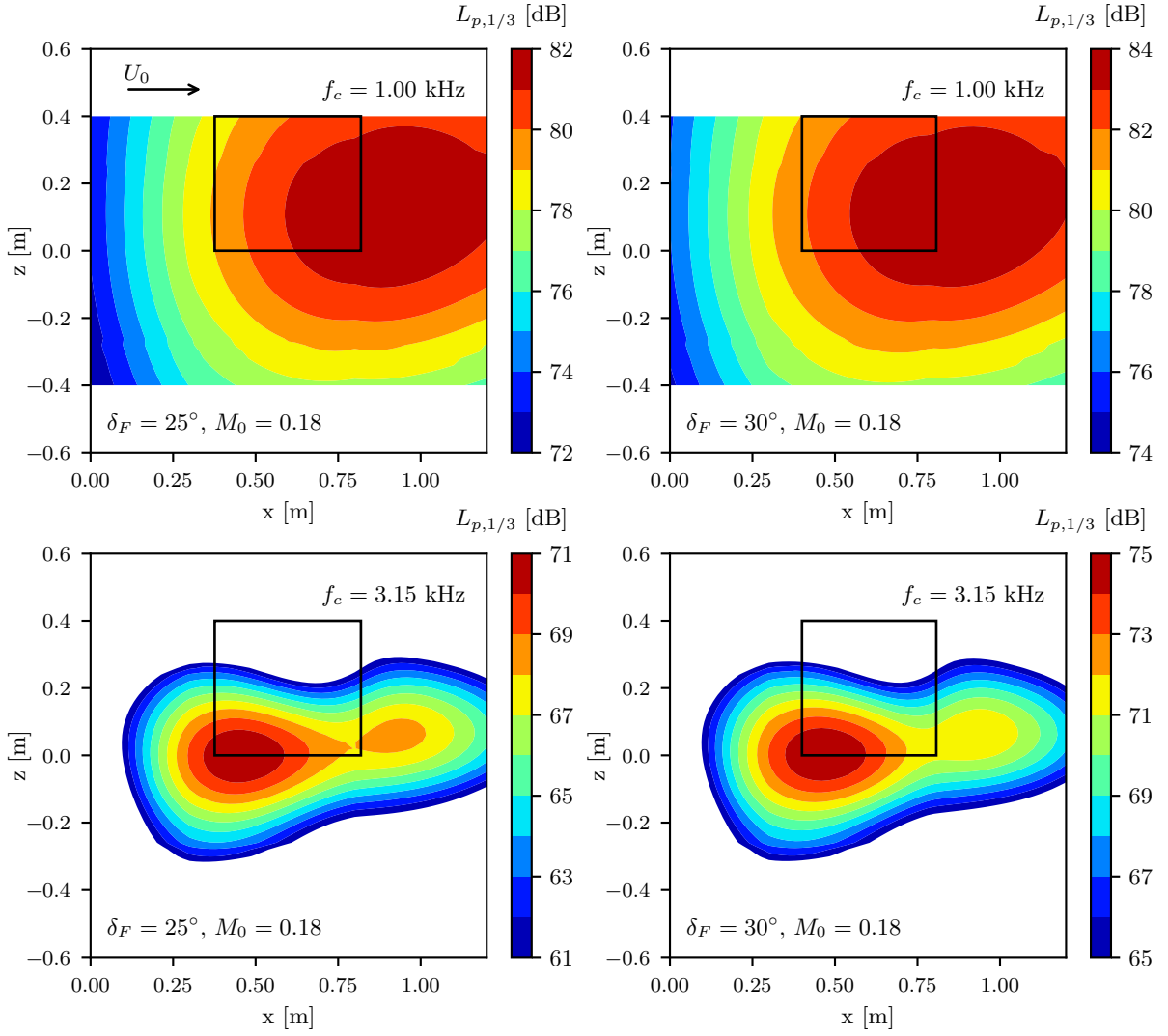


Figure 6.2.: Microphone array noise maps, bottom view, 1/3-octave band frequencies. $M_0 = 0.18$. The model is represented by the solid black line.

between measurements with the solid and porous tips is given in figure 6.3, for two flap settings and two radiation directions. The results show that FSE noise is dominant in the range $0.4 \text{ kHz} < f_c < 16 \text{ kHz}$. Above $f_c = 16 \text{ kHz}$, the porous tip produces excess high-frequency noise, a characteristic of the porous material used and not relevant for the baseline solid tip. Therefore, the above range is extended to $0.4 \text{ kHz} < f_c < 20 \text{ kHz}$ for the large aperture phased microphone array. Corresponding to a Strouhal number range of $3 < St_0 < 158$ (based on the model chord and $U_0 = 60 \text{ m/s}$). Data from the small aperture phased array are considered valid over the range $0.8 \text{ kHz} < f_c < 20 \text{ kHz}$, due to the occurrence of a spurious tone at $f_c = 0.63 \text{ kHz}$. Integrated spectra from both the small and large microphone array measurements are found to agree well over their common frequency range even though their respective point spread functions indicate important loss in spatial resolution at low frequencies (see chapter 4) below $f_c \approx 0.8 \text{ kHz}$ for the large aperture array and below $f_c \approx 2.0 \text{ kHz}$ for the small aperture array. The similarity of the FSE spectra from both arrays at low frequencies is a further confirmation that spurious source contamination is not important.

The impact of a change in M_0 and δ_F on the noise generation is presented in figures 6.4 and 6.5 for both array positions. An increase in upstream velocity leads to a monotonic and broadband increase in noise levels. Also, the overall shape of the spectra does not change noticeably.

A common approach found in the literature to scale the noise spectra is to relate the scales of the source of noise to the free-stream velocity and a characteristic geometric dimension of the model. Usually the free-stream velocity and the wing's chord length (c) or wing's maximum thickness (d) are chosen [19, 21, 55, 82]. These parameters are obviously not dependent on δ_F and therefore can only represent broadband changes in noise radiation due to variations of the free-stream velocity. Also the free-stream velocity, being a global parameter, is not able to account for local changes in tip geometry as well as wing profile. The main advantage of this approach lies in the fact that both parameters can be easily determined and quantified. Scaling the data of figures 6.4 and 6.5 using $p^2 \propto U_0^n$ with $n = 5.5$ and $l = c$, one obtains the results presented in figures 6.6a,b and 6.7a,b. Where the ordinate variable is $L_n = L_{p,1/3} - 10 \cdot n \cdot \log(U/100) + 10 \log(l^2/R^2)$, where $U = U_0$ stands for a characteristic velocity and $R = 1$ m for the reference source-observer distance. This choice of velocity and length scales only provides a good amount of success in scaling the velocity dependency of the radiated noise. Changes due to the flap deployment are not well represented.

Guo [55] and Brooks and Humphreys Jr. [21] first proposed using a local tip velocity instead of the free-stream velocity to scale the acoustic data. They proposed using the flow velocity at the tip lower edge. The data of figures 6.4 and 6.5 are scaled assuming $p^2 \propto U_c^n$ with $n = 5.5$ and the wing's chord $l = c$. U_c will be referred to as *cross-flow velocity*. It is defined as the maximum value of $U_c = \max(\sqrt{U_2^2 + U_3^2})$, along the wing's tip lower edge. It's value as a function of δ_F was obtained in section 5.4.

Scaled spectra using these premises are plotted in figures 6.6c,d and 6.7c,d. The Mach number dependency appears to be well represented by the U_c proportionality assumption, as well as with U_0 . This result emphasizes the linear relationship between U_c and U_0 for $\delta_F = cst$. One notes that, because U_c is a function of δ_F , the effect of flap deflection is better represented and that a good collapse of the spectra can be achieved in the low-frequency range. Changes in high-frequency noise are not well represented. Increasing the power exponent from $n = 5.5$ to $n = 6.5$ does not provide significantly better results. The same conclusion holds for both radiation directions.

From the results of the first scaling attempts, using more fined-grained assumptions appears to be necessary. To achieve this goal, the multi-scale approach, first put forward formally by Guo [54], is further investigated and applied to the present database. Two different length and velocity scales are identified based on the results of the flow investigations presented in chapter 5. The low frequency part of the spectra is assumed to be generated in the aft part of the tip, through interaction of the tip vortex with the airfoil's edges, and is characterized by $u = U_c$ and $l = 0.16c$ as velocity and length scales. The characteristic source scales corresponding to the high-frequency noise radiation are $u = U_H$ and $l = 0.04c$. The flow measurements presented in chapter 5 do not provide enough data for a quantification of the dependency of l on δ_F . Therefore, the above constant length scale values are defined, under consideration of the acquired flow data, e.g. table 5.1. Normalized spectra are shown in figures 6.6e,f and 6.7e,f.

In all four figures, two different scalings are shown, a high- and a low-frequency scaling. The velocity dependency is found to be best represented using $u = U_c$ with $n = 5.5$ as velocity scale at low frequency and using $u = U_H$ and $n = 6.5$ for the high frequencies (see figures 6.6e and 6.7e). The same conclusions also hold for variations in δ_F (see figures 6.6f and 6.7f). See table 5.2 for the characteristic velocity relations. Based on the above power law exponents, the results suggest a source mechanism, at low frequencies, of the classical edge-scattering type [40] and a Curle-like dipole at high-frequencies [29].

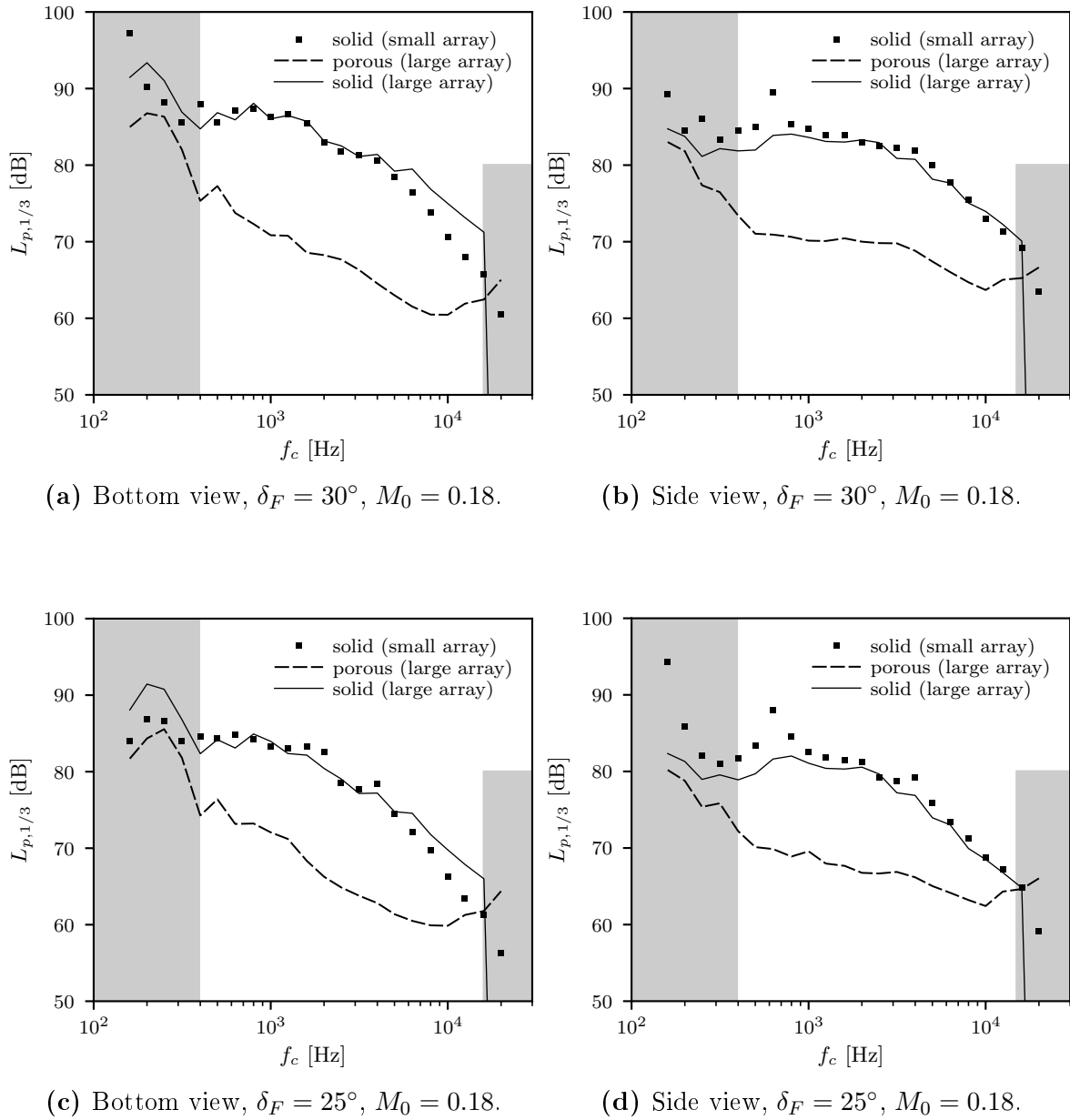


Figure 6.3.: Solid vs. porous FSE noise, comparison of small and large array results. 1/3-octave band integrated SPL spectra. Bottom view power integration performed over the range $0.2 \text{ m} \leq x \leq 1.0 \text{ m}$ and $-0.2 \text{ m} \leq y \leq 0.2 \text{ m}$. Side view power integration performed over the range $0.2 \text{ m} \leq x \leq 1.0 \text{ m}$ and $-0.6 \text{ m} \leq z \leq 0.6 \text{ m}$. The shaded regions indicate the frequency limits of the measurements.

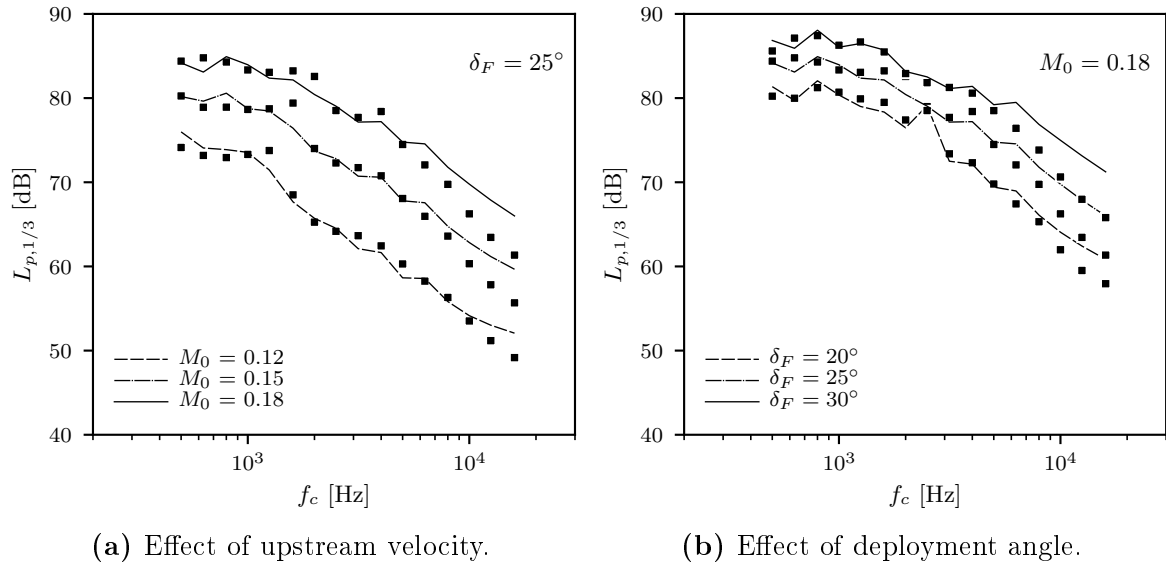


Figure 6.4.: Integrated noise spectra, comparison of small aperture and large aperture arrays. Bottom view, 1/3-octave band frequencies. Symbols : Small aperture array. Lines : large aperture array.

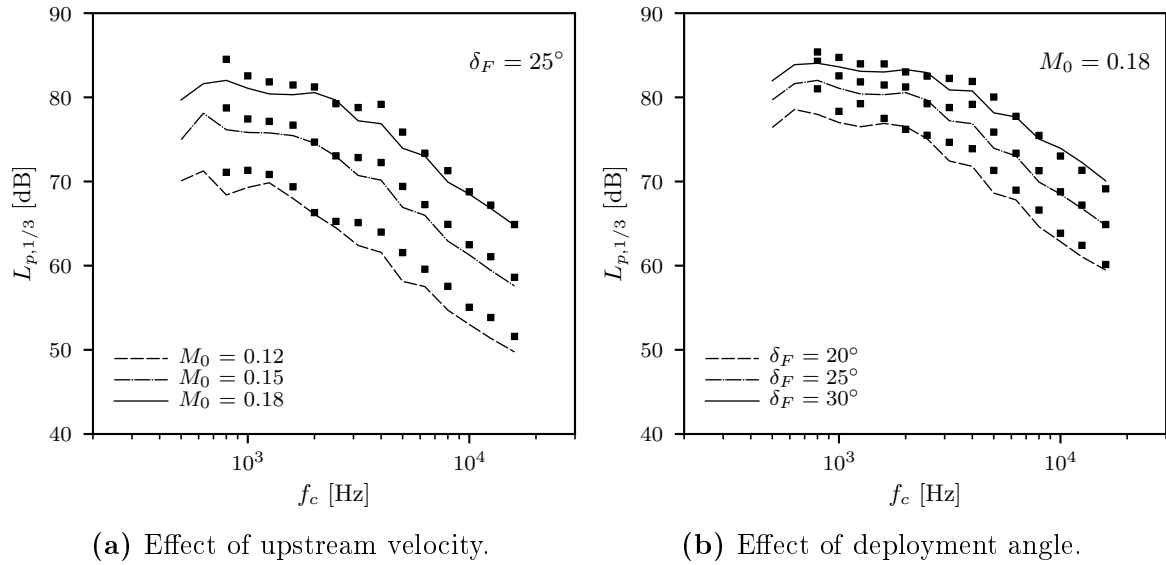
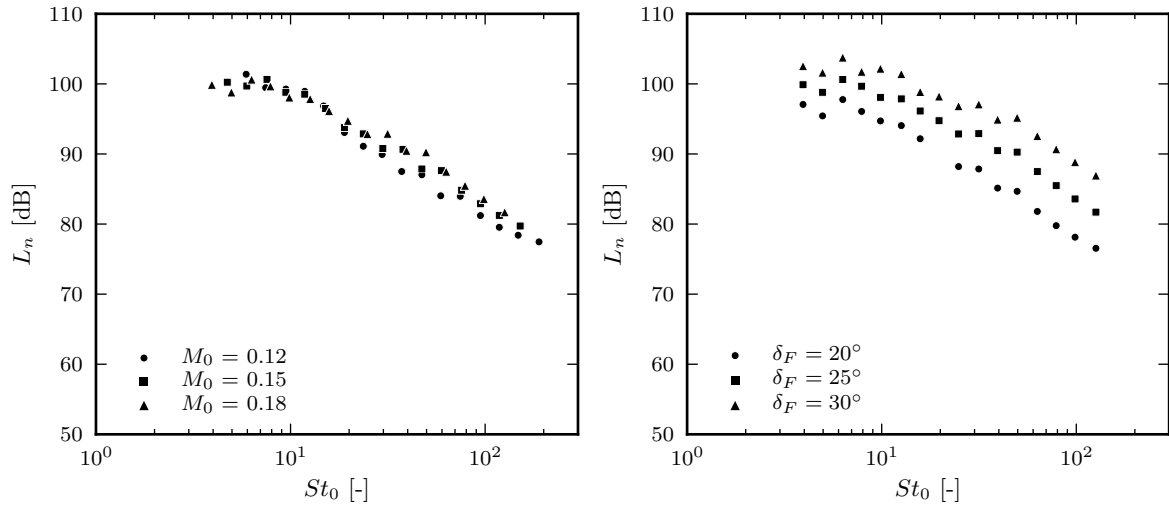
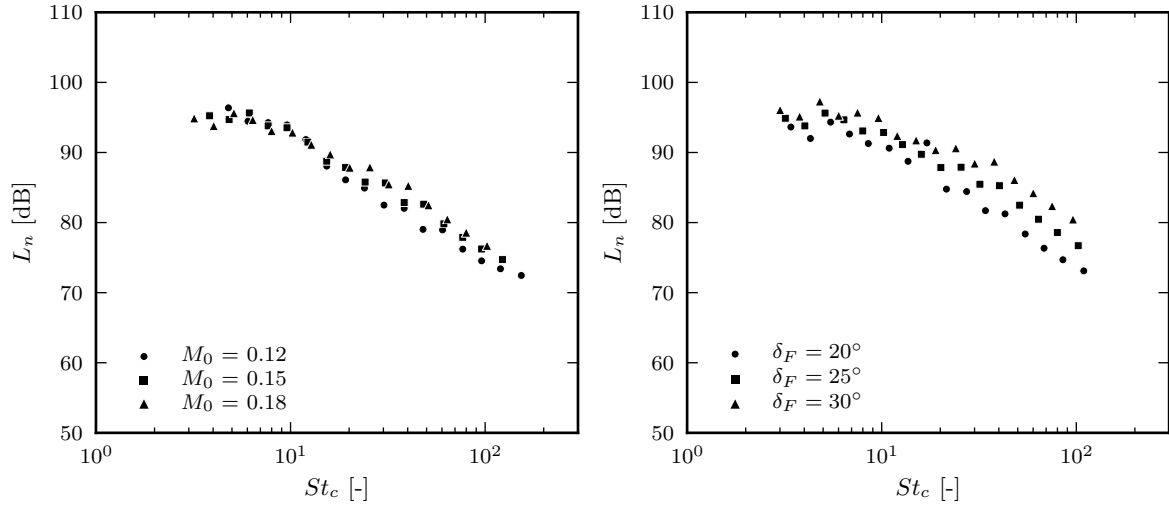


Figure 6.5.: Integrated noise spectra, comparison of small aperture and large aperture arrays. Side view, 1/3-octave band frequencies. Symbols : Small aperture array. Lines : large aperture array.



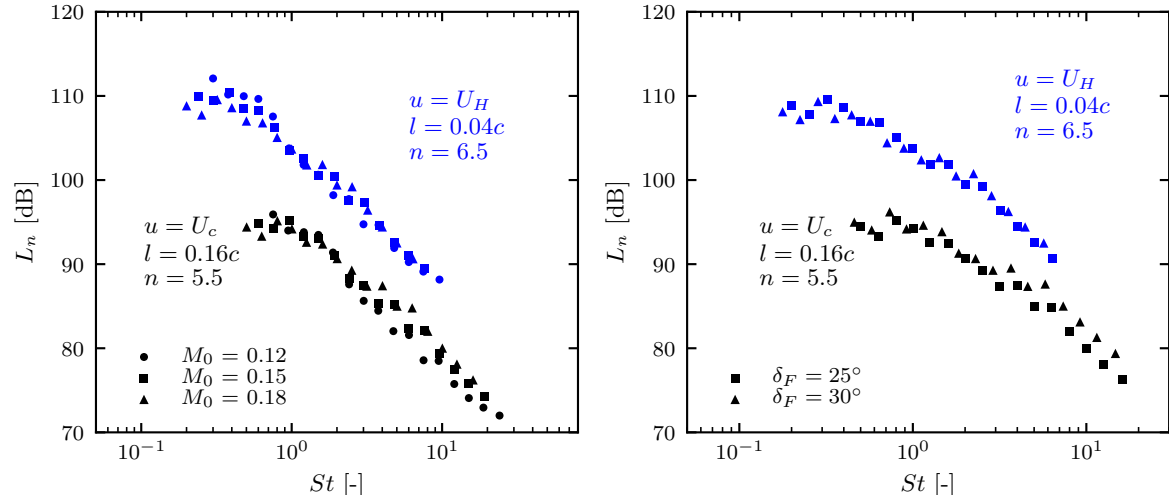
(a) $u = U_0, l = c, n = 5.5, \delta_F = 25^\circ$

(b) $u = U_0, l = c, n = 5.5, M_0 = 0.18$



(c) $u = U_c, l = c, n = 5.5, \delta_F = 25^\circ$

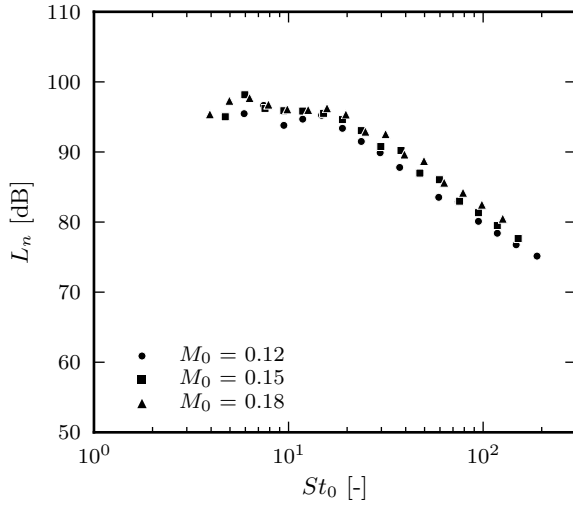
(d) $u = U_c, l = c, n = 5.5, M_0 = 0.18$



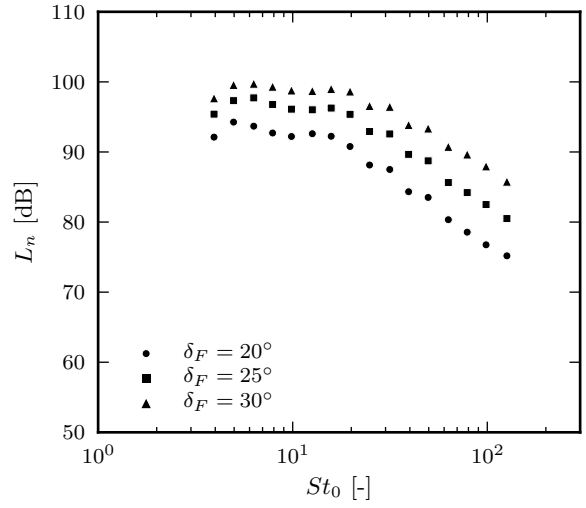
(e) $\delta_F = 25^\circ$

(f) $M_0 = 0.18$

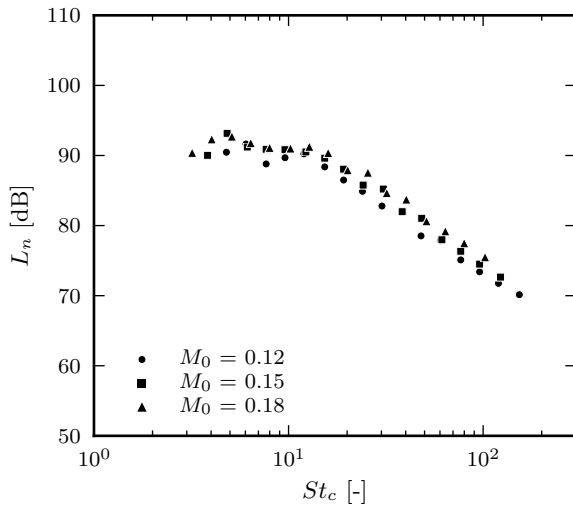
Figure 6.6.: Scaled integrated noise spectra. Bottom view, 1/3-octave band frequencies.



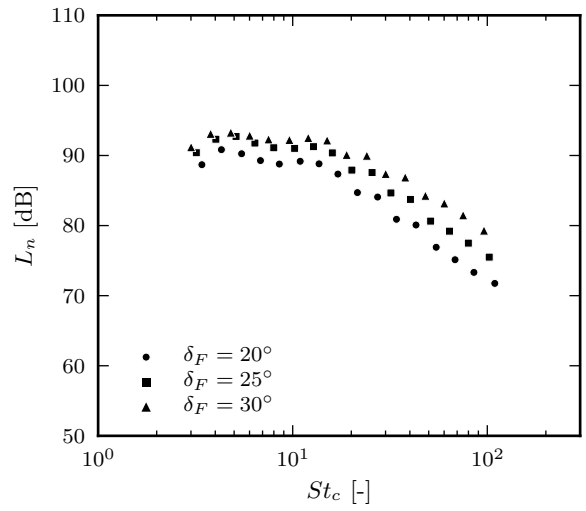
(a) $u = U_0, l = c, n = 5.5, \delta_F = 25^\circ$



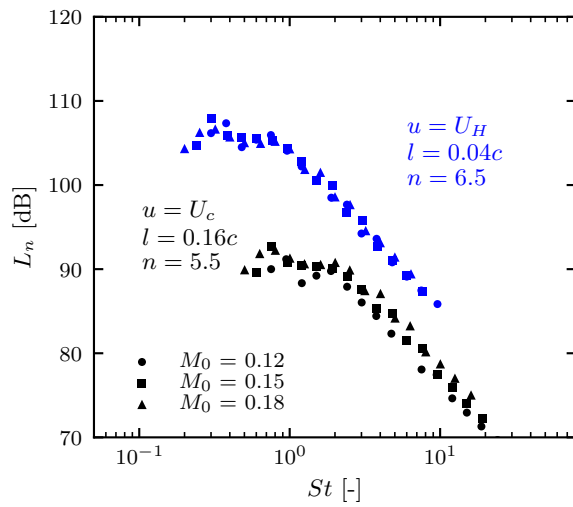
(b) $u = U_0, l = c, n = 5.5, M_0 = 0.18$



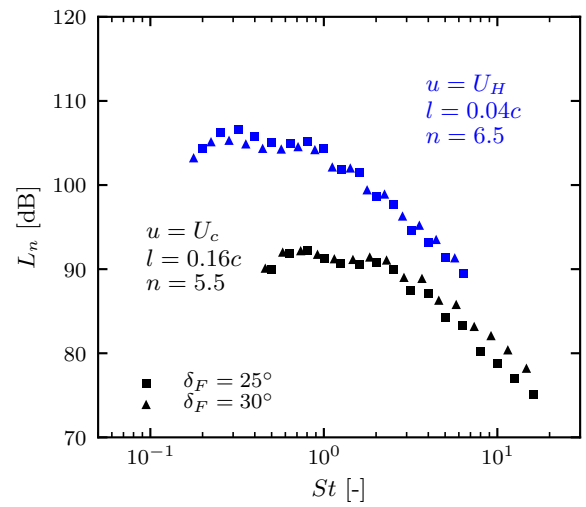
(c) $u = U_c, l = c, n = 5.5, \delta_F = 25^\circ$



(d) $u = U_c, l = c, n = 5.5, M_0 = 0.18$



(e) $\delta_F = 25^\circ$



(f) $M_0 = 0.18$

Figure 6.7.: Scaled integrated noise spectra. Side view, 1/3-octave band frequencies.

6.1.2. Effect of Model Scale

The impact of the wind tunnel model scale was studied in the NWB low-speed anechoic facility using an 1:1 (full-scale) cantilever flap. This flap model is an actual component of an original A319 wing which was unmounted and adapted for use in the wind tunnel environment. Further details about the setup are provided in chapter 3. Phased array source maps are given in appendix F.

The results of the acoustic investigations for the baseline configuration are given in figure 6.8a-b. Results for the raked tip are provided in figures c-d. In each figure, the spectra are scaled according to the multi-scale premises discussed in the previous section. In each figure, scaled spectra from the reference cantilever wing case (scale 1:1.43) are also plotted for comparison purposes. The comparison reveals a very good agreement between the results from both test cases. The good agreement of the absolute scaled spectral levels in figure 6.8 is the result of a calibration relative to the reference test case. Use is made of an effective angle of attack $+2^\circ$ larger than the actual geometrical angle set in the AWB experiment. This means that the flap model in the NWB experiment generates slightly more lift when set at a given angle of attack compared to the AWB experiment. This adjustment is considered as a wind tunnel correction which accounts for the different test environments. Since no static pressure measurements are available in the NWB experiment, the angle of attack correction is derived through a matching of the acoustic data between both tunnels. A $+2^\circ$ increment appears reasonable, as the NWB model has a slightly larger aspect ratio of 1.053 vs. 0.846 for the AWB model. NWB's test section area is also considerably larger, i.e. 9.1 m^2 vs. 0.96 m^2 , thus wind tunnel boundary effects, leading to lift reduction, are expected to be less important in NWB. Note, however, that the geometrical δ_F are given in figure 6.8. Larger discrepancies are observed at the low-frequency end of the spectrum. Those deviations can be explained by the lower resolution of the AWB phased array compared to that of the NWB and also to a smaller aspect ratio in the AWB.

The results of figure 6.8a-b support the hypothesis that the AWB results are representative of the full-scale configuration. Further, the spectral scaling premises provide a good collapse of the measurements similar to previous attempts at the AWB database. Therefore, the scaling parameters derived from the AWB measurements can be assumed to be equally valid in the full-scale case.

6.1.3. Effect of Tip Raking

The effect of a raking of the tip into the flow was also investigated at the full-scale wing in the NWB. The results of the acoustic investigations using the phased array are given in figure 6.8c-d. The spectra in each figure are scaled according to the multi-scale premises discussed in the previous section. Scaling is done using the exact same parameters used to obtain the results of figure 6.6e,f.

Raking the flap tip into the flow leads to an important change in spectral shape, departing from the general results for the reference wing, i.e. with a streamwise aligned flat tip face (e.g. figure 6.8a-b). The levels of the low-frequency part of the scaled spectra are reduced, by approximately 3 dB to 5 dB. At the same time, the high-frequency part of the spectra is slightly increased by about 2 dB compared to the reference case. The

relative weighting of the two mechanisms postulated in the scaling approach appears to have changed [54].

The low-frequency scaling provides the best collapse of the experimental data for both changes in U_0 and δ_F . The high-frequency scaling does also provide a good amount of success in representing changes in upstream velocity, however, the poor scaling at high frequencies in figure 6.8d suggests a reduced dependency on δ_F of the radiated noise for the raked tip flap compared to the baseline flap. The scaling relationship is too strong and over-compensates the impact of a change in δ_F .

This change in behavior could be related to a different tip vortex path compared to the reference tip case. Raking the tip into the flow leads to an earlier movement of the tip vortex to the upper surface therefore reducing the effective length over which a direct interaction of the developing vortex with the tip edges occurs [87], e.g. figure 6.9. The radiated noise is no longer a strong function of δ_F , e.g. figure 6.10, at least not as strong as for the baseline case, and cannot be represented by the velocity and length scales proportionality relationships assumed previously. The source of low-frequency noise is mostly located near the tip TE and is therefore strongly affected by a raking of the tip. Its strength is reduced as the vortex path moves away from the tip edges.

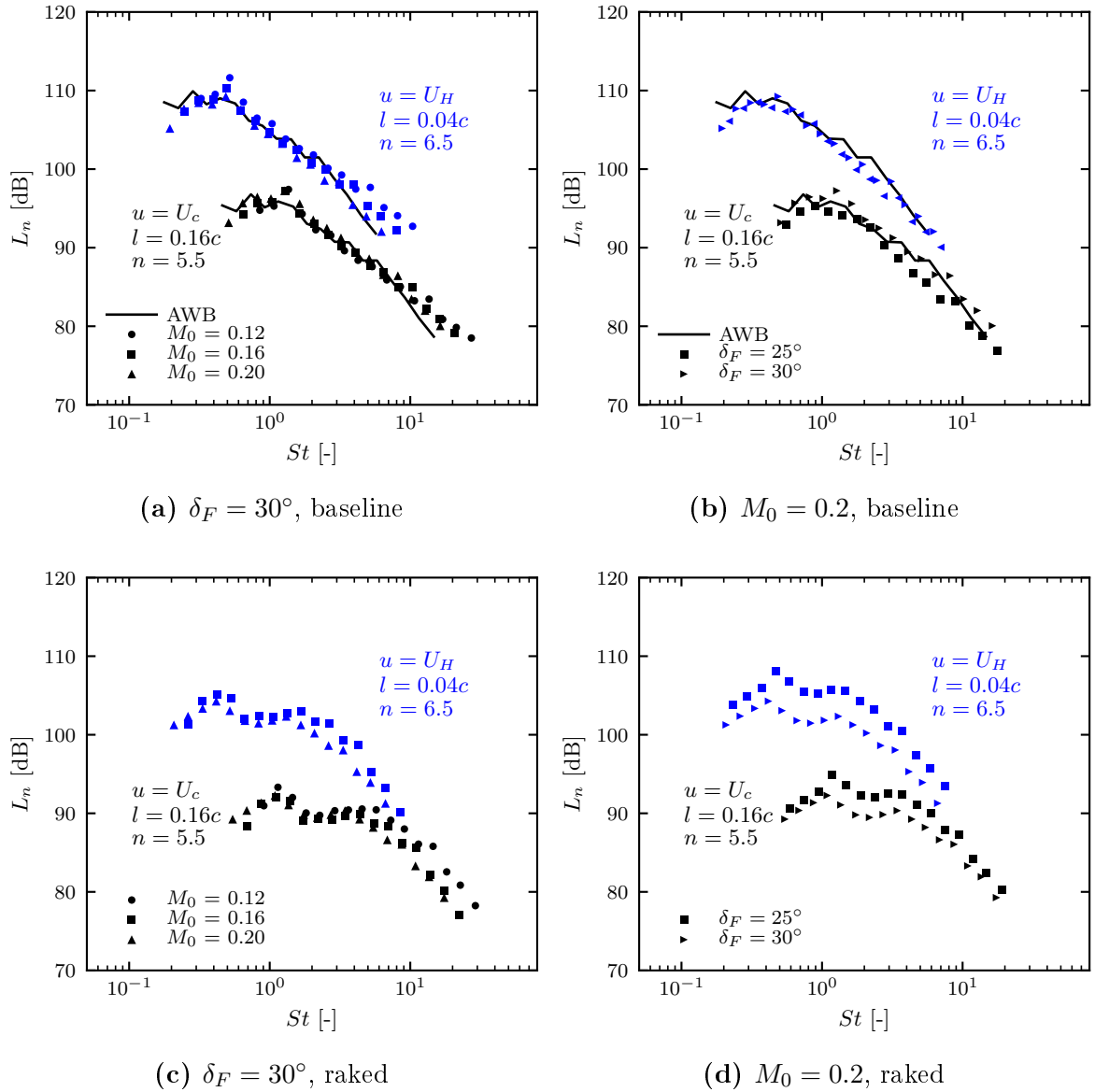


Figure 6.8.: Large scale cantilever flap model. Scaled integrated noise spectra. Bottom view, 1/3-octave band frequencies. δ_F increased by $+2^\circ$ when scaling the full-scale model data compared to the reference cantilever wing data. Geometrical δ_F given in the figures. Solid line indicates scaled results for the reference cantilever wing at $\delta_F = 25^\circ$ and $M_0 = 0.18$.

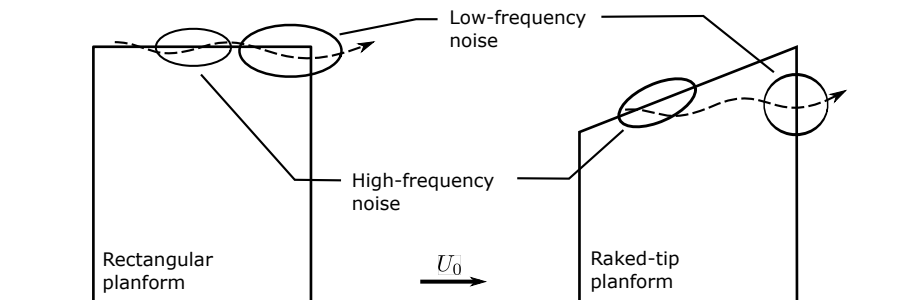


Figure 6.9.: Schematic representation of the tip vortex path on a rectangular and a raked-tip planform according to [87]

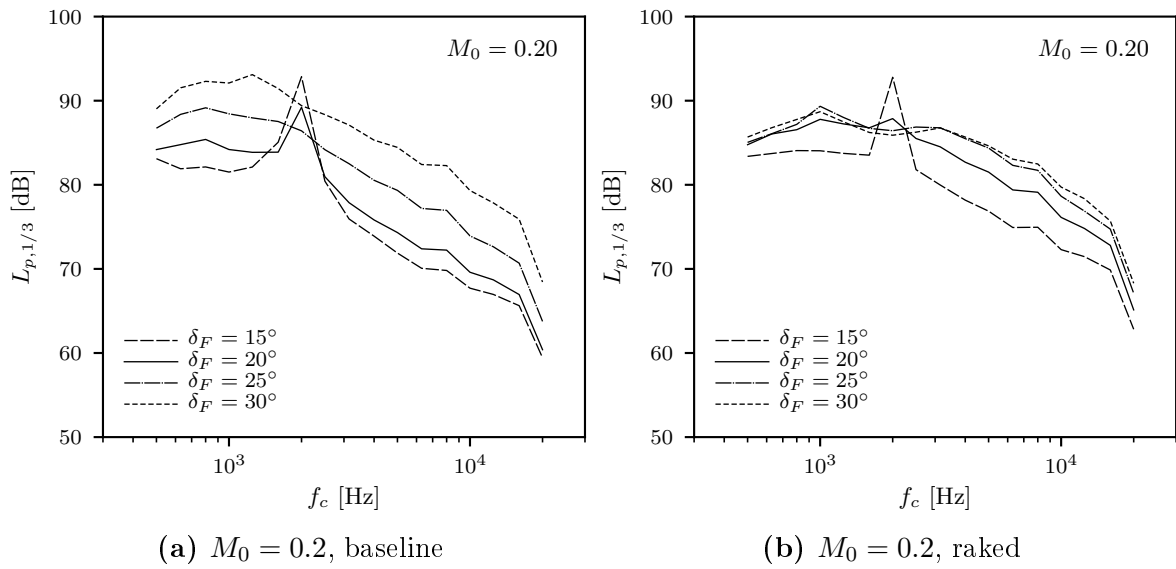


Figure 6.10.: Large scale cantilever flap model. Effect of δ_F , baseline vs. raked tip. Integrated noise spectra. Bottom view, 1/3-octave band frequencies.

6.1.4. Effect of Tip Geometry Variations and LE Vane Add-On

The effect of the add-ons is summarized in figures 6.11 and 6.12. Exhaustive results on the effects of free-stream velocity (U_0) and wing angle as well as data scaling, can be found in appendix C and D. They are not provided here as the scaling assumptions discussed above are found to provide an equally good representation of the results, both for the fly-over and side-line positions.

In figures 6.11 and 6.12, the relative noise impact of the LE vane and of the FSE tip add-ons is presented, as a function of wing angle and for $M_0 = 0.18$. The baseline configuration (wing without add-on) is used as a reference for the comparison. A positive $\Delta L_{p,1/3}$ value implies a noise increase while a negative one implies a noise decrease compared with the baseline configuration.

Effect of the Tip Geometry The effect of a change in flap tip geometry is displayed in figure 6.11, in terms of relative sound pressure levels, i.e. compared to the radiation of the reference flap tip. When Tip #1 or Tip #2 are installed, a noise increase of order 3 dB to 9 dB is measured below 3 kHz for the fly-over radiation direction. For $f_c > 3$ kHz, a noise reduction ranging between 2 dB to 7 dB is observed. A distinctive broadband spectral maximum is observed in the frequency range $1.0 \text{ kHz} < f_c < 3 \text{ kHz}$ irrespective of the tip add-on. As discussed in the previous section, the smooth edges of Tip #1 and #2 allow the tip vortex to develop in a cleaner fashion and an unsteady wandering of the separation line along the chord promoting significantly higher tangential and axial core velocities compared to a flat-tip wing as was found in chapter 5 and in [87]. Moreover, the vortex core size is smaller in comparison to the reference case [87]. Therefore, higher broadband FSE noise levels as well as a slight peak frequency increase, compared to the reference airfoil, are expected. Sharp edges, on the other hand, promote the formation of a complex multiple-vortex flow field near the tip [45, 50], with a corresponding increase in high-frequency noise levels. In figure 6.11, at 2.0-2.5 kHz, a quasi-tonal component can be identified for Tip #1 at all δ_F . It most probably originates from the tip cavity as is suggested by the microphone array data, where a strong noise source is identified near $x/c = 0.5$, e.g. appendix D.

From the results of figure 6.11 and 6.12, the addition of Tip #1 and #2 leads to very similar maximum noise increases of order 3 to 9 dB. The side line relative noise radiation is generally slightly lower. There is also only a very weak dependency of the relative noise levels on the wing's deflection angle for the sideline radiation direction. It is interesting to note that even though both add-ons display very similar noise spectra, their corresponding source maps do have very different characteristics (e.g. appendix D). While Tip #1 promotes a strong low-frequency noise radiation at about $x/c = 0.5$, i.e. inside the tip's cavity, both towards the ground and the side line direction, Tip #2 radiates mostly from the TE corner.

Effect of the LE Vane In figure 6.11 and 6.12, the addition of a LE vane provides a broadband noise reduction of order 2 dB - 4 dB below about $f_c = 2$ kHz. This effect can be explained through a lost in wing's overall circulation, in agreement with the discussion of chapter 5 on the flow characteristics.

The high-frequency part of the spectrum remains almost unaffected by the LE vane for the reference configuration and Tip #1, e.g. figures 6.11 and 6.12, except for the occurrence of a quasi-tonal component at $f_c = 12.5$ kHz. Its origin is most probably due to bluntness noise occurring near the vane tip TE (see figures D.1 and D.2) and amplified under the influence of the vane tip vortex. Bluntness TE noise occurs for $St \approx 0.2$ [17]; taking $l = 0.001$ mm (vane's TE thickness) and a free-stream velocity of $U_0 = 60$ m/s, one gets a sound frequency of $f_c = 12.0$ kHz. Moreover, its radiation pattern has a dipole-like character, and therefore appears reduced from the sideline, and its peak levels are independent of the selected tip add-on. This quasi-tonal source is a dominant spectral feature only at low angles and appears to be hidden by the higher broadband noise levels at $\delta_F = 30^\circ$. The combination of Tip #2 and the LE vane is more beneficial, providing a broadband noise reduction in the frequency range $1 \text{ kHz} < f_c < 9 \text{ kHz}$ (up to 10 dB at $f_c = 8$ kHz). The same trend is observed for the sideline radiation levels, with a maximum noise reduction of order 5 dB in the mid-frequency range.

The high-frequency (broadband) part of the spectrum is strongly dependent on the geometrical features of each configuration. The observed high-frequency quasi-tonal noise increase due to the LE vane is a feature which would need further investigations to evaluate its relevance for the full-scale aircraft in landing configuration.

Summary of Findings The major findings regarding the noise impact of each configuration modification (relative to the reference configuration) can be summarized as follows:

- 1) Tip #1 and #2 cause an increase in low- to mid-frequency noise levels, with a maximum around 1.25 kHz, and a reduction in mid- to high-frequency noise. The noise increase is a direct consequence of the smooth tip edges of Tip #1 and Tip #2.
- 2) The LE vane alone provides only slight low- to mid-frequency noise reduction and no significant high-frequency noise changes (quasi-tonal noise at 12.5 kHz excluded).
- 3) At $f_c = 2.5$ kHz, Tip #1 generates a strong tonal component at about $x/c = 0.4$, through flow disturbance in its tip cavity.
- 4) At $f_c = 12.5$ kHz vane TE bluntness noise (dipole radiation character) is suspected to lead to a large noise increase for all configurations at low angles of attack.

With the exception of item 2, the above observations equally hold for both the fly-over and sideline radiation directions.

The impact of the LE vane cannot be incorporated in a modelling effort as the database is still too limited. The above analysis only provides first qualitative insights in the role played by the LE vane. Still the results suggest that, attempting a low frequency prediction for a flap equipped with a LE vane, without accounting for it in the modelling, will result in slightly overestimated output noise levels.

Scaling Laws The effectiveness of the scaling laws discussed above is found to hold, with a similar level of success, for the modified tips as well as for the vane add-ons. Exhaustive results are provided in appendix C.

Directivity For the configurations with Vane, Tip #1+Vane and Tip #2+Vane, a forward arc dominant radiation is measured at $f_c = 12.5$ kHz, in agreement with the

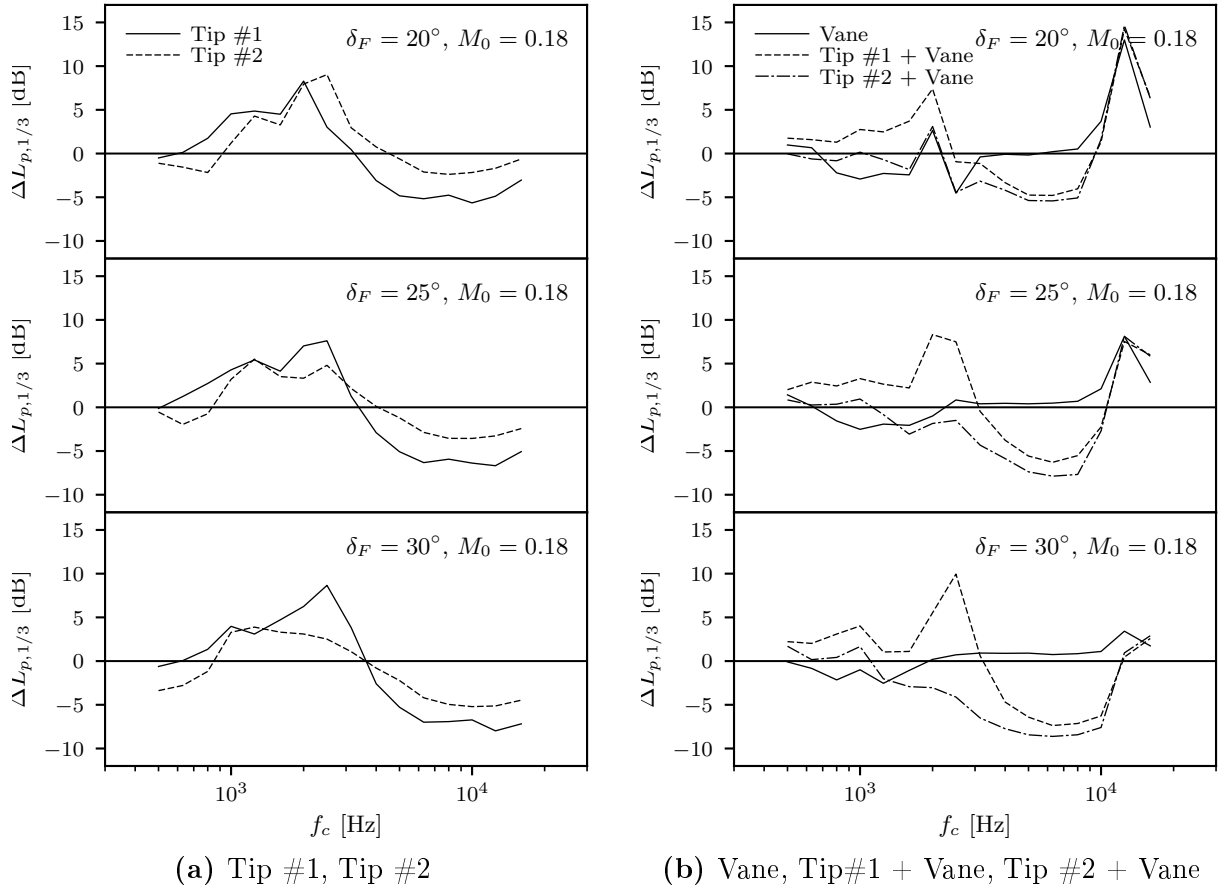


Figure 6.11.: Relative noise impact of the different tip add-ons. Noise spectra measured with the phased array for various flap deflections. $M_0 = 0.18$. Reference spectrum: baseline configuration. Fly-over measurement position, i.e. $\varphi_x = 90^\circ$, $\varphi_y = 0^\circ$, e.g. figure 4.1.

bluntness noise mechanism discussed above. Otherwise, the fly-over noise directivity is uniform and almost symmetrical about $\varphi_y = 0^\circ$. Configuration Tip #1 displays a forward arc maximum at $f_c = 2.5$ kHz, related to the cavity resonance phenomenon discussed previously. Otherwise its noise directivity has a rear-arc radiation maximum $\varphi_x > 90^\circ$. The same can be concluded for configurations Reference and Tip #2 over the whole frequency range.

The sideline radiation features a maximum in directivity at $\varphi_y \approx 20^\circ$ for all configurations, with only a weak dependency on δ_F , e.g. figures E.4 and E.6. Exhaustive far-field noise directivity results for all tested configurations are provided in appendix E.

6.1.5. Effect of Profile Shape

The impact of a variation in airfoil profile was studied using an airfoil with DU-96 section and an airfoil with a Clark-Y section. Results from the acoustic investigations at the Clark-Y wing with a flat tip are given in figure 6.13a and 6.13b. In figure 6.13c and 6.13d, results for the case with round tip are presented. In all four figures, the spectra are scaled using the multi-scale premises discussed above; see table 5.2 for reference. For both tips, the scaling approach is found to provide a good collapse of the measured data i.e.

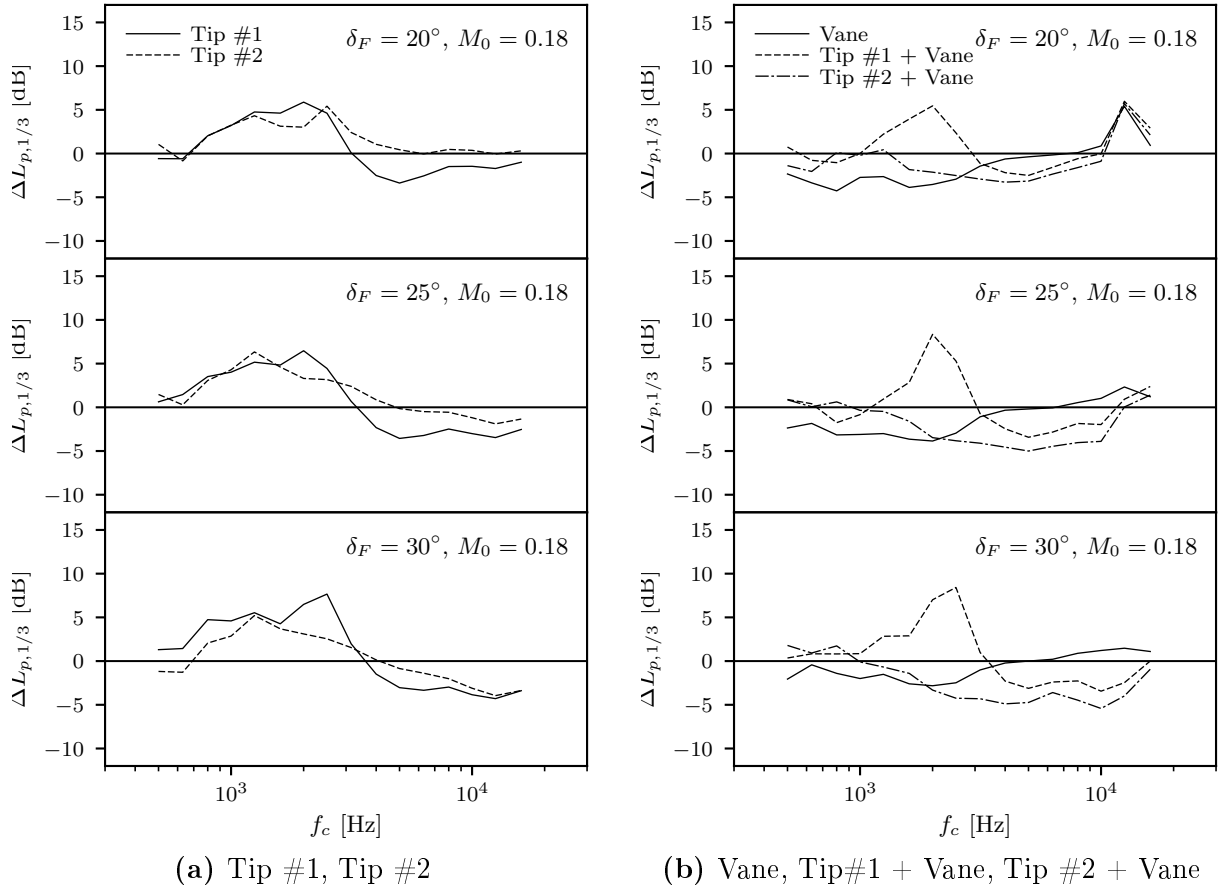


Figure 6.12.: Relative noise impact of the different add-ons ($\Delta L_{p,1/3}$ dB). Noise spectra measured with the phased array for various flap deflections. $M_0 = 0.18$. Reference spectrum: baseline configuration. Side-line measurement position, i.e. $\varphi_x = 90^\circ$, $\varphi_y = 90^\circ$, e.g. figure 4.1.

comparable to the previous results. One notices the clear shape difference between the flat- and round-tip spectra. The former being more flat in the mid-frequency range with rapid low- and high-frequency roll-offs, similar to the results obtained for the reference wing. The latter has a rounder shape with a distinctive mid-frequency maximum. A similar spectral shape was already observed for the reference wing with a round-edge tip (e.g. appendix C).

The DU-96 airfoil was tested only with a flat tip. The results of the investigations are presented in figure 6.14 in a scaled format, using the usual multi-scale premises. Again an excellent collapse of the data can be achieved using the low-frequency scaling parameters for both variations in U_0 and δ_F . The high-frequency scaling does not provide a similar data collapse for variations in δ_F , while it does provide a good scaling of the effect of variation in U_0 . Thus, in the δ_F range considered here, FSE noise is only a weak function of δ_F . The spectra have a shape which is typical for wings with smooth-edge tips, probably due to the more important thickness of the DU-96 wing. It is hypothesized that for thick profiles an interaction between both tip vortices is delayed proportional to the profile thickness, therefore reducing high-frequency noise production, which results from turbulent mixing of the tip vortices. Also, scaled spectra (see figure 6.14) display

a maximum at $St = 3$, which is indicative of a wrong relationship between the velocity and length scales chosen as characteristic of the tip vortex. A reduction in characteristic length scale, as is to be expected through a delayed tip vortex merging, would allow for a shift of the spectral maximum to $St = 1$. More investigations would be needed to clarify this aspect and evaluate the general validity of the scaling assumptions for this class of airfoils.

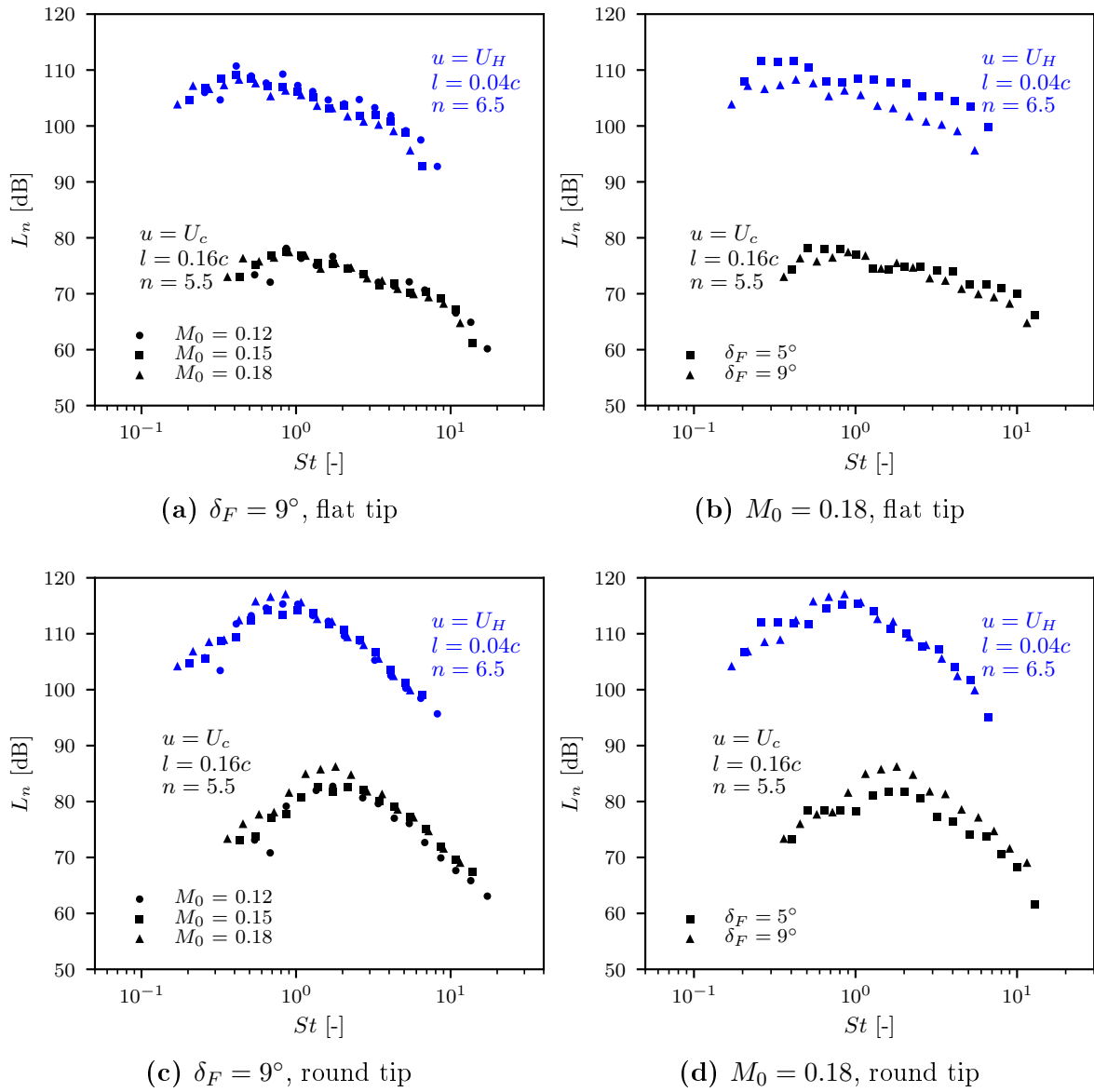


Figure 6.13.: Clark-Y airfoil. Scaled integrated noise spectra. Bottom view, 1/3-octave band frequencies.

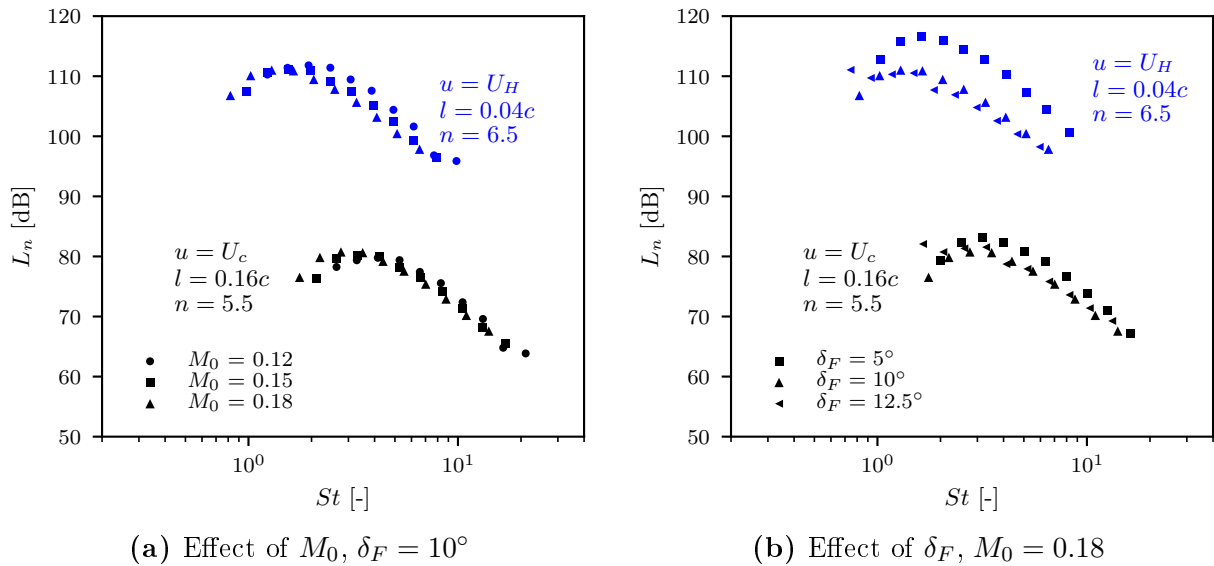


Figure 6.14.: DU96 wing model. Scaled integrated noise spectra. Bottom view, 1/3-octave band frequencies.

6.1.6. Source Directivity

Directivity measurements were performed in both the AWB (at the reference cantilever wing) and in the NWB (at the large scale cantilever wing) using, respectively, the small size directional microphone array technique and far-field microphones (e.g. chapter 4). Results of the AWB investigations are presented in figure 6.15 and 6.16. The results from the DNW-NWB experiments are given in figures 6.17, 6.18, 6.19 and 6.20.

Reference Cantilever Wing In figure 6.15, the contour plots display relative sound pressure levels at each spatial position of the microphone array, in wind tunnel coordinates, as a function of δ_F and St_0 . Noise levels are referenced to the bottom most position of the measurement range, directly below the wing, and marked with the letter C in the top left graph.

The results of figure 6.15 reveal a complex directivity pattern which cannot easily be related to some canonical multipole component. The directivity pattern at the lowest frequencies (i.e. 1 kHz and 2 kHz) in figure 6.15 reaches its maximum below the airfoil at a slight angle towards the sideline direction whereas at 3.15 kHz and 6.3 kHz, radiation occurs mainly towards the sideline. Roughly speaking, the radiation pattern has a principal radiation direction changing from approximately chord-normal at low frequencies to approximately spanwise-aligned at high frequencies. This behavior is related to the frequency dependent shift in the dominant source region's position along the flap side edge, as is suggested by the beamforming results discussed earlier.

Upper side radiation is found to be on the order of 3-4 dB less than below the wing; a trend also noticed in measurements of Brooks and Humphreys Jr. [18] and which Miller [96] interprets as being due to diffraction of the sound field by the flap, for a source region located on the wing's upper side. Low frequency noise occurs predominantly near the flap TE, through an interaction of the tip vortex with the wing. As the wave front propagates upstream it will be diffracted towards the ground at the LE. Below the wing, positive

interference will cause an increase in noise levels [96]. As the sound wave frequency increases the overall directivity pattern becomes more uniform.

Miller's hypothesis cannot, however, explain the existence of a zone of high SPL downstream of the flap, e.g. in figure 6.2, figure F.1 and figure F.2. An analytical derivation by Howe [68] on the scattering of sound waves by a vortex provide a plausible explanation for both the lower upper side noise levels as well as for the downstream source region. According to Howe [68], an acoustic plane wave incident on a rectilinear vortex will interact with the vortex's hydrodynamic field leading to considerable distortion of the incident sound field. The resulting acoustic field will consist of cylindrically spreading sound waves, with origin centered on the vortex axis, and a four-lobe directionality with maxima tilted $\pm 52^\circ$ away from the incident and back-scattered wave direction. No sound radiation will occur parallel to the direction of propagation of the incident wave and a significant amount of back-scattering will be recorded. Howe's [68] derivation is consistent with simulations by Colonius et al. [27] and experimental results by Horne [64].

Results for $M_0 = 0.18$ are shown in figure 6.16. Except for the occurrence of a strong maximum in sound pressure levels for the downstream and slightly above the airfoil direction, at 25° , the overall directivity pattern remains very similar to what was observed for $M_0 = 0.15$. The database does not, however, allow to clarify if this feature is a relevant characteristics of FSE noise or if it is an artifact of the current experimental setup.

Large-Scale Cantilever Wing Sound directivity results for the large scale cantilever wing are presented in figures 6.17, 6.18, 6.19 and 6.20. The data was acquired using free-field microphones mounted to a traversing system, e.g. figure A.7. The sound pressure levels are first normalized to a 1 m distance from the airfoil's tip $x/c = 0.5$ position and then referenced to the SPL value at the cross position ($\varphi_x = 90^\circ$, $\varphi_y = 0^\circ$). The data of figures 6.17, 6.18, 6.19 and 6.20 cover a range of radiation angles not available in the results of figures 6.15 and 6.16, corresponding to a fly-over situation. The background noise corrected free-field microphone data were cross-checked with the phased array results to confirm their validity. In all cases the free-field data presented was at least 3 dB above the background noise levels which was measured as the noise level of the support only. The phased array data confirmed that the FSE was the dominant source of noise in the frequency range of interest by a margin in excess of 10 dB, e.g. figures F.1- F.4.

The effect of a variation in angle of attack at $M_0 = 0.21$ is presented in figures 6.17 and 6.18. At 1 kHz, the directivity pattern has its maximum for $\varphi_x > 90^\circ$. The contours of relative SPL are not symmetric with respect to the $\varphi_y = 0^\circ$ plane, with a distinct region of higher radiation at $\varphi_y \approx 15^\circ$ and for $60^\circ < \varphi_x < 105^\circ$. Otherwise, sound radiation steadily increases in the downstream direction, hinting at a maximum downstream of $\varphi = 105^\circ$. Results for the raked tip airfoil, in figure 6.18, display a different behavior. In contrast to the results of figure 6.17, the maximum of sound radiation appears as a function of δ_F , clearly shifting upstream as δ_F is increased. Except for $\delta_F = 20^\circ$, where the directivity patterns of both the reference and sweep tip airfoils are equivalent, sound radiation becomes more symmetric about $\varphi_y = 0^\circ$ with increasing δ_F . Increasing the Mach number of the incoming flow only has a marginal effect on the directivity pattern of both airfoils (e.g. figures 6.19 and 6.20).

At 3.15 kHz, for the reference airfoil, the directivity patterns has its maximum mostly for $\varphi_x = 100^\circ$ and $\varphi_y < -10^\circ$. Contrarily to the results at 1 kHz, there is only a

single region where sound radiation reaches its maximum. Otherwise, sound radiation also steadily increases in the downstream direction, hinting at a maximum downstream of $\varphi_x = 105^\circ$. The only exception here is the case of $\delta_F = 20^\circ$, where the directivity pattern has its maximum at $\varphi_x \approx 65^\circ$, $\varphi_y \approx -30^\circ$. In comparison, the directivity pattern for the sweep tip airfoil has its maximum towards the sideline direction, i.e. $\varphi_y < -10^\circ$, and covering the whole φ_x range of the measurements. A second important lobe of high sound radiation exists on the opposite side at $\varphi_y \approx 20^\circ$. For both tip configurations, a reduction of the incoming flow Mach number leads to a more pronounced side line radiation, i.e. $\varphi_y > 20^\circ$.

The results of figures 6.17 and 6.19 are, to some extent, consistent with data from an earlier wind tunnel study by Guo et al. [56] at a 4.7% scale model DC-10 aircraft. Guo et al. presented noise directivity data from free-field microphones for the case of fully deflected flaps and slats. Their results provide indications of a broadly spread directivity peak over the fly-over angle range $60^\circ < \varphi_x < 120^\circ$. The authors postulate that such a broad maximum occurs due to the combined contributions from multiple sources, e.g. flap side edge noise, flap trailing-edge noise and slat noise. The results presented in figures 6.17 and 6.19 suggest that, among all the above sources of noise, flap side edge noise radiates mostly in a rear arc direction. This observation is in contrast to the modelling assumption that FSE noise mainly radiates in a direction normal to the airfoil's chord [54, 56]. The results of figures 6.17 and 6.19, at 1 kHz, are consistent with data from Brooks et al. [21] which performed directivity measurements at a NACA63₂-215 airfoil with a 30% chord half-span Fowler flap. Their data shows a rear-arc maximum in noise radiation in the range $73^\circ < \varphi_x < 107^\circ$ for a flap angle of 39° . At 3.15 kHz the agreement with our data is, however, not good. This difference might be related to the half-span flap model utilized in [21], where the flow along the flap side-edge is constrained by the presence of the main wing.

From the discussion of section 6.1.1, it was found that the SPL at low frequencies scales according to a proportionality law $p^2 \propto u^{5.5}$, thus advocating for a classical edge scattering mechanism [40]. At this frequency, the phased array results clearly identify a dominant source near the airfoil's tip trailing-edge. The very weak dependency of the directivity patterns on δ_F and a distinct rear-arc maximum suggest, however, that the dominant acoustic source region has to be located on the suction side and in the aft part of the airfoil. The rear-arc directivity pattern is not consistent with the classical mechanism of edge scattering of flow turbulence which would imply a $\sin(\theta/2)$ directivity with a maximum in the upstream direction, and hints that the wing is working as an acoustic shield. This behavior is consistently depicted in figures 6.17a, c and e at 1 kHz. Therefore the source mechanism by which low frequency noise is generated must be a mixture of classical edge scattering in combination with unsteady force fluctuations on the airfoil as a consequence of vortex unsteadiness [118] and sound wave diffraction [54]. This mechanism could explain, through beaming effects, the existence of a region of lower SPL around $\varphi_y = -5^\circ$ and a stretching in the streamwise direction of the phased array source maps, e.g. figures 6.2, F.1 and F.2.

At 3.15 kHz, the discussion of section 6.1.1 points out a SPL scaling according $p^2 \propto u^{6.5}$, which is close to the typical dipole-like source radiation. It was shown in section 6.1.1 that the maximum in SPL found at 3.15 kHz is related to the merging of the primary tip vortex (forming on the tip face) with the secondary vortex (forming on the airfoil's suction side).

The vortex merging is accompanied by a sudden surge in cross-flow velocity in the vicinity of the top and lower tip edges (see section 5.4), meaning that the flow field is subjected to strong local accelerations. This suggests as source mechanism, a combination of classical edge scattering and unsteady force fluctuations on the airfoil as a result of vortex merging [69, 71, 108]. The higher power law exponent of $n = 6.5$ is also a consequence of the compactness of the source region compared to the airfoil's chord. The directivity patterns revealed in figure 6.17 indicate also a possible shielding of the acoustic source by the wing leading to rear-arc maximum in radiation. Higher SPL levels are measured for $\varphi_y < 0$ indicating that diffraction and reflection on the tip's face are important. The results of figure 6.17b corroborates these assumptions. At 20° , the tip vortex has a smaller diameter and stays closer to the airfoil's surface as it moves along the airfoil's chord. It interacts, therefore, much more strongly with the tip trailing-edge giving rise to a dominant classical edge scattering sound source; which does not scale according to $p^2 \propto u^{6.5}$ (see figure 6.6). A similar shift in directivity with δ_F is also observed in the results of Brooks et al. [21].

The directivity measurement results for the raked tip airfoil presented in figure 6.18 reveal a very different picture compared to the reference case. At 1 kHz, the direction of peak noise radiation is found to strongly depend on δ_F . The results still have a lobed structure, with a valley at $\varphi_y \approx -5^\circ$ and peaks at $\varphi_y \approx \pm 15^\circ$, which can be associated with beaming effects as a results of edge diffraction and reflection [54]. As discussed above, raking the airfoil's tip into the flow leads to an earlier movement of the tip vortex to the upper surface, therefore, reducing the effective length over which a direct vortex-surface interaction can occur [87]. Furthermore, the tip raking forces the winding of the tip flow field to occur in a incoherent manner, and prevents the build up of a strong tip vortex. This potentially leads to a lesser rotation dominated flow field passing over the airfoil's trailing and hence a stronger trailing-edge noise contribution and a $\sin(\theta/2)$ directivity. Although no flow data is available to confirm this hypothesis, the observations of McAlister et al. [87] seem consistent with the results of figure 6.18. At 3.15 kHz, in figure 6.18b, d and e, an important relative increase in noise radiation is observed, in particular towards the sideline direction at $\varphi_y \approx -25^\circ$ over the whole φ_x range of angles. The directivity pattern is also characterized by peaks and valley at $\varphi_y \approx \pm 15^\circ$ and $\varphi_y \approx -5^\circ$ respectively and is a weak functions of δ_F . The source mechanisms postulated for the reference case also apply here, except that for the rake tip case, high frequency noise occurs both near the airfoil's tip and its trailing edge, as revealed by the phase array data, e.g. figures F.3 and F.4. Thus higher SPL are measured as well and a different diffraction pattern is to be expected.

The dependency of the directivity patterns on Mach number is presented in figures 6.19 and 6.20 for the reference and raked tip cases respectively. In both cases, the acoustic radiation directivity is found to be a weak function of upstream flow velocity.

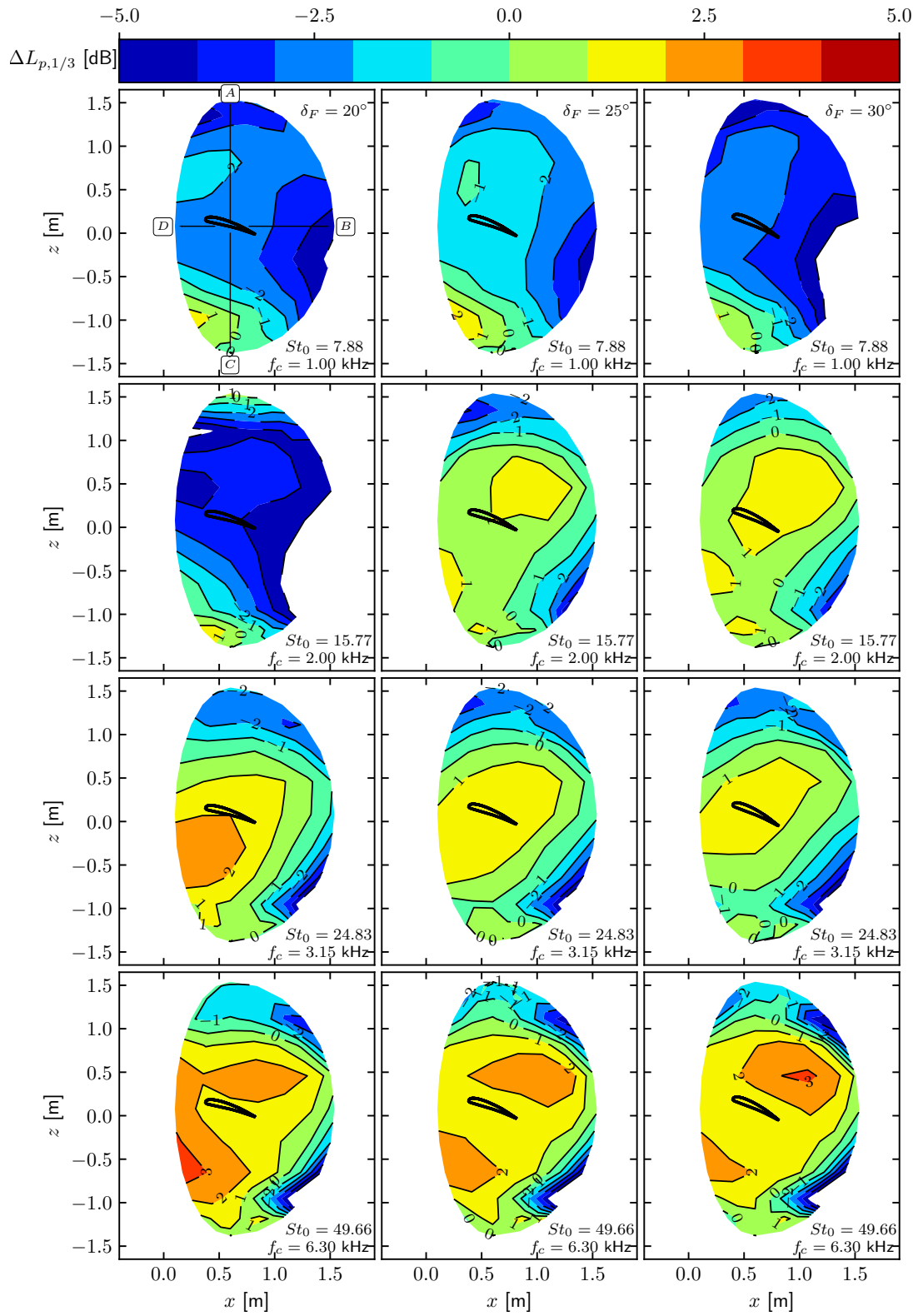


Figure 6.15.: Noise directivity maps vs. St_0 . $M_0 = 0.15$. Maximum angle range given in upper left plot $\rightarrow A : \phi = 0^\circ, \theta = 90^\circ$; $B : \phi = 40^\circ, \theta = 0^\circ$; $C : \phi = 0^\circ, \theta = -90^\circ$; $D : \phi = -20^\circ, \theta = 0^\circ$.

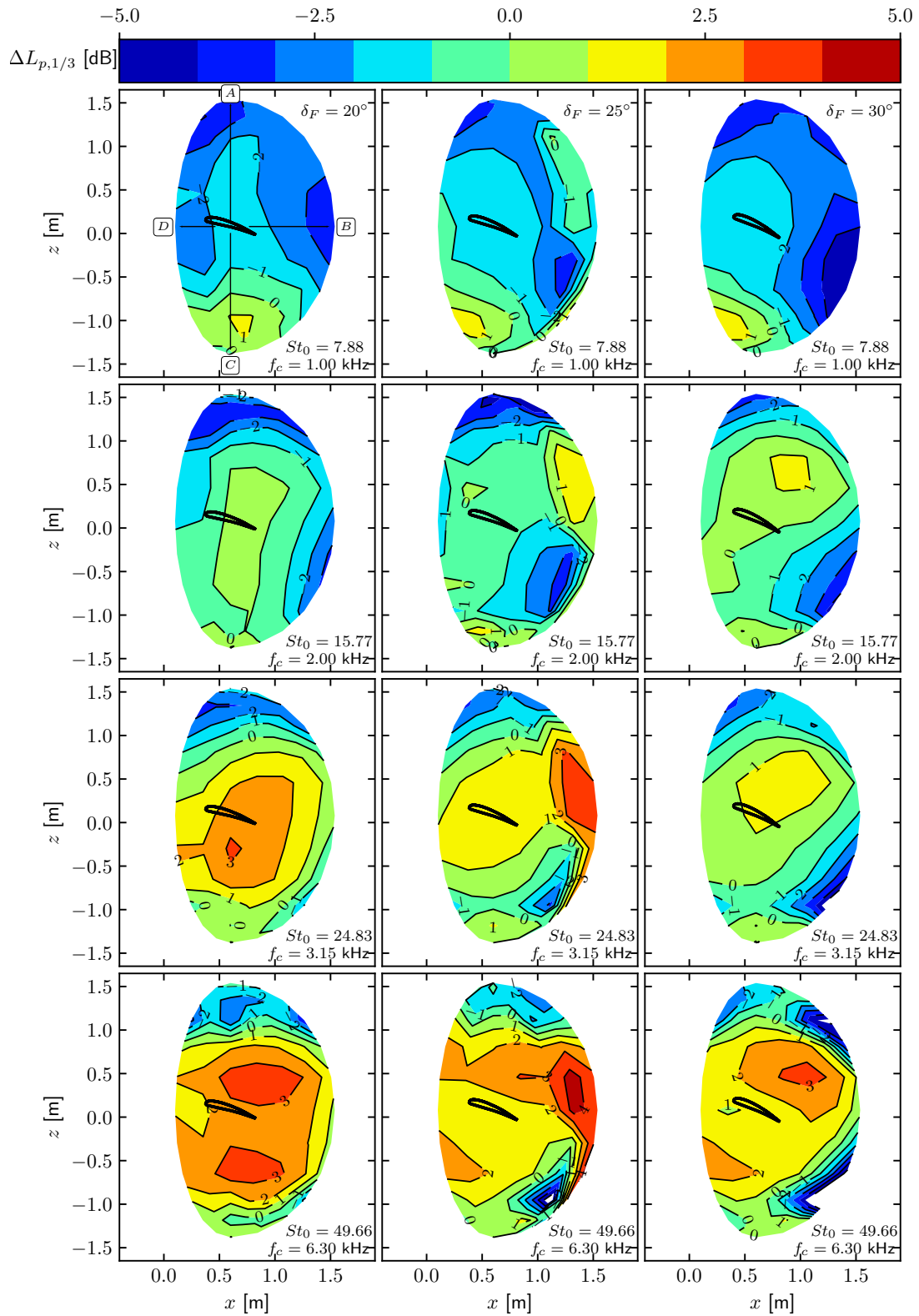


Figure 6.16.: Noise directivity maps vs. St_0 . $M_0 = 0.18$. Maximum angle range given in upper left plot \rightarrow A : $\phi = 0^\circ, \theta = 90^\circ$; B : $\phi = 40^\circ, \theta = 0^\circ$; C : $\phi = 0^\circ, \theta = -90^\circ$; D : $\phi = -20^\circ, \theta = 0^\circ$.

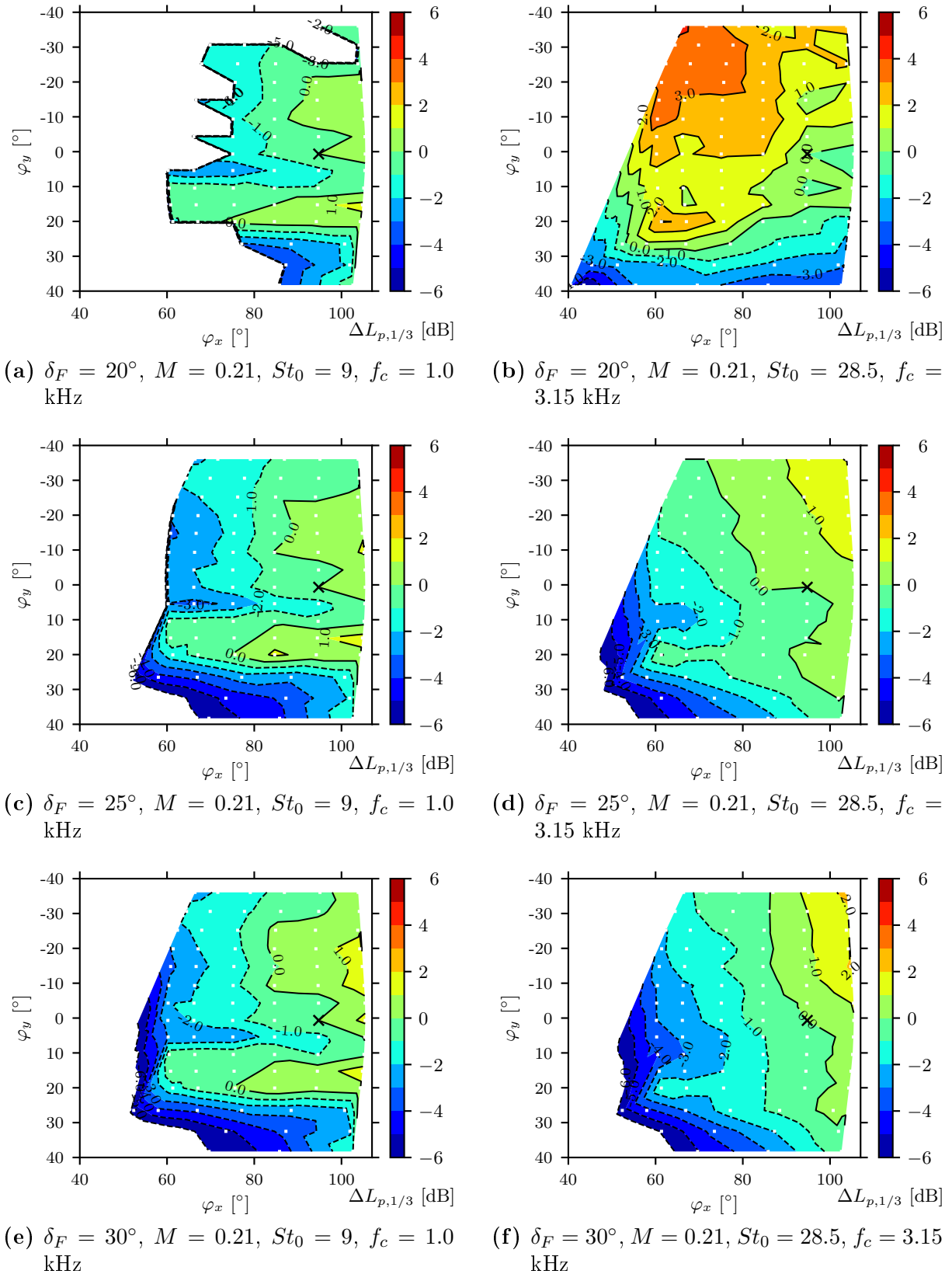


Figure 6.17.: Large scale cantilever wing reference configuration. Contours of constant relative sound pressure levels as a function of emission angles and δ_F and $M_0 = 0.21$. Levels are normalized by the level measured at the position marked by the black "cross" mark at $\varphi_x = 90^\circ$, $\varphi_y = 0^\circ$

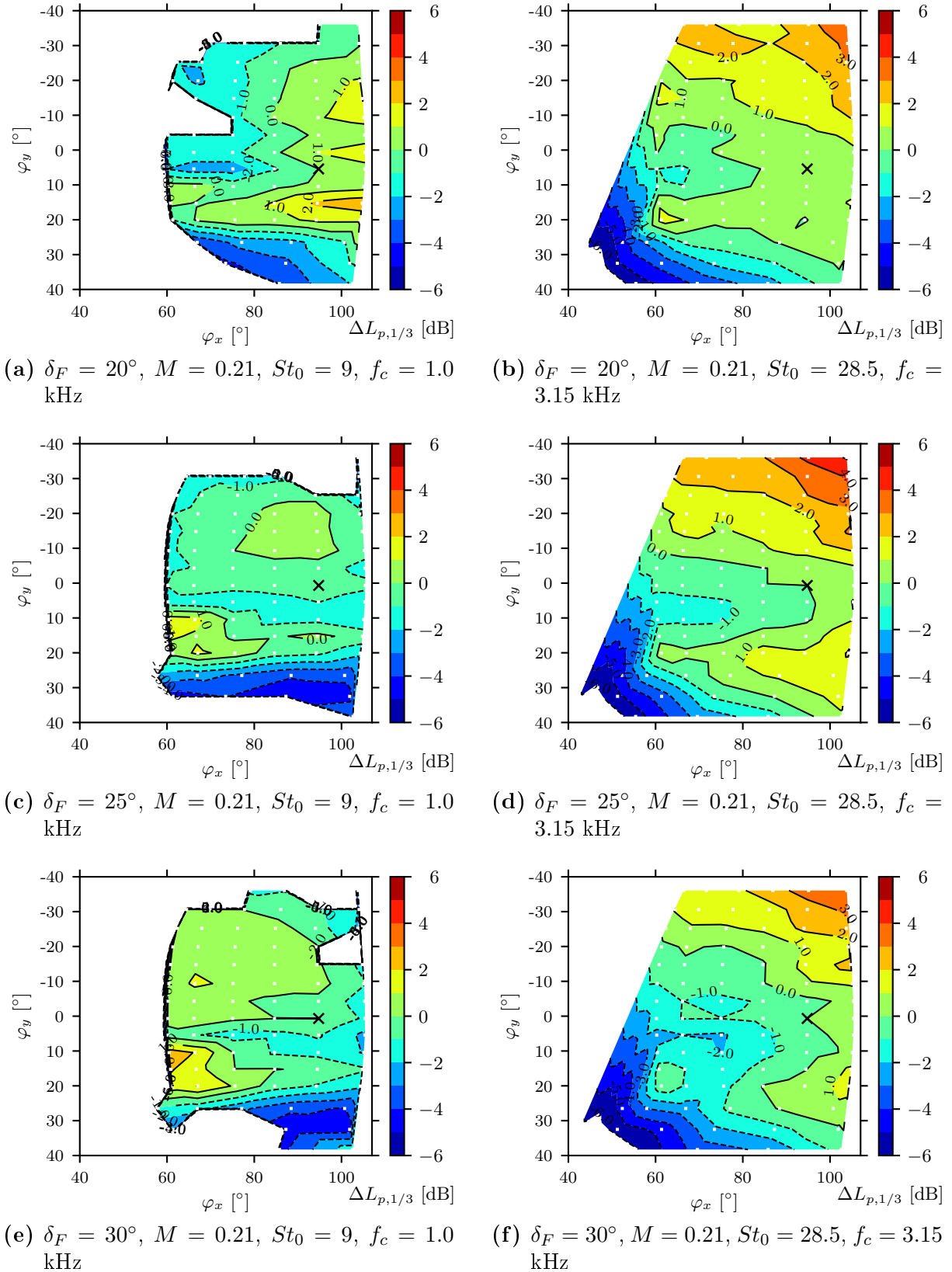


Figure 6.18.: Large scale cantilever wing sweep configuration. Contours of constant relative sound pressure levels as a function of emission angles and δ_F and $M_0 = 0.21$. Levels are normalized by the level measured at the position marked by the black "cross" mark at $\varphi_x = 90^\circ$, $\varphi_y = 0^\circ$

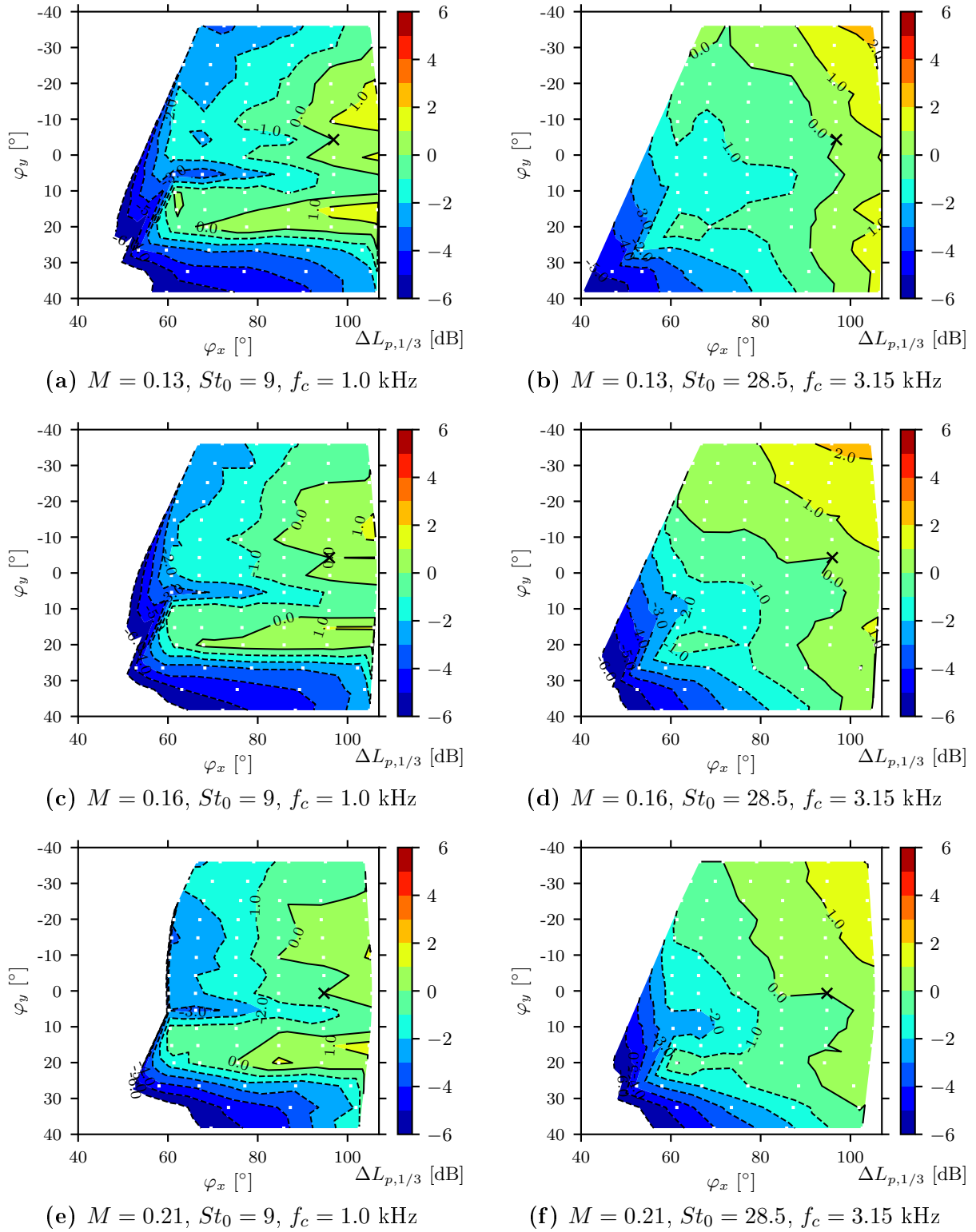


Figure 6.19.: Large scale cantilever wing reference configuration. Contours of constant relative sound pressure levels as a function of emission angles and M_0 , $\delta_F = 25^\circ$. Levels are normalized by the level measured at the position marked by the black "cross" mark at $\varphi_x = 90^\circ, \varphi_y = 0^\circ$

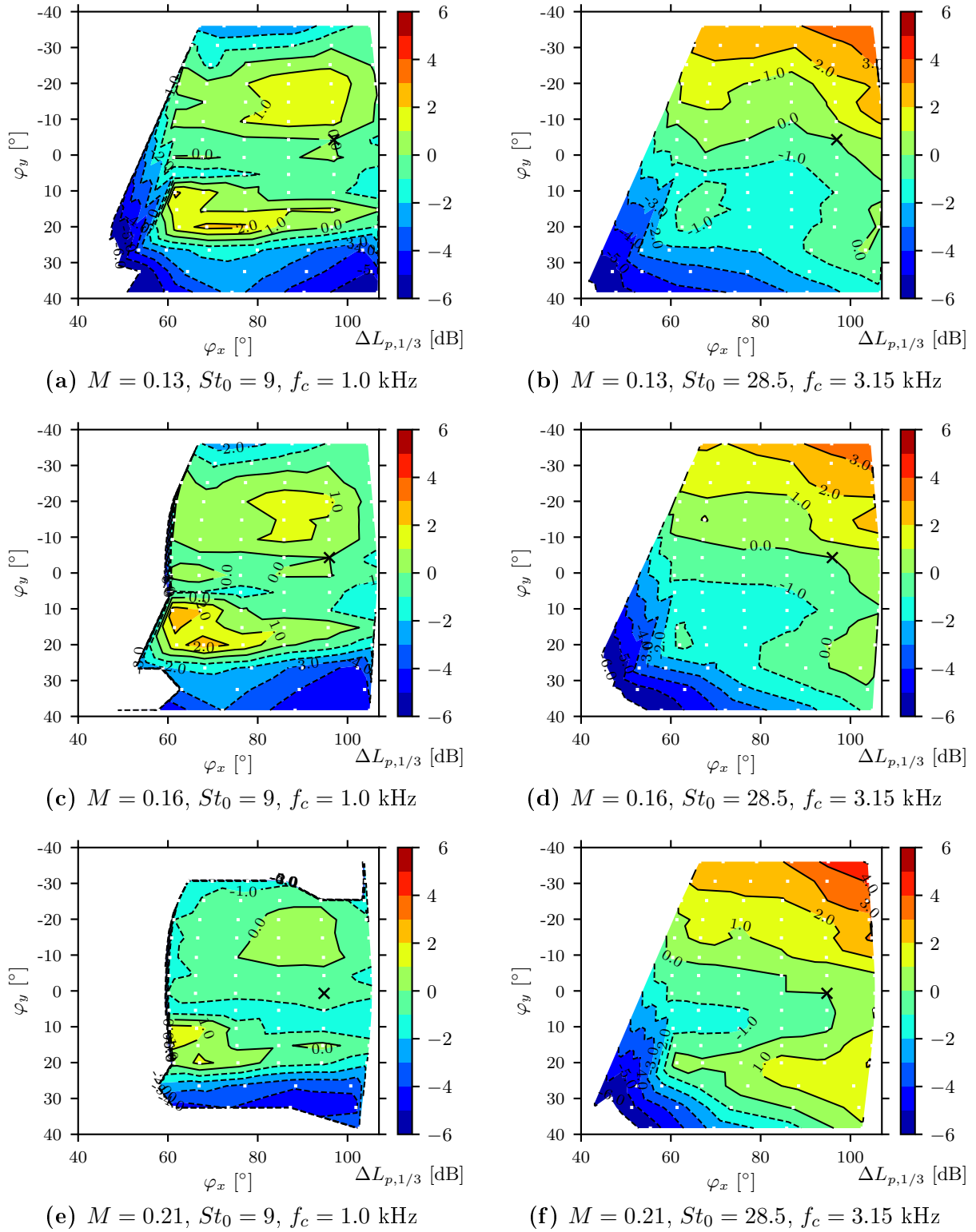


Figure 6.20.: Large scale cantilever wing sweep configuration. Contours of constant relative sound pressure levels as a function of emission angles and M_0 , $\delta_F = 25^\circ$. Levels are normalized by the level measured at the position marked by the black "cross" mark at $\varphi_x = 90^\circ, \varphi_y = 0^\circ$

6.2. High-Lift Wing Configurations

6.2.1. Source Maps and Interated Noise Spectra

SPL contour plots are shown in figure 6.21 for $\alpha_g = 0^\circ$, $\delta_F = 34^\circ$, $M_0 = 0.18$ and selected third octave band frequencies. The results were obtained by CLEAN-SC processing of the large aperture phased array data, e.g. chapter 4. Results are presented for $f_c = 4$ kHz and $f_c = 10$ kHz, which approximately correspond to $f_c = 1$ kHz and $f_c = 3.15$ kHz respectively, for the reference cantilever configuration discussed in section 6.1.1. For $f_c = 12$ kHz, the FSE source SPL have significantly dropped and are comparable in level to neighboring sources of noise. Therefore, the $f_c = 10$ kHz frequency band is preferred for the comparison.

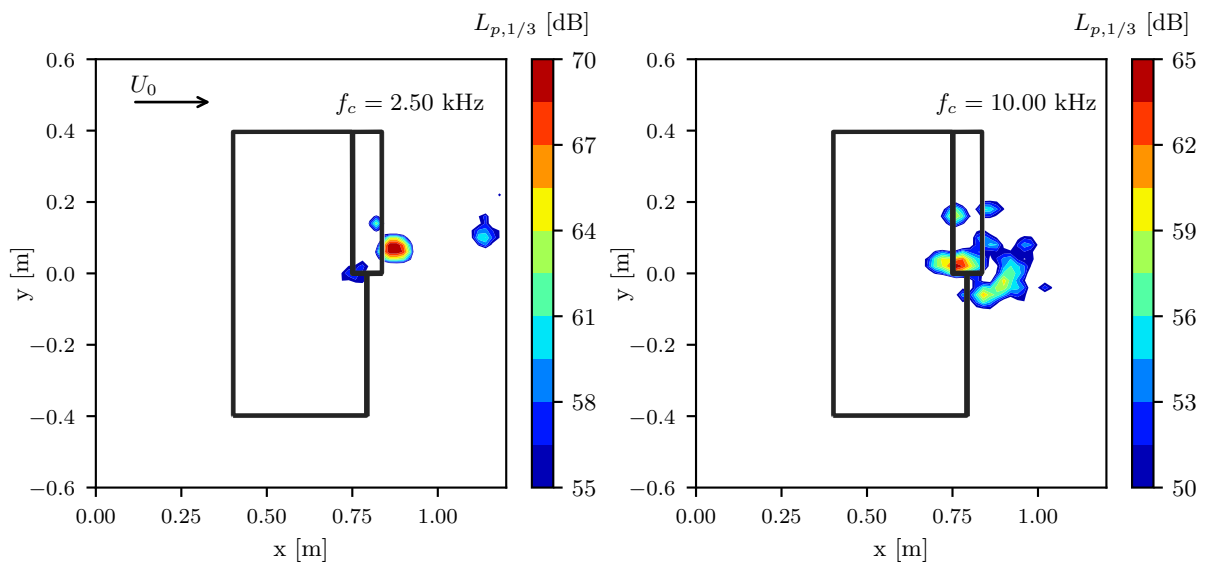


Figure 6.21.: High-lift wing with half-span flap with retracted slat. SPL contour plots, phased array located below the model. Top view, i.e. looking towards the model from above. 1/3-octave band frequencies. $\alpha_g = 0^\circ$, $\delta_F = 34^\circ$, $M_0 = 0.18$.

A strong noise source is identified near the flap side-edge, which appears as a single colored spot compared to the more extended source shown in figure 6.2 for the cantilever wing case. This is mostly due to the small size of the flap which makes it difficult for the microphone array to separate multiple sources at the FSE. Also, the flap track's (at $y = 0.1$ m) noise contribution cannot be isolated and is therefore included in the analysis of the array data. However, due to the streamlined fairing of the tracks, it is unlikely that they are important noise contributors. As for the cantilever wing case, low frequency noise appears to be generated mostly near the tip TE corner while high-frequency noise occurs upstream of the tip TE. At $f_c = 2.5$ kHz, the noise source is identified slightly downstream of the model, suggesting that sound wave diffraction around the TE is important and that the source region is located above the flap, i.e. on the suction side. At $f_c = 10$ kHz, side

lobes in the source maps start to play an increasingly important role, due to lower array SNR. Nonetheless, a maximum in SPL is identified at the FSE forward part.

Integrated spectra from the large aperture microphone array are shown in figure 6.22. One notices that the high-lift wing's main element angle of attack (α_g) has a weak but measurable influence on the noise generated at the flap side-edge, mostly at high-frequencies. A result consistent with investigations by [21, 38, 135], and which suggests that the flap flow is mostly driven by the local flap loading conditions. As for the cantilever case, a broadband monotonous increase in noise levels is observed when increasing the flow Mach number, e.g. figure 6.22a. An increase in δ_F , leads also to a broadband noise increase, however, not constant over all the frequency range; the high-frequency part of the spectrum being most strongly affected, as was the case for the cantilever wing.

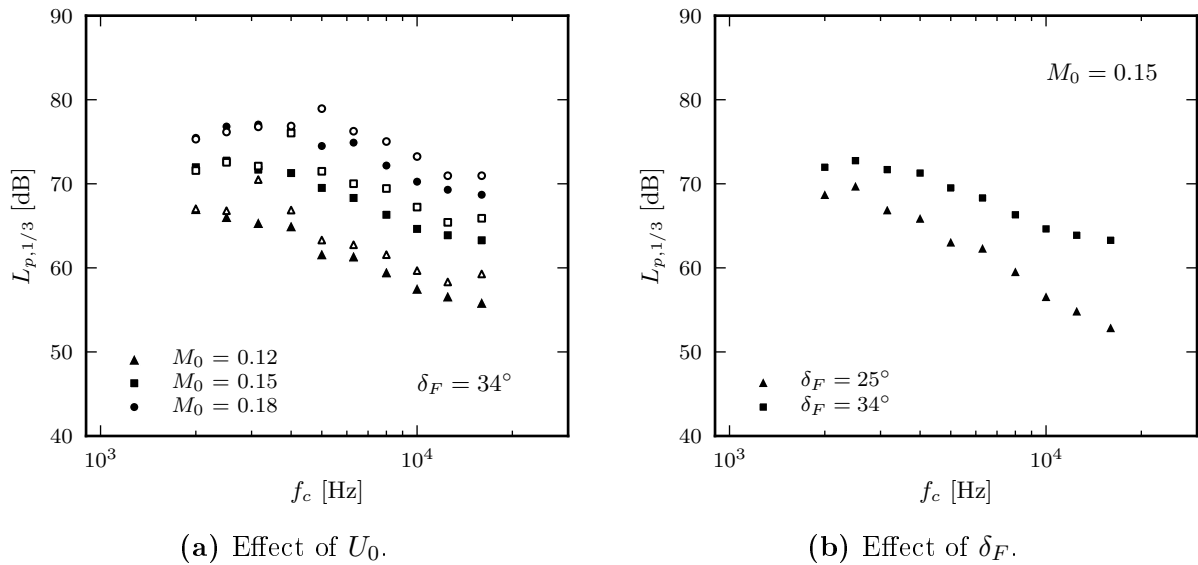


Figure 6.22.: Integrated 1/3-octave band noise spectra. Bottom view. Power integration performed over the range $0.6 \text{ m} \leq x \leq 0.95 \text{ m}$ and $-0.15 \text{ m} \leq y \leq 0.15 \text{ m}$ (see figure 6.21). (a) solid symbols: $\alpha_g = 0^\circ$, empty symbols: $\alpha_g = 7^\circ$. (b) solid symbols only: $\alpha_g = 0^\circ$

The low-frequency noise maximum at $\delta_F = 34^\circ$, $M_0 = 0.18$ appears at about $f_c = 3.0$ kHz, compared to $f_c = 0.8$ kHz for the cantilever wing. This shift in peak frequency corresponds approximately to the scale difference of the models i.e. $0.473/0.12 = 3.94$. The overall shape of the spectra of figure 6.22 do, however, resembles very much those measured for the cantilever wing. With decreasing Mach number the spectral maximum moves to lower frequencies, supporting an increase in tip vortex scale through a weaker stretching of its structure. The measurements at $M_0 = 0.12$ do not capture the spectral peak which has now dropped outside of the measurement range. A change in δ_F does not noticeably affect the frequency of the spectral maximum.

The scaling methodology used to analyze the cantilever wing case spectra is now applied to the above data for the high-lift configuration. Both single scale approaches, i.e. $u =$

U_c, U_0 , provide a very good representation of the impact of a change in M_0 , e.g. figures 6.23a, c. While a scaling with $u = U_c$ does provide a certain amount of success in representing the effect of δ_F , e.g. figures 6.23d, mostly at low frequencies, using U_0 as characteristic velocity scale is not satisfactory, e.g. figure 6.23b. The choice of a δ_F -dependent velocity scale is necessary. In figures 6.23e,f the same spectra are plotted, scaled with different characteristic velocities, i.e. $u = U_c$ and $l = 0.16c$ for the low frequency part, $u = U_H$ and $l = 0.04c$ for the high-frequency part. The choice of scaling parameter is the same as that used for the cantilever wing and it also provides a similar amount of success in collapsing the spectra. In all plots of figure 6.23, the low frequency power exponent is $n = 5.5$ while at high frequencies an exponent of $n = 6.5$ is used. These values are the same as for the cantilever wing case. While the single scale representation provides some amount of success in representing the observed trends, a multiple scale approach is definitely superior.

6.2.2. Source Directivity

Noise directivity for the high-lift wing configuration was investigated using the methodology described in chapter 4 using both the phased array technique as well as free-field microphones. The limited range available for the measurements, due to the presence of the AWB side walls, limits the range of radiation angles available in the results to $\varphi_y \pm 30^\circ$. Nonetheless, the results still provide insights into the sound radiation characteristics of the high-lift wing configuration.

Contours of constant SPL, obtained using the phased array, are given in figure 6.24, for $\delta_F = 20^\circ$ and $\delta_F = 34^\circ$ at $f_c = 3.15$ kHz, corresponding to the frequency of the maximum SPL level in figure 6.22. First, one notes that there is no strong and distinctive feature in the data, i.e. SPL variations on the order of only 1 dB are measured over the whole range. Even so, at $\delta_F = 20^\circ$, the sound radiation is mostly symmetric about $\theta = 0^\circ$, whereas it is directed towards the sideline direction at $\delta_F = 34^\circ$. At $\delta_F = 20^\circ$, a maximum is reached at a slightly more upstream direction, compared to the $\delta_F = 34^\circ$ case.

Free-field microphone data for the fly-over radiation direction, i.e. for $\varphi_y = 0^\circ$ as a function of φ_x , referenced to the flap $x/c = 0.5$, are presented in figure 6.25. The directivity at both $f_c = 2.50$ kHz and $f_c = 3.15$ kHz is very much similar at both $\delta_F = 20^\circ$ and $\delta_F = 34^\circ$. In the forward arc, below $\varphi_x = 70^\circ$ and for $f_c > 3.15$ kHz, the measured sound pressure levels decrease sharply. This observation is consistent with the discussion of section 6.1.6 on the source directivity for the reference cantilever model and lend support to the hypothesis that classical trailing-edge scattering is not the dominant source mechanism at large flap angles but could be at lower δ_F . The $f_c = 3.15$ kHz data appears, however, as a special case which is probably related to the vortex development at low angles, as was also observed for the case of the reference cantilever wing.

In figure 6.26, a comparison is made of the measured fly-over directivity, referenced to the SPL at $\varphi_x = 90^\circ$, between the reference high-lift configuration in AWB (AWB-HL) at $\alpha_g = 7^\circ$, $\delta_F = [20^\circ, 34^\circ]$, $M_0 = 0.18$, the reference cantilever configuration in AWB (AWB-CL), $\delta_F = [20^\circ, 30^\circ]$, $M_0 = 0.18$ and the large scale cantilever configuration in NWB (NWB-CL), $\delta_F = [20^\circ, 30^\circ]$, $M_0 = 0.2$.

For the low frequency cases, e.g. figures 6.26a and 6.26b, the noise level at the SPL peak frequency is plotted against φ_x . For the high-frequency cases, e.g. figures 6.26c and

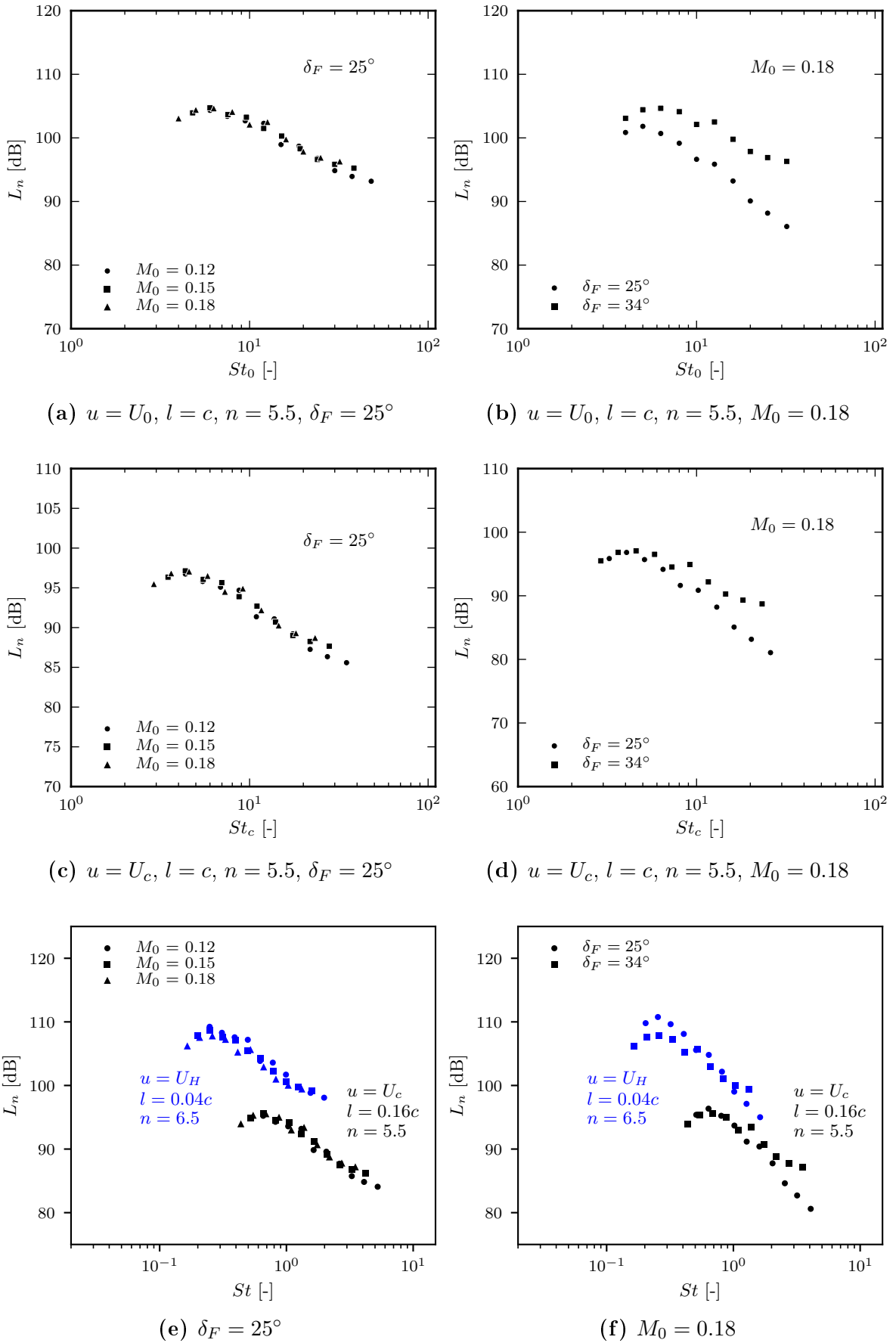


Figure 6.23.: Reference high-lift configuration. Scaled integrated noise spectra. Bottom view, 1/3-octave band frequencies.

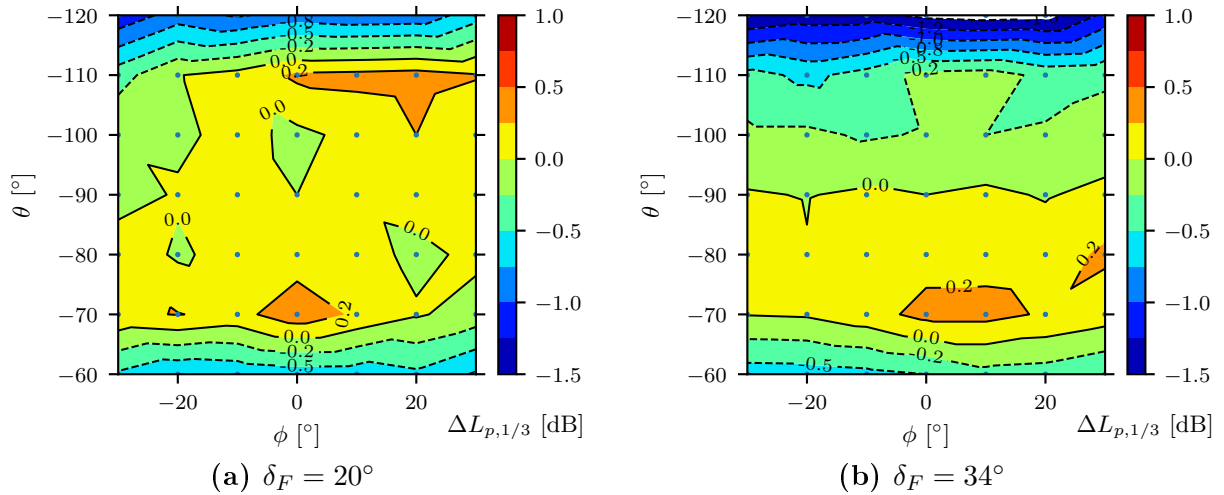


Figure 6.24.: High-lift wing configuration. Contours of phased array integrated SPL as a function of radiation angles and flap deployment angle. The angular emission directions are according to the coordinate system definition of figure 3.3. Levels are first propagated to a reference distance of 1 m from the airfoil center point and normalized by the SPL value at $(\phi = 0^\circ, \theta = -90^\circ)$. $M_0 = 0.18$, $f_c = 3.15$ kHz, $St_0 = 6$.

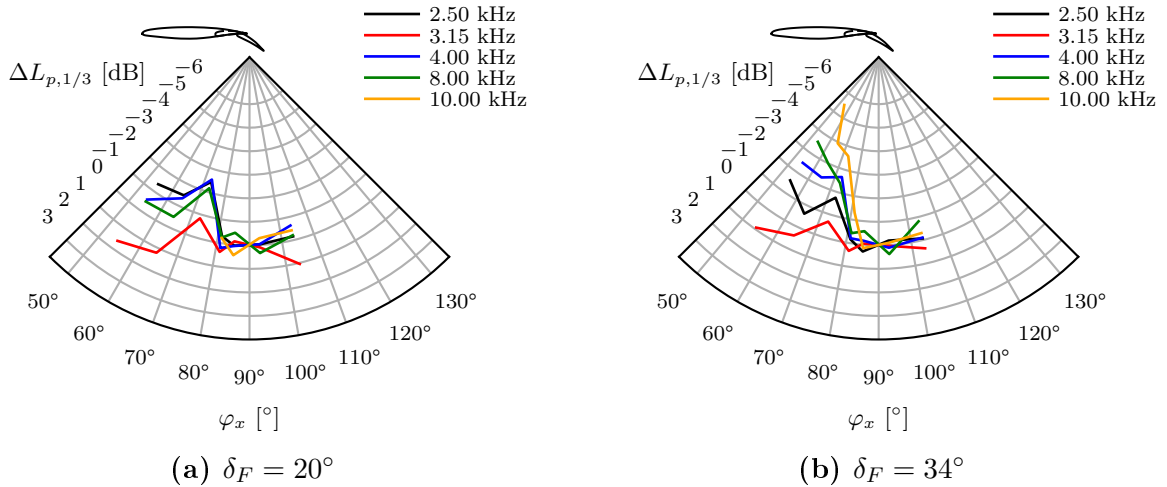


Figure 6.25.: High-lift wing configuration. Fly-over directivity, $\varphi_y = 0^\circ$. $M_0 = 0.18$.

6.26d, a frequency four times higher is considered. The δ_F selection for the comparisons is based on the available data range in each case. It does not imply an exact match between different configurations but rather a qualitative similarity. The choice of frequencies for the comparisons is derived from the geometric flap dimensions of each configuration.

All dataset reveal an increase in noise radiation in the rear-arc direction with a maximum for $\varphi_x > 110^\circ$. At high frequencies and small δ_F , the directivity is markedly more uniform over φ_x , in accordance with the results of figure 6.17b. The precise angle of maximum radiation cannot be quantified using the available data. This result is consistent with fly-over measurement data at an Airbus A319 conducted by Pott-Pollenske et

al. [106], fly-over measurements at a B747-400¹ as well as wind tunnel measurements by Dobrzynski et al. [36–38] and Yokokawa et al. [135]. Wind tunnel measurements at a 4.7% MD-11 aircraft model by Guo et al. [56] also suggest a rear arc dominant directivity in configuration $\delta_S = 20^\circ$ and $\delta_F = 50^\circ$ and for $f > 10$ kHz, which the authors deemed to be the relevant range for flap side-edge noise in their specific experiment. Below $f = 10$ kHz, the acoustic spectrum is mostly defined by noise originating somewhere else on their model high-lift wing [35].

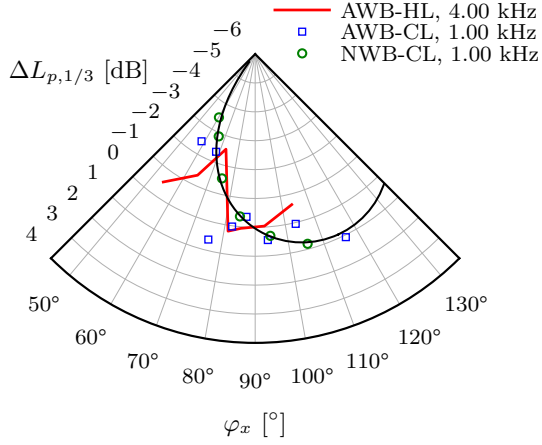
For typical high-lift system landing configuration settings, i.e. $\delta_S = 27^\circ$, $\delta_F = 40^\circ$, the measured fly-over rear-arc noise radiation in Pott-Pollenske et al. [106] is due to both slat and flap side-edge contributions. Dobrzynski et al. [37] have shown, in wind tunnel experiments at a Airbus-type high-lift device, that the total slat noise contribution is dominant in the low-frequency range, i.e. $f < 2$ kHz at full-scale, while the summed contributions from the high-lift system’s flap side-edges and total slat noise are approximately equivalent at mid- to high-frequencies, i.e. $f > 2$ kHz at full-scale. In Pott-Pollenske et al. [106] and Dobrzynski and Pott-Pollenske [36] no account can be made of the flap and slat noise respective directivity. The results of figure 6.26 demonstrate that the flap side edge source radiates sound also with a rear-arc directivity similar to that obtained in fly-over measurements at DLR’s ATRA aircraft. This suggest that both slat and flap-side edge noise could provide an equally important contribution to the rear-arc sound radiation in landing configuration, for $f > 2$ kHz at full scale.

These observations are, however, in contradiction with the common assumption found in the literature that a maximum in FSE noise radiation is to be expected in the forward arc, at a 90° angle to the flap chord, which is modelled as a chord-normal dipole along the flap side-edge [54] or near the flap trailing edge, i.e. as a half-baffled dipole, [3, 91, 92, 94–96]. A contradiction which could be linked to the specific type of trailing-edge flap design, i.e. single- vs multiple-slot flaps, the latter being the subject of the above studies [3, 54, 91, 92, 94–96].

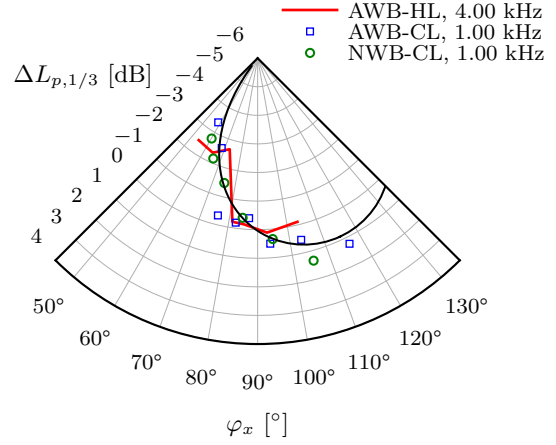
Results for the azimuthal directivity, i.e. $D(\varphi_x = 90^\circ, \varphi_y)$, are presented in figure 6.27 for the low- and high-frequency regimes and the small and large δ_F configurations. In figure 6.27, a comparison is made between wind tunnel measurement data at the reference cantilever wing and the reference high-lift configuration.

In comparison with the results of figure 6.26, considerably different directivity are observed at low-frequency vs. high-frequency. The low frequency directivity peaks to the sideline at $\varphi_y \approx 20^\circ$ while the high-frequency directivity peaks towards the $\varphi_y \approx 90^\circ$. The azimuthal directivity does not appear as a strong function of δ_F . An approximation to the data is given in the figures by the solid black line. Details about the functional constitution of this approximation will be given in chapter 7.

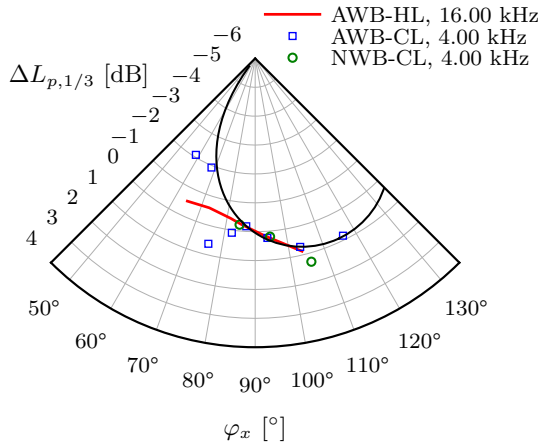
¹Private communication with Werner Dobrzynski, DLR, Institute for Aerodynamics and Flow Technology in Braunschweig, 2010



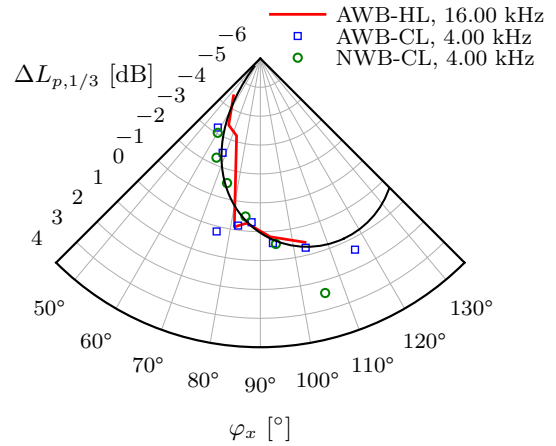
(a) Small δ_F , low-frequencies



(b) Large δ_F , low-frequencies

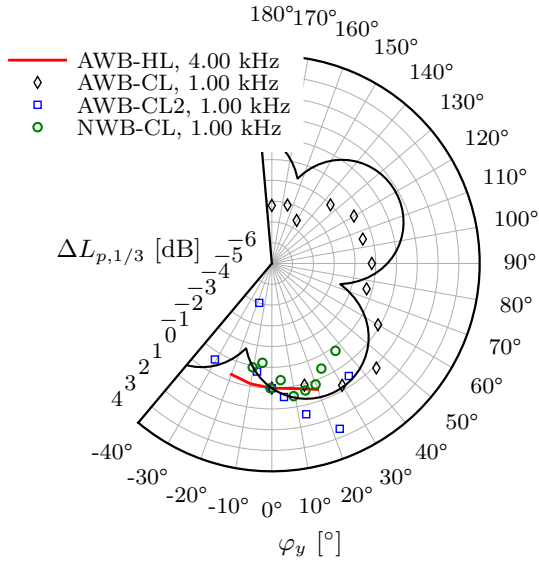


(c) Small δ_F , high-frequencies

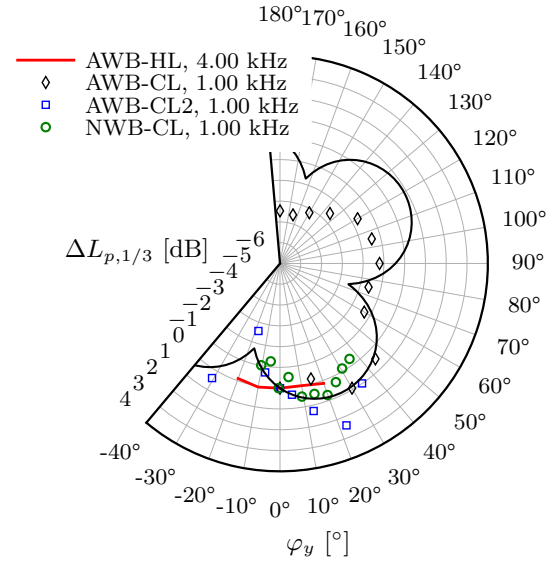


(d) Large δ_F , high-frequencies

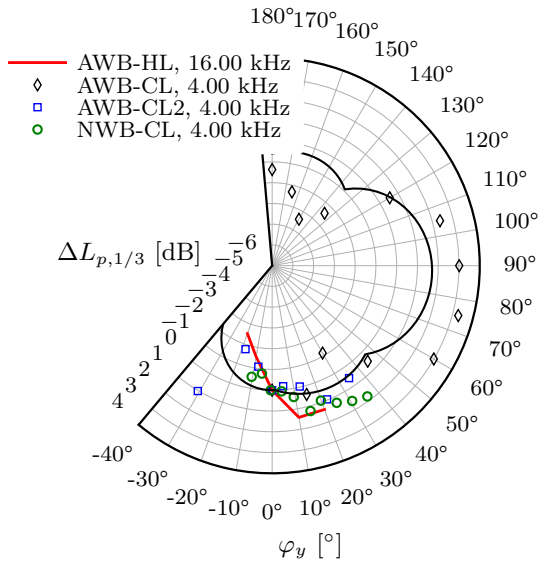
Figure 6.26.: Fly-over directivity, $\varphi_y = 0^\circ$. Comparison between the reference high-lift configuration in AWB (AWB-HL), $\alpha = 7^\circ$, $\delta_F = [20^\circ, 34^\circ]$, $M_0 = 0.18$, the reference cantilever configuration in AWB (AWB-CL), $\delta_F = [20^\circ, 30^\circ]$, $M_0 = 0.18$ and the large scale cantilever configuration in NWB (NWB-CL), $\delta_F = [20^\circ, 30^\circ]$, $M_0 = 0.2$. Solid black line: dipole directivity approximation, i.e. $D(\varphi_x, \varphi_y = 0^\circ) = \cos^2(\varphi_x + 115^\circ)$.



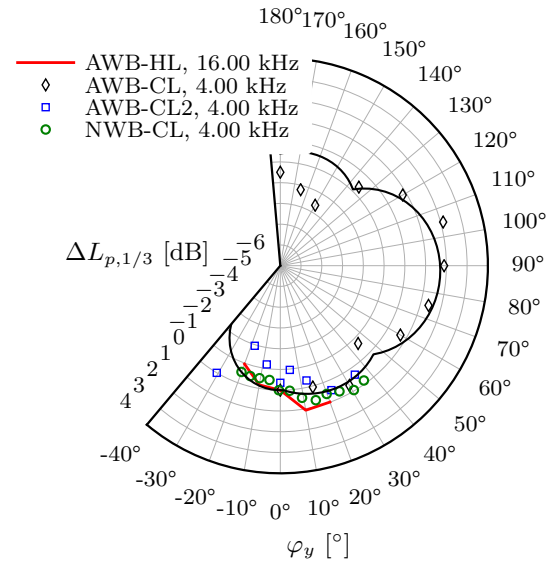
(a) $\delta_F = 20^\circ$, low-frequencies



(b) $\delta_F = 30^\circ$, low-frequencies



(c) $\delta_F = 20^\circ$, high-frequencies



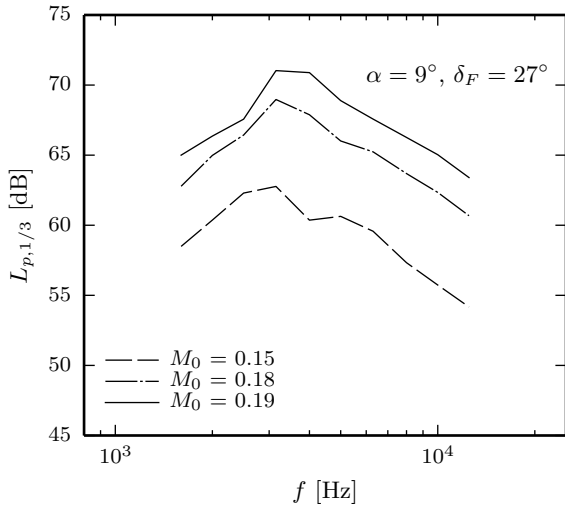
(d) $\delta_F = 30^\circ$, high-frequencies

Figure 6.27.: Azimuthal directivity, $\varphi_x = 90^\circ$. Comparison between the reference high-lift configuration in AWB (AWB-HL), $\alpha = 7^\circ$, $\delta_F = [20^\circ, 34^\circ]$, $M_0 = 0.18$, the reference cantilever configuration in AWB (AWB-CL and AWB-CL2), $\delta_F = [20^\circ, 30^\circ]$, $M_0 = 0.18$ and the large scale cantilever configuration in NWB (NWB-CL), $\delta_F = [20^\circ, 30^\circ]$, $M_0 = 0.2$. Solid black line: directivity approximation. Emission angles definition according to figure 4.1.

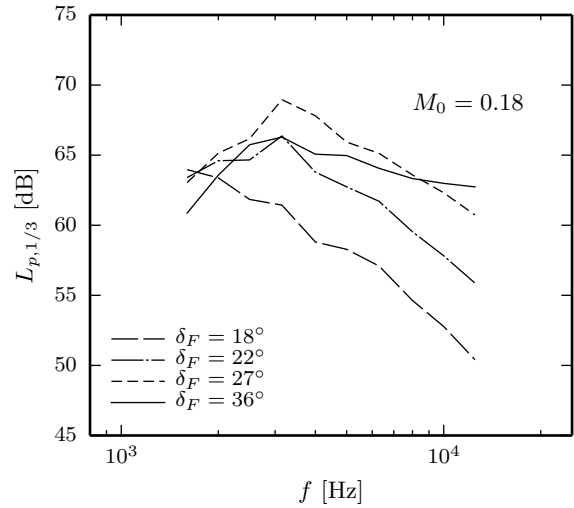
6.2.3. Effect of Airfoil Profile

The impact of the flap profile on the radiated noise was studied using a high-lift wing with 3/4-span flap with a Clark-Y profile. The results of the acoustic investigations are presented in figure 6.28. This time only a flat-tip flap is investigated. The results are presented in normalized form, according to the usual multi-scale scaling premises along with the absolute spectra for each corresponding case.

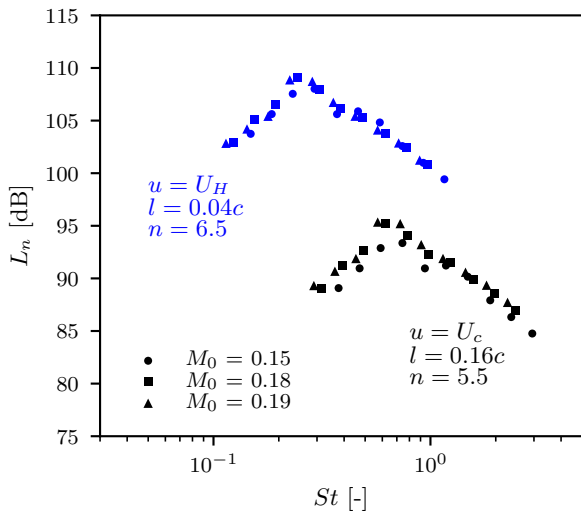
The overall shape of the spectra is reminiscent of the results for the reference wing with flat tip. However, measurements at the very large flap angle i.e. $\delta_F = 36^\circ$ reveal a completely different spectral shape. This is most probably the result of flow separation on the flap accompanied by a disruption of the vortex system. Results at $\delta_F = 36^\circ$ are not considered representative of the full-scale aircraft and are not further investigated in the current work. The effect of a variation in U_0 is nicely represented by both the low- and high-frequency scaling approaches, e.g figure 6.28c,d. The impact of δ_F variations is, however, better captured by the high-frequency scaling, as was also the case for the cantilever wing with Clark-Y profile, e.g. figure 6.13), and also consistent with all test cases discussed previously.



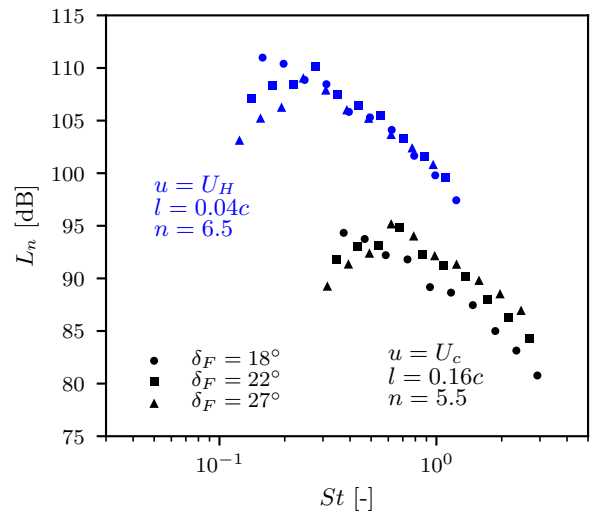
(a) Effect of U_0 .



(b) Effect of δ_F .



(c) Effect of U_0 .



(d) Effect of δ_F .

Figure 6.28.: High-lift configuration with 3/4-span flap with Clark-Y profile. Integrated noise spectra. Bottom view, 1/3-octave band frequencies.

6.3. Summary of Findings

On the Spectral Shape and its Scaling Laws:

1. The multi-scale scaling premises discussed above provide a very good collapse of the measured spectra for all test cases, on their own, both for M_0 and δ_F variations. The results demonstrate that flap side-edge noise levels are proportional to the tip local flow velocity, i.e. $U_c^{5.5}$, at low frequencies and to $U_H^{6.5}$ at high frequencies.
2. The observations made in chapter 6 suggest that noise generation at flap side-edge results from a mixture of classical edge scattering of flow turbulence according to Curle [29] and Roger et al. [113] and from unsteady vortex motion in the proximity of the flap side-edge according to the mechanism proposed by Powell [107], Sen [118], Howe [71] and Howe [69]. The edge scattering mechanism is more important at high frequencies while vortex unsteadiness dominate the low- to mid-frequency radiation.
3. With a reduction in wing's chord length, the low-frequency noise maximum is found to slightly shift to lower St numbers. This behavior is contrary to expectations. Although data scaling is successful for each test case, on its own, the ratio of length scale to velocity, i.e. l/u , obtained from the reference wing data appears not to be appropriate between the different test cases. While the slope of the cross-flow velocity with deployment angle, i.e. U_c vs δ_F , appears to be appropriate, the absolute value of U_c needs to be investigated for a wider range of wing geometries. Furthermore, when comparing different geometries as well as measurements in different wind tunnel, the appropriate definition of an effective deflection angle is still a problem which needs to be addressed.
4. Another aspect which would need further investigation is the length scale definition. Whereas here a value for l proportional to the wing's chord length is assumed, no knowledge is available regarding the functional dependency of l with respect to a change in δ_F . The scaled acoustic data presented above do lend support to the validity of the assumed length scale, with respect to variations in U_0 .
5. The results discussed above show that, at model scale, a low frequency flap side-edge noise reduction on the order of 5 dB can be achieved by raking the tip into the flow. A reduction in high frequency noise can be achieved by eliminating sharp edges in the tip region.

On the Source Directivity:

1. The FSE noise directivity cannot easily be related to some canonical multipole component (or a combination of) due to its complexity. The directivity pattern at the lowest frequencies (i.e. 1.0 kHz and 2.0 kHz) reaches its maximum below the airfoil at a slight angle towards the sideline direction whereas, at 3.15 kHz and 6.3 kHz, radiation occurs mainly towards the sideline. Roughly speaking, the radiation pattern has a principal radiation direction changing from chord-normal at low frequencies to approximately spanwise-aligned at high frequencies. This

behavior is related to a frequency dependent shift in the dominant source region's position along the flap side edge.

2. Upper side radiation, at model scale, is found to be on the order of 3-4 dB less than below the wing. A trend also noticed in measurements of Brooks and Humphreys Jr. [18] which cannot be explained at this stage.
3. FSE noise directivity is only weakly dependent on M_0 and δ_F .
4. Below the flight path, the FSE noise directivity has its maximum in the rear-arc and for $\varphi_x > 100^\circ$. Otherwise the directivity is not symmetric about $\varphi_y = 0^\circ$.
5. The low frequencies spectral data scale according to a proportionality law $p^2 \propto U_c^{5.5}$, thus advocating for a classical edge scattering mechanism [40]. The very weak dependency of the directivity patterns on δ_F and a distinct rear-arc maximum suggest, however, that the dominant acoustic source region has to be located on the suction side and in the aft part of the airfoil. The rear-arc directivity pattern is not consistent with the classical mechanism of edge scattering of flow turbulence which would imply a cardioid directivity with a maximum in the upstream direction, and hints that the wing is working as an acoustic shield. Therefore the source mechanism by which low frequency noise is generate must be a mixture of classical edge scattering in combination with unsteady force fluctuations on the airfoil as a consequence of vortex unsteadiness [69, 71, 118] and sound wave diffraction [54].
6. At high frequencies, spectral data scale according to $p^2 \propto U_H^{6.5}$, which is close to the typical dipole-like source radiation [29]. It was shown in section 6.1.1 that the maximum in SPL found at 3.15 kHz is related to the merging of the primary tip vortex (forming on the tip face) with the secondary vortex (forming on the airfoil's suction side), subjecting the flow field to strong sudden local fluctuations. This suggests as source mechanism, a combination of classical edge scattering and quadrupole-like sound generation due to intense and highly unsteady force fluctuations on the airfoil as a result of vortex unsteadiness during the merging process [69, 71, 108, 113]. The directivity patterns indicate also a possible shielding of the acoustic source by the wing leading to rear-arc maximum in radiation. Higher SPL levels are measured for $\varphi_y < 0$ indicating that diffraction and reflection on the tip's face are important.
7. In contrast to the above observations, for the raked tip flap side-edge configuration, the maximum of sound radiation appears as a function of δ_F , clearly shifting upstream as δ_F is increased. Sound radiation is increasingly symmetric about $\varphi_y = 0^\circ$ with increasing δ_F while variations of the incoming flow Mach number also only has a marginal effect on the directivity pattern. The directivity measurement results for the raked tip airfoil reveal a very different picture compared to the reference case. At 1 kHz, the direction of peak noise radiation is found to strongly depend on δ_F , hence hinting at a stronger trailing-edge noise contribution. The results still have a lobed structure, with a valley at $\varphi_y \approx -5^\circ$ and peaks at $\varphi_y \approx \pm 15^\circ$, which can be associated with beaming effects as a results of edge diffraction and reflection [54]. At 3.15 kHz, in figure 6.18, an important relative increase in noise radiation is observed, in particular towards the sideline direction from $\varphi_y \approx -25^\circ$ over the whole

φ_x range of angles. The directivity pattern is also characterized by peaks and valley at $\varphi_y \approx \pm 15^\circ$ and $\varphi_y \approx -5^\circ$ respectively and is a weak functions of δ_F . The source mechanisms postulated for the reference case also apply here, except that for the rake tip case, high frequency noise occurs both near the airfoil's tip and trailing edge. The acoustic radiation directivity is still a weak function of U_0 .

7. Semi-Empirical Prediction Scheme for Flap Side Edge Noise

In this chapter, the results of the flow field investigations (chapter 5) and of the acoustic investigations (chapter 6) are brought together and a semi-empirical prediction scheme for the flap side-edge noise of the reference configuration is formulated. Example applications are given and the limitations of the prediction scheme are discussed.

7.1. Theoretical Background

We adopt the solution of Ffwoes Williams and Hawkings wave equation for the far-field noise power spectral density in the form presented in Guo [54];

$$\Pi(\mathbf{x}, \omega) = \int_{S(\mathbf{y})} \Pi_0(\mathbf{y}) \Phi_1(\kappa_1) \Phi_2(\kappa_2) l_1 l_2 \tau_0 \Psi(\omega) \left| n_i(\mathbf{y}) \frac{\partial G_0(\mathbf{x} - \mathbf{y})}{\partial y_i} \right|^2 dS(\mathbf{y}), \quad (7.1)$$

with the field coordinates \mathbf{x} , the source coordinate \mathbf{y} , $S(\mathbf{y})$ the surface of integration, t the reception time and τ the source time. Π_0 is a power amplitude factor, Φ_i are the streamwise and spanwise spatial correlation functions dependent on the streamwise and spanwise wavenumbers κ_i , Ψ the temporal coherence function dependent on the circular frequency ω , and τ_0 the characteristic time scale of the surface pressure fluctuations, l_i the characteristic flow length scales and G_0 the Green's function of the problem.

The starting point of the modelling discussed in this chapter is based on a reformulation of equation 7.1 by Guo [54] using dimensional analysis,

$$\Pi(\mathbf{x}, f) = \rho_0^2 a_0^4 A_G A_F W(M) F(f, M) D(\varphi_x, \varphi_y) \frac{l}{a_0} \frac{L_f l}{\Delta^2 R^2} \exp(-\alpha_0 R), \quad (7.2)$$

with each parameter assumed to be encompassing a single functional dependency of the radiated noise. The ambient medium: $\rho_0 a_0^2$, Mach number dependent weighting function: $W(M)$, spherical spreading: $1/R^2$, convective amplification: $\Delta^2 = 1/(1 - M \cos \theta)^4$, atmospheric absorption: $\exp(-\alpha_0 R)$, directivity: $D(\theta, \phi)$, geometry dependent amplitude: A_G , flow dependent amplitude: A_F , spectral shape: $F(f, M)$ and the FSE dimension: $L_f l$, with L_f the flap chord and l a characteristic length scale. The spectral shape of FSE noise in equation 7.1 [54], is characterized by the Green's function as well as the temporal (Ψ) and spatial (Φ_i) coherence of the source in streamwise and spanwise directions. All three are represented through appropriate individual functional expressions, to be derived below. The other parameters serve as amplitude modulators of the power spectrum.

In the following, total FSE sound radiation is modelled as the weighted sum of a low-frequency contribution and a high-frequency contribution, with the corresponding

low- and high-frequencies spectral maxima expected at Strouhal numbers, based on the corresponding low- and high-frequency length and velocity scales, approximately equal to unity. The relevant Strouhal number is defined as $St = fl/u$ with l and u the local length and velocity scales of the flow structures driving the sound generating mechanism. This is in contrast to Guo's work [54], which utilizes geometrical and mean flow quantities to estimate both l and u . Flow measurements presented in chapter 5, provide measurements of both l and u . In particular, the local flow velocity derived in chapter 5, has the advantage of incorporating the effect of flap deflection angle, δ_F . The geometry-dependent and flow-dependent amplitude factors, A_G and A_F , are not considered in the discussion because of insufficient available data for their quantification. The convective amplification, Δ^2 , and atmospheric absorption, $\exp(-\alpha_0 R)$, terms are also omitted from the discussion. The former should however be included in a prediction where the aircraft is moving relative to the receiver while the latter was included in the data processing steps. The FSE source dimension is estimated by the squared characteristic length scale value, i.e. l^2 , which is defined as proportional to the FSE chord length. Equation 7.2 for the source power at field point \mathbf{x} thus reduces to,

$$\Pi(\mathbf{x}, f) = CW(M)F(f, M)D(\varphi_x, \varphi_y) \frac{l^2}{R^2} \exp(-\alpha_0 R), \quad (7.3)$$

with $\rho_0^2 a_0^3 l_i$ included in the calibration constant C .

Table 7.1.: Low- and high-frequency velocity scale relationships as function of δ_F or C_L or Γ_1 respectively as presented in chapter 5.

Case	u	vs. δ_F	vs. C_L	vs. Γ_1
Reference	U_c/U_0	$0.023\delta_F + 0.682$	$0.623C_L + 0.554$	$-0.033\Gamma_1 + 0.819$
Reference	U_H/U_0	$0.020\delta_F + 0.288$	$0.557C_L - 0.173$	$-0.030\Gamma_1 + 0.413$

Low-Frequency Flap Side-Edge Noise: Based on the observations of chapter 6, we make the hypothesis that low-frequency flap side-edge noise occurs **1)** through unsteady force fluctuations imposed on the rigid surface of the flap as a consequence of the complex three-dimensional turbulent tip flow field [29, 41, 69] as well as through oscillation of the vortex itself as a consequence of vortex unsteadiness [69, 118] and **2)** through, but to a lesser extent, as revealed by the non-cardioid directivity identified in chapter 6, edge scattering of turbulent flow velocity fluctuations [40] in the vicinity of the flap tip trailing-edge corner.

From the phased array measurements presented in chapter 6, we know that the low-frequency source region is mostly confined to a region near the tip trailing-edge corner. It also seems reasonable to assume that force fluctuations imposed onto the flap by the tip vortex occur on a time scale of order $T \sim l/u = 0.16c/U_c$, with the the vortex diameter as characteristic length $l = 0.16c$ and the characteristic velocity scale $u = U_c$, according

to the relationships of table 7.1 as defined in chapter 5. The peak frequency of the low-frequency source contribution occurs at a Strouhal number of $St = f(0.16c)/U_c = 0.8$, corresponding to a Helmholtz number of $He = l/\lambda = f(0.16c)/a_0 = 0.18$. Because we have $He < 1$, the source domain can be considered compact and interference effects over the source domain neglected. However, if we consider the chord length of the flap as representative length scale of the body, we have, at the peak frequency, $He = f(0.473 \text{ m})/a_0 = 1.1 > 1$. Hence, for this low frequency, the flap is not a compact body and sound wave diffraction about the flap, as described in Meecham et al. [91], is most probably relevant.

According to the surface noise contribution terms in [29, 41], the sound intensity of a compact dipole scales according to $p^2 \propto U_c^6$. The sound intensity of the classical edge scattering by a half-plane problem, however, scales according to $p^2 \propto U_c^5$ with a cardioid directivity [40]. The scaling relation of $p^2 \propto U_c^{5.5}$ found in the results of chapter 6 is thus indicative of the mixed character of flap side-edge noise; sound radiation from a compact source domain near the tip corner and classical edge scattering as the flow field outside of the vortex is convected over the airfoil's trailing edge.

The following scaling of the far-field sound pressure level is proposed,

$$L_n = L_p - 55 \log U_c/U_0 - 20 \log l/r - 10 \log D(\varphi_x, 0^\circ) - 10 \log D(90^\circ, \varphi_y) + C_1, \quad (7.4)$$

with C_1 as calibration constant, l a characteristic length scale of the sound source mechanism, r the source-observer distance and D an appropriate directivity function, i.e. equation 7.5 and 7.6. U_c is calculated from the relation of table 5.2.

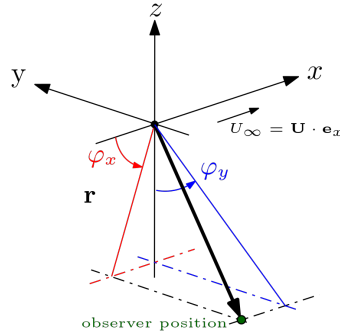


Figure 7.1.: Fly-over coordinate system definition

Directivity data presented in chapter 6 have demonstrated that the azimuthal directivity of flap side-edge noise is more complex than that of a simple dipole. Our data, for the azimuthal directivity, is best represented by a combination of two correlated dipoles, $\pi/2$ radians out of phase and placed at the flap rotation axis, with their axis tilted by $\varphi_y = 2\pi/5$ radians relative to the y direction expressed as,

$$D_{\varphi_y} = D(\varphi_x = 90^\circ, \varphi_y) = \left[\frac{\cos(\varphi_y - 2\pi/5) + \sin(\varphi_y - 2\pi/5)}{\cos(2\pi/5) + \sin(2\pi/5)} \right]^2. \quad (7.5)$$

The coordinate system definition of figure 4.1 is repeated here for convenience in figure 7.1. Equation 7.5 is validated over the angular range $-30^\circ \leq \varphi_y \leq 90^\circ$, e.g. figure 6.27. This approximation overestimates, however, the measured SPL above of $\varphi_y = 90^\circ$ by as much as 2 dB. This issue could not be resolved and is potentially related to sound wave convection and refraction due to the high local velocities and velocity gradients existing across the tip vortex. The polar directivity is best represented by a single dipole, placed at the flap rotation axis, and with its axis tilted by $5\pi/8$ radians relative to the x direction as,

$$D_{\varphi_x} = D(\varphi_x, \varphi_y = 0^\circ) = \left[\frac{\cos(\varphi_x - 5\pi/8)}{\cos(5\pi/8)} \right]^2, \quad (7.6)$$

which is validated over the angular range $60^\circ \leq \varphi_x \leq 120^\circ$, e.g. figure 6.26. The results of chapter 6 demonstrate that the directivity is only a weak function of δ_F and M_0 . Therefore equations 7.5 and 7.6 are both considered as universal functions.

High-Frequency Flap Side-Edge Noise: High-frequency flap side-edge noise was shown to occur over most of the length of the flap side-edge, however with maximum intensities found mostly in the forward part, e.g. see chapter 6 for reference. In chapter 6 we hypothesized that high-frequency flap side-edge noise occurs during the tip vortex merging process as a consequence of sudden and intense localized changes in near-edge velocity. The far-field sound pressure level reaches its peak at a Strouhal number $St = fl/u = f(0.04c)/U_H \approx 1$, with the characteristic length scale $l = 0.04c$ and characteristic velocity scale $u = U_H$; with U_H according to the relations of table 7.1.

The following scaling of the far-field sound pressure level is proposed,

$$L_n = L_p - 65 \log U_H/U_0 - 20 \log l/r - 10 \log D(\varphi_x, 0^\circ) - 10 \log D(90^\circ, \varphi_y) + C_2, \quad (7.7)$$

with C_2 as calibration constant. $D(\varphi_x, 0^\circ)$ is defined in equation 7.6 and $D(90^\circ, \varphi_y)$ in equation 7.8.

The azimuthal directivity data for the high-frequency source mechanism is best represented by the weighted summed contribution of two uncorrelated dipoles with directionality $\cos(2\varphi_y/3)$ according to Roger et al. [113] and a transversal dipole to account for the side sound pressure level maximum, normalized to the overhead position, as,

$$D_{\varphi_y} = D(\varphi_x = 90^\circ, \varphi_y) = \left[\frac{\cos(2\varphi_y/3) + 4/5 \cos(2\varphi_y/3 + 3\pi/2) + 4/5 \sin(\varphi_y)}{1 + 4/5 \cos(3\pi/2)} \right]^2. \quad (7.8)$$

Equation 7.8 is validated over the angular range $-20^\circ \leq \varphi_y \leq 135^\circ$. Above $\varphi_y = 135^\circ$, the approximation overestimates the measurements by as much a 2 dB, e.g. figure 6.27. The source directionality over the angular range $-\pi/2 \leq \varphi_y \leq 0$, is arbitrarily approximated by a vertical dipole, assuming a rapid roll-off of the sound pressure levels below the wing and towards its root. The polar directivity, D_{φ_x} , for the high-frequency regime obeys the same functional dependency as for the low-frequency regime, i.e. see figure 6.26 and equation 7.6.

Spectral Shape Function: According to Guo [54], the temporal correlation $\psi(\tau)$ of the FSE noise source is related to the most energetic flow structures existing in the vicinity of the flap tip. These flow characteristics are assumed to dominate the noise production and their time scale is determined by their characteristic length and velocity scales,

$$\tau_0 = \frac{l}{u} = \mu_0 \frac{l_g}{u}, \quad (7.9)$$

where u , is a relevant local characteristic flow velocity and l_g a characteristic geometrical scale of the FSE. l is a relevant characteristic length scale of the local mean flow structure. Following the discussion of chapter 5, we have $l = \mu_0 l_g = \mu_0 c$, with $l_g = c$ and $\mu_0 = 0.16$ and 0.04 , for the low- and high-frequency source mechanisms respectively. The relevant characteristic velocities are $u = U_c$ and U_H for the low- and high-frequency source mechanisms respectively. The corresponding peak frequency estimate is therefore $f = \tau_0^{-1}$ Hz. Guo assumes for $\psi(\tau)$ an exponential decay over time of the form,

$$\psi(\tau) = \exp\left(-2\pi \frac{\tau}{\tau_0}\right) \quad (7.10)$$

where τ is the time delay and τ_0 is the characteristic time scale of the flow features. In the frequency domain equation 7.10 becomes,

$$\Psi(f) = \frac{1}{1 + (f\tau_0)^2}. \quad (7.11)$$

Combined with equation 7.9, one gets the final expression for the source temporal coherence function,

$$\Psi(f) = \frac{1}{1 + \mu_0^2 St^2}, \quad (7.12)$$

with $St = fc/u$. For the source streamwise spatial correlation, Guo assumes a similar functional form with an exponential decay for increasing spatial separation, ξ_1 , and also accounting for the mean flow in the expression,

$$\phi_1(\xi_1) = \exp\left(-2\pi \left| \frac{\xi_1}{l_1} \right| + 2\pi i \frac{f\xi_1}{u}\right). \quad (7.13)$$

After transformation to the Fourier domain, equation 7.13 becomes

$$\Phi_1(f) = \frac{1}{1 + (k_1 l_1 / 2\pi + f l_1 / u)^2}. \quad (7.14)$$

Using equation 7.9, the wavenumber approximation $k_{1,2,3} \approx 2\pi f / a_0$ and assuming the correlation length scale to be proportional to the characteristic length scales relevant for the source mechanisms, i.e.

$$l_1 = \mu_1 l = \mu_1 \mu_0 l_g \quad \text{and} \quad l_2 = \mu_2 l = \mu_2 \mu_0 l_g \quad (7.15)$$

equation 7.14 becomes,

$$\Phi_1(f) = \frac{1}{1 + \mu_0^2 \mu_1^2 (1 + M)^2 St^2}. \quad (7.16)$$

In a similar fashion, the expression for the spanwise spatial correlation is derived assuming an exponential decay function as in 7.10,

$$\phi_2(\xi_2) = \exp\left(-2\pi\left|\frac{\xi_2}{l_2}\right|\right), \quad (7.17)$$

which becomes, after Fourier transformation,

$$\Phi_2(f) = \frac{1}{1 + (k_2 l_2 / 2\pi)^2}. \quad (7.18)$$

Its final expression in terms of 7.10 is

$$\Phi_2(f) = \frac{1}{1 + \mu_0^2 \mu_2^2 He^2}, \quad (7.19)$$

with $He = fl_i/a_0$, the acoustic Helmholtz number. The constants μ_1 and μ_2 in equations 7.12 to 7.19 are assumed to be of order unity; thus basically assuming isotropic turbulence. With a lack of data on the actual correlation lengths of the flow field no attempt is made to further specify the values of μ_1 and μ_2 . Anisotropy in the turbulent flow field would, however, be expressed by non-similar values for μ_1 and μ_2 .

A model for the spectral shape function of each sub-component, i.e. low- and high-frequency components, of FSE noise is finally obtained by collecting the results of equations 7.12, 7.16 and 7.19 to,

$$F(f, M) = \frac{He^2}{(1 + \mu_0^2 St^2)(1 + \mu_0^2 \mu_1^2 (1 + M)^2 St^2)(1 + \mu_0^2 \mu_2^2 He^2)}, \quad (7.20)$$

where $St = fc/u$ is the Strouhal number based on the local characteristic velocity and the chord length and $M = u/a_0$, the Mach number based on the local characteristic velocity and the speed of sound. The total tip noise spectra is modeled by the sum of two uncorrelated spectral components defined by equation 7.20. Computed values for F according to equation 7.20 are plotted in figure 7.2a along with an example composite spectrum in figure 7.2b.

The total effect of flow Mach number variations on the spectral shape function cannot be represented by a single power exponent scaling relation. This is evident from the curves of figure 7.2a. The findings of chapter 6 suggest, however, that the low- and high-frequency range of FSE acoustic radiation do approximately scale on single power exponents of $n = 5.5$ and $n = 6.5$ near a local Strouhal number of ≈ 1 , respectively. Following Guo's [54] arguments, to impose this single exponent dependence of the sound radiation, the effect of flow Mach number on the spectral shape function has to be normalized out. This is achieved by involving a flow Mach number dependent weighting factor, $W(M)$, which can be derived from,

$$\frac{l}{a_0} W(M) \int_{f_1}^{f_2} F(f, M) df = M^n, \quad (7.21)$$

with the power exponent $n = 5.5$ for low-frequency and $n = 6.5$ for high-frequency. The integral of the spectral shape function is performed over a range covering the dominant frequencies. Guo [54] gives the following definition for the bounds of integration,

$$\frac{f_1 l}{a_0} = 0.01M \quad \text{and} \quad \frac{f_2 l}{a_0} = 100M. \quad (7.22)$$

The combined effects of flow Mach number and spectral shape function are given by,

$$W(M)F(f, M) = M^n \frac{F(f, M)}{I(M)}, \quad (7.23)$$

with

$$I(M) = \frac{l}{a_0} \int_{f_1}^{f_2} F(f, M) df. \quad (7.24)$$

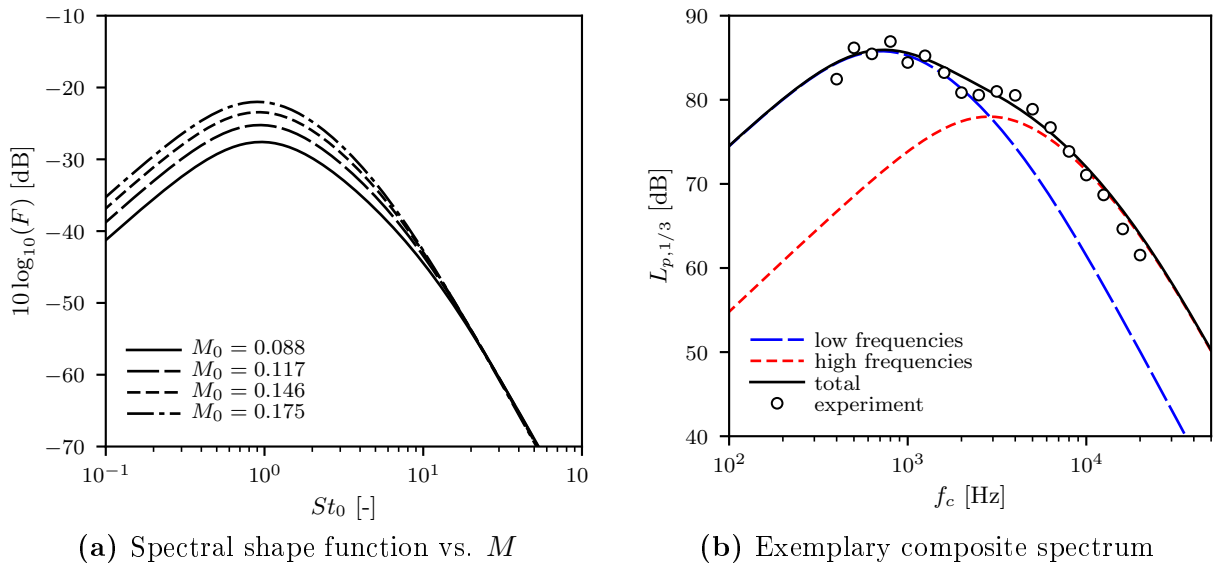


Figure 7.2.: Two-component representation of the FSE noise spectrum

7.2. Application and Validation

In this section the semi-empirical prediction model described in section 7.1 is validated against the experimental results of chapter 6 for the test cases discussed in chapter 4. The predicted spectra consist in the uncorrelated sum of a low-frequency spectrum and a high-frequency spectrum. For the low-frequency part, $l = 0.16c$ is used for the value of the characteristic length scale, whereas for the high-frequency part, the value $l = 0.04c$ is used. The velocity scale estimates are calculated based on the relationships of 7.1, respectively. The prediction results presented below are all for radiation direction $\varphi_x = 90^\circ$ and $\varphi_y = 0^\circ$.

7.2.1. Reference Configurations

The modelled total noise spectra, is computed using equation 7.3. For the low-frequency part of the spectrum we have,

$$L_{low} = 10 \log_{10}(F_{low}) + 55 \log_{10}(U_c/a_0) + 10 \log_{10}((l_{low}/r)^2) - 10 \log_{10}(I_{low}) + C_1, \quad (7.25)$$

and for the high-frequency part of the spectrum,

$$L_{high} = 10 \log_{10}(F_{high}) + 65 \log_{10}(U_H/a_0) + 10 \log_{10}((l_{high}/r)^2) - 10 \log_{10}(I_{high}) + C_2, \quad (7.26)$$

where $C_1 = 137$ and $C_2 = 160$ are empirical calibration constants. The total spectrum is given by,

$$L_{p,1/3} = 10 \log_{10}(10^{(L_{low}/10)} + 10^{(L_{high}/10)}). \quad (7.27)$$

The results of the prediction of equation 7.27 are plotted in figure 7.3 for the reference cantilever airfoil. In this figure, the spectra were calibrated to get the best possible representation of the measured data at $\delta_F = 30^\circ$ and $M_0 = 0.18$ using the empirical calibration constants C_1 and C_2 defined above. The predictions of figure 7.3 assume scaling exponents of $n = 5.5$ and $n = 6.5$, for the low- and high-frequency spectral components respectively. From now on, note that for all following cases, the calibration of figure 7.3 is retained, if not otherwise mentioned.

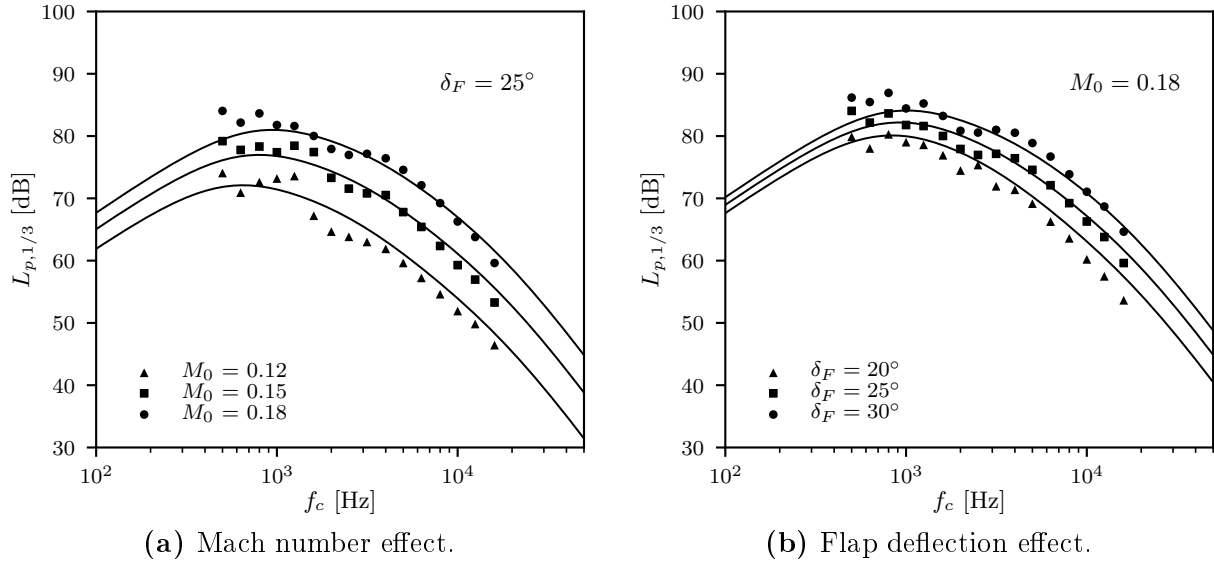


Figure 7.3.: A320-type cantilever wing FSE noise prediction. Solid symbols: measurements. Lines: prediction.

The predicted FSE noise spectra (lines) for the reference high-lift wing with half-span flap are presented in figure 7.4 along with the experimental data (solid symbols). To achieve a good agreement between experiment and prediction, an effective flap deployment angle, δ'_F , is used. This procedure is supported by CFD investigations of both geometries

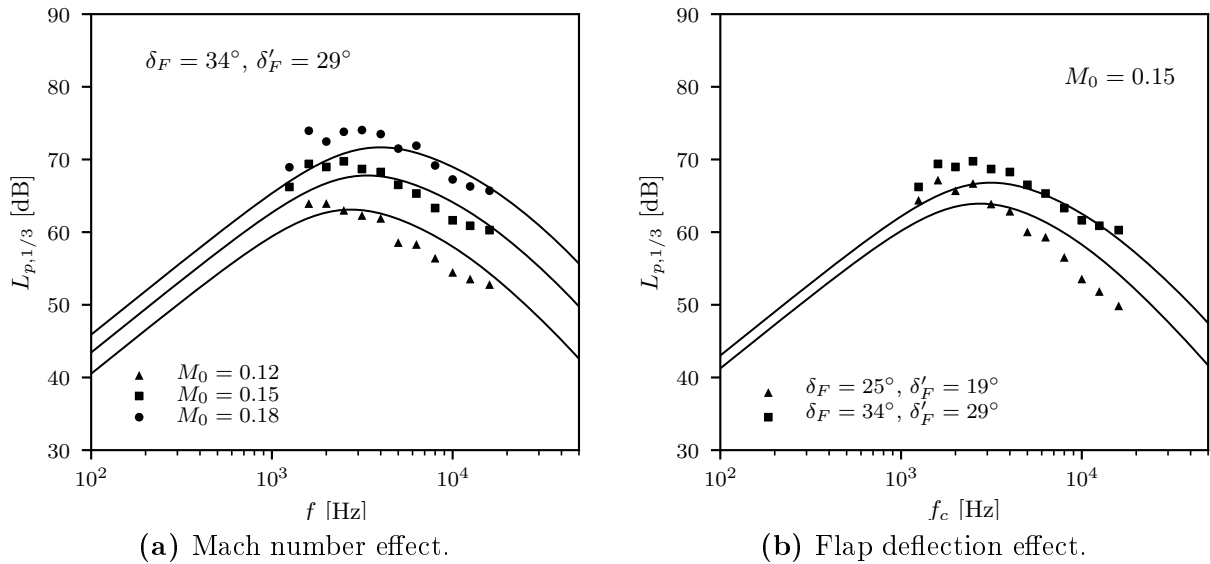


Figure 7.4.: High-lift wing model FSE noise prediction. Solid symbols: measurements. Lines: prediction.

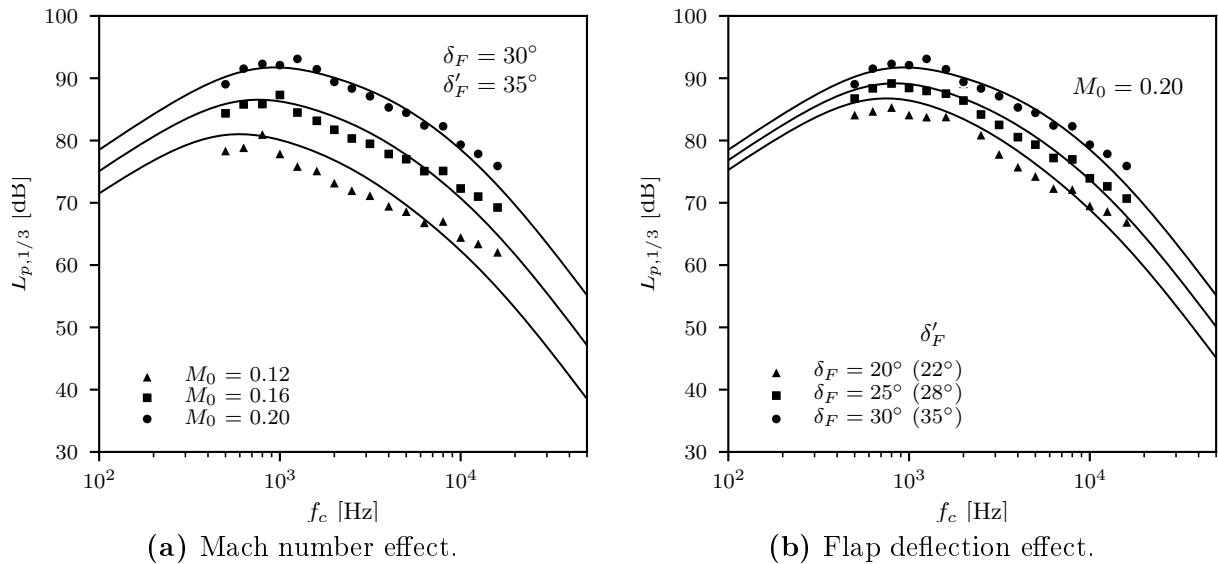


Figure 7.5.: Large scale reference cantilever wing FSE noise prediction for the baseline tip case. Solid symbols: measurements. Lines: prediction.

by Baumann [13]. FSE noise is related to the flap loading and, therefore, the hypothesis is that for similar geometries, similar noise levels are expected at equal loading (C_L). For the remaining results the determination of δ'_F can only be accomplished based on plausibility arguments and further CFD investigations would be required lend confirmation to those estimates.

In practice, knowledge of the C_L for the case of interest would, therefore, suffice to get the corresponding effective δ_F needed to predict the far field noise levels. The same exercise is done using data for the large scale reference wing in its baseline and sweep configurations (see figures 7.5 and 7.6). For the baseline configuration, a very good agreement between prediction and measurements can be obtained with slight adjustment for δ_F , as

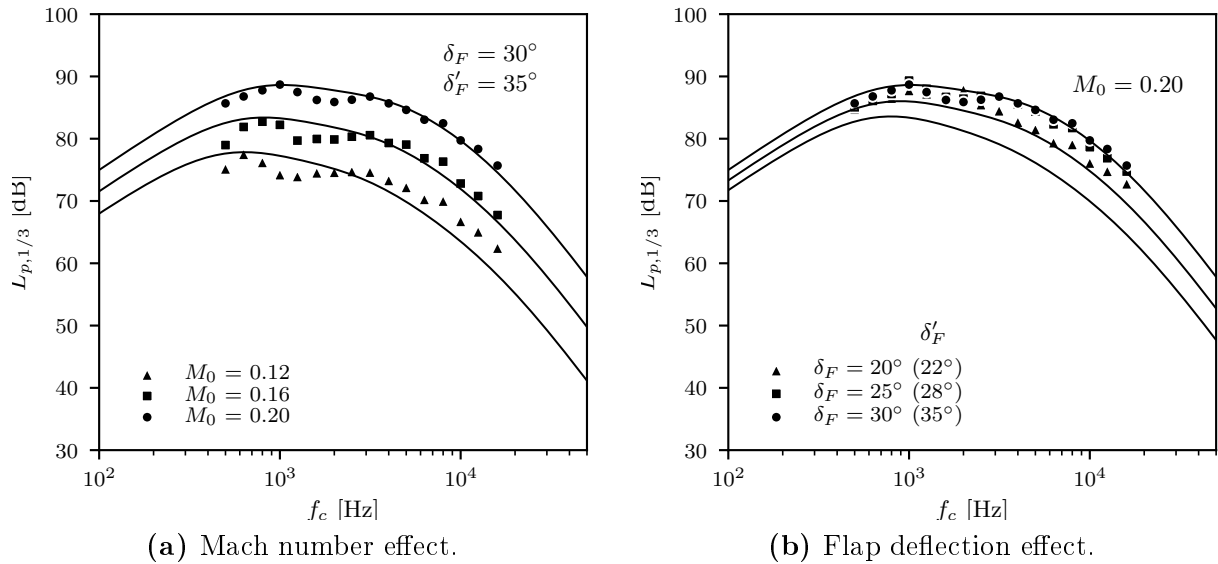


Figure 7.6.: Large scale reference cantilever wing FSE noise prediction, swept tip case. Here slightly modified calibration constants and length scales necessary: $C_1 = 134$ dB, $C_2 = 161$ dB, $l_{low} = 0.145c$, $l_{high} = 0.03c$. Solid symbols: measurements. Lines: prediction.

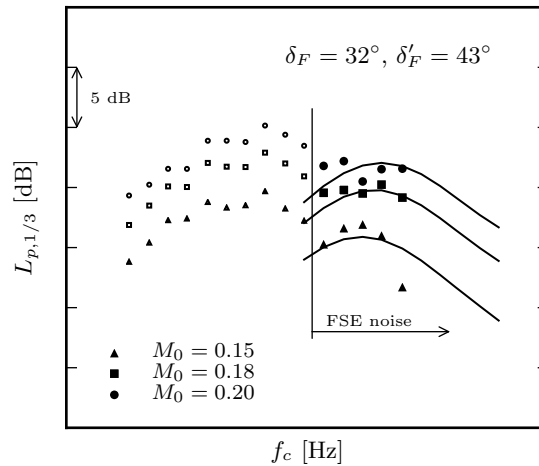


Figure 7.7.: Half-model FSE noise. Solid symbols: measurements. Lines: prediction.

expected. For the swept tip case, a very good prediction of the Mach number effect (e.g. figure 7.6a) requires usage of slightly modified calibration constants and lengths scales ($C_1 = 134$ dB, $C_2 = 161$ dB, $l_{low} = 0.145c$, $l_{high} = 0.03c$). Prediction of the impact of a change in δ_F (fig. 7.6b) is not satisfactory, even when trying to adjust the calibration and the lengths scales values. In fact, the far-field noise levels only weakly depend on δ_F . A change in δ_F has a great impact on the dynamics of the wing tip vortex and its interaction with the solid surface. In the case of swept tip, the vortex path no longer follows the wing tip but, remains a longer extent over the wing, further away from the tip edges. Its interaction with the surface being less dependent on a change in δ_F . In

that case, the streamwise development of the vortex certainly differs from the reference rectangular planform cases i.e. as indicated by the necessary adjustment of the calibration constants and vortex characteristic length scales.

In figure 7.7, far-field noise levels from a fully-configured 3D half-aircraft model with FNG wings are presented for three free-stream velocities. The outboard flap was deployed at $\delta_F = 32^\circ$ and the slats are retracted. The spectra shown in figure 7.7 are for the whole aircraft, the part due to the FSE is emphasized by the solid symbols. A good prediction is shown by the lines, for an effective $\delta'_F = 43^\circ$.

7.2.2. Complementary Test Cases, Profile Variations

A similar exercise is made with experimental acoustic data from the DU-96 and the Clark-Y cantilever wings e.g. figures 7.8 and 7.9 respectively. For the DU-96 case, a simple adjustment of the wing's effective angle of attack, without change to the calibration constants or characteristic length scale values, is sufficient to achieve the agreement between prediction and experiment shown in figure 7.8.

For the Clark-Y data, in figure 7.9, however, both the low- and high-frequency characteristic length scales had to be adjusted to $l_{low} = 0.18c$ and $l_{high} = 0.02c$, respectively. The first calibration constant was adjusted to $C_1 = 125$ dB. To which extent these estimates are realistic cannot be evaluated and would require more investigations, in particular using CFD to gain a better understanding of the tip flow field. Thus, the semi-empirical prediction model is not able to correctly predict FSE noise radiation for this second configuration.

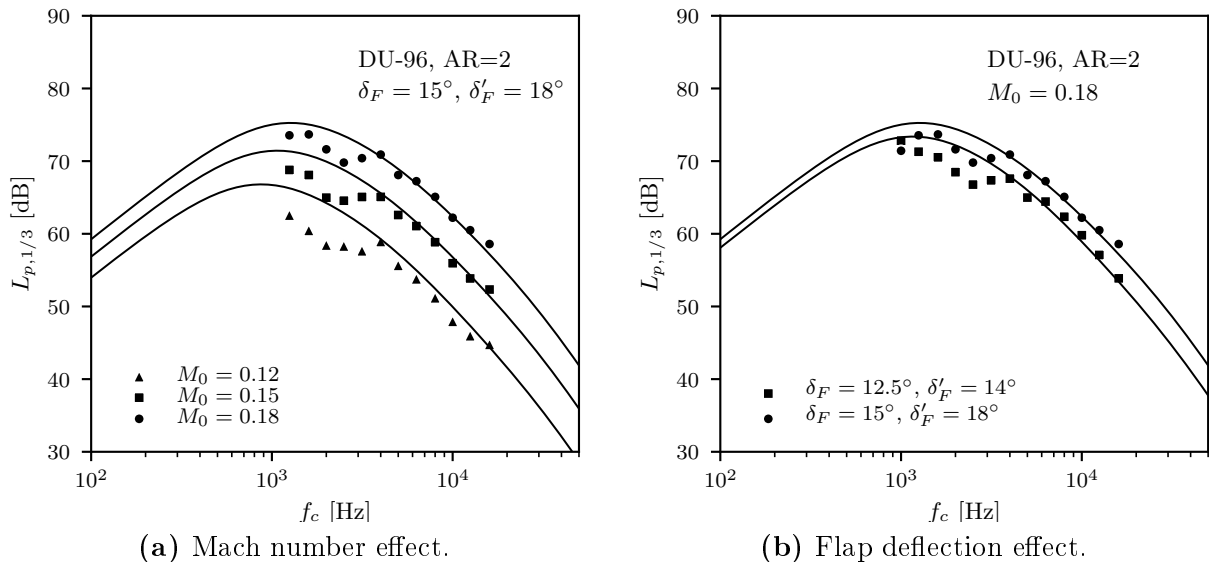


Figure 7.8.: DU-96 cantilever wing FSE noise prediction. Solid symbols: measurements. Lines: prediction.

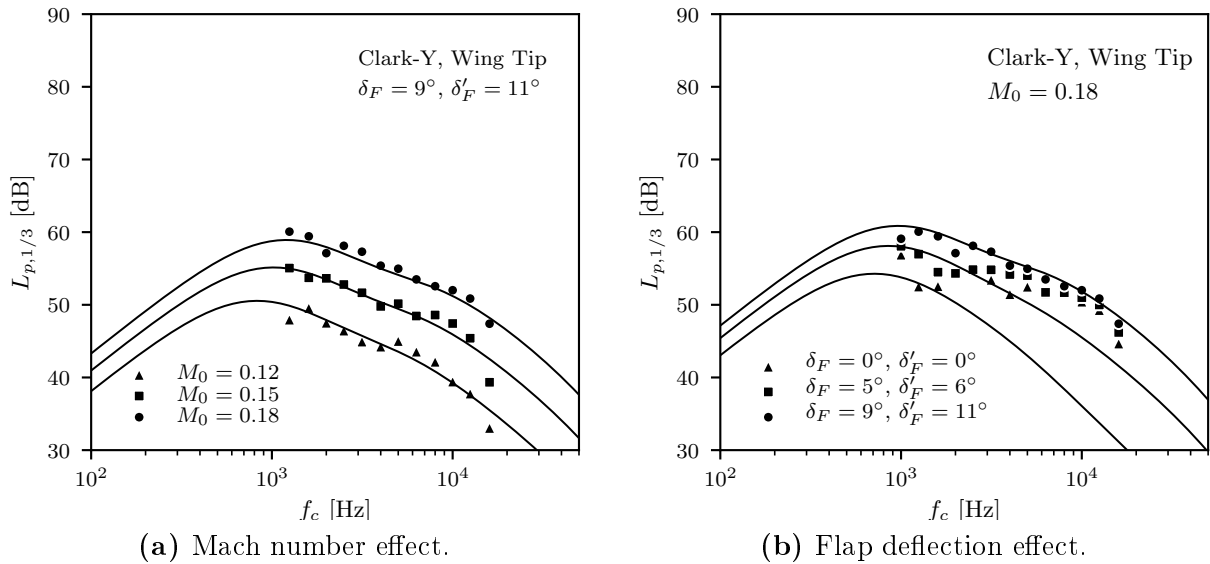


Figure 7.9.: Clark-Y cantilever wing FSE noise prediction. Solid symbols: measurements. Lines: prediction. Here modified length scales necessary: $l_{low} = 0.18c$, $l_{high} = 0.02c$. $C_1 = 125$ dB, $C_2 = 160$ dB

7.2.3. Complementary Test Cases, Tip Shape Variations

In figure 7.10, experimental results (symbols) for the reference cantilever wing with rounded tip edges are compared with the prediction (lines). To obtain the predicted curves in figure 7.10, the calibration constants need adjustment to $C_1 = 139$ dB and $C_2 = 140$ dB; without changing the characteristic length scales. Most of the noise generation occurs at low frequencies, explaining why the constant C_2 had to be reduced by 20 dB. The flow dynamics and scales are most probably strongly affected by the rounded tip FSE and detailed measurements of the tip flow field would be required for a better evaluation of the model's parameters.

7.2.4. Complementary Test Cases, Leading Edge Vane

This case is not relevant for the modelling as not enough experimental data are available. It is also suspected to be most probably a model scale problem which won't occur at full scale aircraft flaps. The impact of the leading edge vane on radiated noise levels was discussed in chapter 6.

7.2.5. Concluding Remarks and Unresolved Issues

The semi-empirical FSE noise prediction model presented in this chapter was shown to provide excellent results for wings of the FNG type with a rectangular planform and flat tip. For wings with a rectangular planform and flat tip but with a different section shape, the prediction model stills deliver good results after an adjustment of its length scales parameters. The assumed velocity and length scales relationships do, however, hold between wing families. Prediction of the effect of tip sweep on FSE noise is also possible, again through an adaptation of the model length scales parameters as well as by a change

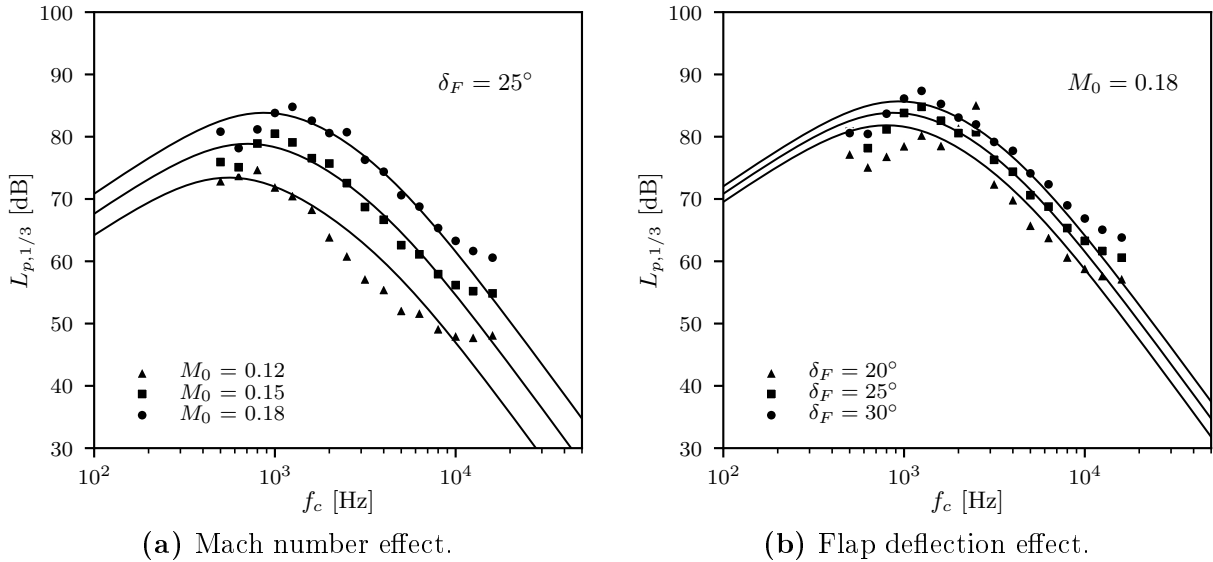


Figure 7.10.: Reference+Tip#2 cantilever wing FSE noise prediction. Solid symbols: measurements. Lines: prediction. Here slightly modified calibration constants necessary: $C_1 = 139$ dB, $C_2 = 140$ dB.

in the spectral components weighting. The effect of a tip shape variations on FSE noise cannot be correctly predicted using the current methodology.

From the preceding discussion, two important aspects still need to be resolved. **(1)** A crude approximation was first made by assuming the invariability of the characteristic length scale of the flow structures responsible for the noise production vs. a change in δ_F . This assumption was justified by the variable chordwise location at which the tip vortex size is evaluated. Larger flap deflection results in higher velocities and a shorter development length for the vortex. Although this seemed appropriate for a given family of profile and independently of the profiles chord lengths, changing the tip profile geometry seems to have an important impact on the flow structures characteristic dimensions. This issue requires a more detailed analysis of the tip vortex flow for a more extensive set of profile families through dedicated experiments and/or CFD. **(2)** When comparing noise radiation from different test configurations, an effective flap deflection angle has to be used to achieve a good agreement of the predicted FSE spectra with the measured acoustic data. This effective δ_F does not, however, corresponds to the free-stream (or flight) flap deployment angle. It merely puts the configurations on a similar basis with the reference cantilever wing, on which the prediction model was calibrated. Using C_L – or Γ -based approaches instead of δ_F to evaluate the correspondence between different models and configurations could be a good alternative. This aspect is crucial for a correct extrapolation of the wind tunnel results to the full-scale aircraft configuration. An evaluation of this correction is, however, beyond the scope of the present work and is left to future research efforts.

8. Conclusion and Perspectives

8.1. Motivation and Goal of the Work

Current efforts towards the development of next generation low-noise aircraft aim at using component based semi-empirical airframe noise prediction methodologies to achieve better, i.e. low-noise, designs. This approach relies on published component-based semi-empirical models, i.e. for each relevant component noise source existing on the airframe (no account is made in the present work of engine noise which is also an important contributor).

There is already an extensive body of work available in the literature which identifies the flap side-edge as an important contributor to the overall airframe noise of modern conventional aircraft. However, there currently exists only one semi-empirical model publicly available in the literature which can be used to perform design-to-noise studies. This prediction scheme was developed by Guo [54]. While the work of Guo represents an important improvement in flexibility and precision compared to earlier attempts [18, 55, 56], its use of geometry-related, i.e. fixed, parameters, poses an important limitation in generality, especially when the flap geometry differs from the basic rectangular planform with flat tip. Using the experimental database acquired in the present work, Guo's model was found to predict the effect of a change in Mach number on flap side-edge noise with a good accuracy, while the effect of change in flap deployment could not be accurately predicted. Lastly, although the work of Guo [54] does address the question of flap-side edge noise directivity modelling, there currently exists no satisfactory semi-empirical model for it.

8.2. Experimental Strategy

An experimental investigation of the noise originating from solid flap side-edges was performed with the goal of developing a new semi-empirical noise prediction scheme for flap side-edge noise circumventing the limitations of Guo's model. The chosen strategy consists in building an extensive database on the acoustic characteristics of a wide range of cantilever wings and flaps. The set of wind tunnel models chosen consists of four FNG wings of different chord lengths and aspect ratios. Two of them are investigated as cantilever wings (1:1.6 and 1:1 scale) while the other two are part of high-lift configurations (1:6, 1:8.5 scale). From these four wings, a reference case is defined (1:1.6 scale), for which the effect of tip shape variations (rounded tip edges, tip cavity) as well as that of a leading edge vane were investigated. For the reference test case, measurements of the tip vortex mean flow characteristics are also done. With these informations, a link was established between the measured acoustics and the flow field. Also, for the full-scale cantilever wing, the impact of raking the tip into the flow was investigated.

Furthermore, the database includes acoustic data for a cantilever wing with a DU-96 profile section (rectangular planform and flat tip) as well as for cantilever wing with a Clark-Y profile section (rectangular planform and flat tip).

8.3. Novel Results Derived from the Present Investigations

Flow Field Characteristics

1. The flow measurements enabled the identification of regions along the flap edges where large mean flow gradients exist. These regions are hypothesized to be regions of high turbulence activity and therefore to be centers of important noise production. At these locations, the diameter of the vortex and its local convection velocity are taken as characteristic length (l) and velocity (u) scales.
2. The velocity scales identified through the flow measurements are found to relate linearly to a variation of the flap (or wing) angle of attack. Therefore simple linear regression procedures can be used to derive an expression for the relationship between u and δ_F .
3. Similar linear relationships can be constructed between the flap lift coefficient, C_L vs. δ_F , and its tip vortex circulation, Γ_1 vs. δ_F . These relations should simplify greatly the task of comparing results from similar experiments done in different wind tunnel environment and using different wing models. Furthermore the lift coefficient of a wing as well as its tip vortex circulation are parameters which can be easily obtained from RANS computations. Only a preliminary step was taken in the present work to demonstrate the feasibility of using CFD to provide input parameters for the semi-empirical prediction scheme. Future work should concentrate on a more involved use of CFD for the quantification of the prediction model parameters.

Acoustic Source Characteristics and Scaling

1. The acoustic data for the reference configuration are found to be broadband in nature with its maximum noise level at a frequency of approximately 0.8 kHz (1:1.6 scale cantilever wing). Measured noise intensities obey a power law of the form $I = \mathcal{F}(U_0, \delta_F) \propto U_c^{5.5}$ for the low-frequency part of the spectrum and $I = \mathcal{F}(U_0, \delta_F) \propto U_H^{6.5}$ for its high-frequency part. Using the cross-flow velocity as a single global velocity scale i.e. $I \propto U_c^n$ does also achieves a good scaling of the effect of a change in Mach number but less for a change in δ_F . The least effective velocity scale to use remains the free-stream velocity, U_0 . These observations holds throughout the results for all four wing models with FNG section profile, but also for DU-96 and Clark-Y wing models, as long as they have a flat tip.
2. Results for a tip with rounded edges and a tip with a cavity are presented. Removing the edges of the wing tip has a great impact of the vortex formation and the resulting noise production. The tip vortex is less impeded in its development, and is allowed

to develop smoothly. This directly relates to an increase in low-frequency noise in the measurements, which is due to the increased tangential velocity in the tip vortex core. Also, the high frequency part of the spectrum appears to lose importance as a consequence of the smoother development of the tip vortex due to the lack of sharp edges.

3. The effect of a tip raking into the flow is also investigated using the full-scale flap in a cantilever setup. The results indicate a significant reduction in low-frequency noise due to a displacement of the tip vortex system inboard, away from the tip edges. Usage of raked-tip flaps with smooth or rounded edges could potentially result in a noise reduction on the order of 5 dB at model scale.
4. The flap side-edge noise directivity was investigated using a small aperture microphone array as well as standard far-field microphones. The results indicate that the low frequencies spectral data scale according to a proportionality law $p^2 \propto u^{5.5}$, thus advocating for a classical edge scattering mechanism [40]. However, the distinct rear-arc radiation maximum is not consistent with the classical mechanism of edge scattering of flow turbulence which would imply a cardioid directivity with a maximum in upstream direction. The sound radiation can be attributed to a mixture of classical edge scattering in combination with unsteady force fluctuations on the airfoil as a consequence of vortex unsteadiness [69, 71, 118] and sound wave diffraction [54].
5. With regard to the rear-arc dominant directivity of flap side-edge noise, it was shown that a close similarity exists with landing configuration flight test directivity data. Based on knowledge gained from earlier research efforts [37, 38] and the above observation, one can state that for an A320-type aircraft, with single-slotted trailing-edge flaps, above a full-scale frequency of $f = 2$ kHz, both slat and flap side-edge noise contribute equally to the rear-arc acoustic radiation of the high-lift system.
6. At high frequencies, spectral data scale according to $p^2 \propto U_H^{6.5}$, which is close to the typical dipole-like source radiation [29]. It was shown in section 6.1.1 that the maximum in SPL found at 3.15 kHz is related to the merging of the primary tip vortex (forming on the tip face) with the secondary vortex (forming on the airfoil's suction side), subjecting the flow field to strong sudden local fluctuations. This suggests as source mechanism, a combination of classical edge scattering and quadrupole-like sound generation due to intense and highly unsteady force fluctuations on the airfoil as a result of vortex unsteadiness during the merging process [69, 71, 108, 113]. The directivity patterns indicate also a possible shielding of the acoustic source by the wing leading to rear-arc maximum in radiation. Higher SPL levels are measured for $\varphi_y < 0$ indicating that diffraction and reflection on the tip's face are important.
7. A comparison between the acoustic results for the 1:6 scale cantilever wing vs. those from the full-scale cantilever wing do not reveal a strong Reynolds number dependency.

Semi-Empirical Modelling

1. A modelling approach for FSE noise is presented which is based on characteristics of the flow field in the vicinity of wing tip edges. Along the lines of Guo [54], the proposed scheme assumes the total flap side-edge noise spectrum to be the summed contributions from two independent source components. Unsteady vorticity fluctuations, originating from the unstable pressure side shear layer, sweeping over the forward half of the upper tip edge at high velocities is assumed to be the source of mid-to-high frequency noise. Vortex instabilities, over the suction side surface near the flap tip aft half, is assumed to be the main contributor in the low-to-mid frequency range.
2. Using the flow measurements, the characteristic length and velocity scales of both the low- and high-frequency source mechanisms are quantified. The spectral shape of each spectral contribution to the total FSE noise is represented according to Guo's formulation [54] adapted to make use of the identified local parameters. Because the proposed velocity scales are dependent on flap deployment, an accurate prediction of both Mach and flap angle effects is achieved. There is no need for additional correction factor, as proposed by Guo [54].
3. The proposed semi-empirical model provides an accurate representation of FSE noise for a large range of wing configurations. Ranging from a single isolated cantilever wing to a complex half-model with a conventional high-lift wing. The successful application of the model between different wing models tested in different wind tunnels requires the definition of an effective deployment angle, resulting in an offset of the predicted spectra to better fit the experimental data. Plausibility arguments do support the required adjustment of δ_F in the prediction. Further research efforts need, however, to be put into establishing methodologies for the comparison of results from different experiments and for the extrapolation of wind tunnel results to the full-scale aircraft.
4. Modelling of the flap side-edge noise directivity is accomplished through the combination of sets of point sources to represent the measurement data. We concentrate on dealing with only two frequencies of interest corresponding to the frequencies at which peak low- and high-frequency noise radiation occurs. Only the azimuthal and polar directivity are modelled. Contrary to assumptions encountered in the literature, our results suggest a rear-arc radiation pattern when considering the fly-over case, while the azimuthal directivity has a complex lobed structure.

8.4. Open Questions and Perspectives

A new semi-empirical model was proposed which can accurately predict noise produced by flaps with rectangular planform and flat tips. More precisely, both the Mach number dependency and flap deployment angle of FSE noise are accurately represented by the methodology presented herein. The prediction scheme is also valid for models of various sizes, i.e. through a change in chord length but not in model thickness. The prediction scheme relies solely on the knowledge of the wing's tip chord length and its effective

angle to the incoming flow. The latter being defined as the C_L or Γ -equivalent angle corresponding to that of the reference cantilever wing.

Although the proposed semi-empirical prediction model does work well in many situations, it still suffers from the following limitations:

1. Accurate noise predictions are possible for wing models of a certain family. Variations in section profile for example, are not well rendered by the prediction scheme. Although, in those cases, the proportionality relationship between noise intensity and the flow speed still remains valid, the frequency of the maximum noise level is not correctly predicted. This result is indicative of the need to input accurate flow information for the specific wing model considered. Since flow measurements were performed only at the reference wing, it is clear that a simple transposition of these results cannot be made between families of wing models. Future efforts should be focused on the extension of the database to a more diversified set of wing models. This could be accomplished through dedicated acoustic and flow experiments and/or RANS computations.
2. Furthermore, it was found that the prediction scheme is not able to correctly predict the effect of a change of tip shape, i.e. round tip, rounded edges or cavity. In this case, both the velocity and length scales identified at the reference wing are not representative of the wing tip flow field and, therefore both the velocity proportionality of the sound intensity as well as the frequency of its maximum noise level cannot be correctly predicted. Here also, future efforts should be focused on the extension of the database towards a wider set of wing tip shapes. This aspect is of practical importance when considering an application of the prediction scheme to noise generation at wind turbine blades.
3. Preliminary efforts were done in the present work regarding the establishment of an equivalence of the flap deployment angle between different test cases. Lift (C_L) and circulation (Γ) equivalent angles do provide a possible avenue into dealing with this difficulty. However, more validation is still needed to ensure the robustness of the method. This issue has to be dealt with in dedicated flow experiments and RANS computations. This is a necessary first step towards the later extrapolation of the results to the full-scale configuration. This remains, however, outside of the scope of this thesis and is left to future work.

A. Experimental Setups

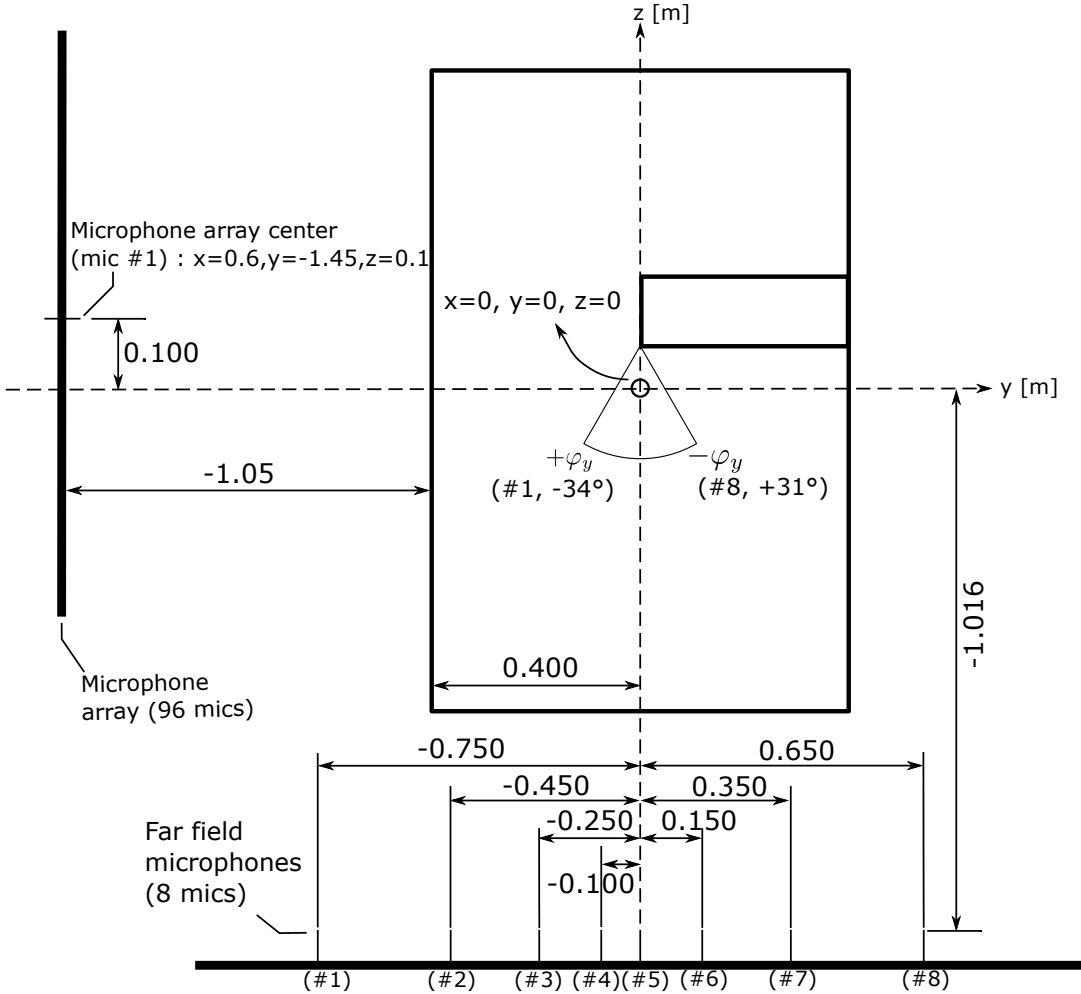


Figure A.1.: Reference cantilever wing setup in the AWB. Coordinate system definition and microphone locations (towards upstream perspective). Microphone array located on the left hand side, far-field microphones mounted on a linear support lying on the ground. The flow direction is in positive x direction.

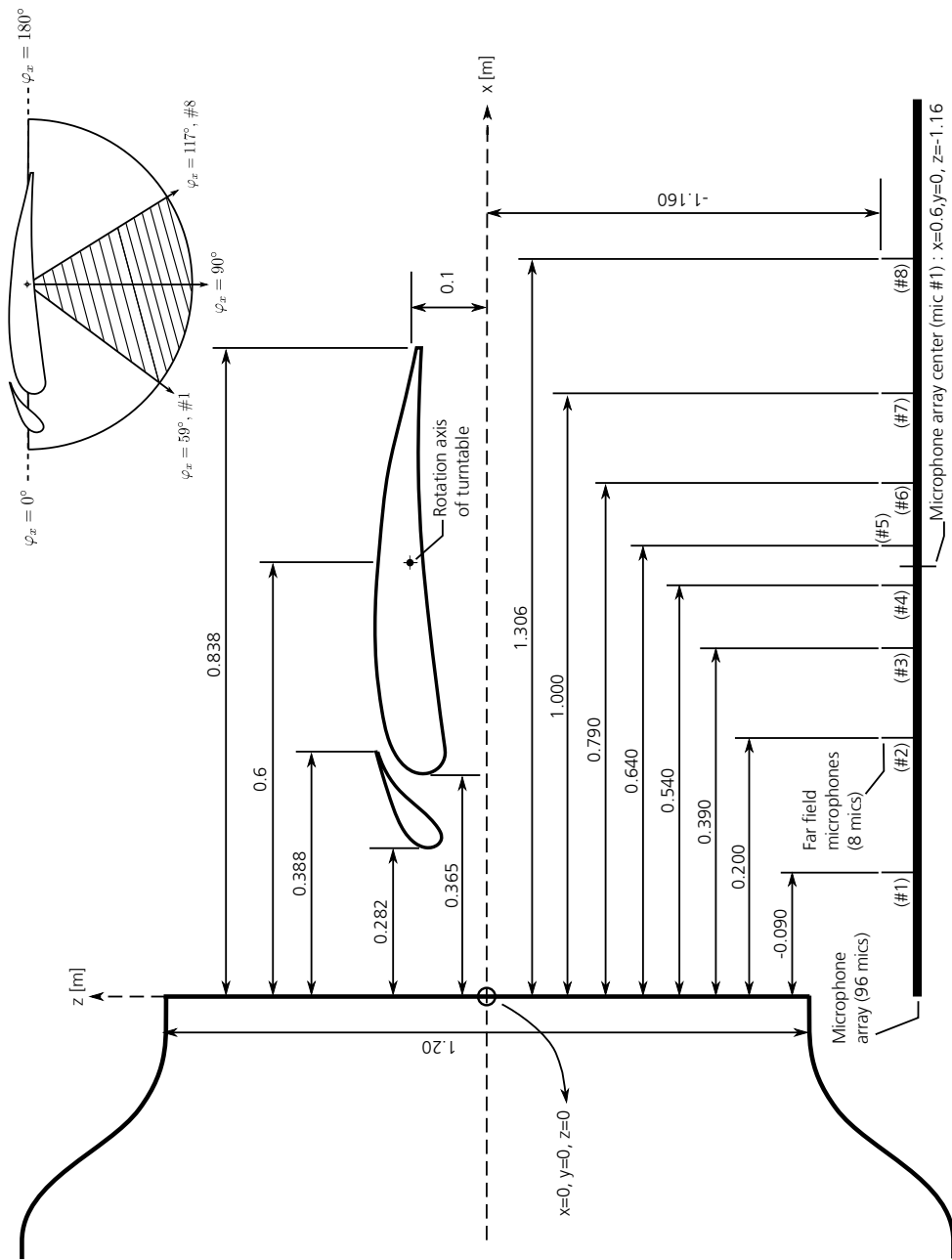


Figure A.2.: Reference cantilever wing setup in the AWB. Coordinate system definition and microphone locations (side perspective). Note that free-field microphone #1 is actually located upstream of the nozzle exit plane (negative x -coordinate). Both the microphone array and the free-field microphone are below the wing. The flow direction is in positive x direction.

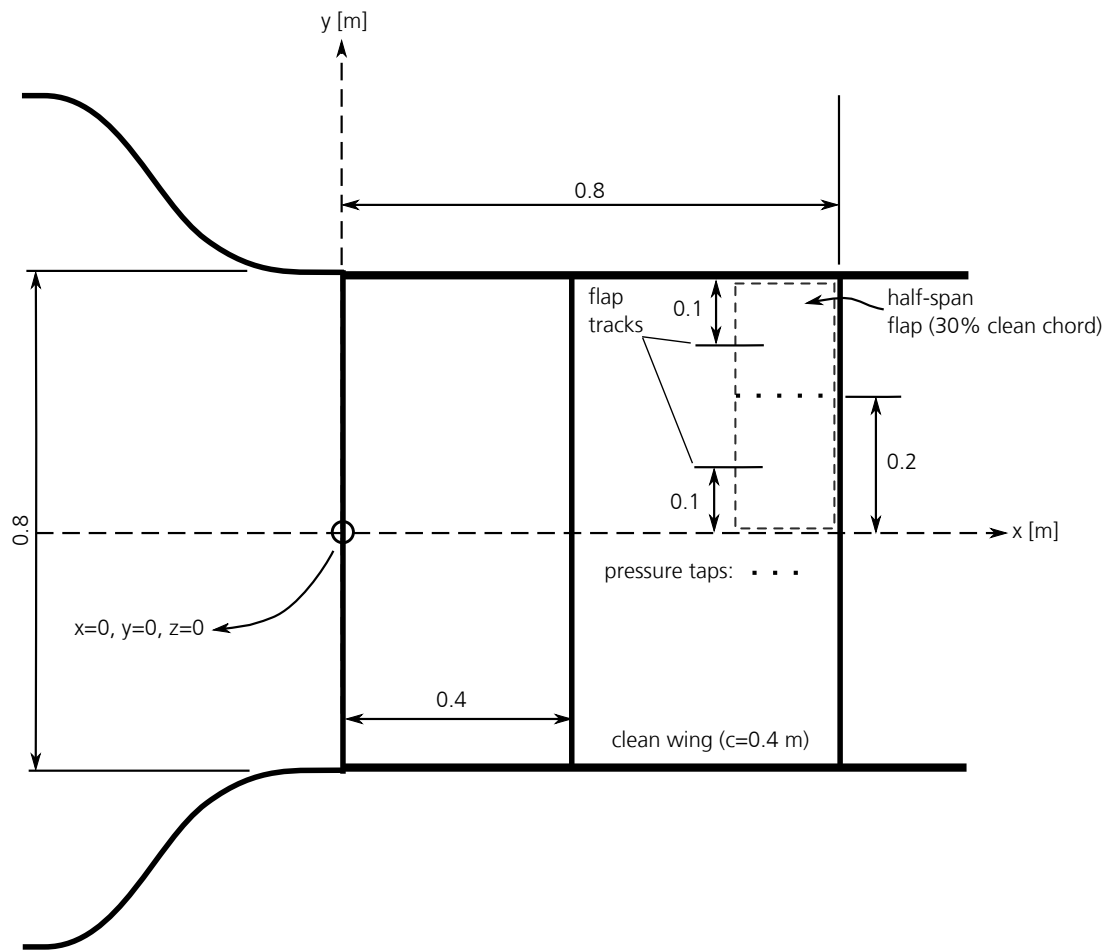


Figure A.3.: Reference high-lift wing setup in the AWB. Coordinate system definition (top perspective). The flow direction is in positive x direction.

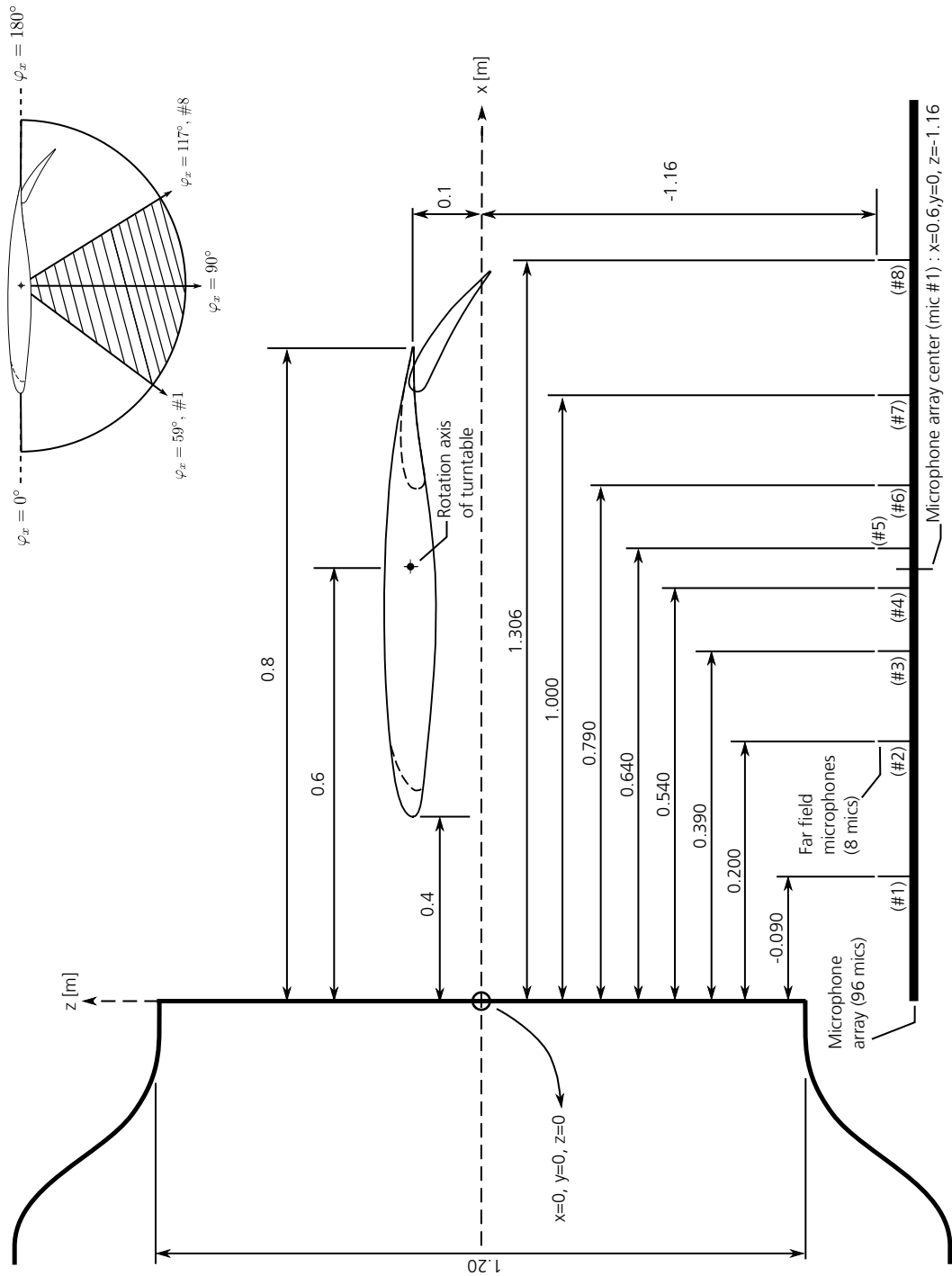


Figure A.4.: Reference high-lift wing setup in the AWB. Coordinate system definition and microphone locations (side perspective). Note that far-field microphone #1 is actually located upstream of the nozzle exit plane (negative x-coordinate). Both the microphone array and the far-field microphone are below the wing. The flow direction is in positive x direction.

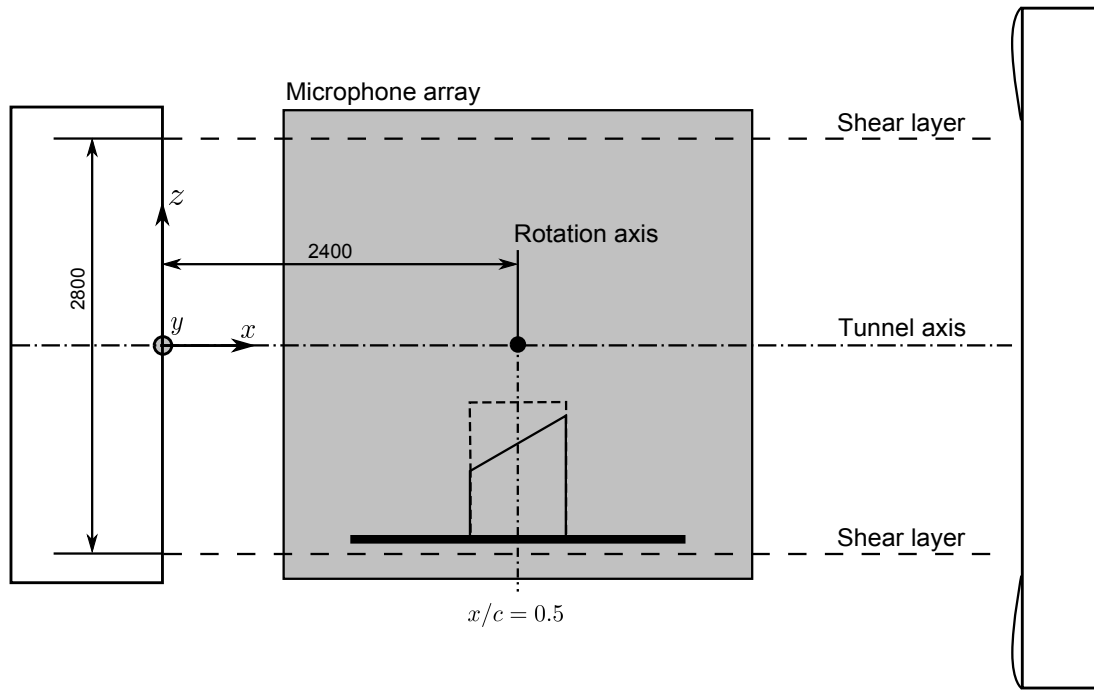


Figure A.5.: Large scale cantilever wing setup in the NWB. Coordinate system definition and microphone array location (top perspective on the model). The flow direction is in positive x direction.

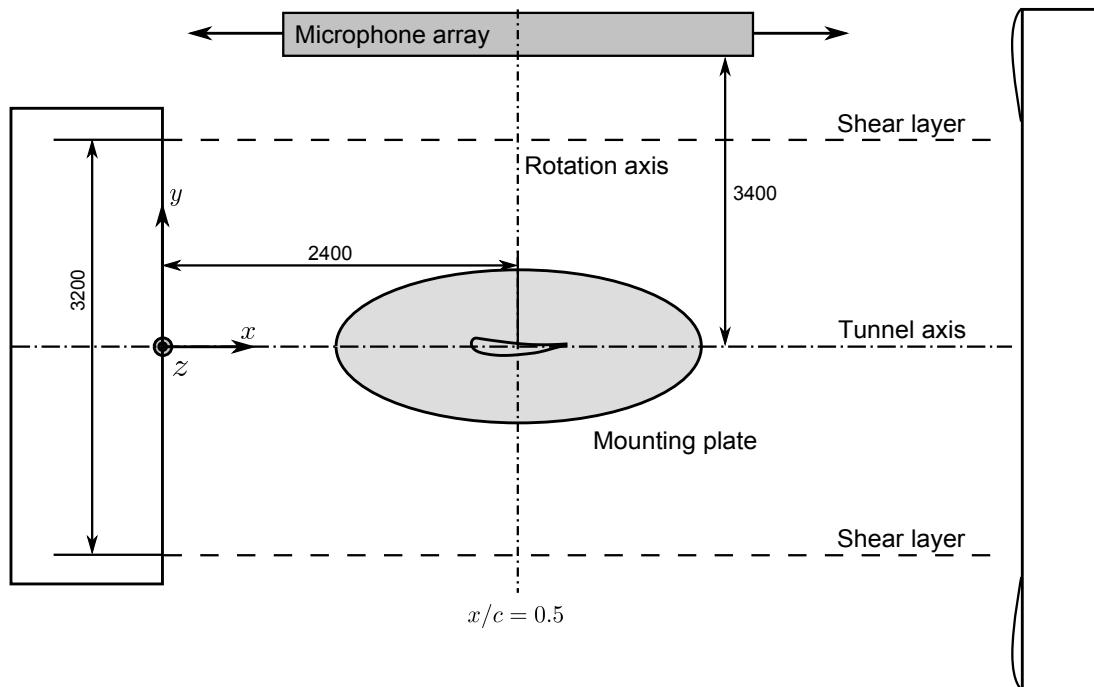


Figure A.6.: Large scale cantilever wing setup in the NWB. Coordinate system definition and microphone array location (side perspective on the model). The flow direction is in positive x direction.

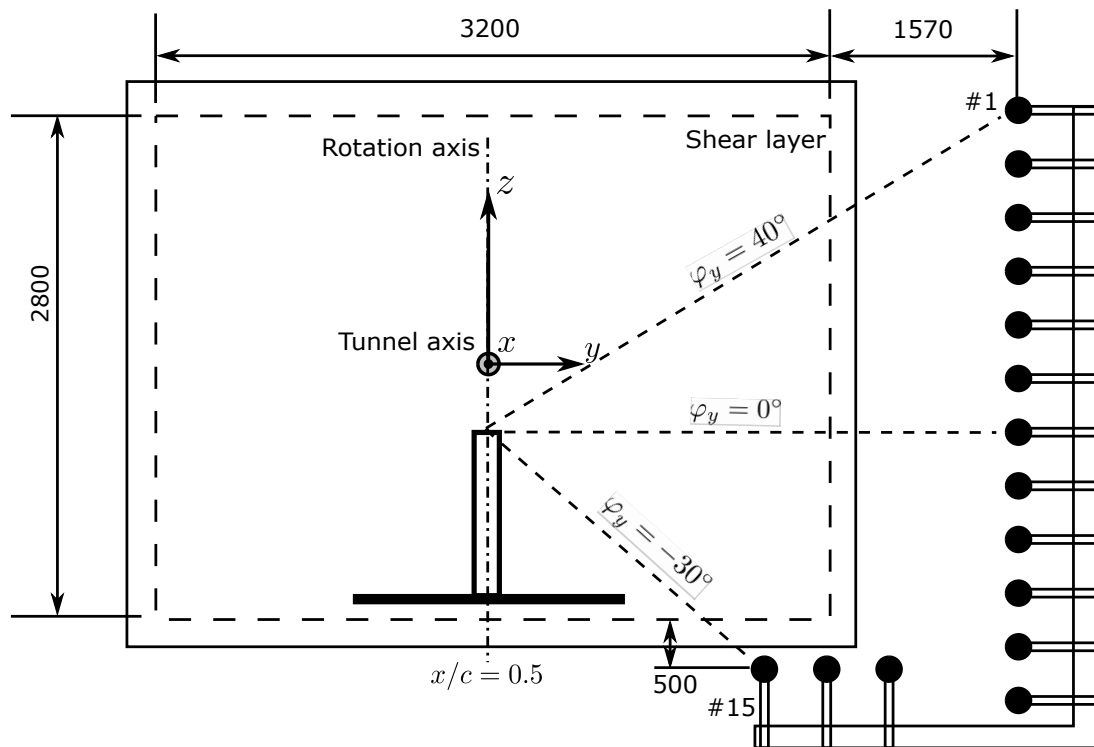


Figure A.7.: Large scale cantilever wing setup in the NWB. Coordinate system definition and free-field microphone locations (downstream perspective on the model). The flow direction is in positive x direction.

B. Static Pressure Distributions

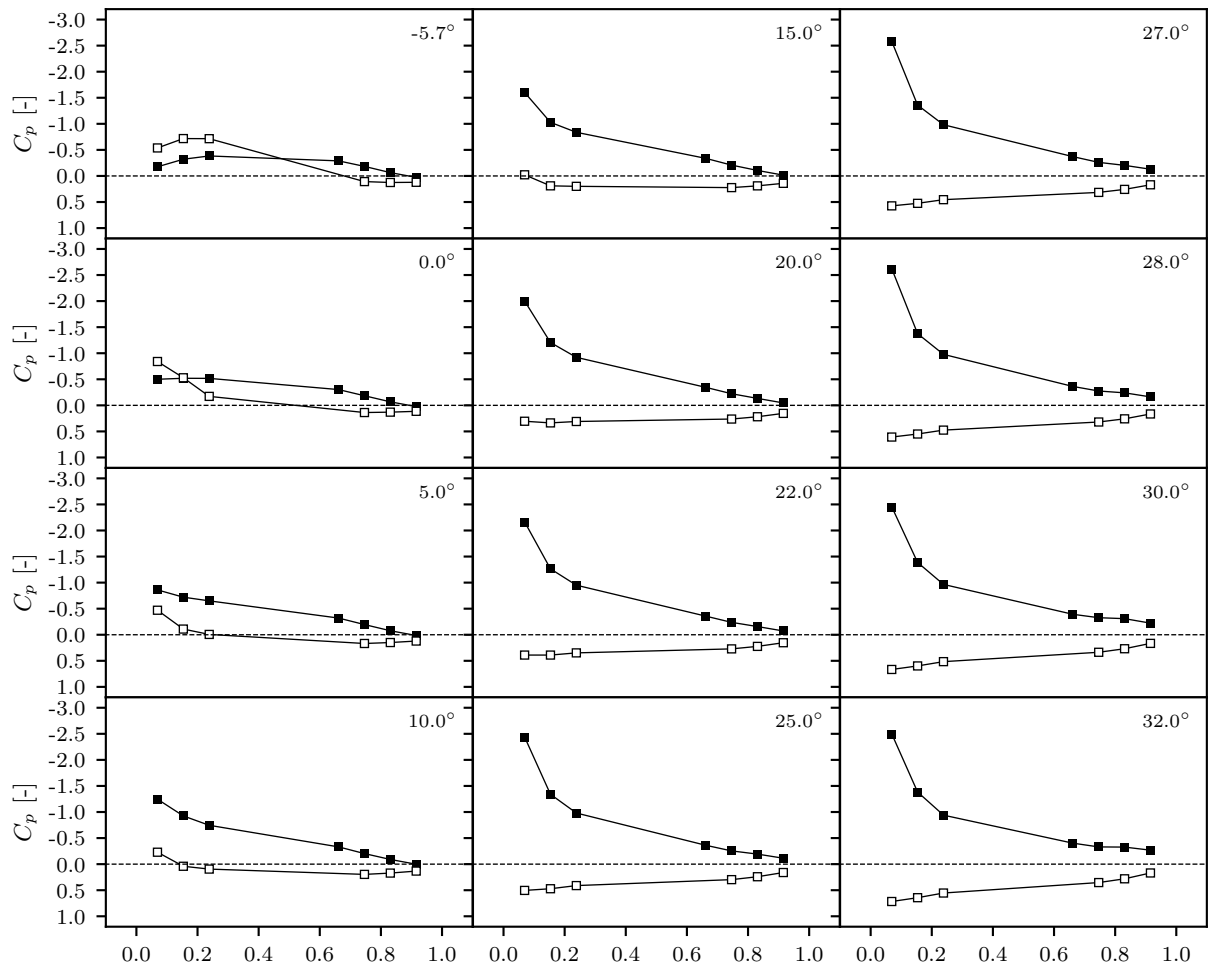


Figure B.1.: Distribution of surface static pressure coefficient (C_p) vs. normalized streamwise position (x/c) for different incidence angles. Configuration: Reference, $U_0 = 60$ m/s. Solid symbols: suction side. Empty symbols: pressure side.

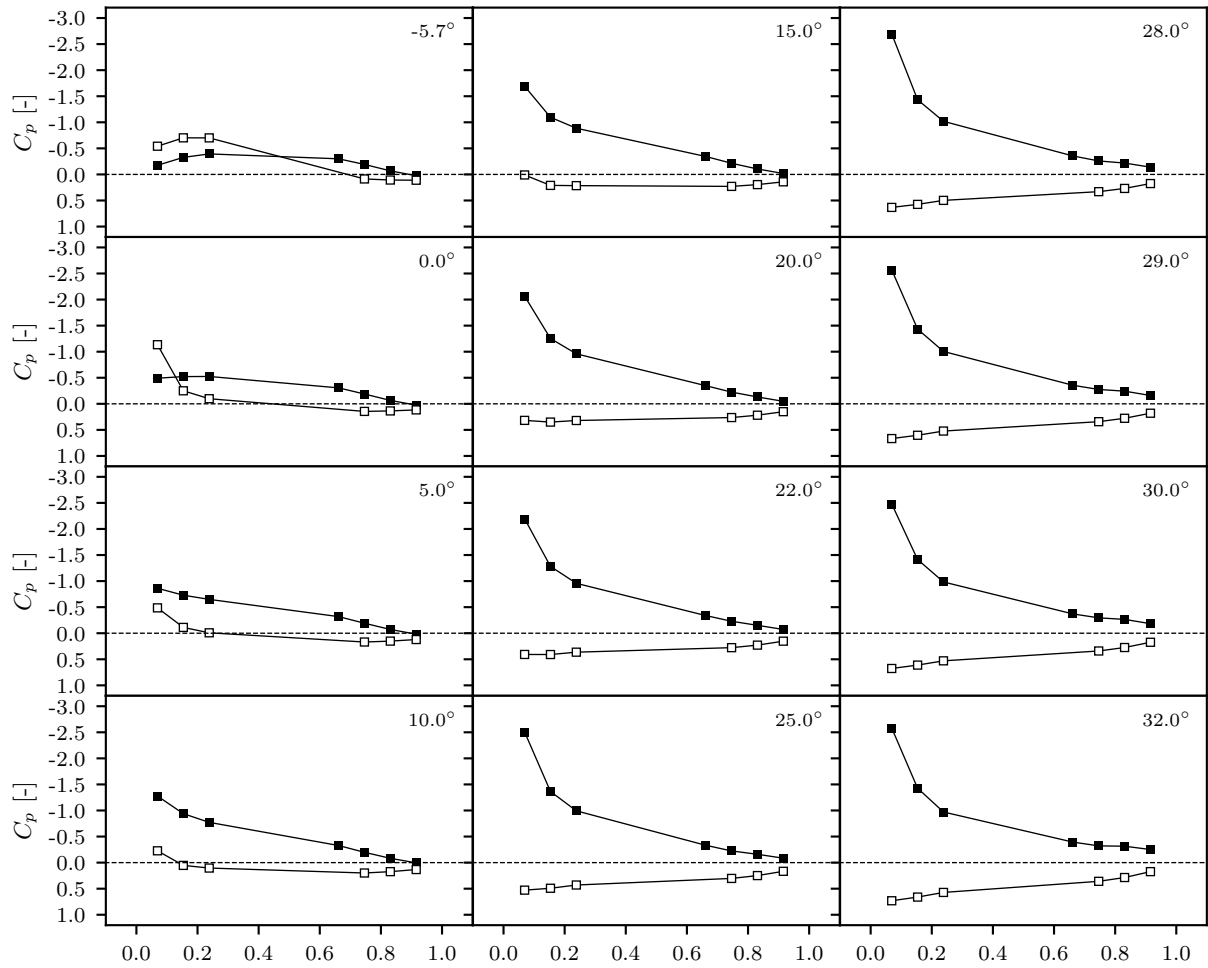


Figure B.2.: Distribution of surface static pressure coefficient (C_p) vs. normalized streamwise position (x/c) for different incidence angles. Configuration: Tip #1, $U_0 = 60$ m/s. Solid symbols: suction side. Empty symbols: pressure side.

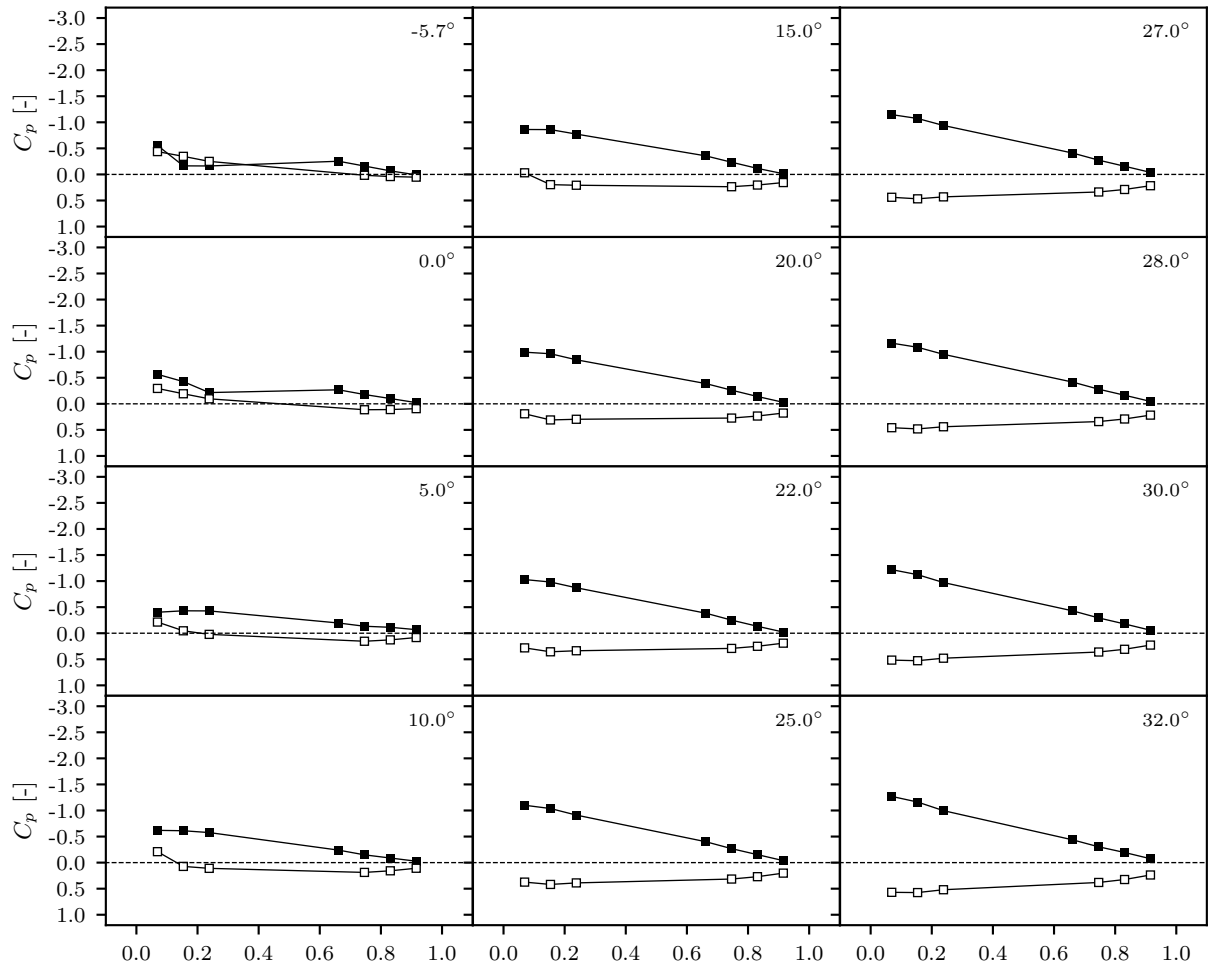


Figure B.3.: Distribution of surface static pressure coefficient (C_p) vs. normalized streamwise position (x/c) for different incidence angles. Configuration: Tip #1+Vane, $U_0 = 60$ m/s. Solid symbols: suction side. Empty symbols: pressure side.

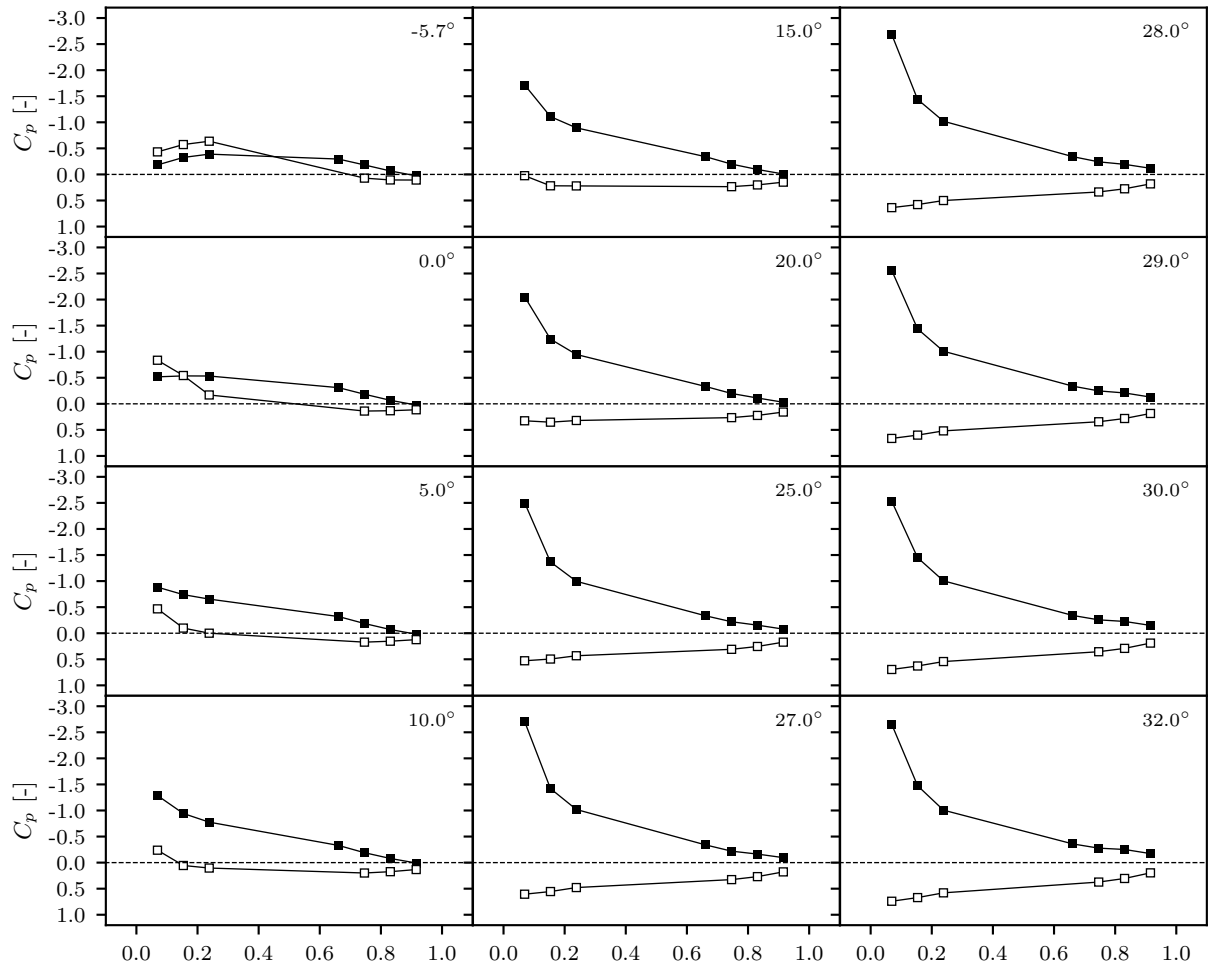


Figure B.4.: Distribution of surface static pressure coefficient (C_p) vs. normalized streamwise position (x/c) for different incidence angles. Configuration: Tip #2, $U_0 = 60$ m/s. Solid symbols: suction side. Empty symbols: pressure side.

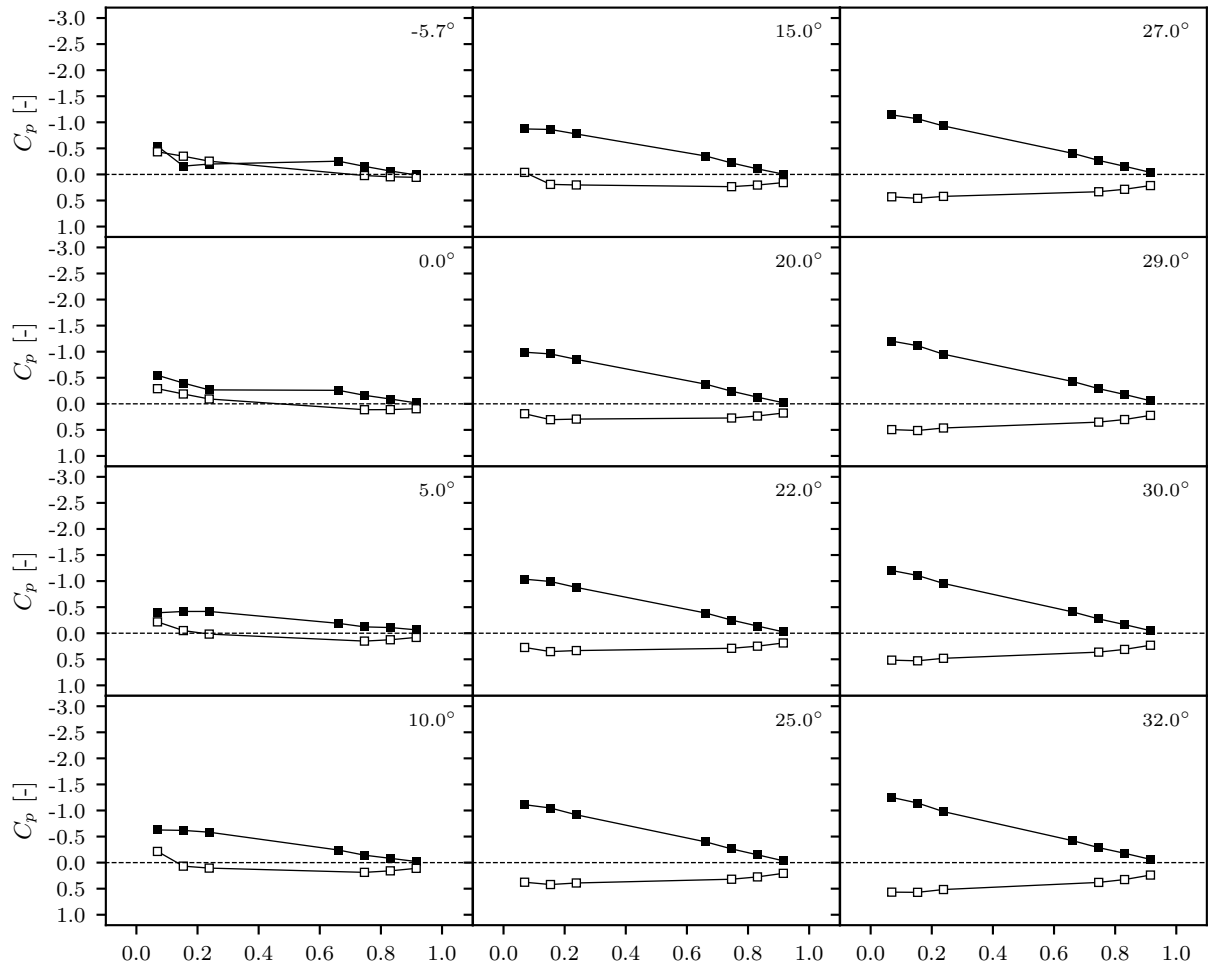


Figure B.5.: Distribution of surface static pressure coefficient (C_p) vs. normalized streamwise position (x/c) for different incidence angles. Configuration: Tip #2+Vane, $U_0 = 60$ m/s. Solid symbols: suction side. Empty symbols: pressure side.

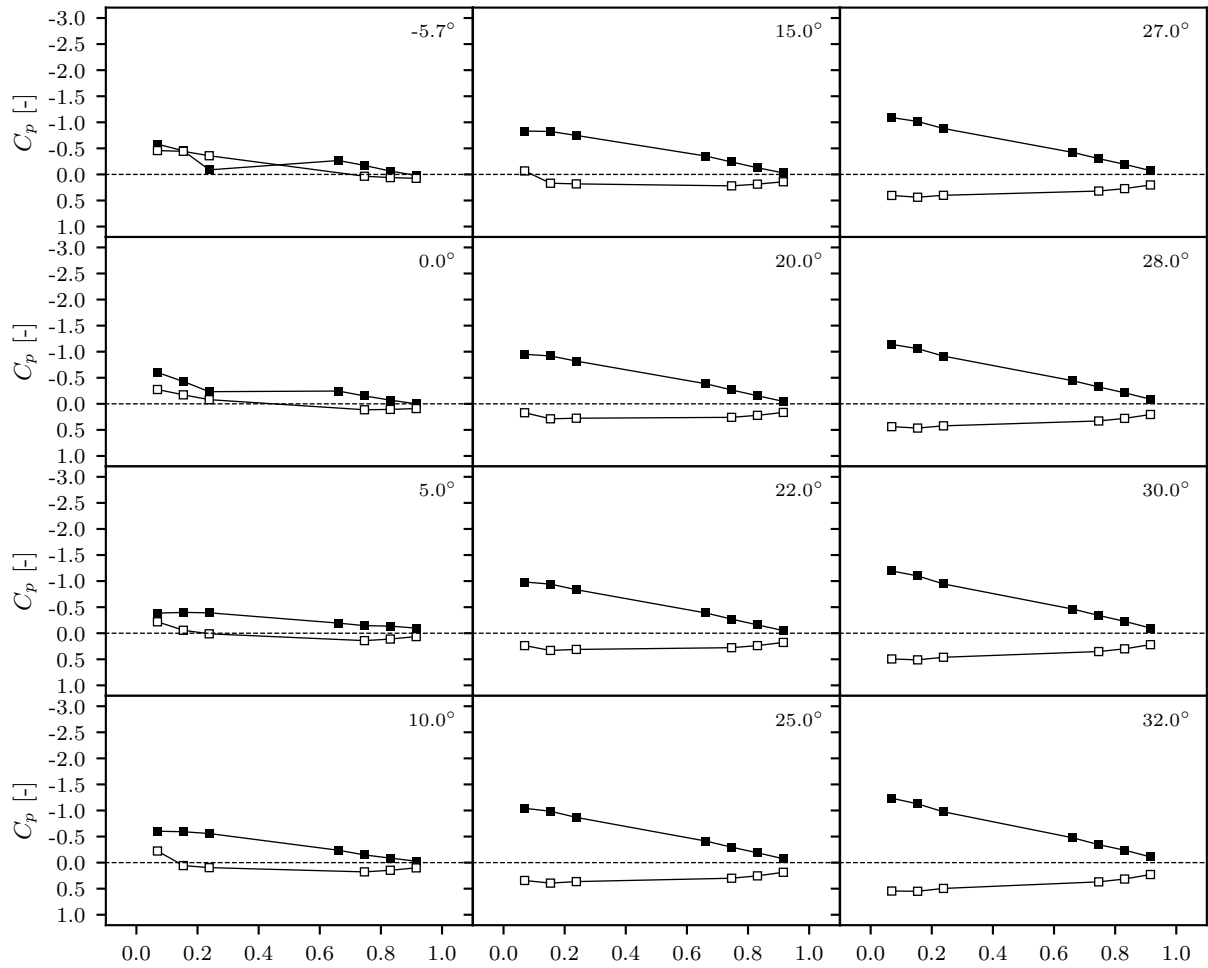


Figure B.6.: Distribution of surface static pressure coefficient (C_p) vs. normalized streamwise position (x/c) for different incidence angles. Configuration: Vane, $U_0 = 60$ m/s. Solid symbols: suction side. Empty symbols: pressure side.

C. Spectral Results for Various Tip Modifications

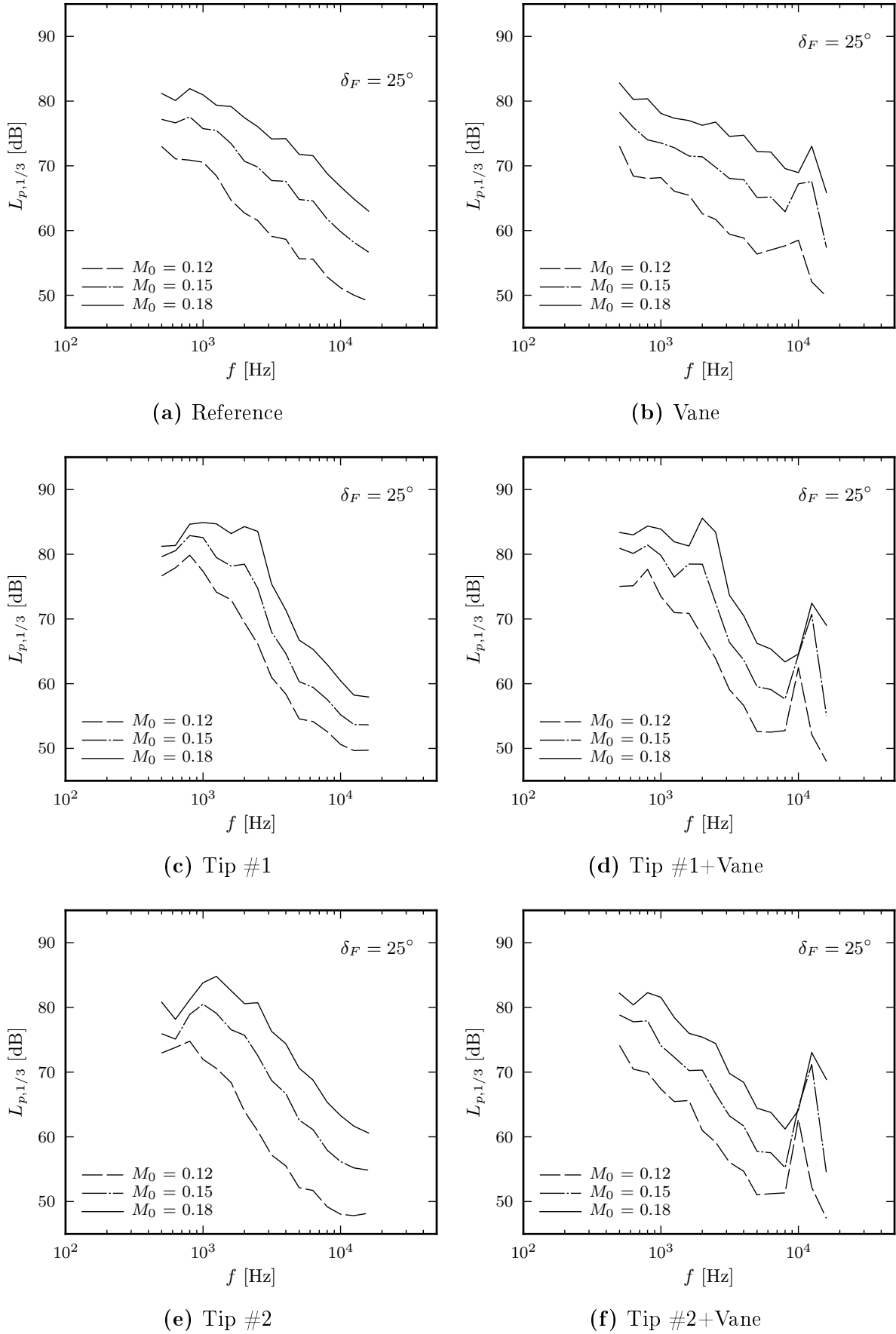


Figure C.1.: Effect of M_0 , bottom view, 1/3-octave band spectra. Power integration of the microphone array noise maps. $\delta_F = 25^\circ$.

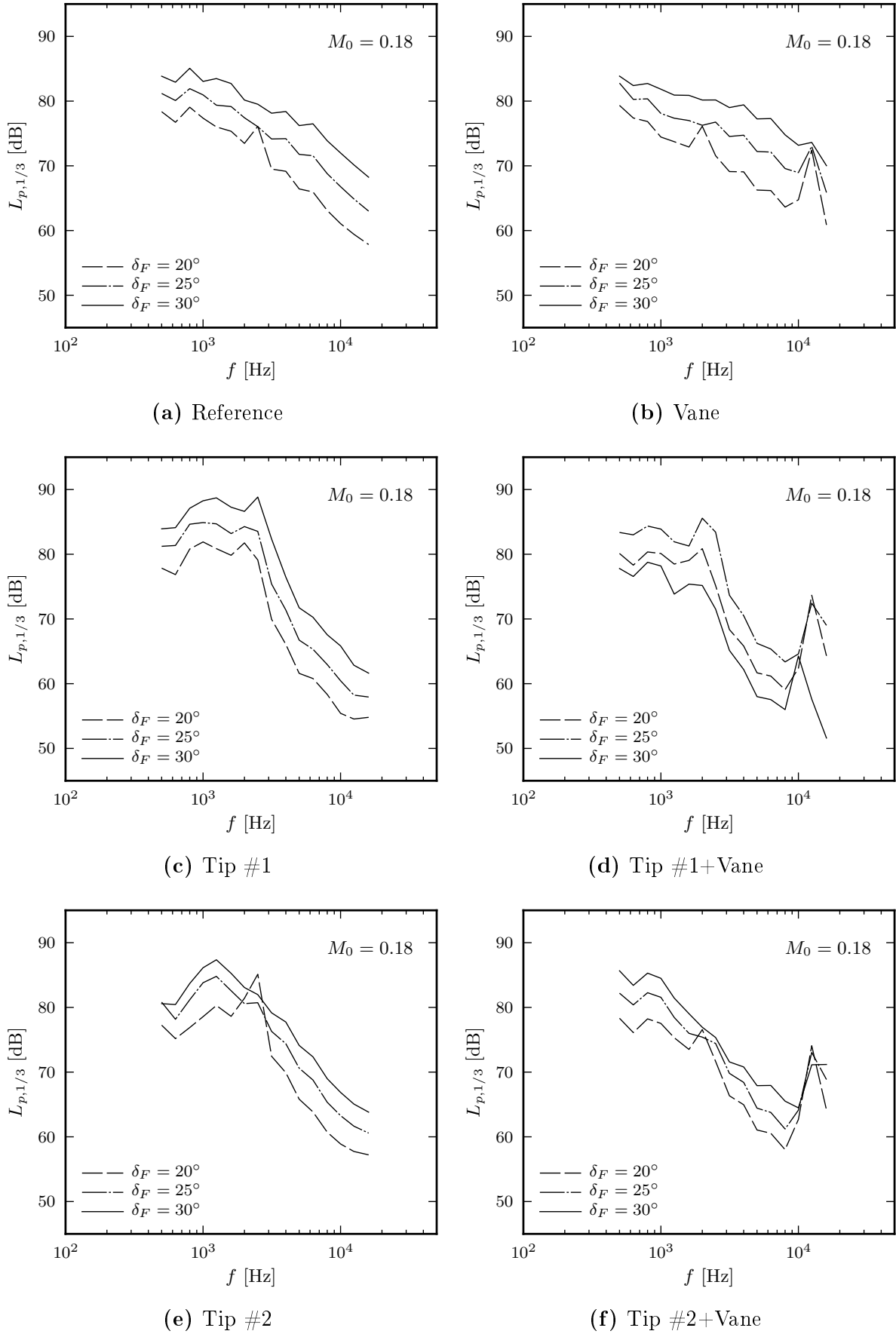


Figure C.2.: Effect of δ_F , bottom view, 1/3-octave band spectra. Power integration of the microphone array noise maps. $M_0 = 0.18$.

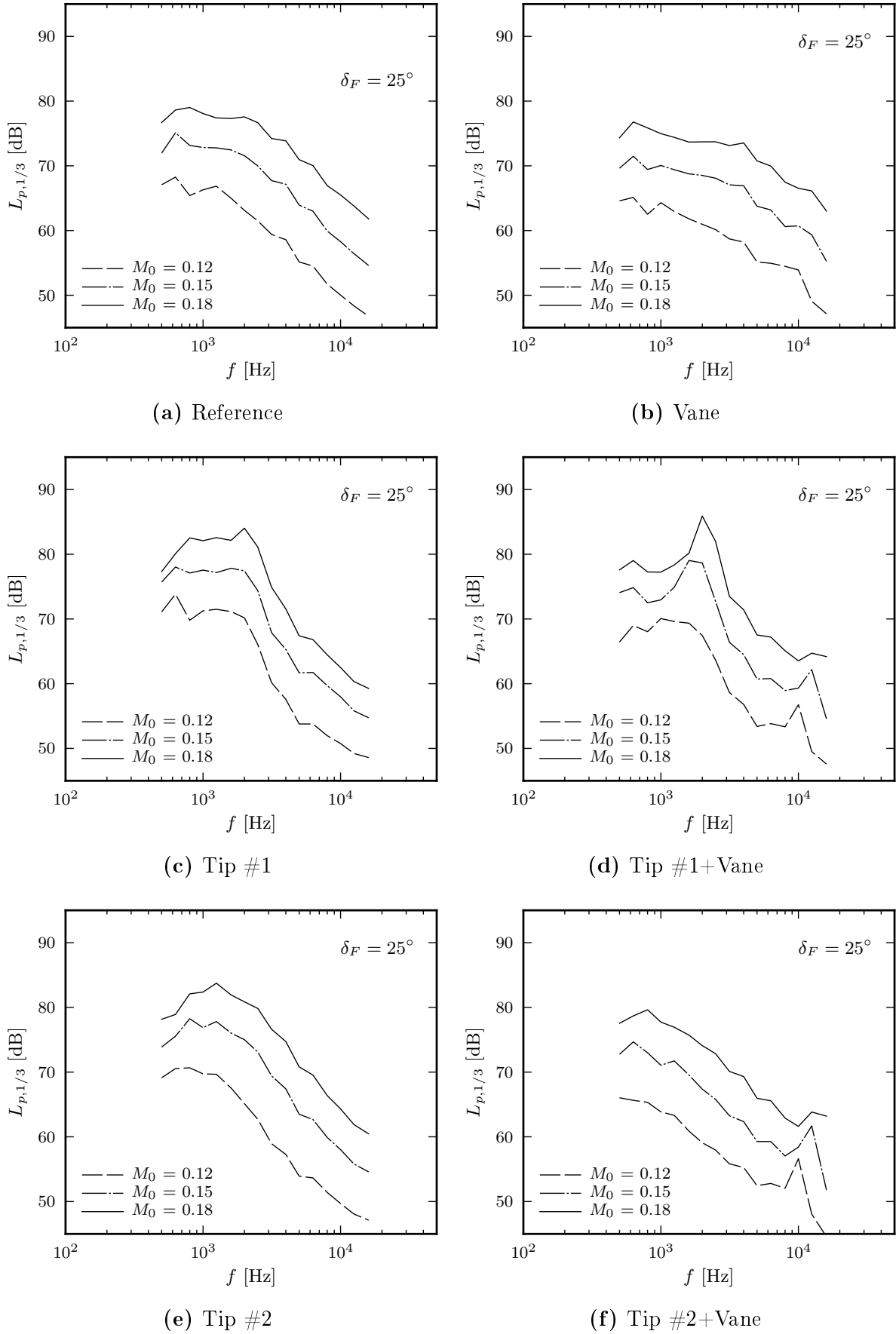


Figure C.3.: Effect of M_0 , side view, 1/3-octave band spectra. Power integration of the microphone array noise maps. $\delta_F = 25^\circ$.

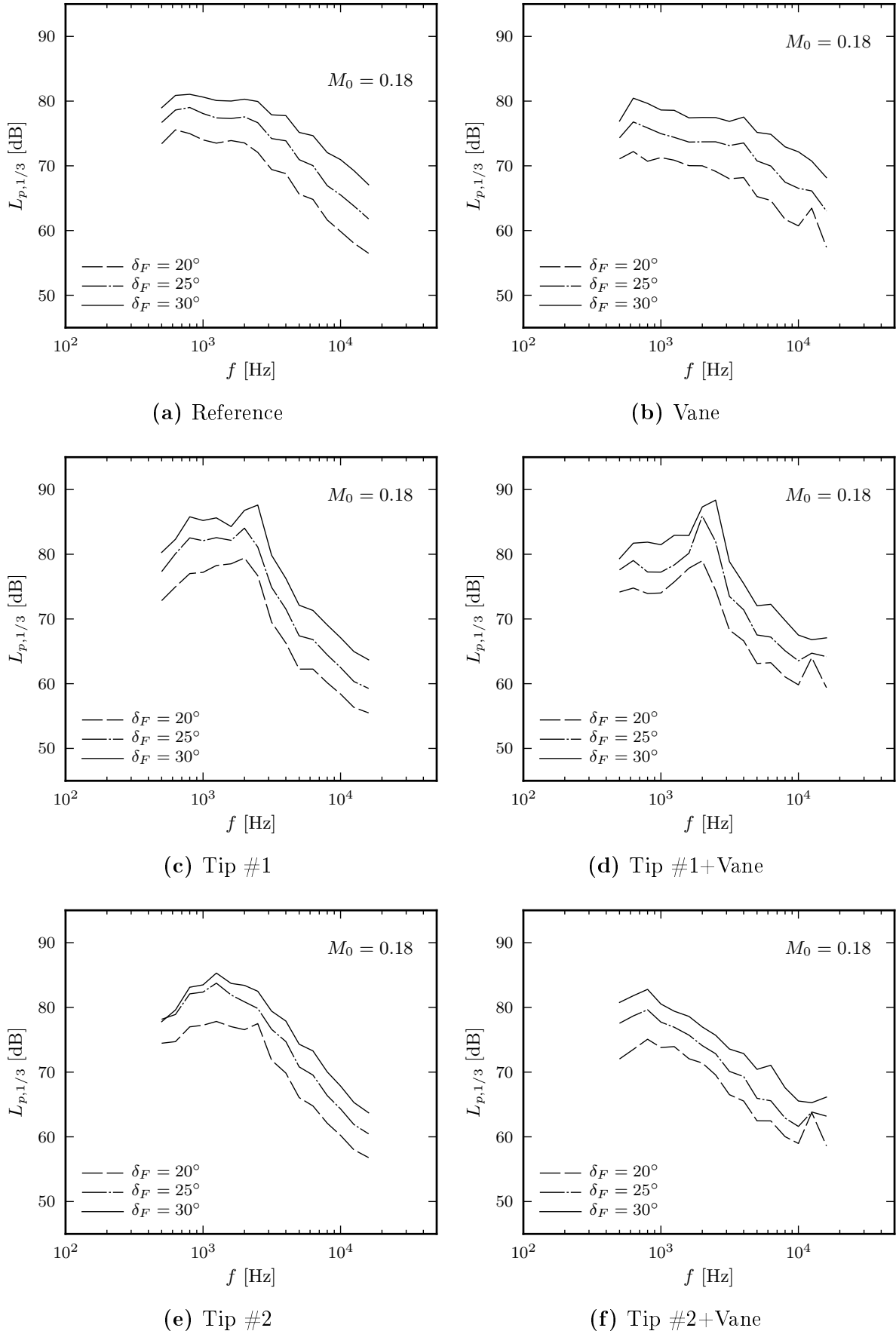


Figure C.4.: Effect of δ_F , side view, 1/3-octave band spectra. Power integration of the microphone array noise maps. $M_0 = 0.18$.

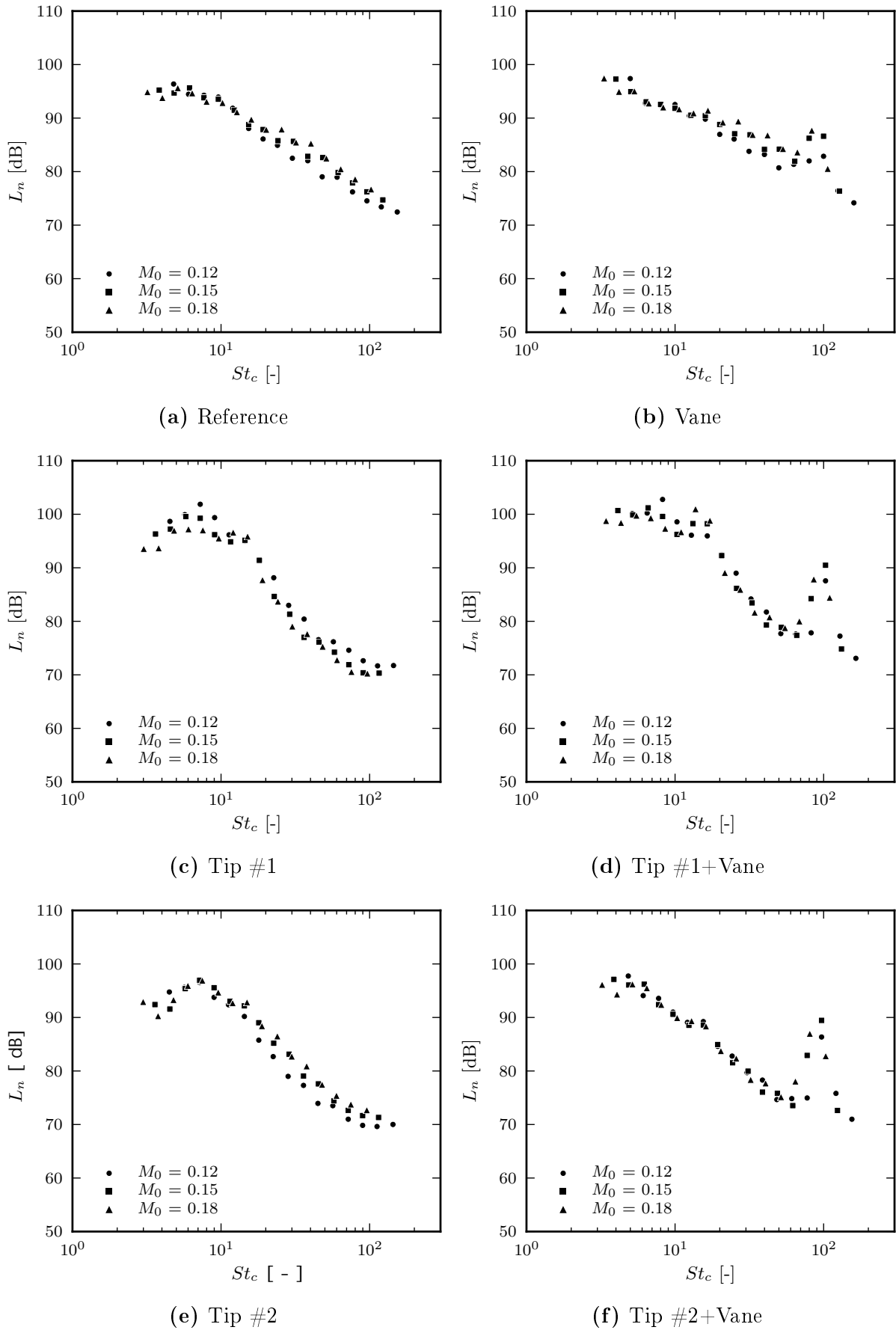


Figure C.5.: Scaled noise spectra. Bottom view. Effect of M_0 , $\delta_F = 25^\circ$.

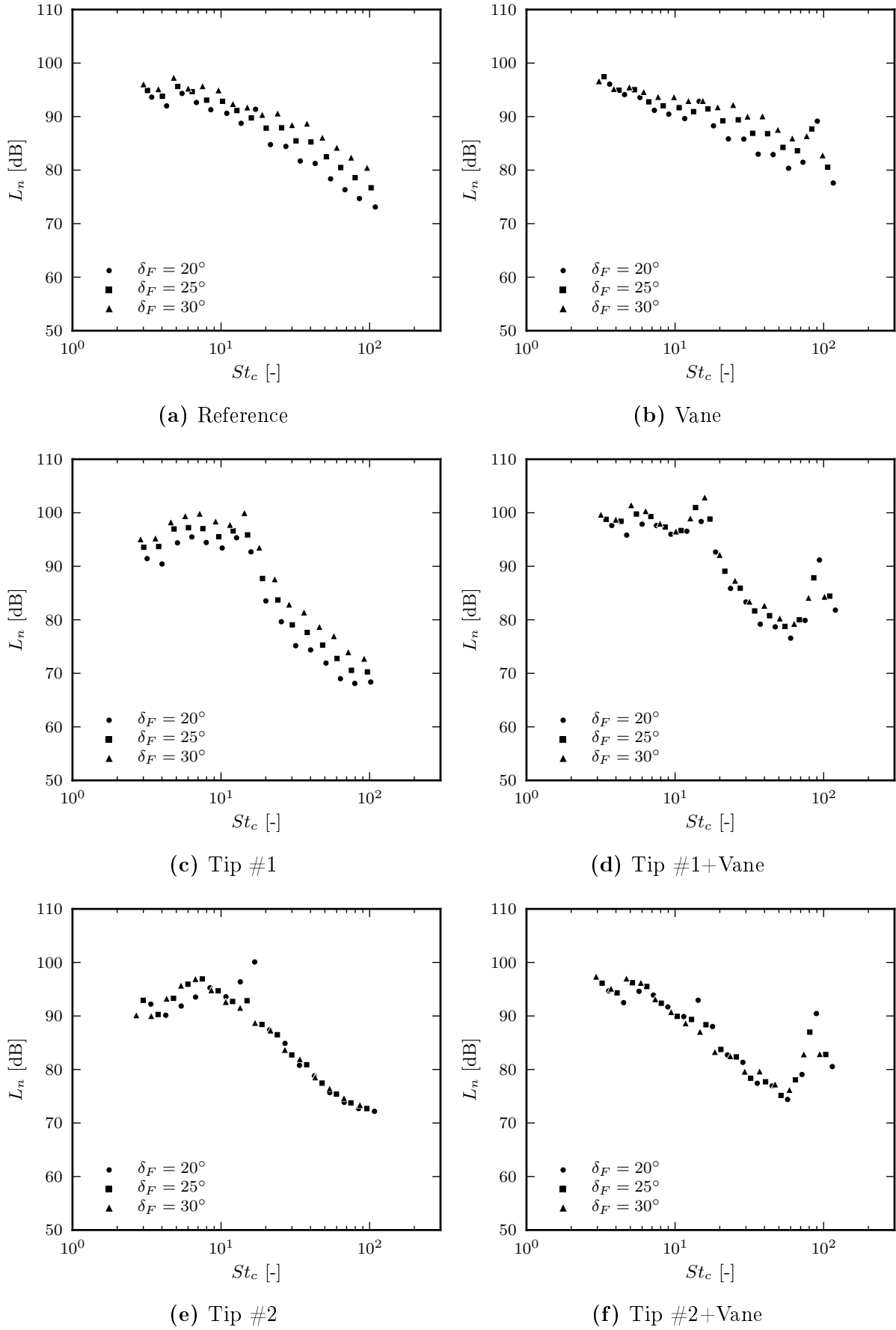
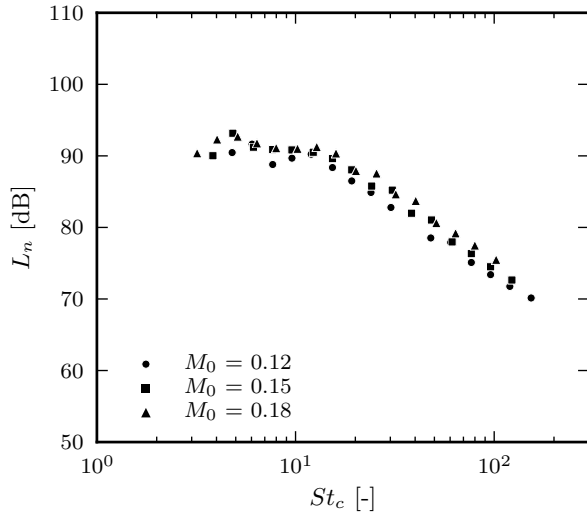
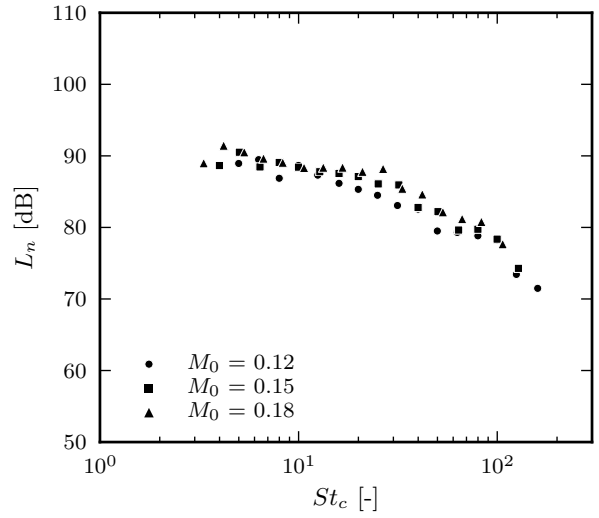


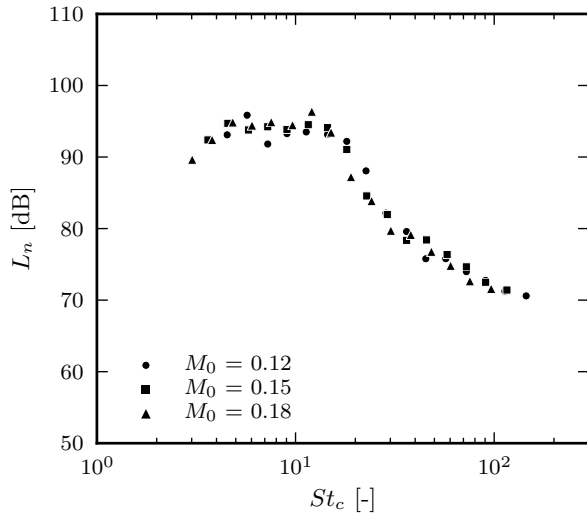
Figure C.6.: Scaled noise spectra. Bottom view. Effect of δ_F , $M_0 = 0.18$.



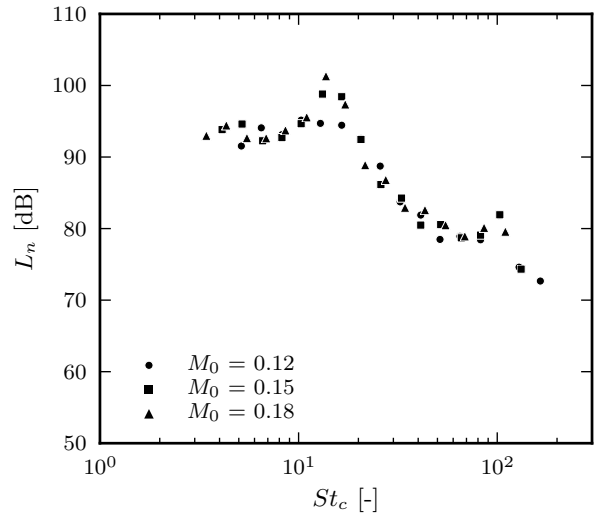
(a) Reference



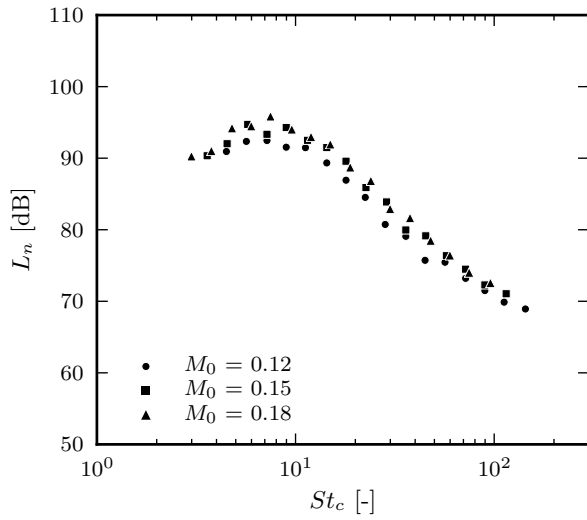
(b) Vane



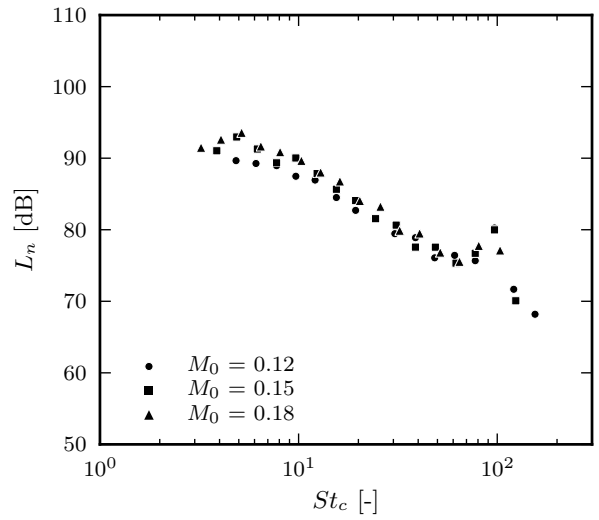
(c) Tip #1



(d) Tip #1+Vane



(e) Tip #2



(f) Tip #2+Vane

Figure C.7.: Scaled noise spectra. Side view. Effect of M_0 , $\delta_F = 25^\circ$.

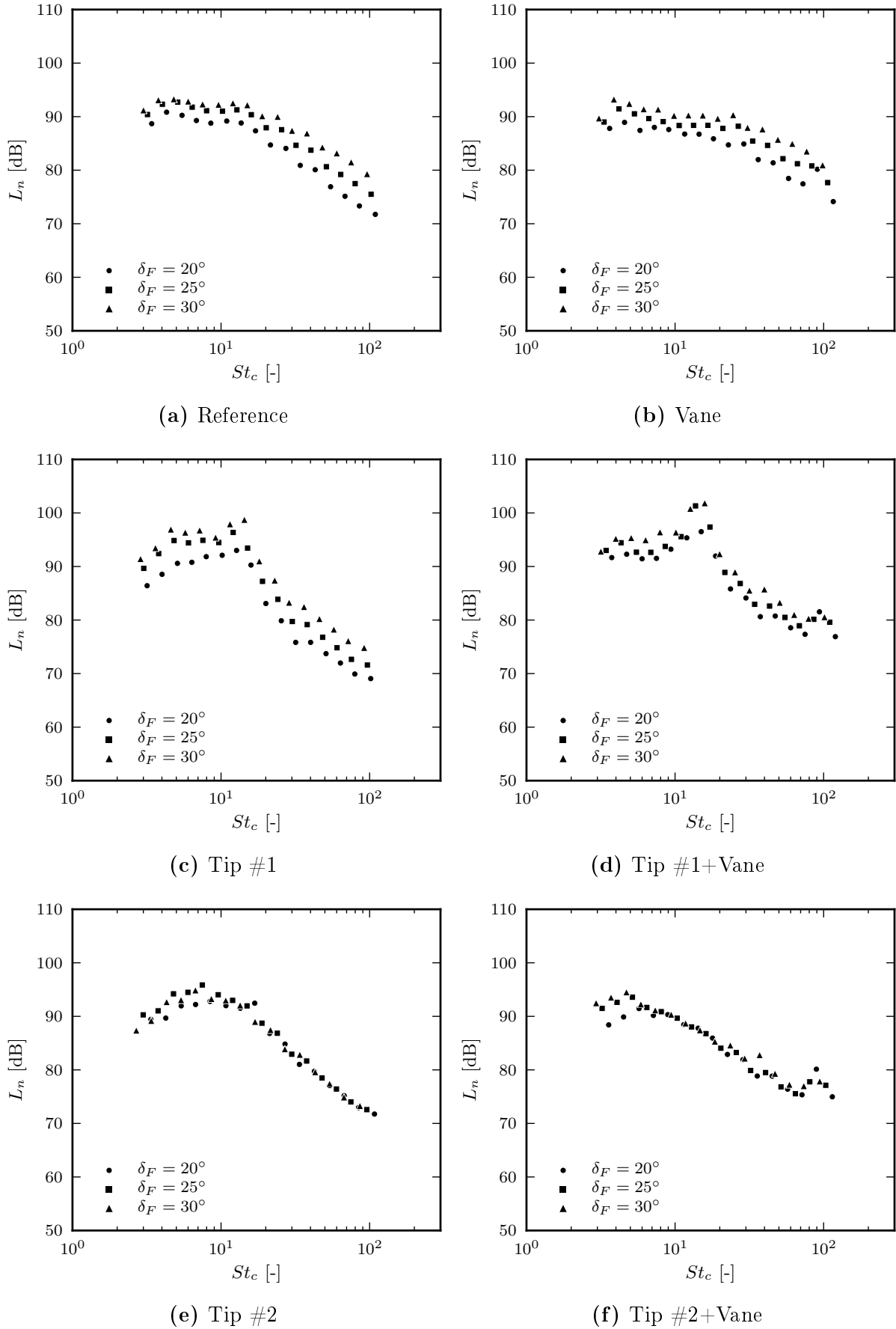


Figure C.8.: Scaled noise spectra. Side view. Effect of δ_F , $M_0 = 0.18$.

D. Beamforming Source Maps for Various Tip Modifications

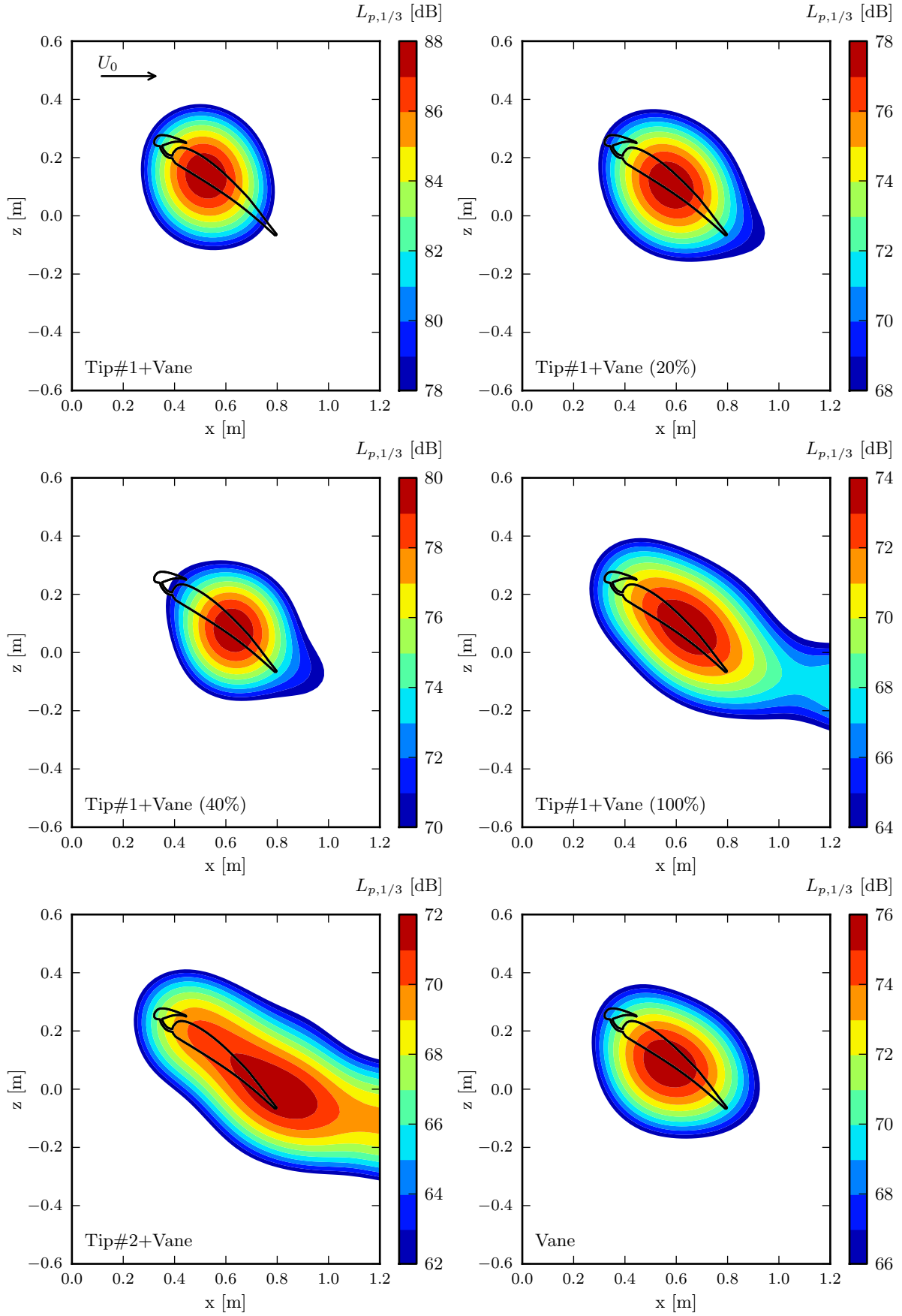


Figure D.1.: Identification of a quasi-tonal source for configuration Tip #1+Vane. Source map at $f_c = 2.5$ kHz, $\delta_F = 32^\circ$, $M_0 = 0.18$. The given percentages refer to the taped extent (ex.: 20% \rightarrow up to $x/c = 0.2$).

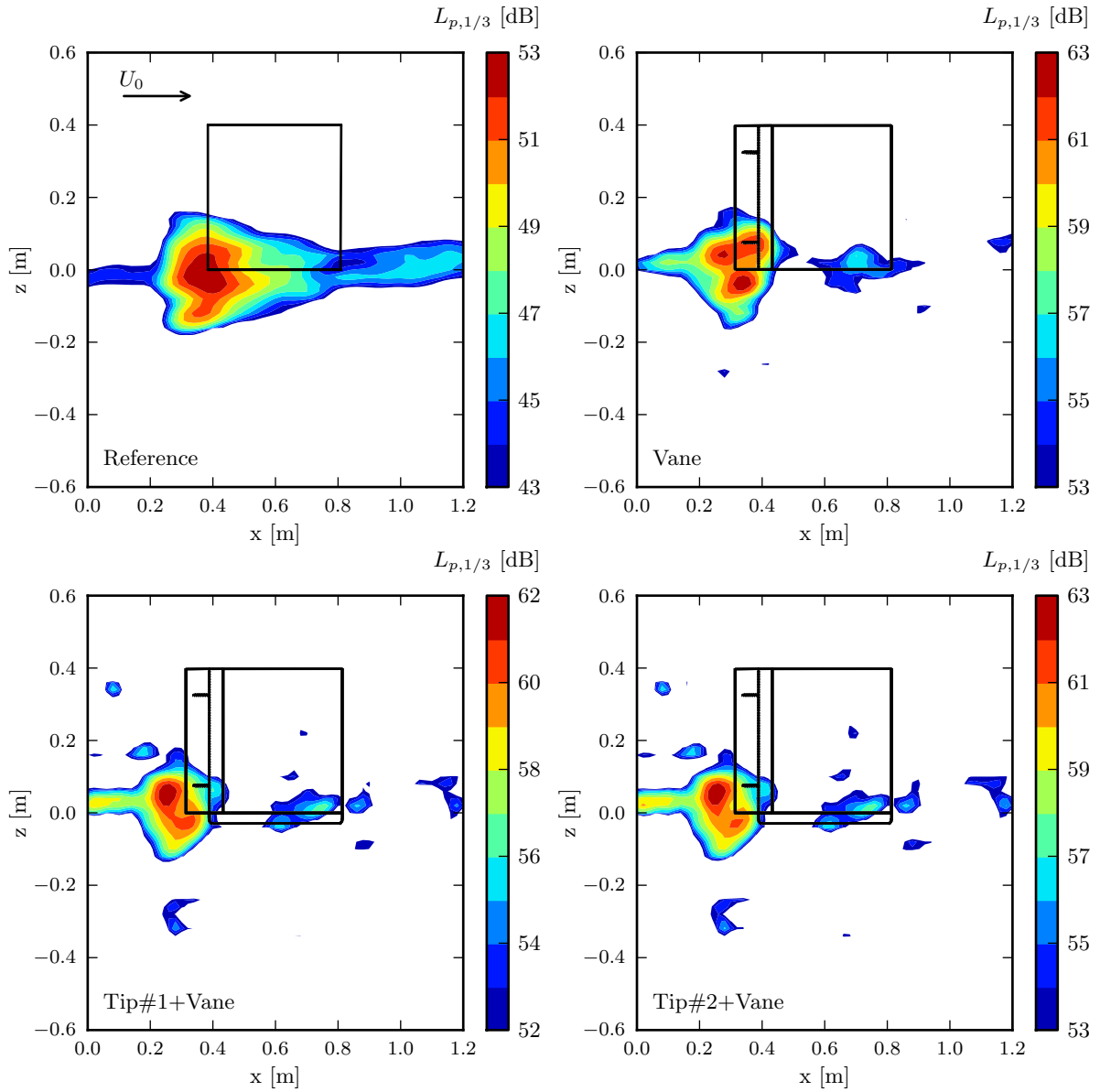


Figure D.2.: Identification of a high-frequency tonal source for configuration Tip #1+Vane. Source map at $f_c = 12.5$ kHz, $\delta_F = 25^\circ$, $M_0 = 0.18$.

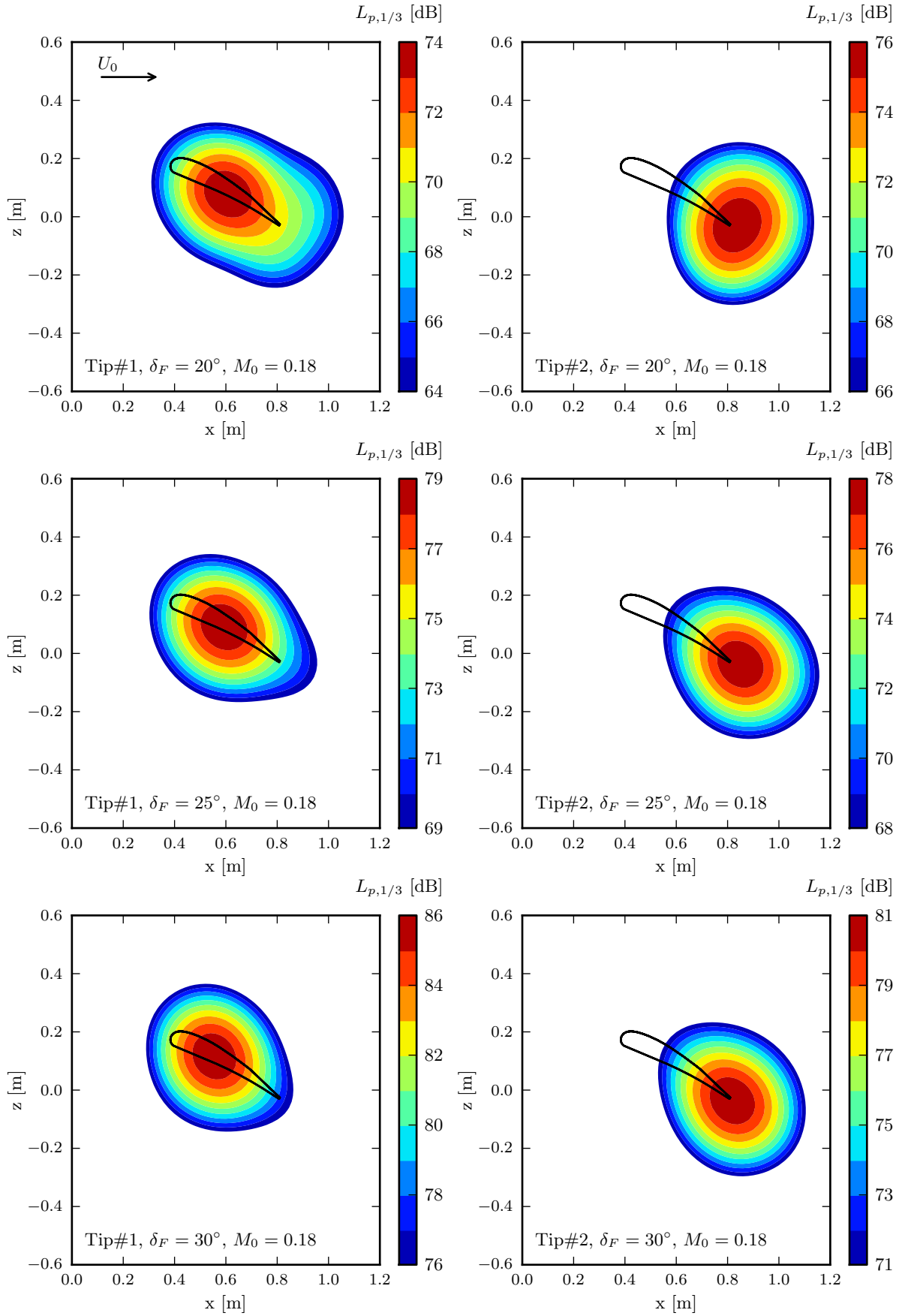


Figure D.3.: Comparison of the source distributions for configurations Tip #1 and Tip #2. Source map at $f_c = 2.5$ kHz, $M_0 = 0.18$, side view.

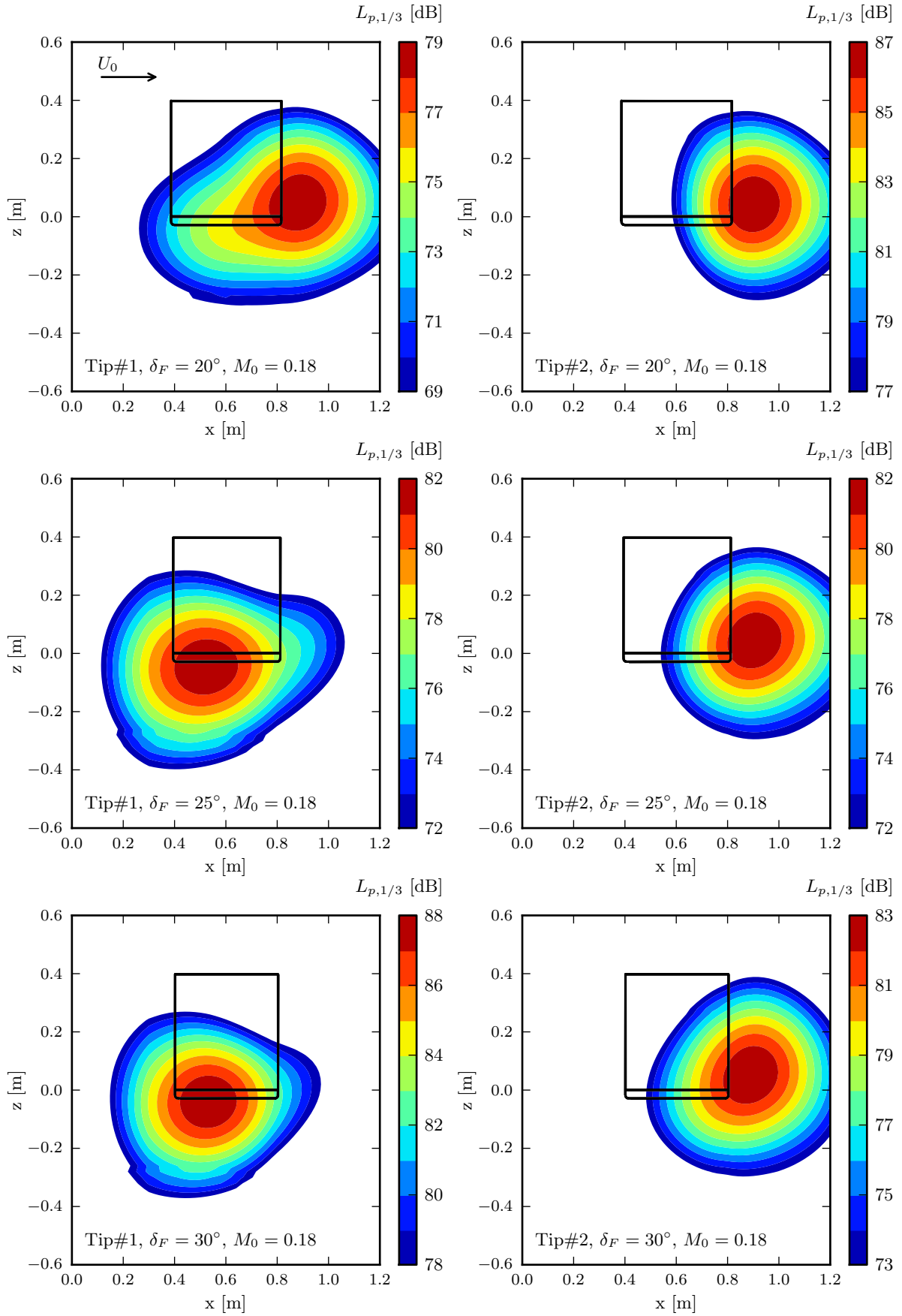


Figure D.4.: Comparison of the source distributions for configurations Tip #1 and Tip #2. Source map at $f_c = 2.5$ kHz, $M_0 = 0.18$, bottom view.

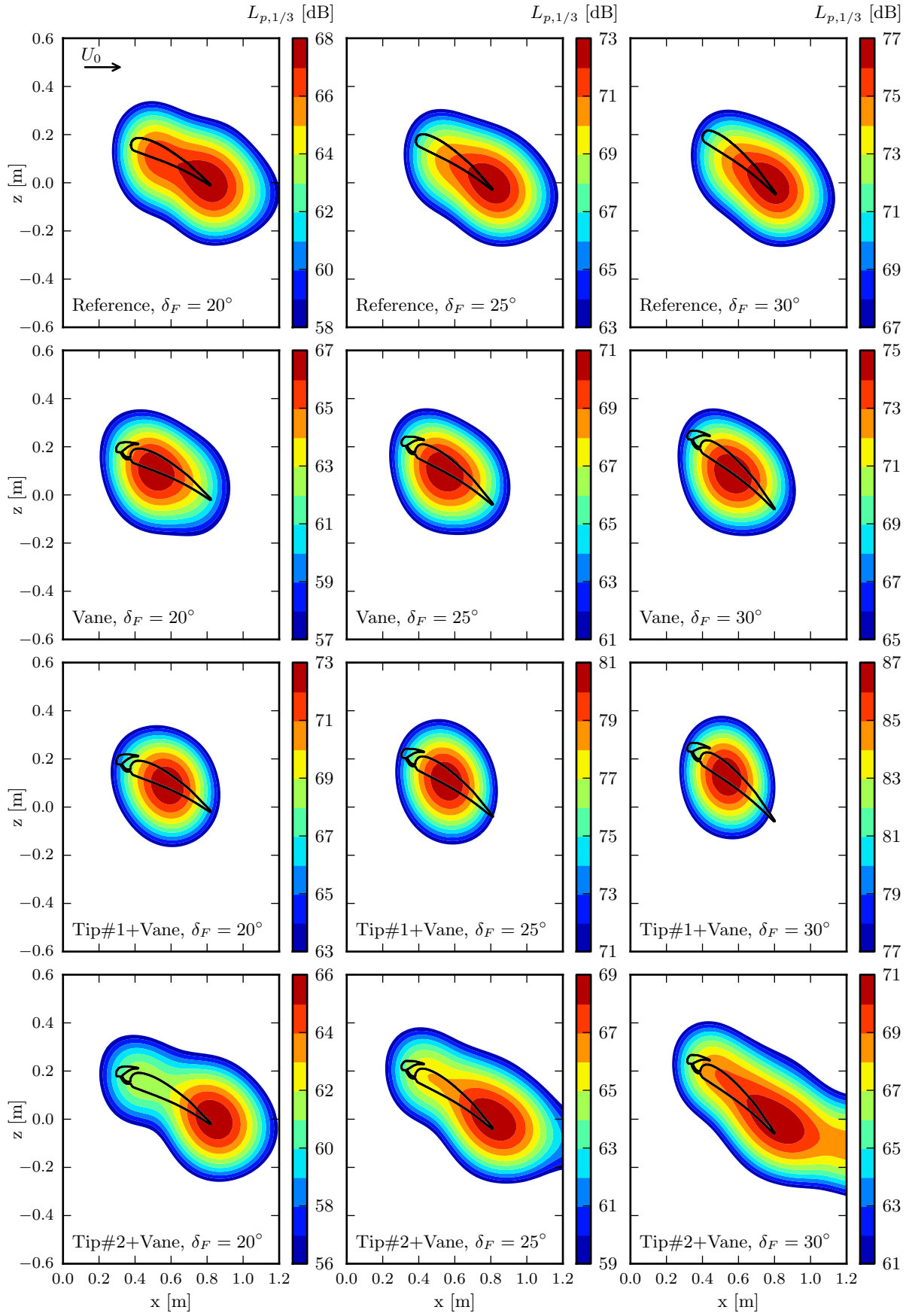


Figure D.5.: Comparison of the source distributions for configurations Reference, Vane, Tip #1+Vane and Tip #2+Vane. Source map at $f_c = 2.5$ kHz, $M_0 = 0.18$, side view.

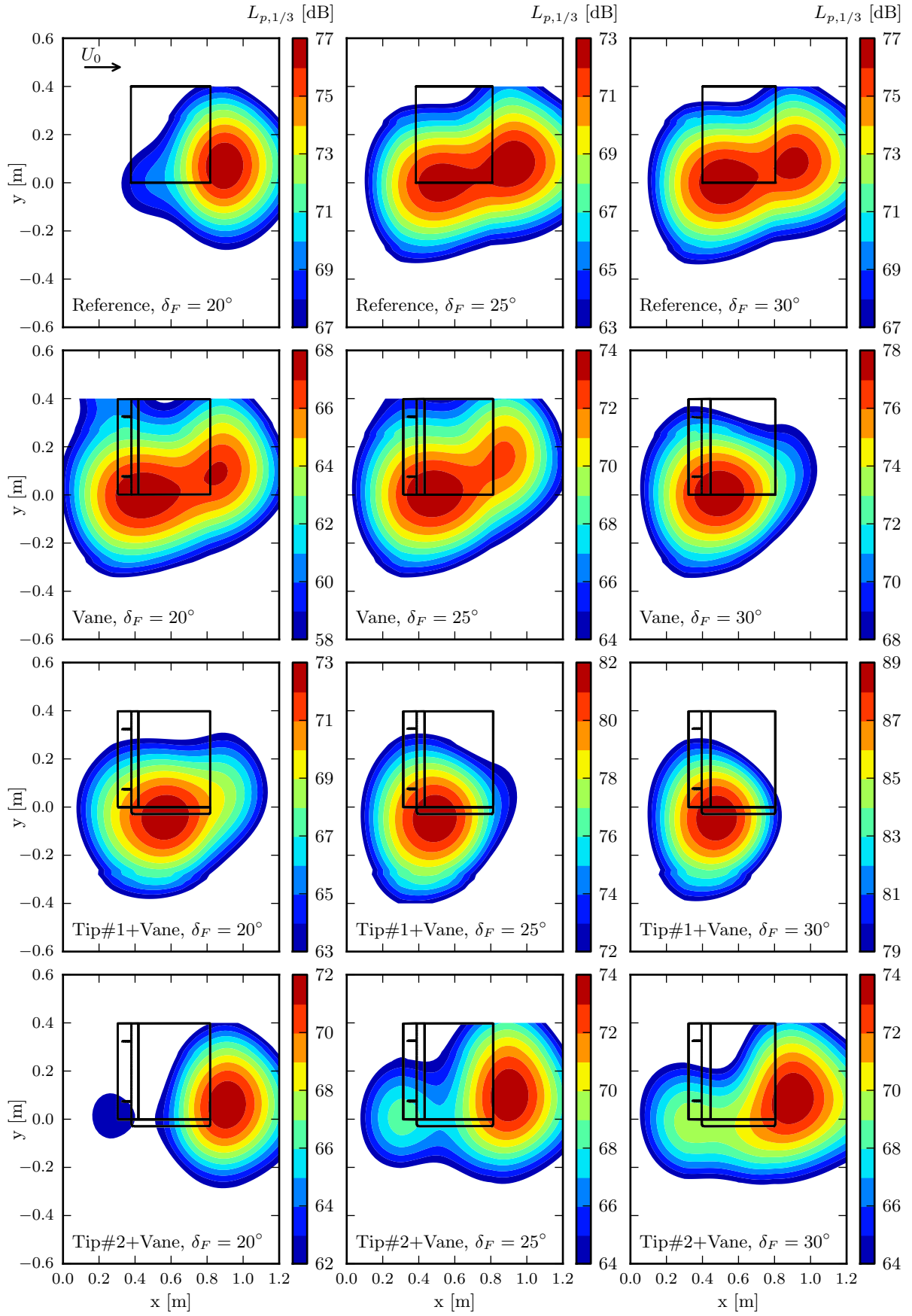


Figure D.6.: Comparison of the source distributions for configurations Reference, Vane, Tip #1+Vane and Tip #2+Vane. Source map at $f_c = 2.5$ kHz, $M_0 = 0.18$, bottom view.

E. Effect of Tip Add-ons and Geometry on FSE Noise Directivity

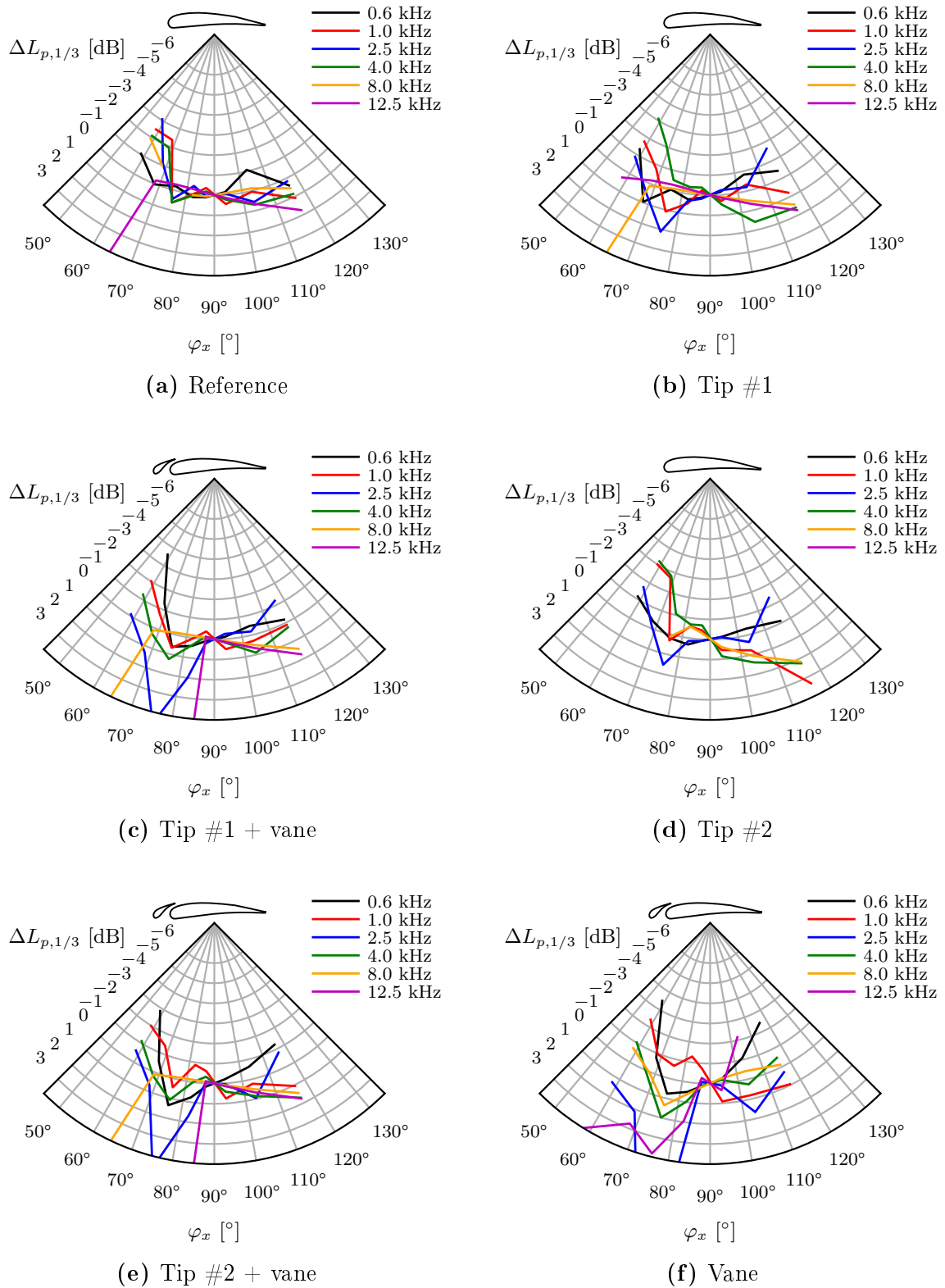
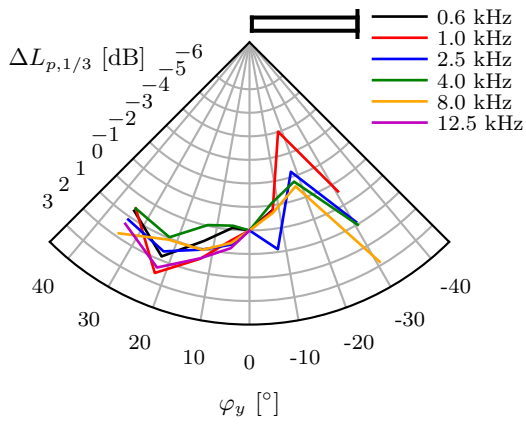
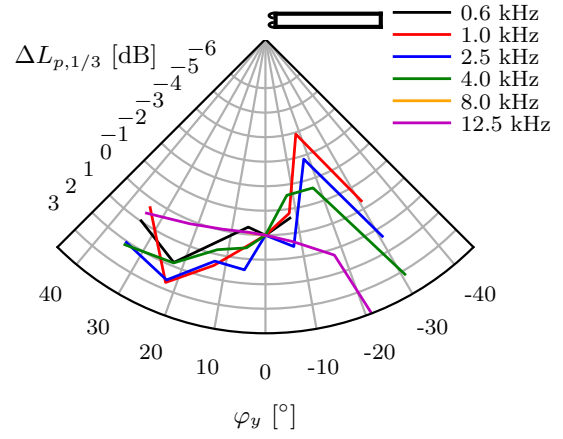


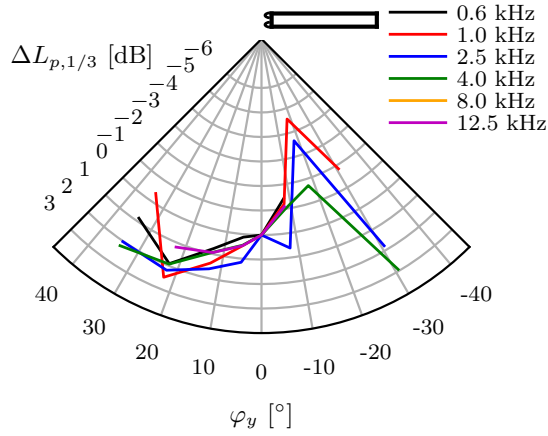
Figure E.1.: Fly-over directivity. Effect of tip geometry modifications. $\varphi_y = 0^\circ$, $\delta_F = 20^\circ$, $M_0 = 0.18$.



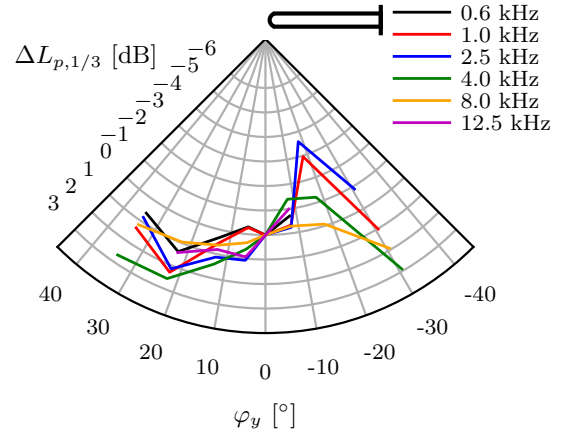
(a) Reference



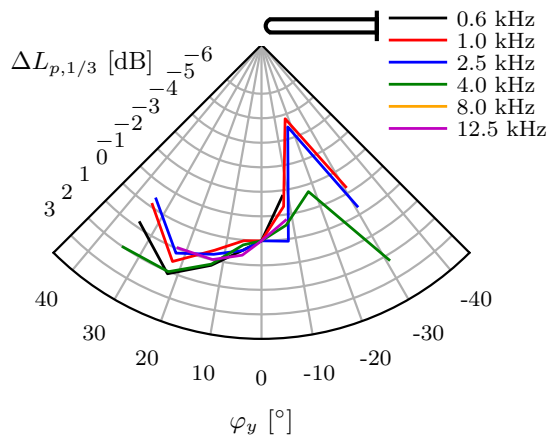
(b) Tip #1



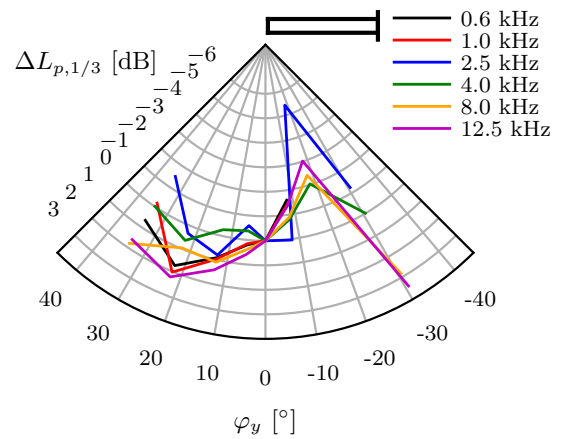
(c) Tip #1 + vane



(d) Tip #2



(e) Tip #2 + vane



(f) Vane

Figure E.2.: Sideline directivity. Effect of tip geometry modifications. $\varphi_x = 90^\circ$, $\delta_F = 20^\circ$, $M_0 = 0.18$.

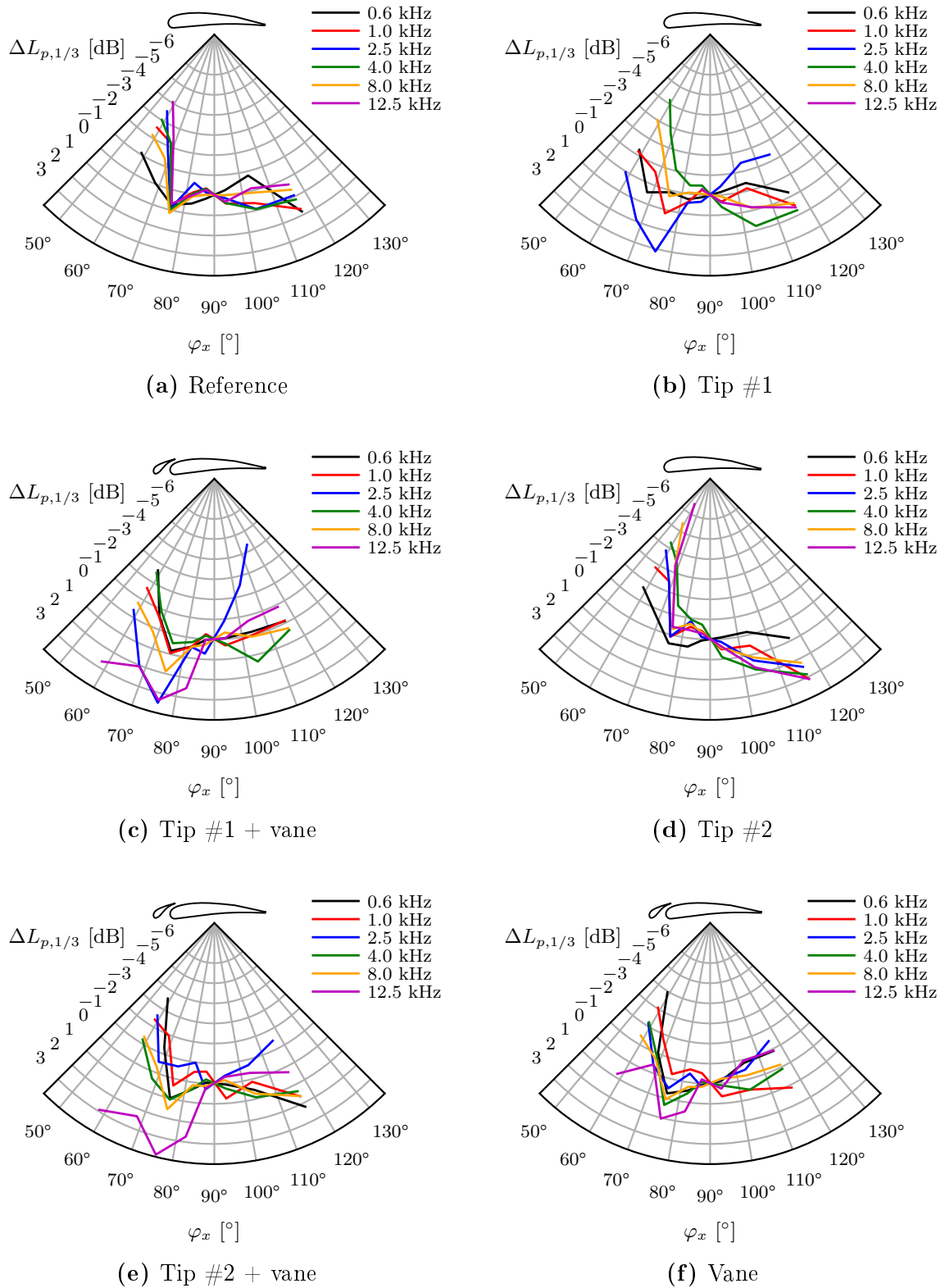
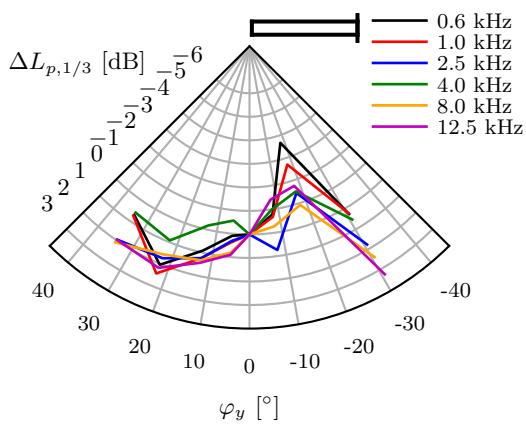
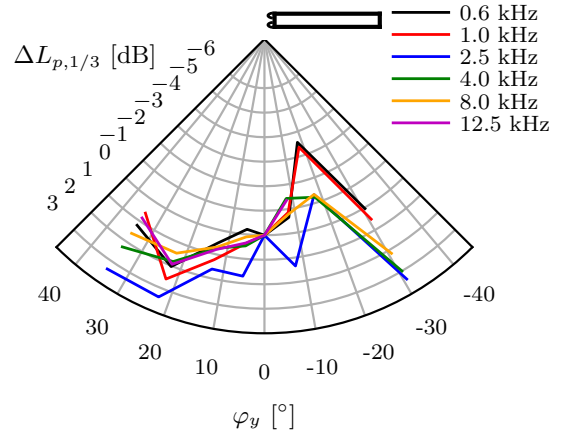


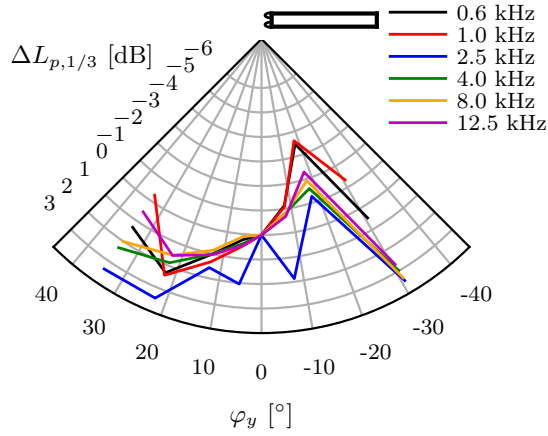
Figure E.3.: Fly-over directivity. Effect of tip geometry modifications. $\varphi_y = 0^\circ$, $\delta_F = 25^\circ$, $M_0 = 0.18$.



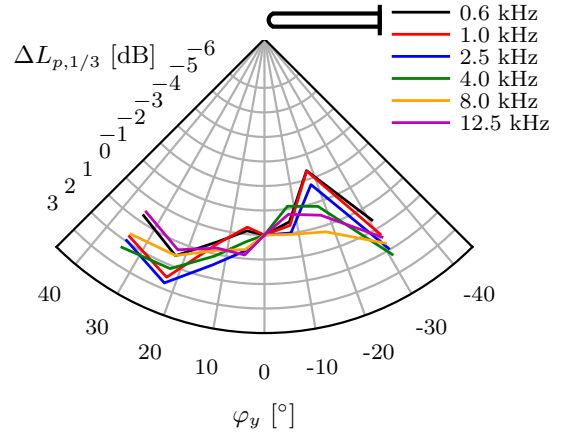
(a) Reference



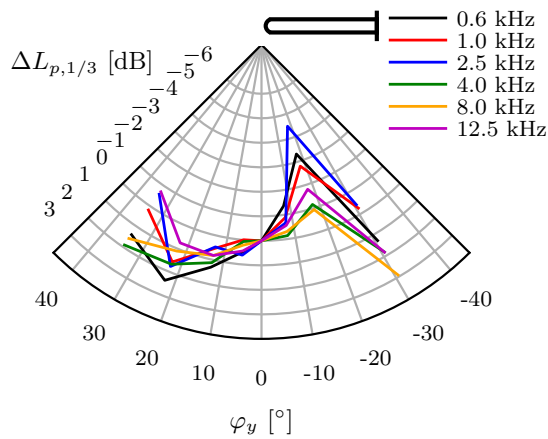
(b) Tip #1



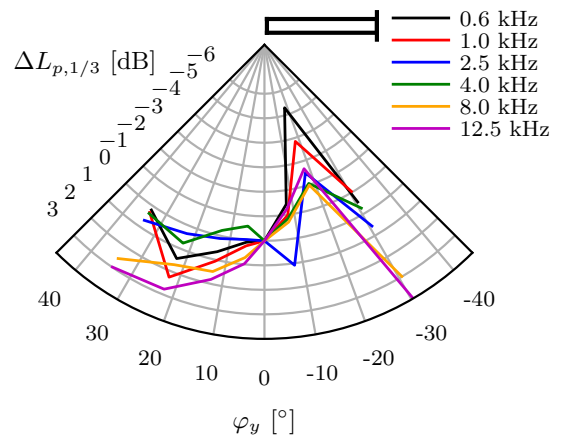
(c) Tip #1 + vane



(d) Tip #2



(e) Tip #2 + vane



(f) Vane

Figure E.4.: Sideline directivity. Effect of tip geometry modifications. $\varphi_x = 90^\circ$, $\delta_F = 25^\circ$, $M_0 = 0.18$.

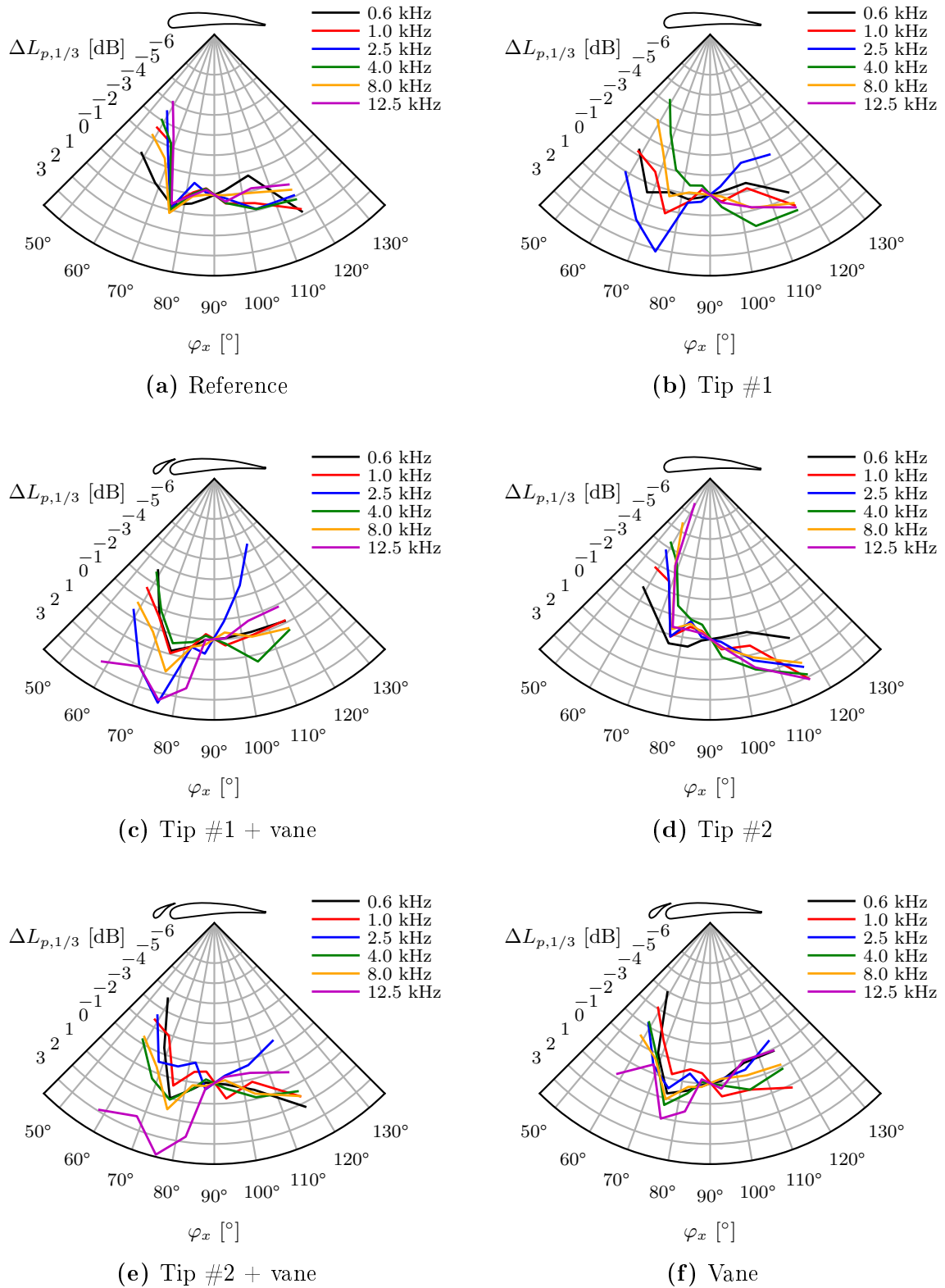
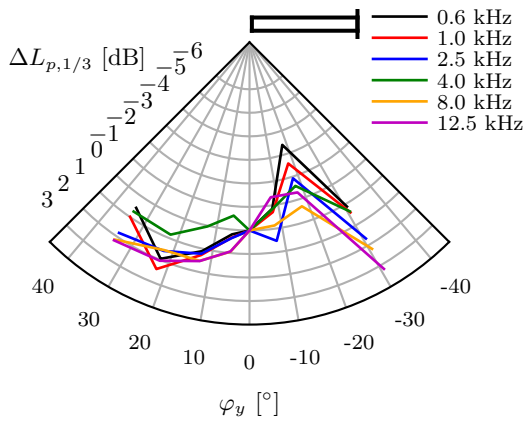
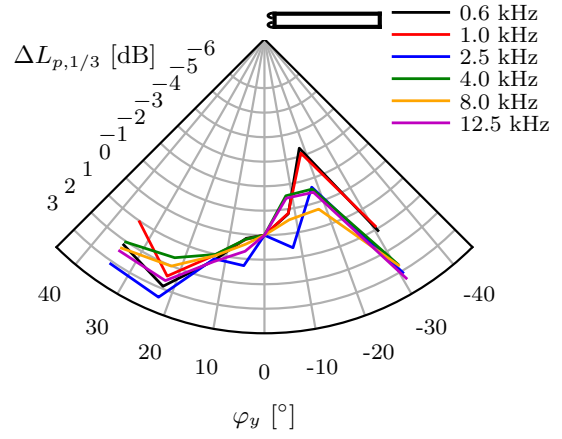


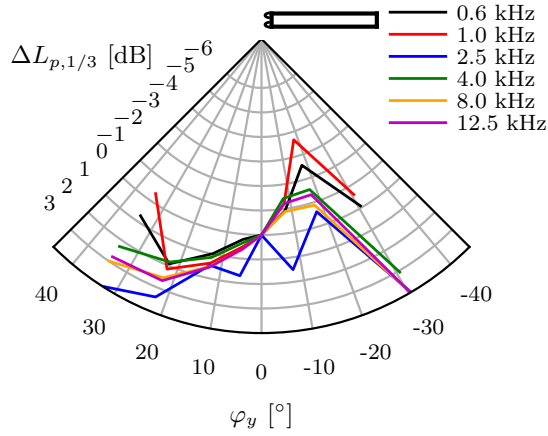
Figure E.5.: Fly-over directivity. Effect of tip geometry modifications. $\varphi_y = 0^\circ$, $\delta_F = 25^\circ$, $M_0 = 0.18$.



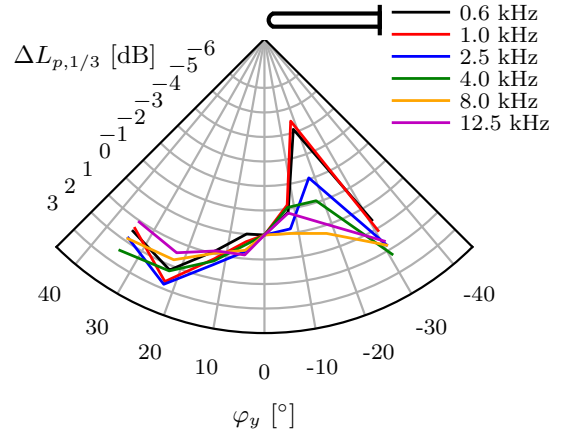
(a) Reference



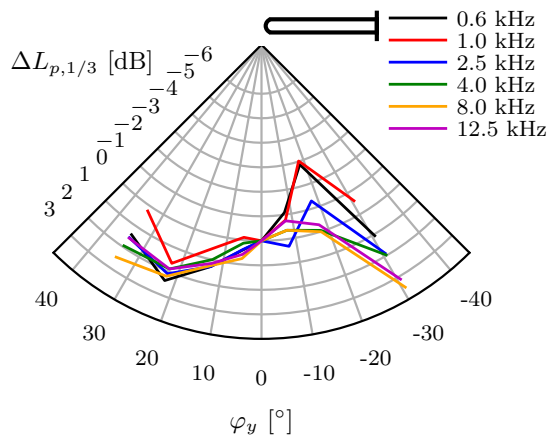
(b) Tip #1



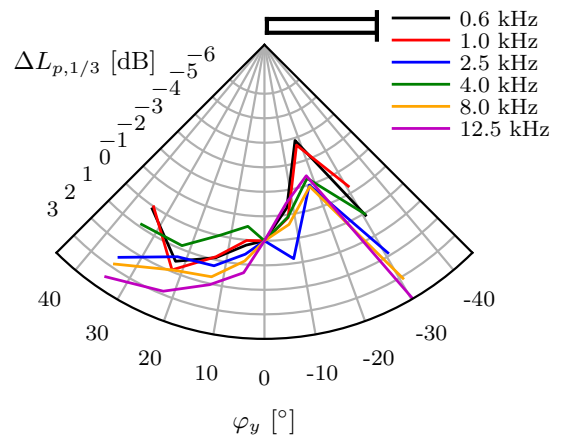
(c) Tip #1 + vane



(d) Tip #2



(e) Tip #2 + vane



(f) Vane

Figure E.6.: Sideline directivity. Effect of tip geometry modifications. $\varphi_x = 90^\circ$, $\delta_F = 30^\circ$, $M_0 = 0.18$.

F. Phased Array Source Maps From DNW-NWB Experiment

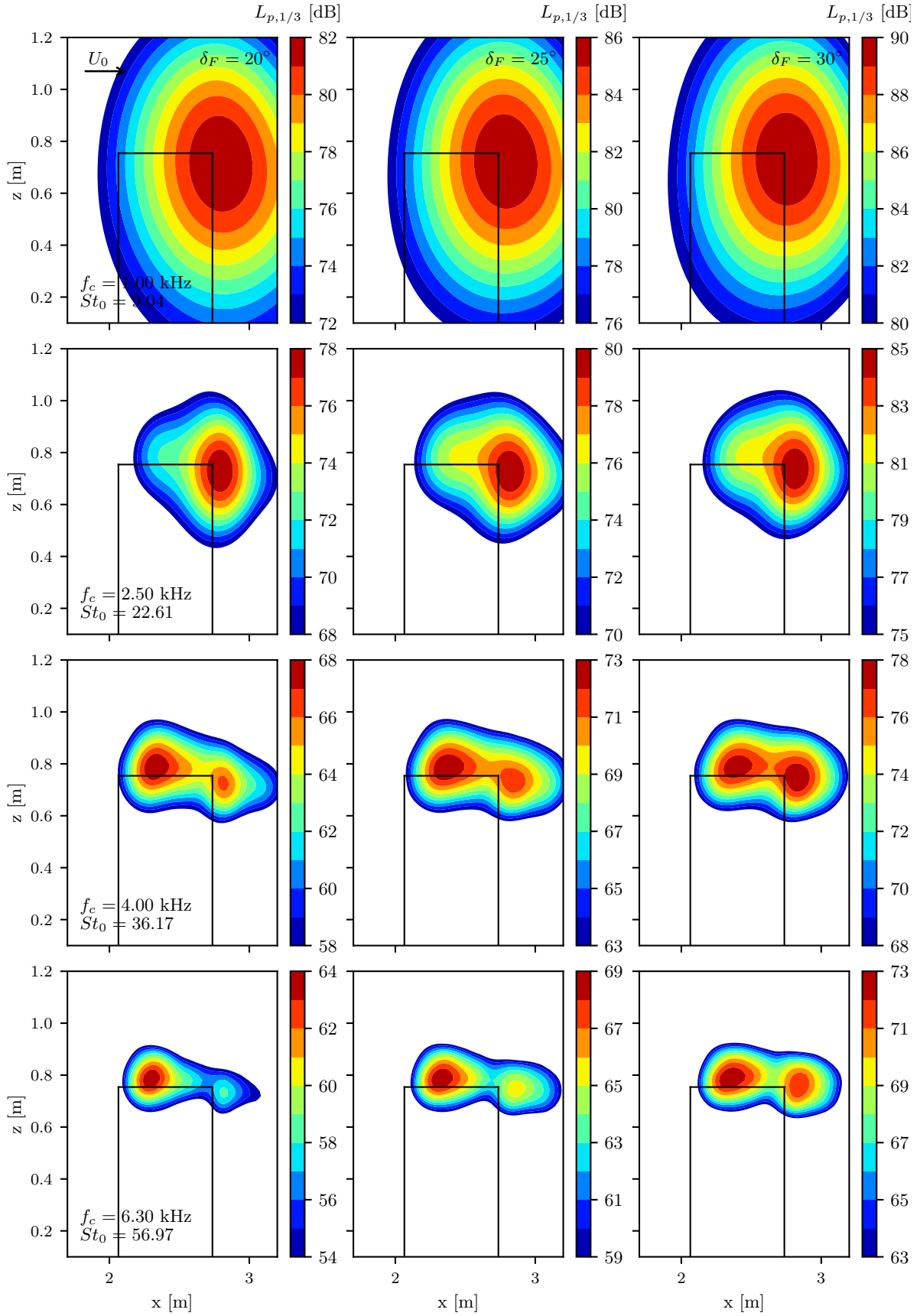


Figure F.1.: Reference configuration. SPL contour plots. $M_0 = 0.21$.

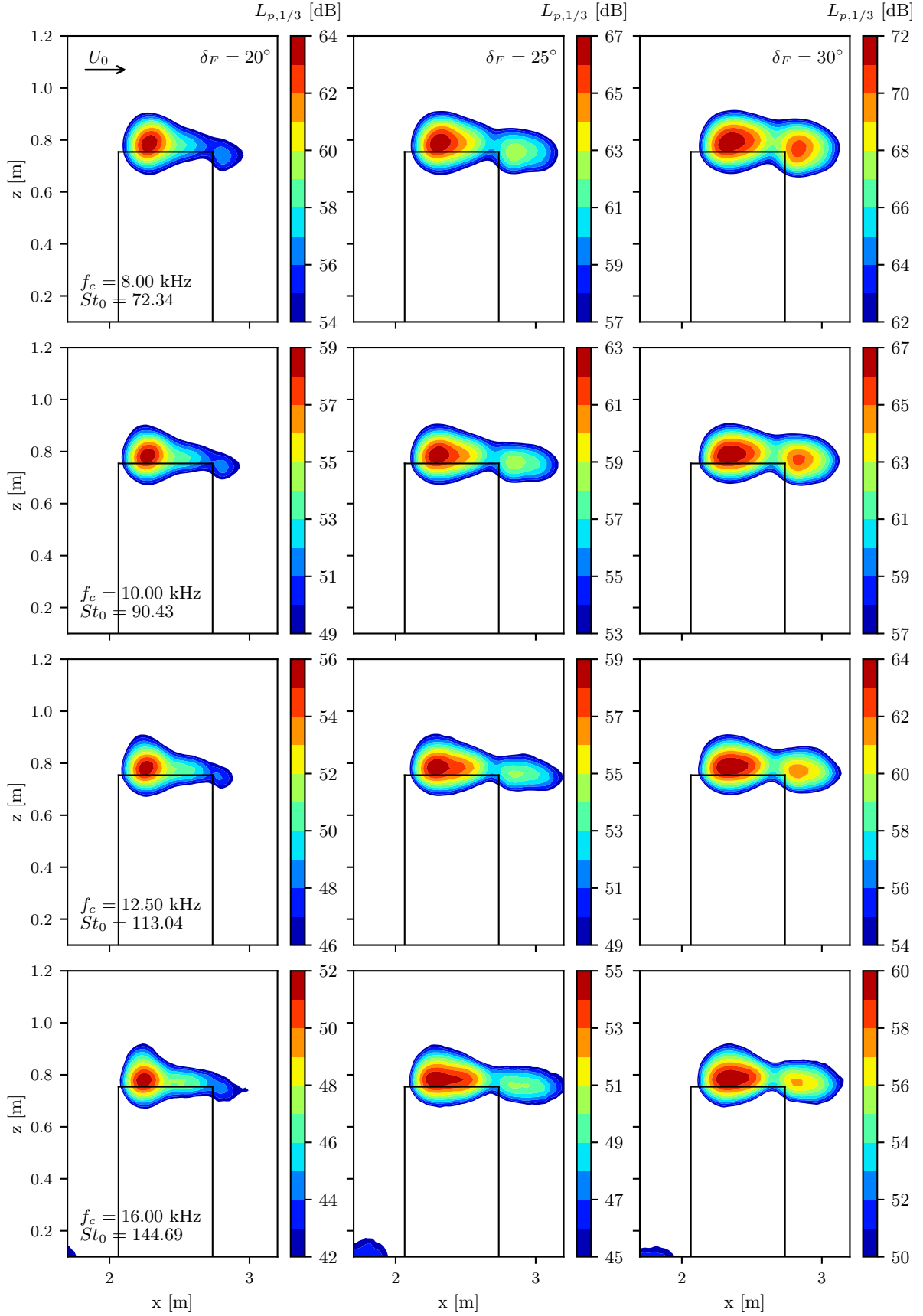


Figure F.2.: Reference configuration. SPL contour plots. $M_0 = 0.21$.

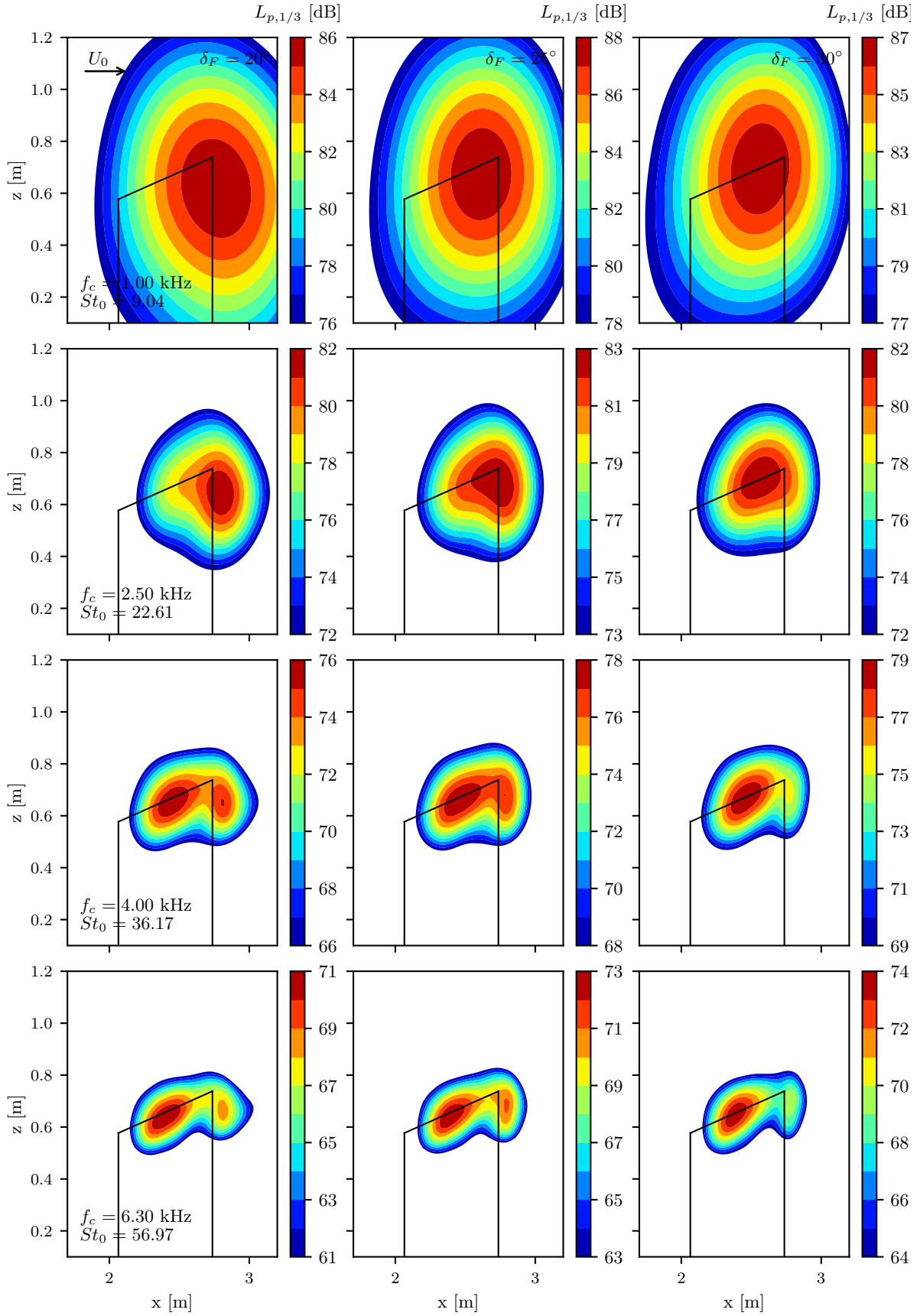


Figure F.3.: Raked tip configuration. SPL contour plots. $M_0 = 0.21$.

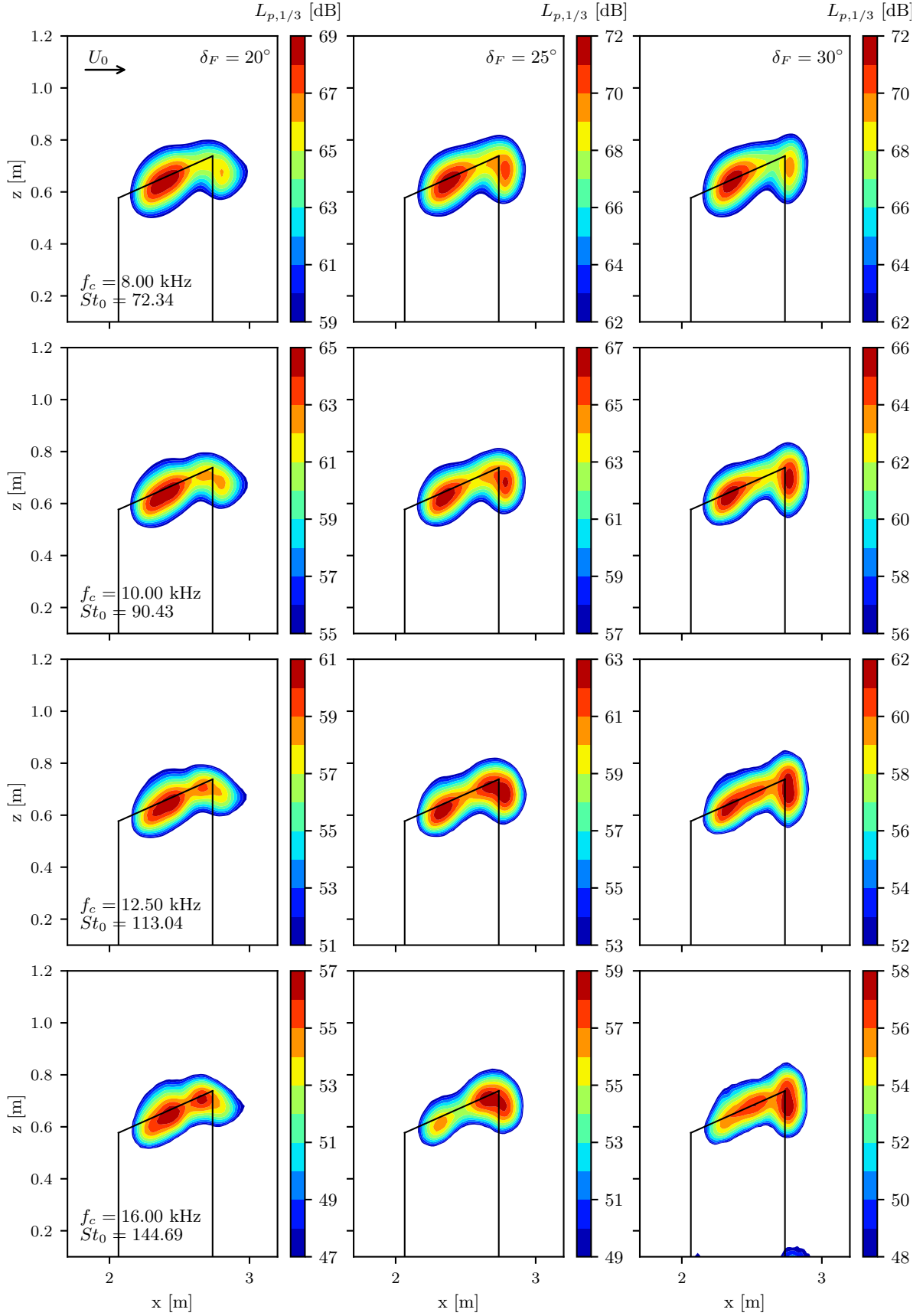


Figure F.4.: Raked tip configuration. SPL contour plots. $M_0 = 0.21$.

Bibliography

- [1] European aeronautics: A vision for 2020, January 2001.
- [2] Vision 2050. Technical report, IATA, Singapore, February 2011.
- [3] Warren F. Ahtye, Miller R. Wendell, and Meecham William C. Wing and flap noise measured by near- and far-field cross-correlation techniques. In *AIAA 5th Aeroacoustics Conference*, March 1979.
- [4] F. Albano, F. De Gregorio, and A. Ragni. Trailing vortex detection and quantitative evaluation of vortex characteristics by piv technique. In *Instrumentation in Aerospace Simulation Facilities, 2003. ICIASF '03. 20th International Congress on*, pages 31–43, 2003.
- [5] R.K. Amiet. Refraction of sound by a shear layer. *Journal of Sound and Vibration*, 58(4):467–482, June 1978. ISSN 0022-460X. URL <http://www.sciencedirect.com/science/article/B6WM3-4951K5F-PP/2/15b627f8726c6ec80646f154fbb79ae2>.
- [6] D. Angland. *Aerodynamics and Aeroacoustics of Flap Side-Edges*. PhD thesis, University of Southampton, February 2008.
- [7] D. Angland, X. Zhang, N. Molin, and L.C. Chow. Measurements of flow around a split flap configuration. In *45th AIAA aerospace science meeting and exhibit*, number AIAA-2007-225, January 2007.
- [8] David Angland, Xin Zhang, and N Molin. Measurements of flow around a flap side edge with porous edge treatment. *AIAA journal*, 47(7):1660–1671, 2009. ISSN 0001-1452.
- [9] Sean CC Bailey, Stavros Tavoularis, and Benedict HK Lee. Effects of free-stream turbulence on wing-tip vortex formation and near field. *Journal of aircraft*, 43(5): 1282–1291, 2006. ISSN 0021-8669.
- [10] H. E. Bass, L. C. Sutherland, and A. J. Zuckerwar. Atmospheric absorption of sound: Update. *The Journal of the Acoustical Society of America*, 88(4):2019–2021, 1990. doi: <http://dx.doi.org/10.1121/1.400176>. URL <http://scitation.aip.org/content/asa/journal/jasa/88/4/10.1121/1.400176>.
- [11] GK Batchelor. Axial flow in trailing line vortices. *Journal of Fluid Mechanics*, 20 (04):645–658, 1964. ISSN 1469-7645.
- [12] G.K. Batchelor. *An introduction to Fluid Dynamics*. Cambridge University Press, 1967.

-
- [13] Christoph Baumann. Cfd-basierte anstellwinkelkorrektur für 3d-windkanalmodelle. Master's thesis, Technische Universität München, 2014.
- [14] Mert E Berkman, Mehdi R Khorrami, Meelan Choudhari, and Shelly S Sadowski. Investigation of high-lift flowfield of an energy efficient transport wing. *Journal of aircraft*, 37(1):45–52, 2000. ISSN 0021-8669.
- [15] D Birch, T Lee, F Mokhtarian, and F Kafyeke. Rollup and near-field behavior of a tip vortex. *Journal of aircraft*, 40(3):603–607, 2003. ISSN 0021-8669.
- [16] D Birch, T Lee, F Mokhtarian, and F Kafyeke. Structure and induced drag of a tip vortex. *Journal of aircraft*, 41(5):1138–1145, 2004. ISSN 0021-8669.
- [17] T.F. Brooks and T.H. Hodgson. Trailing edge noise prediction from measured surface pressures. *Journal of Sound and Vibration*, 78(1):69–117, September 1981. URL <http://www.sciencedirect.com/science/article/B6WM3-4MVF6CW-6/2/5784a17fd3cb695ed567273225ccd2eb>.
- [18] Thomas Brooks and William M. Humphreys Jr. Flap edge aeroacoustic measurements and prediction. In *6th AIAA/CEAS Aeroacoustics Conference*, 2000.
- [19] Thomas Brooks and M. Marcolini. Airfoil tip vortex formation noise. *AIAA Journal*, 24(2):246–252, 1986.
- [20] Thomas F. Brooks and William M. Humphreys. Effect of directional array size on the measurement of airframe noise components. In *5th AIAA/CEAS Aeroacoustics Conference*, number 99-1958, May 1999.
- [21] Thomas F. Brooks and William M. Humphreys Jr. Flap-edge aeroacoustic measurements and predictions. *Journal of Sound and Vibration*, 261(1):31–74, 2003. ISSN 0022-460X.
- [22] Thomas F Brooks, D Stuart Pope, and Michael A Marcolini. *Airfoil self-noise and prediction*, volume 1218. National Aeronautics and Space Administration, Office of Management, Scientific and Technical Information Division, 1989.
- [23] KL Chandiramani. Diffraction of evanescent waves, with applications to aerodynamically scattered sound and radiation from un baffled plates. *The Journal of the Acoustical Society of America*, 55(1):19–29, 1974. ISSN 0001-4966.
- [24] Meelan M. Choudhari, David P. Lockard, Michele G. Macaraeg, Bart A. Singer, Craig L. Streett, Guy R. Neubert, Robert W. Stoker, James R. Underbrink, Mert E. Berkman, and et al. Khorrami, Mehdi R. Aeroacoustic experiments in the nasa langley low-turbulence pressure tunnel. Technical Report L-18131; NASA/TM-2002-211432, Langley Research Center, February 2002.
- [25] J. S. Chow, G. G. Zilliac, and P. Bradshaw. Mean and turbulence measurements in the near field of a wingtip vortex. *AIAA Journal*, 35(10), October 1997.

-
- [26] J. S. Chow, G. G. Zilliac, and P. Bradshaw. Turbulence measurements in the near-field of a wingtip vortex. Technical Report TM 110418, NASA, February 1997.
- [27] Tim Colonius, Sanjiva K Lele, and Parviz Moin. The scattering of sound waves by a vortex: numerical simulations and analytical solutions. *Journal of Fluid Mechanics*, 260:271–298, 1994.
- [28] DG Crighton. Radiation from vortex filament motion near a half plane. *Journal of Fluid Mechanics*, 51(02):357–362, 1972. ISSN 1469-7645.
- [29] N Curle. The influence of solid boundaries upon aerodynamic sound. *Proceedings of the Royal Society of London. Series A. Mathematical and Physical Sciences*, 231(1187):505–514, 1955. ISSN 1364-5021.
- [30] Jennifer Dacles-Mariani, Gregory G Zilliac, Jim S Chow, and Peter Bradshaw. Numerical/experimental study of a wingtip vortex in the near field. *AIAA journal*, 33(9):1561–1568, 1995. ISSN 0001-1452.
- [31] William J Devenport, Michael C Rife, Stergios I Liapis, and Gordon J Follin. The structure and development of a wing-tip vortex. *Journal of Fluid Mechanics*, 312(67):106–, 1996.
- [32] L Dieterle, K Ehrenfried, R Stuff, G Schneider, P Coton, JC Monnier, and JF Lozier. Quantitative flow field measurements in a catapult facility using particle image velocimetry. In *Instrumentation in Aerospace Simulation Facilities, 1999. ICIASF 99. 18th International Congress on*, pages 1–1. IEEE, 1999.
- [33] W. Dobrzynski. Almost 40 years of airframe noise research: What did we achieve? *Journal of Aircraft*, 47(2):353–367, March-April 2010.
- [34] W Dobrzynski, H Bieler, S Chow, and H Remy. The airframe noise reduction challenge: lessons learned from the european silencer project. In *Proposed Paper for DGLR Conference "Deutscher Luft und Raumfahrt Kongress" in Braunschweig*, pages –, 2006.
- [35] W. Dobrzynski, K.-S Rossignol, and D. Almoneit. Handbuch zum modularen quellmodell für das umströmungsgeräusch von verkehrsflugzeugen profan (prediction model for airframe noise), version 3.2. Technical report, DLR, February 2011.
- [36] Werner Dobrzynski and Michael Pott-Pollenske. Slat noise source studies for farfield noise prediction. In *7th AIAA/CEAS Aeroacoustics Conference and Exhibit*, page 2158, 2001.
- [37] Werner Dobrzynski, Kiyoshi Nagakura, Burkhard Gehlhar, and Andreas Buschbaum. Airframe noise studies on wings with deployed high-lift devices. *AIAA paper*, 2337:1998–, 1998.
- [38] Werner Dobrzynski, Burkhard Gehlhar, and Heino Buchholz. Model and full scale high-lift wing wind tunnel experiments dedicated to airframe noise reduction. *Aerospace Science and Technology*, 5(1):27–33, January 2001. ISSN 1270-9638.

URL <http://www.sciencedirect.com/science/article/B6VK2-42M2B0K-4/2/d16f71e78c9bbd75d633f2f0a1de7bcb>.

- [39] Roger Drobietz and Ingo U. Borchers. Generic wind tunnel study on side edge noise. *AIAA Journal*, (AIAA-2006-2509), 2006. 12th AIAA/CEAS Aeroacoustics Conference (27th AIAA Aeroacoustics Conference).
- [40] J. E. Ffwoes Williams and L. H. Hall. Aerodynamic sound generation by turbulent flow in the vicinity of a scattering half plane. *Journal of Fluid Mechanics Digital Archive*, 40(04):657–670, 1970.
- [41] J. E. Ffwoes Williams and D. L. Hawkings. Sound generation by turbulence and surfaces in arbitrary motion. *Philosophical Transactions of the Royal Society of London. Series A, Mathematical and Physical Sciences (1934-1990)*, 264(1151):321–342, May 1969. URL <http://dx.doi.org/10.1098/rsta.1969.0031>.
- [42] Martin R Fink. Airframe noise prediction method. Technical report, 1977.
- [43] Martin R Fink. Noise component method for airframe noise. *Journal of Aircraft*, 16(10):659–665, 1979. ISSN 0021-8669.
- [44] Michael S Francis and Donald A Kennedy. Formation of a trailing vortex. *Journal of Aircraft*, 16(3):148–154, 1979. ISSN 0021-8669.
- [45] TB Francis and J Katz. Observations on the development of a tip vortex on a rectangular hydrofoil. *Journal of fluids engineering*, 110(2):208–215, 1988. ISSN 0098-2202.
- [46] P Freymuth, W Bank, and F Finaish. Visualization of wing tip vortices in accelerating and steady flow. *Journal of Aircraft*, 23(9):730–733, 1986. ISSN 0021-8669.
- [47] Albert R George and Shau-Tak Chou. Broadband rotor noise analyses. *Final Report Cornell Univ., Ithaca, NY. School of Mechanical and Aerospace Engineering.*, 1, 1984.
- [48] P Gerontakos and T Lee. Near-field tip vortex behind a swept wing model. *Experiments in fluids*, 40(1):141–155, 2006. ISSN 0723-4864.
- [49] Reza Ghias, Rajat Mittal, Haibo Dong, and Thomas S. Lund. Study of tip-vortex formation using large-eddy simulation. In *43th Fluid dynamics conference and exhibit*, number AIAA-2005-1280, January 2005.
- [50] Michea Giuni. *Formation and early development of wingtip vortices*. PhD thesis, University of Glasgow, 2013.
- [51] Michea Giuni and Richard B Green. Vortex formation on squared and rounded tip. *Aerospace Science and Technology*, pages –, 2013. ISSN 1270-9638.
- [52] SP Govindaraju and PG Saffman. Flow in a turbulent trailing vortex. *Physics of Fluids*, 14:2074–, 1971.

-
- [53] Y. Guo. Modeling of noise reduction by flap side edge fences. *AIAA Journal*, (AIAA-00-2065), 2000.
- [54] Y. Guo. Aircraft flap side edge noise modeling and prediction. In *Proceedings of the 17th AIAA/CEAS Aeroacoustic Conference, Portland, Oregon*, number AIAA 2011-2731, June 2011.
- [55] Y.P. Guo. Prediction of flap side edge noise. *AIAA Journal*, 1:35–45, 1999.
- [56] YP Guo and MC Joshi. Noise characteristics of aircraft high lift systems. *AIAA journal*, 41(7):1247–1256, 2003.
- [57] Y.P. Guo, M.C. Joshi, P.H. Bent, and K.J. Yamamoto. Surface pressure fluctuations on aircraft flaps and their correlation with far-field noise. *Journal of fluid mechanics*, 415:175–202, 2000.
- [58] Yueping Guo. On noise reduction by flap side edge fences. *Journal of sound and vibration*, 277(1):369–390, 2004. ISSN 0022-460X.
- [59] J. C. Hardin. Noise generation at the side edges of flaps. *AIAA Journal*, 18(5): 549–552, 1980.
- [60] JAYC Hardin and JAMESE Martin. Flap side-edge noise: acoustic analysis of sen’s model. *AIAA journal*, 35(5):810–815, 1997. ISSN 0001-1452.
- [61] J.A. Hayes, W.C. Horne, P.T. Soderman, and P.H. Bent. Airframe noise characteristics of a 4.7In *Proceedings of the 3rd AIAA/CEAS Aeroacoustics Conference*, number AIAA/CEAS-97-1594, 1997.
- [62] Hiroshi Higuchi, JOSE C QUADRELLI, and CESAR FARELL. Vortex roll-up from an elliptic wing at moderately low reynolds numbers. *AIAA journal*, 25(12): 1537–1542, 1987. ISSN 0001-1452.
- [63] E. R. Hoffmann and P. N. Joubert. Turbulent line vortices. *Journal of Fluid Mechanics*, 16(03):395–411 M3 – 10.1017/S0022112063000859, 1963. ISSN 1469-7645. URL href="<http://dx.doi.org/10.1017/S0022112063000859>."
- [64] W Horne. Measurements of the scattering of sound by a line vortex. In *8th Aeroacoustics Conference*, page 676, 1983.
- [65] W. C. Horne, Julie Hayes, James C. Ross, and Bruce L. Storms. Measurements of unsteady pressure fluctuations on the surface of an unswept, multi-element airfoil. In *Proceedings of the 3rd AIAA/CEAS Aeroacoustics Conference*, number AIAA/CEAS-97-1645, 1997.
- [66] M. S. Howe. A review of the theory of trailing edge noise. *Journal of Sound and Vibration*, 61(3):437–465, December 1978. URL <http://www.sciencedirect.com/science/article/B6WM3-494T6X5-24/2/0bbade00ee6ec587de41f94dd27e27d9>.

-
- [67] M. S. Howe. On the generation of side-edge flap noise. *Journal of Sound and Vibration*, 80(4):555–573, February 1982. URL <http://www.sciencedirect.com/science/article/B6WM3-4951D07-5S/2/dd33db055a0ca712c730e958cdfc4874>.
- [68] M. S. Howe. On the scattering of sound by a rectilinear vortex. *Journal of Sound and Vibration*, 227(5):1003–1017, 1999. ISSN 0022-460X. doi: <https://doi.org/10.1006/jsvi.1999.2393>. URL <https://www.sciencedirect.com/science/article/pii/S0022460X99923933>.
- [69] Michael S Howe. *Theory of vortex sound*, volume 33. Cambridge University Press, 2003.
- [70] MS Howe. Contributions to the theory of aerodynamic sound, with application to excess jet noise and the theory of the flute. *Journal of Fluid Mechanics*, 71(04):625–673, 1975. ISSN 1469-7645.
- [71] MS Howe. Noise generated by a coanda wall jet circulation control device. *Journal of Sound and Vibration*, 249(4):679–700, 2002.
- [72] Florence V Hutcheson, Thomas F Brooks, and William M Humphreys. Noise radiation from a continuous mold-line link flap configuration. *International Journal of Aeroacoustics*, 10(5):565–588, 2011. ISSN 1475-472X.
- [73] Taro Imamura, Shunji Enomoto, Hiroyuki Kato, Yuzuru Yokokawa, and Kazuomi Yamamoto. Numerical simulation of naca0012 wingtip flow leading to noise generation. *AIAA paper*, 2864:2005–, 2005.
- [74] Li Jiang, Jiangang Cai, and Chaoqun Liu. Large-eddy simulation of wing tip vortex in the near field. *International Journal of Computational Fluid Dynamics*, 22(5):289–330, 2008. ISSN 1061-8562.
- [75] Heinrich Kaden. Aufwicklung einer unstablen unstetigkeitsflaeche. *Archive of Applied Mechanics*, 2(2):140–168, 1931. ISSN 0939-1533.
- [76] T Kambe, T Minota, and Y Ikushima. Acoustic wave emitted by a vortex ring passing near the edge of a half-plane. *Journal of Fluid Mechanics*, 155:77–103, 1985. ISSN 1469-7645.
- [77] J. Katz and J. B. Galdo. Effect of roughness on rollup of tip vortices on a rectangular hydrofoil. *Journal of aircraft*, 26(3):247–253, 1989. ISSN 0021-8669.
- [78] Joseph B Keller. Geometrical theory of diffraction. *Josa*, 52(2):116–130, 1962.
- [79] Mehdi R. Khorrami, Bart A. Singer, and Ronald H. Jr. Radeztsky. Reynolds avaraged navier-stokes computations of a flap side-edge flow field. *AIAA Journal*, (AIAA 98-0768), January 1998.
- [80] Mehdi R Khorrami, David P Lockard, William M Humphreys, and Patricio A Ravetta. Flight-test evaluation of airframe noise mitigation technologies. In *2018 AIAA/CEAS Aeroacoustics Conference*, page 2972, 2018.

-
- [81] Alexander Kolb, Simone Mancini, Karl-Stéphane Rossignol, and Roland Ewert. Flap side-edge noise simulation using rans-based source modelling. In *AIAA AVIATION 2020 FORUM*, page 2581, 2020.
- [82] Lars Koop. *Aktive und passive Strömungsbeeinflussung zur Reduzierung der Schallabstrahlung an Hinterkantenklappen von Tragflügeln*. PhD thesis, Technische Universität Berlin, 2005.
- [83] Lars Koop, Klaus Ehrenfried, and Andreas Dillmann. Reduction of flap side-edge noise: Passive and active flow control. *AIAA Paper*, 2803:2004–, 2004.
- [84] Michael J Lighthill. On sound generated aerodynamically. i. general theory. *Proceedings of the Royal Society of London. Series A. Mathematical and Physical Sciences*, 211(1107):564–587, 1952. ISSN 1364-5021.
- [85] Michael J Lighthill. On sound generated aerodynamically. ii. turbulence as a source of sound. *Proceedings of the Royal Society of London. Series A. Mathematical and Physical Sciences*, 222(1148):1–32, 1954. ISSN 1364-5021.
- [86] David P Lockard and Geoffrey M Lilley. The airframe noise reduction challenge. *NASA/TM*, 213013:–, 2004.
- [87] Kenneth W McAlister and RK Takahashi. Naca 0015 wing pressure and trailing vortex measurements. Technical report, 1991.
- [88] S. A. McInerny, W. C. Meecham, and P. T. Soderman. An experimental investigation of wing tip turbulence with applications to aerosound. In *AIAA 10th Aeroacoustics Conference*, June 1986.
- [89] SA McInerny, WC Meecham, and PT Soderman. Pressure fluctuations in the tip region of a blunt-tipped airfoil. *AIAA Journal*, 28(1):6–13, 1990. ISSN 0001-1452.
- [90] Kristine Meadows, Thomas F. Brooks, William M. Humphreys, William Hunter, and Carl H. Gerhold. Aeroacoustic measurements of a wing-flap configuration. In *3rd AIAA/CEAS Aeroacoustics Conference*, 1997.
- [91] W. C. Meecham, T. D. Bui, and W. R. Miller. Diffraction of dipole sound by the edge of a rigid baffle. *The Journal of the Acoustical Society of America*, 70(5):1531–1533, 1981. doi: <http://dx.doi.org/10.1121/1.387112>. URL <http://scitation.aip.org/content/asa/journal/jasa/70/5/10.1121/1.387112>.
- [92] WC Meecham. Aerosound from corner flow and flap flow. *AIAA Journal*, 21(2):228–234, 1983. ISSN 0001-1452.
- [93] W Möhring. On vortex sound at low mach number. *Journal of Fluid Mechanics*, 85(04):685–691, 1978. ISSN 1469-7645.
- [94] Wendell R. Miller, William C. Meecham, and Warren F. Ahtye. Large scale model measurements of airframe noise using cross-correlation techniques. *J. Acoust. Soc. Am.*, 71(3):591–599, March 1982. URL <http://link.aip.org/link/?JAS/71/591/1>.
-

-
- [95] W.R. Miller. *Flap noise characteristics measured by pressure cross-correlation techniques*. PhD thesis, University of California, Los Angeles, 1980.
- [96] WR Miller. Flight effects for jet-airframe interaction noise. *AIAA Paper*, 784:–, 1983.
- [97] DW Moore and PG Saffman. Axial flow in laminar trailing vortices. *Proceedings of the Royal Society of London. A. Mathematical and Physical Sciences*, 333(1595): 491–508, 1973. ISSN 1364-5021.
- [98] Harry L Morgan Jr. Model geometry description and pressure distribution data from tests of eet high-lift research model equipped with full-span slat and part-span flaps. *NASA TM-80048*, pages –, 1979.
- [99] Thomas J. Mueller, editor. *Aeroacoustic Measurements*. Number ISBN : 978-3-540-41757-6. Springer, 2002.
- [100] Mitsuhiro Murayama, Yuzuru Yokokawa, Kazuomi Yamamoto, Hiroki Ura, Taro Imamura, and Tohru Hirai. Numerical investigation on change of airframe noise by flap side-edge shape. In *19th AIAA/CEAS Aeroacoustics Conference*, pages –. American Institute of Aeronautics and Astronautics, May 2013. doi: 10.2514/6.2013-2067. URL <http://dx.doi.org/10.2514/6.2013-2067>.
- [101] Mitsuhiro Murayama, Kazuomi Yamamoto, Yuzuru Yokokawa, Yasushi Ito, Takehisa Takaishi, Tohru Hirai, and Kentaro Tanaka. Noise reduction design for flap side-edges toward fquroh flight demonstration. In *23rd AIAA/CEAS Aeroacoustics Conference*, page 4031, 2017.
- [102] Stefan Oerlemans and Pieter Sijtsma. Acoustic array measurements of a 1: 10.6 scaled airbus a340 model. *AIAA paper*, 2924:2004–, 2004.
- [103] WRC Phillips. The turbulent trailing vortex during roll-up. *Journal of Fluid Mechanics*, 105:451–467, 1981. ISSN 1469-7645.
- [104] Allan D Pierce. Diffraction of sound around corners and over wide barriers. *The Journal of the Acoustical Society of America*, 55(5):941–955, 1974.
- [105] M. Pott-Pollenske and J. Delfs. Enhanced capabilities of the aeroacoustic wind tunnel braunschweig. In *14th AIAA/CEAS Aeroacoustics Conference*, number AIAA-Paper 2008-2910, May 2008.
- [106] Michael Pott-Pollenske, Werner Dobrzynski, Heino Buchholz, Sebastien Guérin, Gerd Saueressig, and Ullrich Finke. Airframe noise characteristics from flyover measurements and prediction. In *12th AIAA/CEAS Aeroacoustics Conference (27th AIAA Aeroacoustics Conference)*, page 2567, 2006.
- [107] Alan Powell. Theory of vortex sound. *The journal of the acoustical society of America*, 36(1):177–195, 1964. ISSN 0001-4966.

-
- [108] Alan Powell. Why do vortices generate sound? *Journal of Mechanical Design*, 117 (B):252–260, 1995. ISSN 1050-0472.
- [109] Clemans A. Powell and John S. Preisser. Nasa subsonic jet transport noise reduction research. In *ICAS 2000 Congress*, 2000.
- [110] Ronald H. Jr. Radeztsky, Bart A. Singer, and Mehdi R. Khorrami. Detailed measurements of a flap side-edge flow field. In *AIAA 36th Aerospace Sciences Meeting & Exhibit*, number 98-0700, January 1998.
- [111] Raihan Ramdjanbeg, Lothar Bertsch, Karl-Stéphane Rossignol, and Dick Simons. Flap side-edge noise prediction within conceptual aircraft design. In *19. DGLR-Fachsymposium der STAB, 04. - 05. Nov. 2014, München, Deutschland*, 2014.
- [112] A. Revell, G. Iaccarino, and X. Wu. Advanced rans modeling of wingtip vortex flows. In *Center for turbulence proceedings of the summer program*. MACE, University of Manchester, UK, 2006.
- [113] Michel Roger, Stéphane Moreau, and Korcan Kucukcoskun. On sound scattering by rigid edges and wedges in a flow, with applications to high-lift device aeroacoustics. *Journal of Sound and Vibration*, 362:252–275, 2016.
- [114] K.-S Rossignol. Empirical prediction of flap tip noise. In *Proceedings of the 17th AIAA/CEAS Aeroacoustics Conference, Portland, Oregon*, number AIAA 2011-2733, June 2011.
- [115] PG Saffman. Structure of turbulent line vortices. *Physics of Fluids*, 16(8):1181–, 1973. ISSN 1070-6631.
- [116] Philip G Saffman. *Vortex dynamics*. Cambridge university press, 1992.
- [117] R. Sen. Local dynamics and acoustics in a simple 2d model of airfoil lateral-edge noise. In *2nd AIAA/CEAS Aeroacoustics Conference*, 1996.
- [118] R. Sen. Vortex-oscillation model of airfoil side-edge noise. *AIAA Journal*, 35(3): 441–449, March 1997.
- [119] R. Sen, B. Hardy, and G. Miller. Airframe noise sub-component definition and model. Technical Report CR-2004-213255, NASA, 2004.
- [120] Pieter Sijtsma. Clean based on spatial source coherence. In *13th AIAA/CEAS Aeroacoustics Conference (28th AIAA Aeroacoustics Conference)*, Rome, Italy, number AIAA-2007-3436, May 2007.
- [121] PT Soderman, F Kafyeke, J Boudreau, NJ Burnside, SM Jaeger, and R Chandrasekharan. Airframe noise study of a bombardier crj-700 aircraft model in the nasa ames 7-by 10-foot wind tunnel. *International Journal of Aeroacoustics*, 3(1): 1–42, 2004. ISSN 1475-472X.
- [122] B. Storms, D. L. Mathias, and J. C. Ross. Aerodynamic effects of flap-tip treatments of an unswept wing. In *14th Applied Aerodynamics Conference*, pages –, 1996.

-
- [123] BL Storms, TT Takahashi, WC Horne, JC Ross, RP Dougherty, and JR Underbrink. Flap-tip treatments for the reduction of lift-generated noise. *NASA CDTM-21006*, pages –, 1996.
- [124] Bruce L. Storms, James C. Ross, Clifton W. Horne, Julie A. Hayes, Robert P. Dougherty, James R. Underbrink, Daniel F. Scharpf, and Patrick J. Moriarty. An aeroacoustic study of an unswept wing with a three-dimensional high-lift system. Technical Report NASA/TM-1998-112222, NASA, February 1998.
- [125] C.L. Streett. Numerical simulation of fluctuations leading to noise in a flap-edge flowfield. In *36th Aerospace Sciences Meeting and Exhibit*, 1998.
- [126] CL Streett, DP Lockard, BA Singer, MR Khorrami, and MM Choudhari. In search of the physics: The interplay of experiment and computation in airframe noise research; flap-edge noise. *AIAA*, 979:6–9, 2003.
- [127] Takehisa Takaishi, Hiroki Ura, Kenichiro Nagai, Yuzuru Yokokawa, Mitsuhiro Murayama, Yasushi Ito, Ryotaro Sakai, Hirokazu Shoji, and Kazuomi Yamamoto. Fly-over array measurements with jaxa flying test bed ?hisho? In *22nd AIAA/CEAS Aeroacoustics Conference*, page 2710, 2016.
- [128] SK Tang and NWM Ko. Sound sources in the interactions of two inviscid two-dimensional vortex pairs. *Journal of Fluid Mechanics*, 419:177–201, 2000. ISSN 0022-1120.
- [129] SK Tang and NWM Ko. Basic sound generation mechanisms in inviscid vortex interactions at low mach number. *Journal of sound and vibration*, 262(1):87–115, 2003. ISSN 0022-460X.
- [130] C. Tiedemann. *Experimentelle Untersuchungen des Klappenseitenkantenlärm*. PhD thesis, RWTH Aachen, 2009.
- [131] C Tiedemann, G Neuwerth, and R Henke. Localisation of flap edge sound sources by use of spectral analysis and flow investigation. In *12 th AIAA/CEAS Aeroacoustics Conference(27 th AIAA Aeroacoustics Conference)*, pages –, 2006.
- [132] Kazuomi Yamamoto, Kenji Hayama, Toshiyuki Kumada, and Kensuke Hayashi. Fquroh: A flight demonstration project for airframe noise reduction technology-concept and current status. In *22nd AIAA/CEAS Aeroacoustics Conference*, page 2709, 2016.
- [133] Kazuomi Yamamoto, Takehisa Takaishi, Mitsuhiro Murayama, Yuzuru Yokokawa, Yasushi Ito, Masataka Kohzai, Hitoshi Arizono, Ryotaro Sakai, Hirokazu Shoji, Yosuke Ueno, et al. Fquroh: A flight demonstration project for airframe noise reduction technology—the 2nd flight demonstration. In *2018 AIAA/CEAS Aeroacoustics Conference*, page 4087, 2018.
- [134] T. Yardibi, C. Bahr, N.S. Zawodny, F. Liu, L.N. Cattafesta III, and J. Li. Uncertainty analysis of the standard delay-and-sum beamformer and array calibration. In

15th AIAA/CEAS Aeroacoustic Conference (30th AIAA Aeroacoustic Conference), number 2009-3120, Miami, Florida, May 2009.

- [135] Y. Yokokawa, M. Murayama, Y. Ito, H. Ura, D. Kwak, H. Kobayashi, S. Shindo, and K. Yamamoto. Noise generation characteristics of a high-lift swept and tapered wing model. In *19th AIAA/CEAS Aeroacoustics Conference, May27-29*, pages –, Berlin, 2013.
- [136] Yuzuru Yokokawa, Takehisa Takaishi, Hiroki Ura, Masataka Kohzai, Mitsuhiro Murayama, Yasushi Ito, Kazuomi Yamamoto, Kazuhide Isotani, Yosuke Ueno, and Kenji Hayama. Acoustic wind tunnel test with 18% scale half-span model toward fquroh flight demonstration. In *23rd AIAA/CEAS Aeroacoustics Conference*, page 4032, 2017.
- [137] G. G. Zilliac. Modelling, calibration, and error analysis of seven-hole pressure probes. *Experiments in Fluids*, 14(1):104–120, December 1993. URL <http://dx.doi.org/10.1007/BF00196994>.